CARDIOVASCULAR FLUID MECHANICS:

I. FLUID DYNAMICS OF PROSTHETIC AORTIC VALVES

II. USE OF THE FAST FOURIER TRANSFORM IN THE ANALYSIS OF CARDIOVASCULAR SOUNDS

Thesis by

Ajit Prithiviraj Yoganathan

In Partial Fulfillment of the Requirement

For the Degree of

Doctor of Philosophy

California Institute of Technology

Pasadena, California

1978

(Submitted July 25, 1977)

This thesis is dedicated to my wife, Rajini,

and to my parents.

Copyright (c) by

Ajit P. Yoganathan

1977

ACKNOWLEDGMENTS

I wish to thank my advisor, Dr. William H. Corcoran, for his support and guidance in all phases of this investigation. I also wish to thank Dr. Earl C. Harrison and Dr. Richard Bing for their advice and for giving me the opportunity to work in close collaboration with them.

The financial support of the Donald Baxter Foundation is gratefully acknowledged.

I wish to thank Edwards, Shiley and Cutter Laboratories for supplying me with the different heart valve prostheses used in this work.

The construction of the different experimental systems and their operation would have been impossible without the help of Hollis Reamer, George Griffith, Ray Reed and John Yehle.

I also wish to thank all the undergraduates who have worked with me, especially John DeSilva, John Loo and Bing Ho Ko.

The moral support of my colleagues in the Chemical Engineering Department and the undergraduates of Ruddock House is deeply appreciated.

Finally, I would like to thank Ruth Stratton who spent many hours typing this thesis, and Donna Johnson who typed all my publications.

ABSTRACT

Pressure drops across ten prosthetic aortic heart valves have been measured under both steady and pulsatile flow using two different Newtonian liquids having viscosities of 0.01 dyne sec/cm^2 and 0.035 dyne sec/cm^2, respectively. The experimental results and the theory developed indicate that for a given aortic valve it is possible to predict peak systolic and mean systolic pressure drops from experimental pressure-drop data for steady flow. The difference in viscosities of the test fluids, 0.01 and 0.035 dyne sec/cm^2, seemed to have negligible effect within experimental error on the pressure drops over a range of flow rates from 83.0 cm^3/sec to 500.0 cm^3/sec.

A laser-Doppler anemometer was used to study the *in vitro* velocity profiles in the near vicinity of a Starr-Edwards 1260 ball valve, a Smeloff-Cutter ball valve, a Cooley-Cutter disc valve, and a Björk-Shiley tilting disc aortic prosthesis. The experiments were conducted under steady flow conditions. The experimental results indicate that all the aortic prostheses studied create very disturbed flow fields and cause large wall and bulk turbulent shear stresses in their near vicinity. If such stresses occur *in vivo* they could damage the endothelial lining of the ascending aorta, red blood cells and platelets, and could lead to thrombus formation and hemolysis.

A detailed study of the Björk-Shiley tilting disc aortic prosthesis reveals that it is possible to correlate the *in vitro* velocity measurements with two late pathological failure modes observed in recovered Björk-Shiley aortic prostheses.

The fast Fourier transform (FFT) was used in the frequency analysis of the first and second heart sounds in normal man, and the closing sounds of aortic prostheses produced in a pulse duplicator. An initial study indicates that frequency analysis via the FFT technique could be used as a non-invasive diagnostic tool for some cardiovascular problems.

TABLE OF CONTENTS

Figure Captions

List of Tables

Chapter 1

GENERAL INTRODUCTION

The human cardiovascular system is very complex, and the diseases which affect it are to a large extent interlinked with the fluid dynamics of the system. A better understanding of the flow characteristics would help in obtaining basic insight and treating pathological conditions such as atherosclerosis, hardening of the arteries, formation of aneurysms, valvular heart disease and malfunctioning prosthetic heart valves. Cardiovascular fluid mechanics has over the past 15 years become a field of active research. Many of the problems encountered in the field are, however, very complex and as yet not fully understood.

In order to enhance the understanding of cardiovascular fluid mechanics the present experimental study was undertaken. The study is divided into two parts. In Part I certain fluid dynamic aspects of prosthetic-aortic heart valves are studied under in vitro conditions in the laboratory. It is hoped that a better understanding of the fluid mechanics of the different designs of prosthetic valves will help reduce or eliminate the problems and complications associated with these valves. It is also the long-term goal of such research to develop an ideal prosthetic heart valve, or at least a better and longer-lasting prothesis.

Part II of the study was the non-invasive measurements of heart sounds from normal humans and the in vitro sound measurements in the near vicinity of prosthetic aortic valves in a pulse duplicator system. The work is an initial study to determine base-line frequency

characteristics, if any, of some of the sounds produced in the cardiovascular system. The sounds produced are interlinked to the fluid mechanics. The results are potentially applicable to non-invasive methods for detection of pathological conditions in the cardiovascular system, with particular interest in predicting possible failure modes of prosthetic heart valves.

In order to give the reader some general background information, a brief anatomic and physiologic description of the left heart is given in the next section.

1.1 Brief Anatomical and Physiological Description of the Human Left Heart

The left heart of the human cardiovascular system receives oxygenated blood from the lungs and pumps this blood to various parts of the body. It consists of a low-pressure collecting tank known as the left atrium and a high pressure pump known as the left ventricle. As oxygenated blood returns from the lungs through the pulmonary veins it collects in the left atrium. During the isovolumic relaxation phase of the left ventricle, the pressure in the ventricle falls rapidly. When the pressure in the left ventricle falls below the pressure in the left atrium, the mitral valve opens, and blood flows into the ventricle. The period of relaxation and ventricular filling is known as diastole. During the filling period, blood flows continuously into the atrium and the ventricle. Most of the ventricular filling during diastole occurs passively. At the beginning of the isovolumic contraction phase of the left ventricle, the mitral valve closes, and the pressure rises in the ventricle. A properly functioning mitral valve prevents any flow of

blood from the ventricle into the atrium during this period. When the pressure in the left ventricle rises above the pressure in the ascending aorta, the aortic valve swings open, and blood is ejected into the aorta. The period of isovolumic contraction and ejection is known as systole. At the end of systole the aortic valve closes and prevents any blood from flowing back into the ventricle.

Figure 1 schematically shows typical events of the cardiac cycle which occur with a heart rate of about 78 beats/min. This figure should not, however, be used to obtain accurate values. In a normal human being at rest, the atrium pressure oscillates between about 0 and 10 mm Hg, the ventricular pressure between 0 and 120 mm Hg, and the aortic pressure between 80 and 120 mm Hg. The cardiac output under these conditions is about 4 to 6 l/min. The systolic period is about 30% to 42% of the full cycle time. Under vigorous exercise, this same normal heart may have a cardiac output up to 35 l/min and a heart rate of 180 beats/min.

Proper functioning of the mitral and aortic valves is necessary for maintaining proper blood flow throughout the cardiovascular system. It should be noted that these two valves are unidirectional valves. For the normal adult heart which varies in weight from about 280 to 350 grams, the normal adult mitral valve measures about 35 mm across its major diameter, and the aortic valve measures about 25 to 27 mm. The mean internal diameter of the ascending aorta is about 25.4 mm and it has a wall thickness of about 2 mm. The mean pressure drop at normal cardiac output across a normally operating aortic valve is about 2 mm Hg, while the corresponding pressure drop across a normal mitral valve

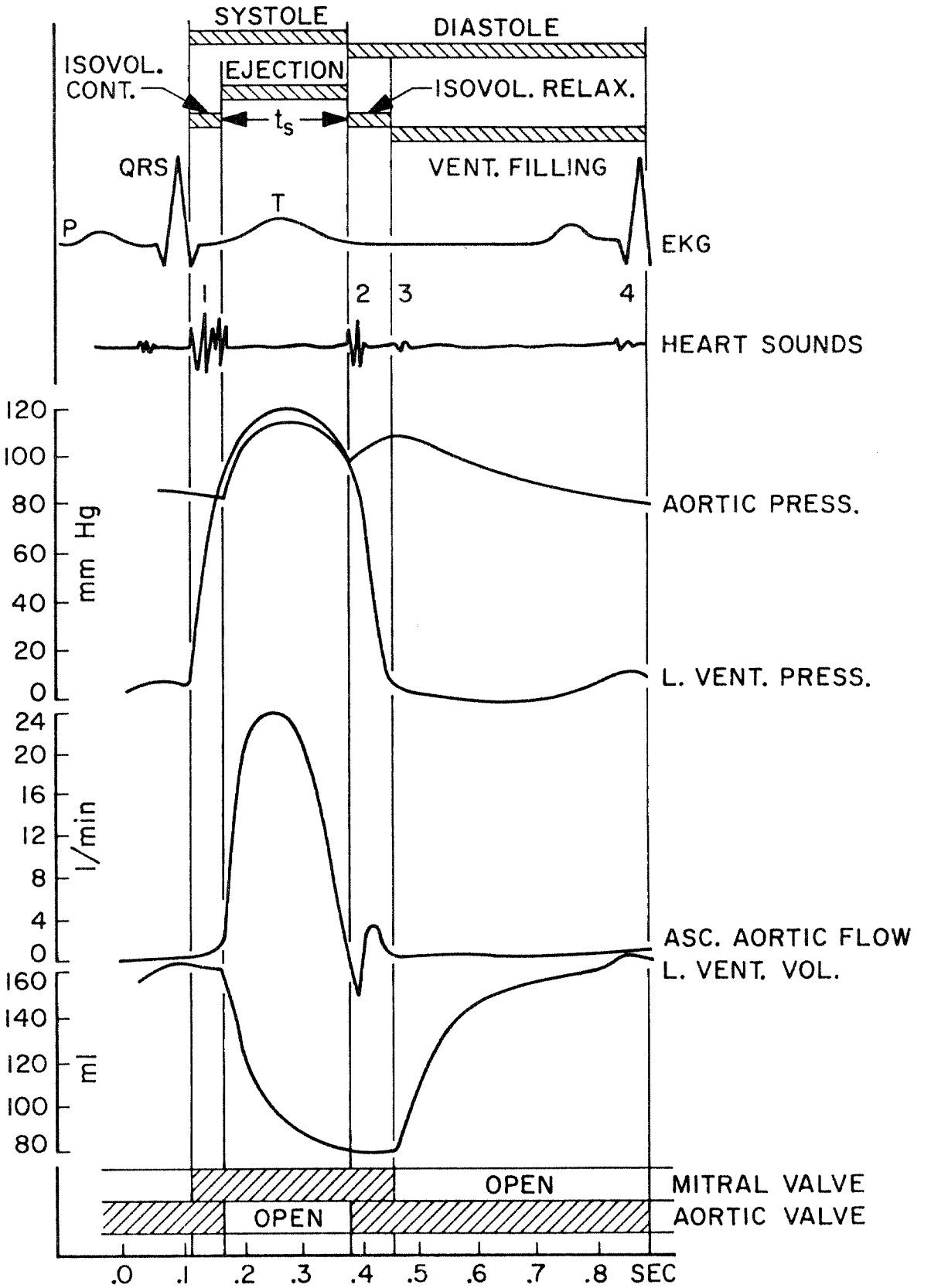

Fig. 1. Events of the cardiac cycle

is less than 1 mm Hg.

Blood is a non-Newtonian fluid, which may be assumed to be Newtonian when flowing in the large arteries such as the aorta. It has a viscosity of about 0.030 to 0.050 dyne sec/cm^2 and a density of about 1.05 g/cm^3.

PART I

FLUID DYNAMICS OF PROSTHETIC AORTIC VALVES

Chapter 2

INTRODUCTION AND BACKGROUND TO PROBLEM

Heart disease is at present the major cause of death in the United States of America. Of the roughly two million deaths occurring annually in the U.S.A., 37.8% are due to heart disease, 19.5% to cancer, 10.2% to strokes, 4.3% to lung disease, 5.3% to accidents, 1.9% to diabetes, 1.7% to cirrhosis of the liver, 1.4% to suicide and 1.1% to homicide [1]. Heart-valve disease is one of the main afflictions of the cardiovascular system. It is common and can be caused by rheumatic fever, ischemic heart disease, bacterial or fungal infection, connective-tissue disorders, trauma and malignant carcinoid. In advanced form it leads to various disabilities and ultimately death. The valves that are most commonly affected are the mitral, aortic, and tricuspid valves. Malfunction of the valves affects their hemodynamic performance. The hemodynamics are affected by a defective valve in two primary ways:

1. By stenosis, which is a narrowing of the valve to give a larger resistance to blood flow and therefore a larger pressure drop across the valve;
2. By incompetence, which is the failure of the valve to close completely. Blood then flows in the reverse direction (regurgitation) when the valve should be shut.

Both of these conditions reduce the efficiency of the heart and place additional stress and strain upon it.

The decision to perform corrective surgery on the natural valve or replace it with a prosthetic valve is often made on the basis of an

evaluation of the functional impairment of the natural valve. Table 1 shows a classification for such an evaluation as proposed by the New York Heart Association [2]. Usually, surgery is limited to patients belonging to classes 3 and 4. Wright [3,4] gives a fluid-dynamic method of classification for the aortic valve as shown in Table 2.

An ideal prosthetic heart valve has not yet been developed. Wright [3,4] and Soderlund [5] give some of the main requirements for an ideal prosthetic valve, which are summarized below. It must

1. Be fully sterile at the time of the implantation and nontoxic;
2. Be surgically convenient to insert at or near the normal ring structure of the heart;
3. Conform to the heart structure rather than the heart structure conform to the valve (i.e., the size and shape of the prosthesis should not interfere with cardiac function);
4. Show a minimum resistance to flow so as to prevent a significant pressure drop across the valve (less than 20 mm Hg);
5. Have a minimal reverse flow necessary for valve closure so as to keep the incompetence of the valve at a low level (less than 20%);
6. Show low mechanical and structural wear of the valve;
7. Be long-lasting (25 years), and its functional performance must not deteriorate with time;
8. Cause minimum blood trauma so as not to cause anemia;

Table 1. Classification of Organic Heart Disease by the New York Heart Association [2]

Class 1 (0–15% impairment)	Class 2 (20–40% impairment)	Class 3 (50–70% impairment)	Class 4 (80–95% impairment)
Organic heart disease exists, but without resulting symptoms	Organic heart disease exists, but without resulting symptoms at rest	Organic heart disease exists, but without resulting symptoms at rest	Organic heart disease exists with symptoms even at rest
Walking, climbing stairs freely, and the performance of the usual activities of daily living do not produce symptoms	Walking freely on the level, climbing at least one flight of stairs, and the performance of the usual activities of daily living do not produce symptoms	Walking more than one or two blocks on the level, climbing one flight of ordinary stairs, or the performance of the usual activities of daily living produce symptoms	The performance of any of the activities of daily living beyond the personal toilet or its equivalent produces increased discomfort
Prolonged exertion, emotional stress, hurrying, hill-climbing, recreation,[a] or similar activities do not produce symptoms	Prolonged exertion, emotional stress, hurrying, hill-climbing, recreation, or similar activities produce symptoms	Emotional stress, hurrying, hill-climbing, recreation, or similar activities produce symptoms	Symptoms of cardiac insufficiency or of the anginal syndrome may be present even at rest
Signs of congestive heart failure are not present	Signs of congestive heart failure are not present	Signs of congestive heart failure may be present, and if so, are usually relieved by therapy	Signs of congestive heart failure, if present, are usually resistant to therapy

[a]Prophylactic restriction of activity such as strenuous competitive sports does not exclude a patient from class 1.

Table 2. Fluid Dynamic Classification of Aortic Valve Disease

Level of Stenosis or Incompetence	Mean Systolic* Pressure Drop, mm Hg	Incompetence* %
Severe	> 100	> 60
Moderate	50 to 100	30 to 60
Mild	20 to 50	20 to 30
Not Significant	< 20	< 20

*Based on a cardiac output of 4 to 5 l/min.

According to the classifications in Table 2 the natural aortic valve will be replaced only if the level of stenosis or incompetence is classified as severe or moderate.

9. Show a low probability for thromboembolism without the use of anticoagulants;
10. Should not be noisy and disturb the patient;
11. Should have a modest price.

Aortic prostheses have been used successfully since 1960, and a review of the early work is given in a book by Merendino [6]. As stated by Roberts [13] the decade of 1960 will probably be remembered most in the annals of cardiology as the decade during which cardiac valve replacement became a successful reality. Of the nearly 50 different cardiac valves introduced over the past 16 years, many have been discarded due to their lack of success, and of those remaining several modifications have been made or are being made at the time of this writing. The most commonly used basic types of aortic valves at present are (a) caged ball, (b) tilting disc, (c) caged disc, (d) tissue valve. At present over 90,000 prosthetic valves of different designs are used annually throughout the world. Even after 16 years of experience the problems associated with the aortic prostheses have not been totally eliminated. The most serious problems and complications associated with them are: (a) red-cell destruction, (b) thromboembolism, (c) valve failure due to material fatigue or chemical change, (d) leaks caused by failure of the valve to close properly, (e) infection, and (f) tearing of sewing sutures [7-13]. A review of the disadvantages and complications associated with the use of heart-valve prostheses is given by Wieting [14]. Roberts [13], in an excellent article, reviews the current status of prosthetic heart valves. Problems (a) and (b) are directly related to the fluid dynamics associated with prosthetic aortic heart valves, and will be discussed in

further detail in the main body of the thesis.

Over the past ten to fifteen years, investigators have concentrated their efforts on experiments to obtain flow patterns around aortic prostheses and to measure pressure drops and retrograde flow across these prostheses [5,15-21]. Davey et al. [15] and Smeloff et al. [16] studied the flow patterns around the Smeloff-Cutter, Kay-Suzuki, Starr-Edwards, Gott-leaflet and Roe-leaflet valves. Swanson [20] observed the flow patterns around caged ball aortic valves. These studies have been very useful but do not provide all the required information for comparison of the fluid dynamic characteristics of various types of aortic valves. Flow visualization experiments only yield qualitative information and no quantitative information. At present the most important information required is the velocity profiles in the near vicinity of the aortic prostheses. Such information is virtually nonexistent in the literature. Weiting [14] attempted to measure velocity profiles under pulsatile flow conditions, using a photographic technique which, however, had some serious drawbacks which are discussed in the main body of the thesis. Wright at Liverpool [22] attempted to measure velocities with hot-wire probes, but found because of the high levels of turbulence, he obtained signals with low signal-to-noise ratios. He was therefore unable to obtain satisfactory results. Recently, Falsetti and Swope [23] measured velocities with a hot-wire anemometer, but their results leave much to be desired.

Most of the <u>in vitro</u> pressure-drop studies carried out up to now with aortic prostheses have been comparative in nature. Forrester et al. [24] studied fifteen different types of aortic prostheses using steady flow of a glycerine-water solution. Björk and Olin [17] compared the

pressure-drop characteristics of the Björk-Shiley tilting disc valve with the Starr-Edwards, Kay-Shiley, Smeloff-Cutter, and Wadda-Cutter valves under pulsatile flow. Kaster et al. [19] compared the Lillehei-Kaster pivoting disc aortic valve with the Wadda-Cutter, Smeloff-Cutter, Starr-Edwards, and fascialata graft-Ionescue prostheses under pulsatile flow in a glycerine-water solution. Duff [18] studied six different aortic prostheses in a pulse duplicator with a Polyol-water solution. Jorgensen et al. [25] compared a trileaflet valve with the Starr-Edwards and Wadda-Cutter valves in a Polyol solution under steady-flow conditions. Soderlund [5] compared the University of Washington trileaflet valve with the Smeloff-Cutter, Starr-Edwards, Wadda-Cutter, and Björk-Shiley valves under pulsatile flow. There are many more steady-flow pressure drop studies performed with either a blood-analog fluid or water which have been published (Nauman and Kramer [26] and Klinzig, et al. [27]), and most of these have been referenced in Roschke's article [28], which gives a good review on prosthetic heart valves from an engineer's point of view. In addition to the in vitro data, there is a large amount of clinical data available in the medical literature on the different types of aortic prostheses.

In the present search through the literature pertaining to pressure drop studies across prosthetic aortic valves, the following important information was found to be missing:

(a) Comparisons of pressure-drop data obtained with water and a blood-analog fluid for the same prosthetic valves in the identical flow channel, and under conditions of both steady and pulsatile flow.

(b) Comparison of values of steady-flow pressure drop with those for peak systolic or mean systolic pressure drop in the same flow channel.

2.1 Statement of Problem

In the summer of 1976, Senators Kennedy and Javits proposed Senate Bill #510, which advocated consumer protection relative to prosthetic medical devices. Legislation was passed "to protect the public health by amending the Federal Food, Drug and Cosmetics Act to assure safety and effectiveness of prosthetic medical devices." In order to enforce this law, the Food and Drug Administration (FDA) is at present working on standard procedures and guidelines for the testing of all prosthetic devices, including prosthetic heart valves.

Prior discussion in Chapter 2 (see pages 12 and 13) indicates that some of the important fluid dynamic aspects of aortic valve prostheses have been overlooked or could not be established due to experimental difficulties. The impetus for the research work reported in this thesis is to provide answers to some of the missing information.

The goals of the present research work were the following:

1. The primary goal was to develop a new and accurate technique for in vitro velocity measurements in the near vicinity of aortic prostheses. A laser-Doppler anemometer was utilized to measure velocities under steady-flow conditions in the near vicinity of four commonly used aortic prostheses. The four valves are shown in Figure 2 and are also listed, together with their sewing ring and primary orifice diameters, in Table 3. Porcine xenograft valves were not tested. Hot-wire or

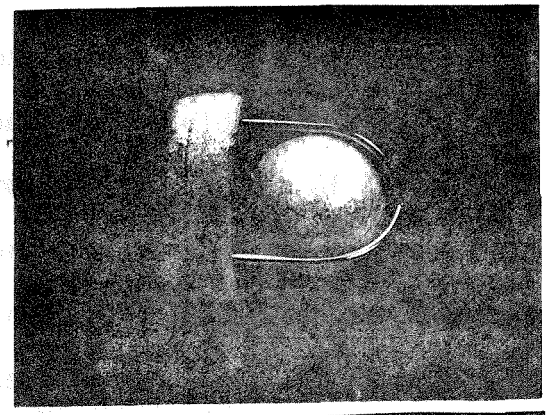

(a) Starr-Edwards 1260-12A ball valve

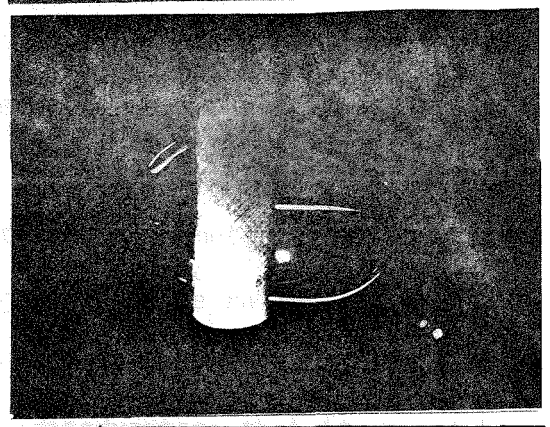

(b) Smeloff-Cutter A-5 ball valve

(c) Cooley-Cutter A-25 disc valve

(d) Björk-Shiley 27 XMBRP tilting disc valve

Fig. 2. Aortic valves used in velocity measurement studies

hot-film anemometers were not used in this work because it was felt that the probes would disturb the flow in the near vicinity of the aortic prosthesis. The use of a 1 or 2 mm probe in a 25.4 mm diameter would, for example, superimpose unwanted disturbances on an already disturbed flow field. Laser-Doppler anemometry is a relatively new technique which has major applications in the field of prosthetic-valve fluid dynamics and other areas of biomedical fluid mechanics. The laser-Doppler anemometer has the advantages that it is a measuring system that requires no probes to be inserted in the flow channel. Unlike the hot-wire or hot-film anemometers, it requires no calibration. It also has a high signal-to-noise ratio, and therefore can be used to measure velocities in highly disturbed flow fields with good accuracy. It does, however, have the disadvantage that it cannot be used to measure velocities in an opaque system. With the laser-Doppler anemometer, velocities very close to the valves and very close to the flow channel walls have been obtained accurately. The velocity profile measurements are used to measure wall-shear stresses and to estimate the turbulent shear stresses in the bulk fluid, as well as to identify areas of high and low flow in the near vicinity of the prosthesis. Such velocity measurements are required to test the hemodynamic performance of the existing valves and to obtain necessary information to improve their designs.

2. Another goal of major importance was to use the velocity measurements obtained in the near vicinity of a commonly used aortic valve to explain the distribution of thrombus formation and tissue overgrowth on the valve. The Björk-Shiley tilting disc aortic prosthesis was studied in detail in such a manner. The work was conducted in close

collaboration with the Cardiology Section of the Los Angeles County-U.S.C. Medical Center.

3. Another goal was to investigate the effects of viscosity on the pressure-drop across aortic prostheses under both steady and pulsatile flow.

4. Also, it was hoped to develop a correlation between steady-flow pressure-drop data with those for peak systolic or mean systolic pressure drops in the same flow channel.

In the pressure-drop studies (goals 3 and 4), ten different valves were used, and these are listed in Table 4.

Table 3. Prosthetic Aortic Valves Used in Velocity Measurement Experiments

Type of Valve	Size	Orifice diameter (mm)	Sewing ring diameter (mm)
Starr-Edwards caged ball valve (1260)	12A	16.62	27
Björk-Shiley tilting disc valve	27XMBRP*	21.98	27
Semloff-Cutter caged ball valve	A5	17.23	26
Cooley-Cutter caged disc valve	A25	19.25	25-26

*The mitral type Björk-Shiley prosthesis was used since it was suggested by the manufacturer that the mitral sewing ring would best fit the aortic heart valve chamber used in the present study.

Table 4. Prosthetic Aortic Valves Used in Pressure-Drop Experiments

Type of Valve	Size	Orifice Diameter (mm)	Sewing Ring Diameter (mm)
Starr-Edwards caged ball valve (1260)	12A	16.62	27
Starr-Edwards caged ball valve (1260)	10A	15.47	24
Starr-Edwards caged ball valve (2320)	10A	15.62	24
Starr-Edwards caged ball valve (2400)	10A	15.75	24
Björk-Shiley tilting disc valve	27XMBRP*	21.98	27
Björk-Shiley tilting disc valve	25XMBRP*	19.88	25
Smeloff-Cutter caged ball valve	A5	17.23	26
Smeloff-Cutter caged ball valve	A4	16.24	24
Cooley-Cutter caged disc valve	A25	19.25	25-26
Cooley-Cutter caged disc valve	A24	18.16	24-25

*See footnote in Table 3

The pulsatile flow experiments were conducted in a pulse duplicator developed and built in the Chemical Engineering Laboratory at Caltech.

Chapter 3

EXPERIMENTAL APPARATUS AND TECHNIQUE

3.1 Flow Channel

All the fluid dynamic experiments were conducted in the flow channel shown schematically in Figure 3. It was constructed of lucite tubing which had an inner diameter of 25.4 mm and a wall thickness of 3.18 mm. The flow channel was patterned after an adult with a 25.4 mm internal diameter ascending aorta, and an aortic valve size of 24 to 27 mm. The flow channel consists of three sections. "A" is the inlet section and represents the outflow tract from the left ventricle into the aorta. When the ventricle is pumping blood into the aorta, its dimensions keep rapidly changing. It is therefore very hard to estimate an exact size and shape for the ventricle during this time period, so it was decided in consultation with Dr. Harrison to make the inlet section (i.e., the outflow tract into the aorta) the same size as the ascending aorta (25.4 mm). Such a size estimation was considered fairly realistic.

"B" is the heart valve chamber and simulates the root of the aorta and the sinuses of Valsalva. The sinuses of Valsalva are three bulges, which appear symmetrically at the root of the aorta. The three cusps of the natural aortic valve open into these three sinuses respectively, when the valve opens. The valve cusps therefore stay out of the way and offer no resistance to the flow. From two of these sinuses the coronary arteries take origin. The dimensions of chamber "B" were obtained from fluoroscopic movies made of patients with aortic prostheses whose ascending aortas had mean internal diameters of 25.4 mm, and

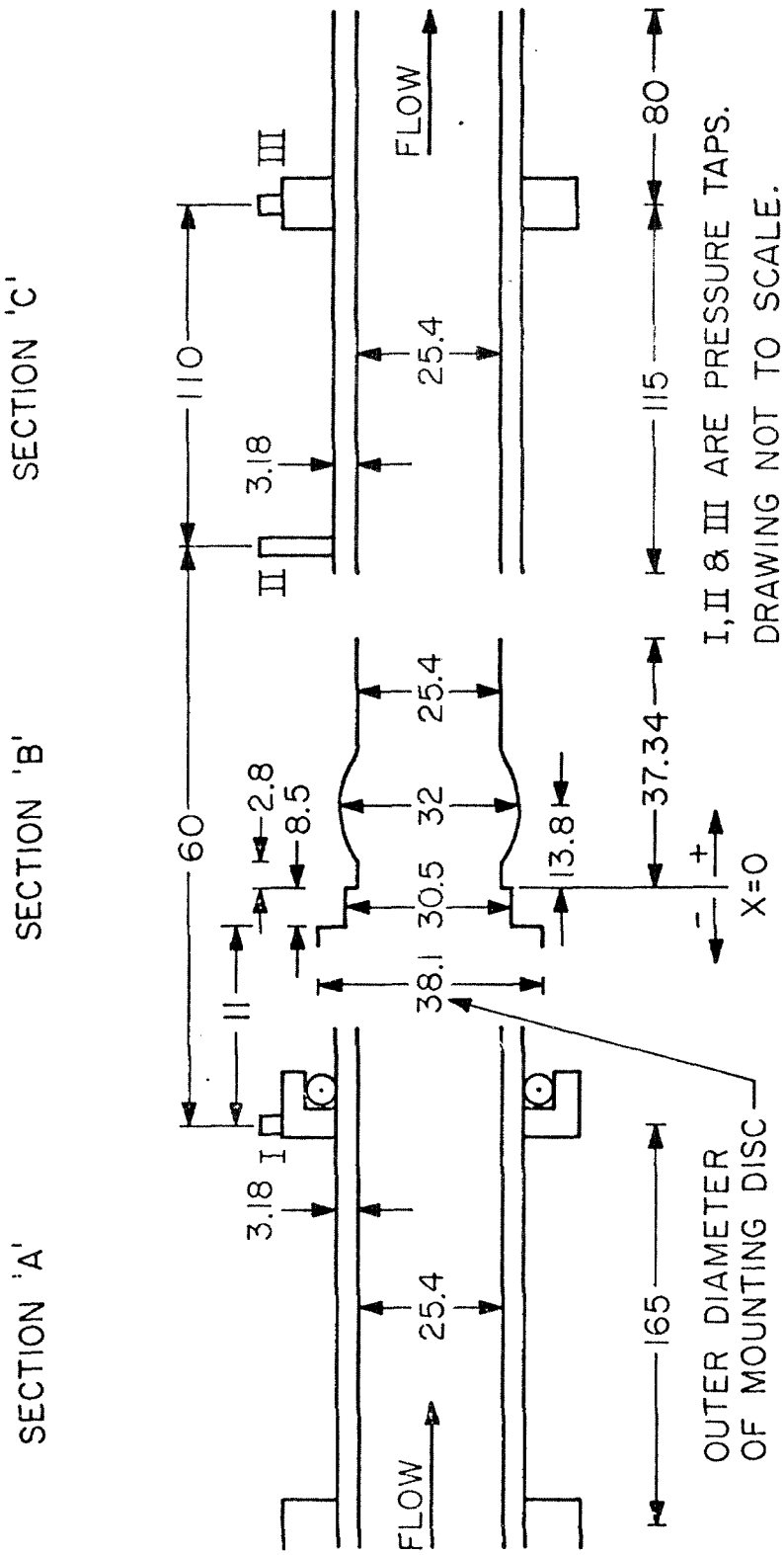

Fig. 3. Schematic of flow channel

aortic valve sizes ranging from 24 to 27 mm. A casting of the left heart and the ascending aorta of a patient obtained at autopsy by Dr. Harrison was also used. Therefore, the heart valve chamber used in this study could anatomically accommodate prosthetic aortic valves with sewing ring diameters of 24 to 27 mm. The valve chamber was cast from lucite. Figure 3 shows schematically one sinus at the top and one at the bottom. In reality, however, the heart valve chamber had one sinus at the top and two on the sides, as shown in Figure 4, with the three sinuses about 120° apart from one another. In order to measure velocities with the laser-Doppler anemometer in the sinus region, a hollow lucite box 44 x 67 mm was built around the sinus section.

"C" is the outlet section, and it represents the ascending aorta and has an ID of 25.4 mm. There are three pressure taps placed on the flow channel as shown in Figure 3.

3.2 Steady-Flow Apparatus

The flow apparatus as shown in Figure 5 consists of the following sections: (a) immersible centrifugal pump (Little Giant), (b) entrance section, (c) flow channel, (d) rotameter (Brooks 10-1110), and (e) needle valve. The outlet of the pump is connected to the entrance section by a 1675 mm length of 25.4 mm ID rubber hosing. The entrance section consists of a 1400 mm length of 25.4 mm ID lucite tubing. This lucite tube is coupled to the flow channel and held in place and aligned by a lucite collar. The entrance section insures that the flow entering the flow channel has reached a steady state (i.e., entrance effects are not present).

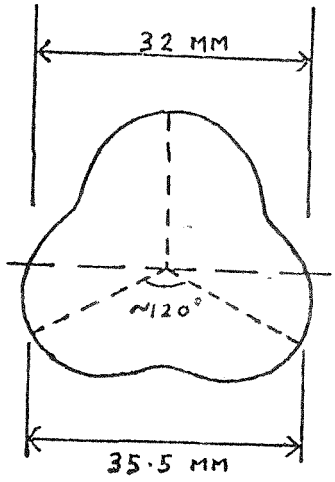

DIAGRAM NOT TO SCALE

AT CENTERLINE, INSIDE
WALL TO WALL DISTANCE = 32 MM

SINUS TO SINUS DISTANCE = 35·5 MM

Fig. 4. Schematic diagram of the sinuses of Valsalva

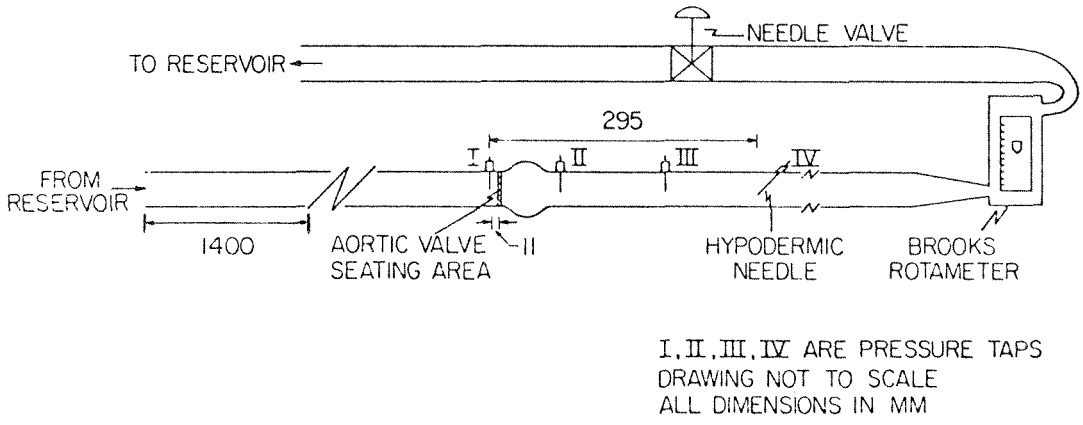

Fig. 5. Flow system for steady flow experiments

The prosthetic valves were mounted on thin metallic circular discs which had been carefully machined so that the sewing rings of the valves fitted the orifices for the respective discs. The outer dimensions of all the discs were identical and fitted into the heart-valve chamber. The valves were placed in the flow channel so that the front ends of their valve seats were against the shoulder in the flow channel at the position X = 0 as shown in Figure 3. In doing this, if there was any space between the back end of the valve seat and the metallic disc, this space was filled by a lucite disc with an orifice diameter equal to that of the metallic disc, and an outer diameter of 30.5 mm (see Figure 3). Therefore the prosthetic valves were held firmly in place between their respective metallic discs and the shoulder in the flow channel at the position X = 0. It should be noted that all distances upstream or downstream of the valves are measured from the position X = 0.

3.3 Pulse Duplicator System

In the course of the heart valve protheses studies, it became necessary to develop a flow system which would duplicate the flow and pressure characteristics of the human heart. The system, which was entirely developed in the Chemical Engineering Department and is known as the Caltech pulse duplicator, is shown in Figures 6 and 7.

The system has been divided up into 8 main units. Each unit was developed to serve a particular purpose, as described below:

Unit 1: Fluid Reservoir and Atrial Pressure Simulator. The primary purpose of this unit is to simulate the atrial pressure of the human

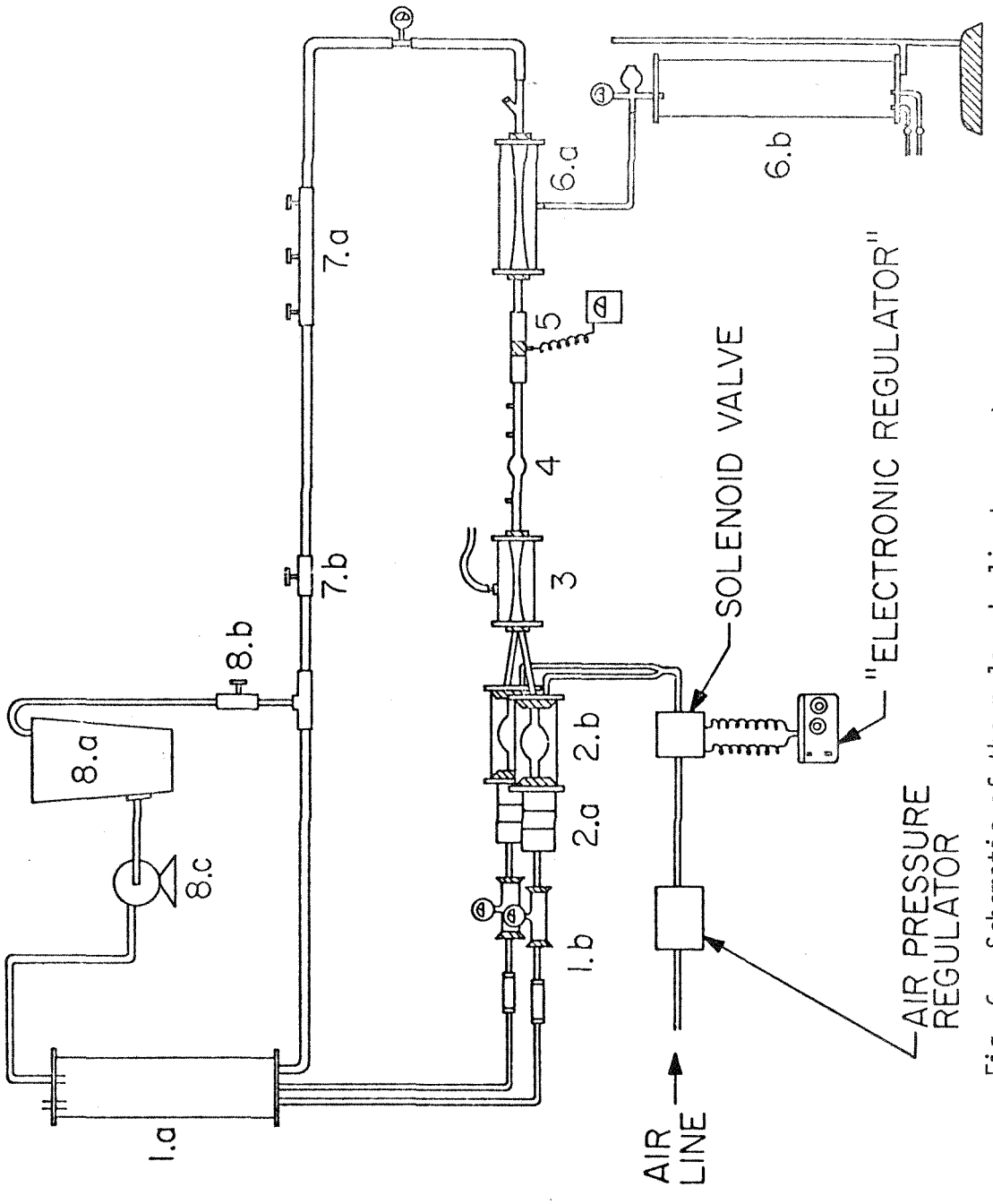

Fig. 6. Schematic of the pulse duplicator system

heart. It also acts as a fluid reservoir for the system. It consists of a tank (1.a), some "shock absorbing" Gooch tubing, and pressure gauges (1.b). The tank consists of a 51 cm long section of 7.6 cm OD lucite tubing with the ends plugged by rubber stoppers. The stoppers are held in place with metal endplates, connected by brass tie rods. The tank is held with the central axis vertical. In the top stopper, a vent pipe (with hand operated valve) and a fill pipe (from an external reservoir) are mounted. The return flow pipe and two outlet pipes are mounted in the bottom stopper. All of these pipes consist of 1.27 cm ID lucite tubing.

Each of the two outlet pipes is connected to a 23 cm section of Gooch tubing by short lengths of heavy rubber hose. The Gooch tubing, because of its extremely flexible nature, acts as a "shock absorber" for the many extraneous pressure oscillations. The Gooch tubing for each line is directly connected to a blood pressure gauge. The gauge taps the pressure through a bronze T-fitting.

In practice, a fair duplication of the human atrial pressure (0 to 10 mm Hg) is attained by maintaining the appropriate level of fluid in the reservoir. The atrial pressure is monitored by the blood pressure gauges. During each heart cycle the fluid level in the reservoir changes only slightly (2-3 cm). The fluid used in our experiments had a density approximately that of water, which implies a pressure variation of .15-.22 torr for liquid level change of 2 to 3 cm in the reservoir.

It was found that because of the large amount of flexible material in the system, the total volume of the system was pressure-dependent. If the average pressure was high, the various Gooch tubings and rubber

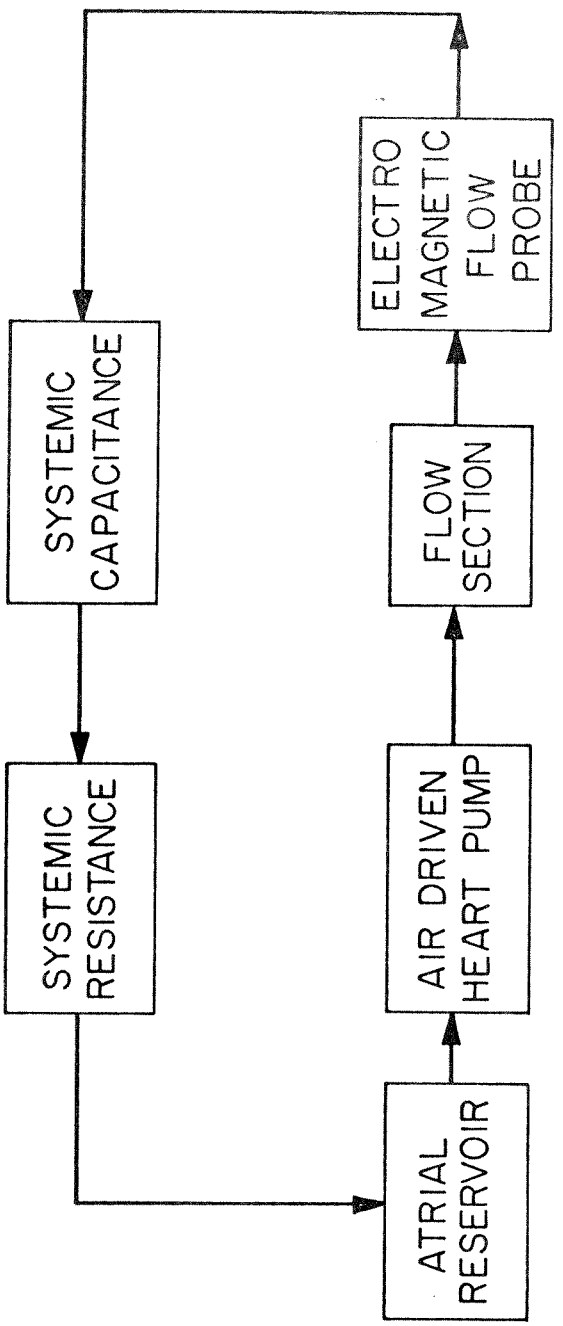

Fig. 7. Flow diagram of the Caltech pulse duplicator

hoses would expand, increasing the volume of the system and altering the level of fluid in the reservoir. Thus, the fluid tank also served as a holding area for excess fluid which might have been generated or needed while adjusting the flow parameters.

Unit 2: Pumps and Electronic Regulator. This unit consists of two identical subunits. They control flow direction, pulse rate, systolic time period, and also partially control the volumetric flow rate and systemic pressure.

The basic subunit contains a 80 ml rubber bulb which has two outlets and is commonly used in analytical chemistry laboratories for pipetting liquid chemicals. The bulb is mounted lengthwise in a 16.2 cm long, 7.6 cm OD lucite chamber. The ends of the chamber are plugged with rubber stoppers and metal end plates as in Unit 1.a. Two lengths of copper wire run lengthwise through the chamber, and are placed in such a manner that they slightly compress the sides of the rubber bulb. On either end, short lengths of 1.27 cm ID lucite tubing pass through the stoppers and the necks of the bulb. The upstream lucite tube connects through another rubber stopper to a 7.6 cm long 3.2 cm OD lucite tube chamber (2.a). This chamber houses a one-way rubber leaflet valve. The leaflet valve is supposed to represent the human mitral valve, and it opens only in the downstream direction. The leaflet valve chamber (2.a) is attached to the upstream metal end plate of bulb chamber (2.b) with brass tie rods, making the two chambers into a single subunit.

On the downstream end of the bulb chamber, a copper tube passes through the rubber stopper and enters the chamber. The copper tube vents

or exhausts high pressure air into or from the chamber surrounding the rubber bulb. The copper tube is connected to an air line via a three-way (intake, exhaust, and closed) solenoid valve. The solenoid valve is activated by an "electronic regulator" which controls the length of time during which the solenoid valve is in the intake, exhaust, or closed position.

In use, the solenoid receives an electrical signal from the "electronic regulator" and flips to the intake position. High pressure air (12 to 25 psi) passes through the solenoid valve and enters the bulb chamber (2.b), compressing the bulb. When the bulb is compressed the liquid in it is "pumped" in the downstream direction towards the flow channel (Unit 4). Flow direction is maintained by the leaflet valve which stays closed during the period of compression of the bulb. The air pressure is controlled by a pressure regulator. The total time of compression of the bulb known as the systolic period is controlled by the "width setting" on the "electronic regulator". At the end of the systolic period a second signal is sent to the solenoid valve, which then moves to the "exhaust" position, relieving the air pressure in the bulb chamber (2.b) and allowing the bulb to expand and draw in more liquid from the fluid reservoir (1.a). During this phase the leaflet valve remains open. The rate at which the artificial heart pumps is known as the pulse rate, and is controlled by the "rate setting" on the "electronic regulator". The pulse rate can be varied from 40 to 140 beats per minute, while the systolic time can be varied from 30 to 860 msec. It should be noted, however, that the total cycle time must be greater than the systolic time interval.

The volume of liquid pumped by each bulb could be controlled to a certain extent by adjusting the pressure of the incoming air and also by adjusting the squeeze clamps which are placed on the 1.27 cm ID rubber tubes connecting Unit 2 with Unit 3.

Unit 3: Ventricular Pressure Wave Control. Unit 3 controls the ventricular pressure ("ventricular" meaning the area upstream of the aortic prothesis, but downstream of Unit 2.a), the ventricular pressure waveform, and partially controls the flow rate and also acts as a junction for the two fluid lines coming from the two subunits of Unit 2.

This unit consists of a 17.2 cm long section of lucite chamber that is 5.1 cm OD. A 19 cm, 3.2 cm OD section of Gooch tubing is stretched lengthwise through the lucite section, and is held in place by curling the ends of the Gooch back along the outside of the ends of the lucite. Furthermore, there are also rubber stoppers in each end, with metal plates and tie rods holding the stoppers in place. An air tap and hose are mounted on top of the lucite tubing, but for our tests the chamber was generally vented to the atmosphere. Such a setup was adequate to maintain physiological ventricular pressures and waveforms. The waveforms obtained were quite smooth.

In the upstream stopper, two sections of 1.27 cm OD lucite tubing are mounted to collect the flow from the two subunits of Unit 2. These tubes channel the flow into the Gooch tubing. The downstream stopper has a 3.18 cm diameter hole bored through it.

Changing the ambient pressure in the lucite chamber affects the ventricular pressure waveform and also the systolic/diastolic

ventricular pressure ratio. It was also found that increasing the pressure within the chamber increased the magnitude of the flow curve.

Unit 4: Flow Channel. This unit consists of the flow channel which is shown in Figure 3 and described previously. The upstream end of the flow channel, section "A", is slotted into the hole bored in the downstream stopper of Unit 3.

Unit 5: Electromagnetic Flow Meter (Statham SP-2202). This unit is used to measure and monitor instantaneous flow rates downstream of the flow channel. The flow meter measures the induced voltage which is created when an electrolytic fluid passes through an applied magnetic field. The magnetic field is created in the cannulating type flow probe (Statham SP-7507-250), which resembles a plastic tube with a lumen diameter of 25 mm. The flow probe was connected to the adjacent flow sections by 25.4 mm ID rubber hoses. In the test performed in the pulse duplicator either a 0.9 percent-by-weight NaCl in water or an aqueous Polyol solution was used as the electrolytic solution. The electromagnetic flow meter was calibrated against a rotameter at various steady flow rates prior to use in the pulse duplicator system.

Unit 6: Aortic Pressure Waveform Control: Capacitance Section. Unit 6.a is essentially similar to Unit 3 but it controls the aortic pressure waveform instead of the ventricular pressure form. It is also longer (44.5 cm) and has a separate device (6.b) for maintaining the pressure around the Gooch tubing in Unit 6.a.

This second device (6.b) is constructed in a fashion similar to the fluid reservoir in Unit 1. Its dimensions are 50 x 9 cm. It has a

single outlet at the top which is connected to a metal T-fitting. One end of this T is fitted to a pressure regulator device and the other end to the air tap on Unit 6.a as shown in Figure 6. The pressure regulator device consists of a rubber bulb which is connected to a pressure gauge with an exhaust valve. This regulator system is identical to that used in a standard blood pressure measuring device. By closing the exhaust valve and squeezing the rubber bulb it is possible to increase the air pressure in Unit 6. At the bottom of Unit 6.b there are two outlet copper tubes of 6 mm ID. At the end of each of these tubes is a small needle valve which could be shut air-tight. Therefore the entire unit (6.a and 6.b) could be maintained air-tight at a given pressure. Total pressure in the unit is monitored by the blood pressure gauge. The outlet tubes at the bottom of Unit 6.b are used to partially fill it with water and to control the level of water in 6.b. In practice, by partially filling Unit 6.b with water it is possible to decrease the volume of air in Unit 6. By adjusting the volume of air in the tank 6.b, it is possible to control the elasticity of the Gooch tubing in unit 6.a during systole and diastole. Therefore it was possible to reproduce physiologic aortic pressures and waveforms relatively easily during the various experiments.

Unit 7: Aortic Pressure Control: Resistance Section. This unit consists of two subunits. Its primary function is to help control the total systemic pressure during the experiment. One subunit (7.a) consists of a 38 × 5.1 × 5.1 cm section of square aluminum channel, a 41 × 4.5 cm strip of 0.65 cm aluminum plate and three bolts which could pass through the top of the channel. The return tube, which is a 3.2 cm OD rubber hose, passes through the square aluminum channel. The aluminum plate is placed between the hose and the top of the channel. The three bolts are then screwed in through the holes in the top of the channel. As the screws are tightened the rubber hose is constricted between the aluminum plate and the bottom of the aluminum channel, thereby increasing the resistance to flow and the systemic pressure. The second subunit (7.b) consists of 2.54 cm needle valve. The needle valve subunit applies resistance at a point, while the aluminum channel subunit applies resistance over a given length of rubber hose. The use of the needle valve by itself leads to very jagged aortic pressure wave forms. Using it together with the aluminum channel subunit gives smoother aortic pressure wave forms and easier control over the systemic resistance. By adjusting these two subunits together it is possible to vary the total systemic pressure and the flow rate in the system. The needle valve (7.b) also serves another purpose, which is described in the next section.

Unit 8: Drainage Reservoir and Return Pump. Unit 8 serves as a holding area for the fluid when changing the prosthetic valve in the pulse duplicator, or when performing maintenance on the system. The unit consists of a plastic pail (8.a) which is used as a holding tank, a plastic needle valve (8.b) and a small centrifugal pump (8.c). A T-connection is attached to a hose which leads to the inlet of the plastic pail via the

plastic needle valve.

To drain the pulse duplicator system, the plastic valve (8.b) is opened, valve 7.b is closed and the pulse duplicator is started. This diverts the flow into the plastic pail. To refill the system, valve 8.b is closed and valve 7.b opened. Then the centrifugal pump which is connected to the outlet of the plastic pail is started. The outlet of the pump (8.c) is connected by a plastic hose to the top of the fluid reservoir (Unit 1.a) as shown in Figure 6. The pulse duplicator system is filled in this manner.

3.4 Pressure Drop Measuring System

3.4.1 Steady-Flow System

Experiments were conducted at six different flow rates ranging from 83 cm^3/sec to 425 cm^3/sec. The Brooks rotameter had a 100 percent reading of 425 cm^3/sec for water and 417 cm^3/sec for the Polyol solution. The rotameter was calibrated before use, and pressures were measured with either a Statham P23De or P23 Db physiological pressure transducer which was connected to a Honeywell 218-1 bridge amplifier. Pressures were measured in the center of the channel via hypodermic needles (#18 gauge) in the four locations (I,II,III and IV) as shown in Figure 5. The pressure transducer was connected directly to the hub of a hypodermic needle. The rotation of the needles through 360°, such that the orientation of the beveled ends of the needles varied with respect to the direction of the axial flow, had no effect on the measured pressure. This observation indicated that only static pressures were being measured and no pitot-static effect was occurring. The transducers

had a frequency response of at least 30 Hz. The transducer and needle pressure measuring system had a natural frequency of about 185 Hz (tests carried out by Statham Instruments).

The liquids used in the steady flow experiments were water at 22°C and a 6 percent-by-weight Pluracol Polyol V-10 (Wyandotte Chemicals) aqueous solution at 32°C. Water at 22°C had a viscosity of 0.01 dyne sec/cm^2, and the Polyol solution had a viscosity of 0.035 dyne sec/cm^2 at 32°C and a density of about 1.01 g/cm^3. The Polyol solution was Newtonian at the low concentrations. The viscosity of the Polyol solution was checked every 2 to 3 days. The temperatures of the liquids were controlled by lightly blowing air with a table fan over the bucket in which the pump was submerged.

The most common blood analog fluid that is presently used is approximately a 45 percent-by-weight glycerine-water solution. The three main reasons for not using this solution are:

(a) The viscosity is very temperature dependent.

(b) It is fairly expensive.

(c) When it spills in the laboratory everything becomes a sticky mess.

At low concentrations the viscosity of the Polyol V-10 solution has temperature dependence similar to that of water. A forty gallon drum of Polyol costs about $40.00. Since it is used in such low concentrations the solution is not sticky when it spills. One word of caution, however, is that if it is made in large quantities and left to stand it tends to form algae. It is therefore imperative to add some algae inhibitor.

The pressure transducers were calibrated by Statham Instruments prior to purchase. They were, however, recalibrated about every six weeks. The calibration factors remained relatively constant and agreed with those originally obtained by Statham. The pressure readings were obtained by feeding the output from the Honeywell bridge amplifier into an analog integrator (a brief description of which will be given in the next section) where the signal was integrated for about 5 sec. The integrated signal was displayed on a digital voltmeter (Tektronix TM 504) which was also hooked up to an on-line digital printer (Digitec 6130). In this manner a printed output of the pressure readings at each tap was obtained. At any given flow rate, five consecutive pressure readings were made at each tap on a given day, and five more were obtained a few days later. Therefore, for a specific flow rate, the pressure measurement at a given tap was obtained by averaging the ten readings. The experimental procedure led to consistent data and minimized the possible experimental errors. The estimated maximum error in measuring pressure drops was ± 667 dyne/cm^2 ($\pm$ 0.50 mm Hg). The flow rate through the system was controlled by the needle valve shown in Figure 5, and three bypass valves attached to the pump. By means of the bypass valves the total pressure in the flow channel was limited to less than 250 mm Hg. The maximum pressure that could be recorded by either transducer was 300 mm Hg. A larger pressure than this value could damage the transducers.

3.4.2 Pulsatile-Flow System

The pulsatile flow experiments were conducted in the pulse duplicator described previously. In these experiments pressure measurements

were made only at taps I, II, and III. Since the ascending aorta is normally between 60 and 100 mm in length, it was decided that it was not physiologically reasonable to measure pressures at tap IV.

In all the pulsatile flow experiments a pulse or heart rate of 70 beats/min and a systolic ejection time period, t_s, of 300 msec was used. The aortic pressure was maintained at $1.6 \times 10^5/1.07 \times 10^5$ dyne cm^{-2} (120/80 mm Hg). Two different types of experiments were performed under pulsatile flow. One group measured peak pressure-drop and flow during systole. In the second group mean pressure-drop and flow were measured during the systolic ejection period, t_s. Pressure measurements were made with the same equipment used in steady flow, while the flow rate was monitored by a Statham 2202 electromagnetic flow meter and a cannulating type flow probe having an ID of 25.4 mm. The aortic and ventricular pressure-wave signals were not filtered in the Honeywell bridge amplifier.

In the pulsatile and steady flow experiments an analog integrator was used. This integrator was specifically built for this study by the electronic shop in the Chemical Engineering Department. The integrator could be used to integrate signals for as short as 2 msec and for as long as 5 sec. It also had the versatility that it could delay the start of the integration from 1 msec to as long as 2 sec. The integrator was triggered by a positive-going pulse. Such a trigger pulse was emitted by the electronic regulator unit of the pulse duplicator at the beginning of systole of each heart cycle.

The peak aortic peak-pressure-drop occurred over a time span of 5 to 10 msec, and this time span varied from valve to valve. There

was a time delay of about 30 msec between the peak pressure drop and peak flow. The difference, however, is not small enough to assume that the peak pressure drop and the peak flow rate occurred simultaneously. Brockman et al. [29] in looking at *in vivo* pressure drop curves across Starr canine aortic valves, observed that the peak pressure drop and peak flow rate occurred very nearly at the same time. Therefore, the peak pressure drop and flow measurements were obtained by integrating the signals for the appropriate time spans and obtaining the output on the digital printer. Each set of measurements was obtained by averaging readings from 10 to 15 consecutive heart beats. In doing this, any variability introduced by the heart pump was averaged out. It was observed that once the heart pump reached a steady state, the pressure and flow readings were fairly consistent for as long as five minutes. Throughout the experiments, the aortic and ventricular pressure waves and the aortic flow were monitored on a dual-trace-storage oscilloscope (Tektronix TM 406). From polaroid photographs of the flow curve, the acceleration of the fluid at various times could be estimated.

The mean aortic and ventricular pressures were obtained by integrating the aortic and ventricular waves over the systolic ejection time period, t_s, for 10 to 15 heart beats. Systolic ejection time period, t_s, was defined as the time period over which positive aortic flow occurred. In addition, the peak aortic flow rate was also monitored together with oscilloscope tracings of the aortic flow curve on the storage oscilloscope. Polaroid photographs of three or four tracings of the flow curves were then obtained. From these photographs

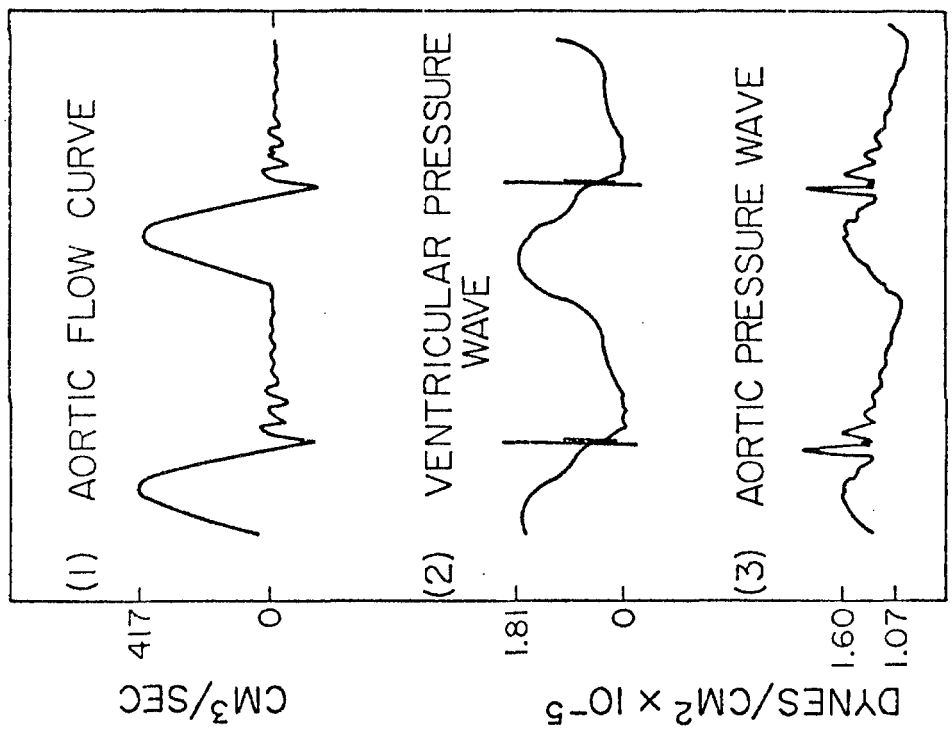

Fig. 8 (pressure curves unfiltered)

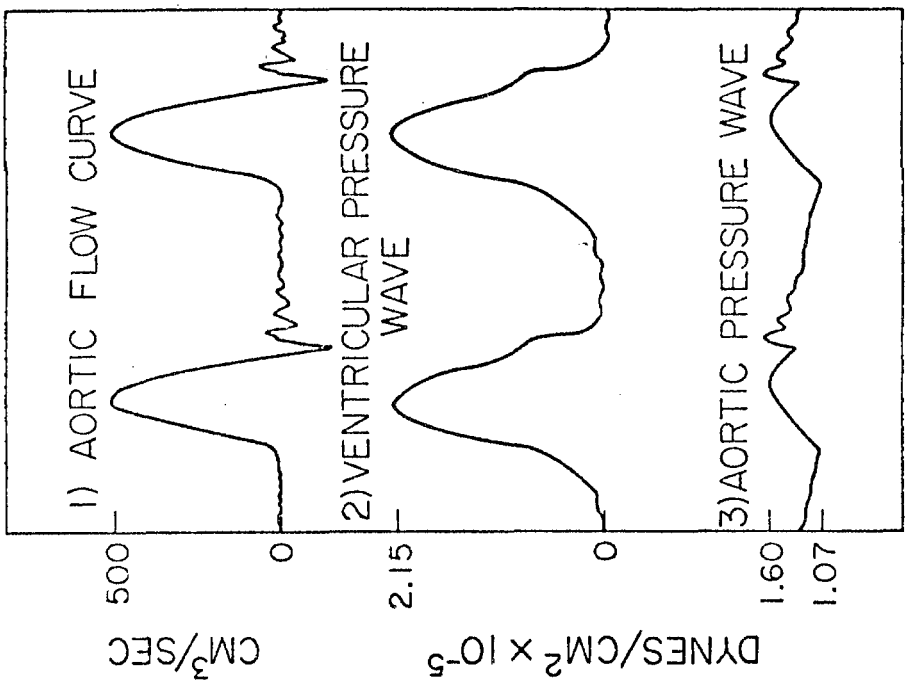

Fig. 9 (pressure curves filtered)

Typical flow and pressure curves obtained in the pulse duplicator

plots of Q^2 vs time were graphed, and an average value of $\overline{Q^2}$ (mean square flow rate) was readily obtained.

For the peak-pressure-drop experiments, saline solution (0.9 percent-by-weight NaCl in water) and a 4.6 percent-by-weight Polyol V-10 aqueous solution which contained 0.9 percent-by-weight NaCl were used. The test temperature was 22°C and the Polyol solution had a viscosity of about 0.035 dyne sec/cm^2. For the mean-pressure-drop experiments, only the Polyol solution was used, because within experimental error there was no observed difference in the pressure drop data in using either saline or Polyol solution. Figures 8 and 9 show typical ventricular and aortic pressure waves and an aortic-flow curve obtained in the pulse duplicator.

3.5 Laser-Doppler Anemometer

3.5.1 General Principle and Theory of Operation of the Laser-Doppler Anemometer

When a laser beam is passed through a flowing fluid, light is scattered by the particles suspended in the fluid. The scattered light suffers a frequency shift which has to be interpreted by electro-optic techniques to obtain information on the velocity of the particles. This method of velocity measurement therefore requires that the flow medium be translucent and contain particles which scatter light.

The frequency relationship between a forward scattered light wave and the incident light wave is given by the vector equation:

$$f_s = f_i + \frac{1}{\lambda} \overline{V} \cdot (\hat{j}_s - \hat{j}_i) \qquad (1)$$

where

f_i = frequency of incident light

f_s = frequency of scattered light

$\hat{j}_i$ = unit vector in incident direction

$\hat{j}_s$ = unit vector in scattering direction

$\overline{V}$ = velocity vector

λ = wavelength of incident light

Now the Doppler frequency f_D is

$$f_D = f_s - f_i$$

Therefore,

$$f_D = \frac{1}{\lambda} \overline{V} \cdot (\hat{j}_s - \hat{j}_i) \qquad (2)$$

The laser-Doppler anemometer uses two incident beams where the beam intersection forms the point of measurement in the flow. The scattered light is collected by a photomultiplier. When two intersecting beams are used, the component of local-flow velocity which is normal to the bisector of the beam intersection angle θ and parallel to the beam plane is related to the Doppler frequency by the equation:

$$V = f_D \cdot \lambda/(2 \sin \theta/2) \qquad (3)$$

where

V = component of local velocity which is normal to the bisector of the beam intersection angle

f_D = Doppler frequency

θ = angle of beam intersection

Therefore,

$$V = f_D \cdot d_f \qquad (4)$$

with

d_f = $\lambda/(2 \sin \theta/2)$ with units of meter/sec/MHz

It can be seen from equation (4) that the Doppler frequency is directly proportional to the velocity. The constant of proportionality is a direct function of the wavelength of the laser and the optical arrangement used in the experiment.

The simple principle of laser anemometry given by equation (3) has some serious limitations in flow measurement. For example, positive or negative values of Doppler frequency shift will result in ambiguity of the actual direction of flow, and Doppler frequencies which approach zero cannot be processed by the electronics (i.e., zero velocity cannot be measured). To overcome these limitations the LDA system that was used incorporates frequency translation and signal processing as explained in the block diagram given in Figure 10.

The block diagram shows how the system combines the fixed-optical-frequency translation (f_o = 40 MHz) of the laser beam with electronic mixing of the detected signal f_{pm} (= f_o+ f_D) and with an electronic local oscillator f_{lo} to produce a total frequency span from -10 to +40 MHz. The fixed-optical-frequency translation is introduced by an acousto-optic modulator.

A photomultiplier picks up the Doppler-shifted light from the point of measurement. The signal contains the Doppler signal as well

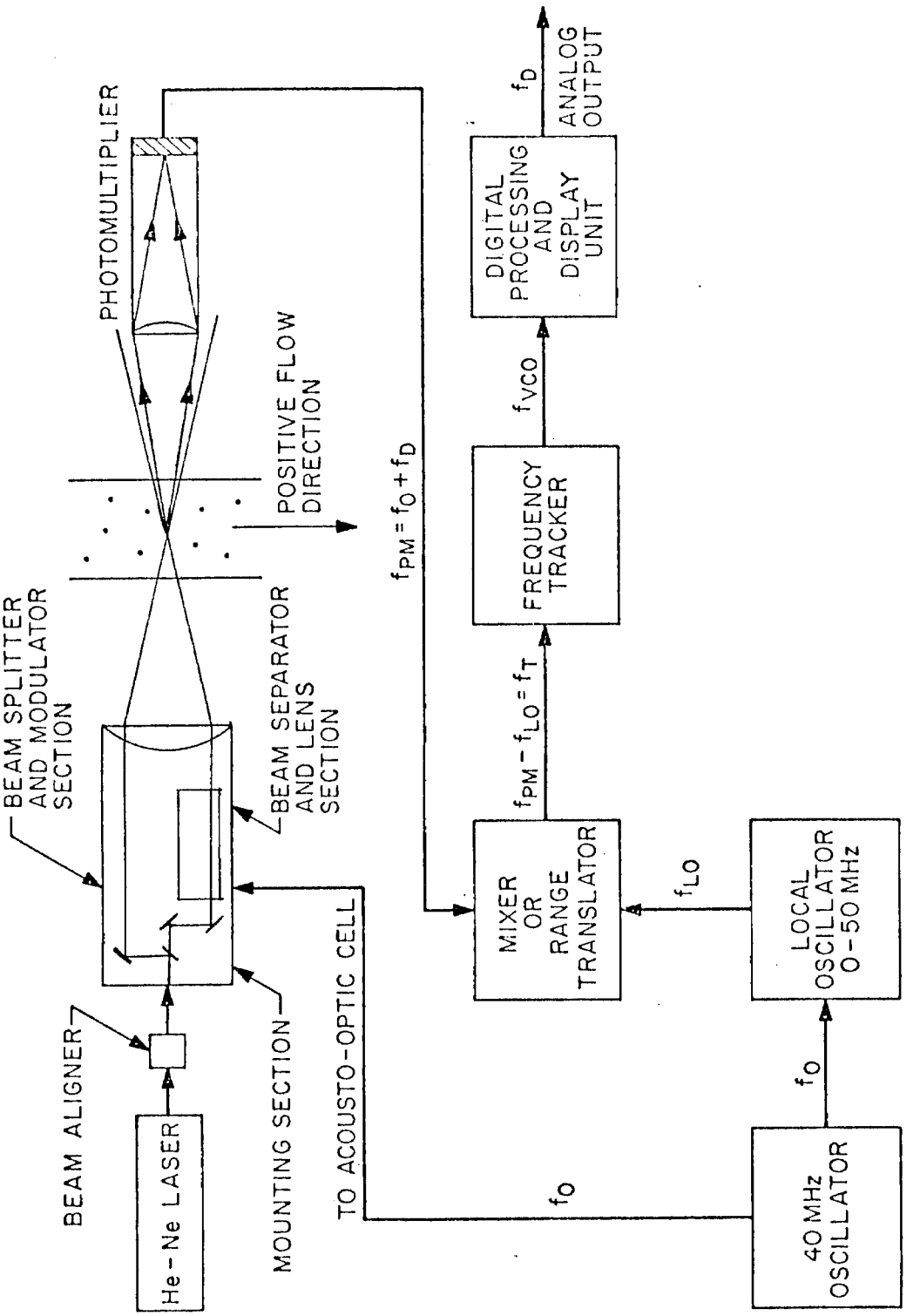

Fig. 10. Block diagram of laser-Doppler anemometer

as the frequency translation from the acousto-optic cell which results in a photomultiplier-signal frequency of $f_{pm} = f_o + f_D$. In the mixer, the photomultiplier signal is mixed with a signal from the local oscillator, and the difference frequency $(f_{pm} - f_{lo})$ is fed into the preamplifier of the frequency tracker for signal processing. The tracker mixes the preamplified signal $(f_{pm} - f_{lo})$ with the signal f_{vco} from a voltage-controlled oscillator. The difference frequency $[f_{vco} - (f_{pm} - f_{lo})]$ is automatically centered at the middle frequency of a relatively narrow band-pass filter in the tracker. This centering is achieved by means of a fast servo loop that controls the value of f_{vco} so that the relation $[f_{vco} - (f_{pm} - f_{lo})] = f_c$ is satisfied. In the display electronics, the frequency of the vco signal $[f_{vco} = f_{pm} - f_{lo} + f_c = f_o + f_D - f_{lo} + f_c]$ is counted. By use of digital techniques, the nonvarying frequency $(f_o - f_{lo} + f_c)$ is subtracted from f_{vco} which leaves the Doppler frequency which is displayed as a voltage.

Equations (1), (2), (3), and (4) are valid for measurements in air. For measurements in a liquid of refractive index η_1, we have from the laws of refraction

$$\lambda_1 \eta_1 = \lambda \eta \tag{5}$$

and

$$\eta_1 \sin \theta_1/2 = \eta \sin \theta/2 \tag{6}$$

where

η = refractive index of air

η_1 = refractive index of liquid

λ_1 = wavelength of laser light in liquid

θ_l = beam intersection angle in liquid

θ = beam intersection angle in air

Therefore from equation (3) we have

$$V = f_D \cdot \lambda/(2 \sin \theta/2) = f_D \cdot \lambda_l/(2 \sin \theta_l/2) \qquad (7)$$

It can be seen from equations (3) and (7) that the expression

$$V = f_D \cdot \lambda/(2 \sin \theta/2)$$

is also valid for velocity measurements in a liquid.

3.5.2 Description of LDA Apparatus

Velocity measurements were made using a laser-Doppler anemometer operated in the dual-beam, forward-scatter mode. Because the laser-Doppler anemometer is a relatively new technique for velocity measurements, a detailed description of it will be given in this section. Figure 10 shows the laser-Doppler system which consists of a He-Ne laser (Spectra Physics 124A) which has a power output of 15 mw and a wavelength of 632.8 nm. The diameter of the laser beam is 1.1 mm measured at the $1/e^2$ points on a Gaussian distribution. The beam from the laser then passes through a laser-beam aligner (Oriel Corp.) on its path toward the optics. The beam aligner has four individual controls which allow for horizontal and vertical translation and horizontal and vertical angle deflection of the laser beam.

The aligned laser beam now enters the LDA transducer unit which is comprised of a mounting section, a beam splitter and modulator section, a beam separator and lens, and a photomultiplier tube. The beam first

axially enters the beam splitter and modulator section (DISA 55L83) through a small window in the mounting section. It then passes through a beam-splitting prism which splits the beam in two, with either a 50/50 or 90/10 intensity ratio. The splitting is achieved by thin metal deposits of two different thicknesses at the interface of the two prisms which make up the beam splitter. The splitting ratio is adjustable by means of the ratio knob. One beam then passes through a Bragg cell where it is diffracted and experiences a frequency shift of ±40 MHz, depending on the orientation of the Bragg cell with respect to the incident laser beam. In the present experimental setup the beam is shifted by -40 MHz. The nonshifted beam is marked on the transducer body as +40 MHz, so that the direction of the flow may be deduced from the sign of the Doppler frequency. A wedge prism is placed between the Bragg cell and the rear prism so that the diffracted beam can be adjusted to make it parallel to the transducer axis. The beam that emerges from the Bragg cell consists of a shifted and an unshifted beam. An adjustable "beam stop" is placed in the path of these two beams so that only the frequency-shifted beam emerges from the Bragg cell section. The other split beam is transmitted through the beam splitter and modulator section so that the optical-beam lengths of the two beams emerging from the transducer are equal. There is one prism in the nonshifted beam path which can be adjusted externally during the experiment to ensure that the two beams intersect.

The Bragg cell consists of a block of isotropic glass with a series of piezoelectric transducers rigidly bonded on one side and an acoustic absorber on the opposite side. The piezoelectric transducers are driven

by an RF voltage which sends a series of acoustic wave fronts across the Bragg cell material. If a laser beam passes through the Bragg cell, there is interaction between the light waves and the acoustic waves. The incident laser beam is diffracted in a number of definite directions, each of them frequency shifted. The direction of diffraction and the frequency shift are direct functions of the direction of the incident laser beam and the frequency of the acoustic wave. At one particular angle of incidence, the incident laser beam is scattered in such a direction that it appears to be reflected from the acoustic wave fronts as if they were mirrors. This angle is known as the Bragg angle, in analogy to the selective reflection of x-rays by the lattice planes of crystals as first observed by Bragg. The value of the frequency shift under these conditions will be equal to the frequency of the acoustic waves in the Bragg-cell material. Depending on whether the laser light is directed to meet the acoustic wave or catch up with it, the frequency shift may be positive or negative.

The two beams (shifted and unshifted) which emerge from the beam splitter and modulator section enter the beam separator, lens, and mounting sections (DISA 55L87). These sections house the beam separating prisms and the focusing lens. Three lenses with focal lengths of 120, 300, and 600 mm, respectively, are available. The beam separation is controlled by means of the beam-separation knob which has the selections of 80, 40, and 20 mm. The mounting section allows the transducer housing to be rotated through 360 degrees which permits measurement of any flow component in a plane orthogonal to the transducer axis without need for realignment even during rotation.

The two emerging beams from the lens are focused so as to cross each other. The point at which the two beams cross is known as the measuring volume. This measuring volume is ellipsoidal in shape. The photomultiplier detects the Doppler-shifted signal which is scattered from the measuring point. The PM tube has a very high upper frequency limit so that it can detect the Doppler signal which has been shifted by 40 MHz. The photomultiplier consists of an optical section and a photomultiplier tube section which operate together. For each lens on the transducer unit (focal lengths of 120, 300 and 600 mm), there is a corresponding lens for the photomultiplier (0.25, 3.25 and 1.75 diopters, respectively.) If the correct corresponding lens is not used, the quality of the signal will deteriorate. The correct lens is mounted on the objective lens which is permanently fixed on the front end of the photomultiplier. The objective lens has a focal length of 105 mm. To ensure that only light from the measuring volume reaches the photomultiplier, a pinhole with a diameter of 0.1 mm is placed in the lens section. The pinhole is at the focal point of the objective lens.

The Bragg cell and the photomultiplier are electro-optic units. The electronic unit used with the optics is the DISA 55L70 LDA control unit. This unit consists of three sections: (a) light modulator exciter (DISA 55L74), (b) photomultiplier exciter (DISA 55L76), and (c) range translator or mixer (DISA 55L72). The light modulator (LM) exciter delivers a 40 MHz signal to the power amplifier for the acousto-optic cell which comprises the Bragg cell. The LM exciter has a crystal-controlled oscillator from which the frequency of the local oscillator in the range-translator is also derived. The cable carrying the 40 MHz signal to the

Bragg cell is triple shielded to eliminate 40 MHz electronic interference. Even so, care must be taken to ensure that this cable is well separated from the photomultiplier cables when making measurements. The PM exciter generates an adjustable high voltage for the PM tube. The anode current from the photomultiplier tube is dependent on the amount of light reaching it and on the voltage supplied. The photomultiplier may be operated at either constant output current or constant input voltage. Control is achieved by selecting either the AUTO or MAN settings, respectively, of the AUTO-MAN selector switch. The range translator has four thumb-wheel switches for setting the electronic-frequency shift f_{lo}. This shift is adjustable between 0 and 50 MHz in steps of 10 kHz. It is obtained from the 40 MHz oscillator in the LM exciter by means of digital-frequency division together with analog mixing and filter techniques. Use of the 40 MHz signal from the LM exciter provides maximum stability for f_{lo} signal. The output frequency, f_{pm}, from the PM tube is fed into the range translator and mixed with the frequency f_{lo}.

In the signal processing, the output signal from the mixer is fed into the preamplifier of the TSI 1090 frequency tracker by way of a low-pass filter and a high-pass filter. The model 1090 tracker is essentially a combination of a tracking filter, a frequency-to-voltage converter, and a sample-and-hold circuit. In addition, it has provisions for verifying the signal before it is allowed to appear at the output. The signal validation circuit which contains a phase-locked loop (PLL) is an important feature of the tracker. The signal-validation procedure provides two main functions:

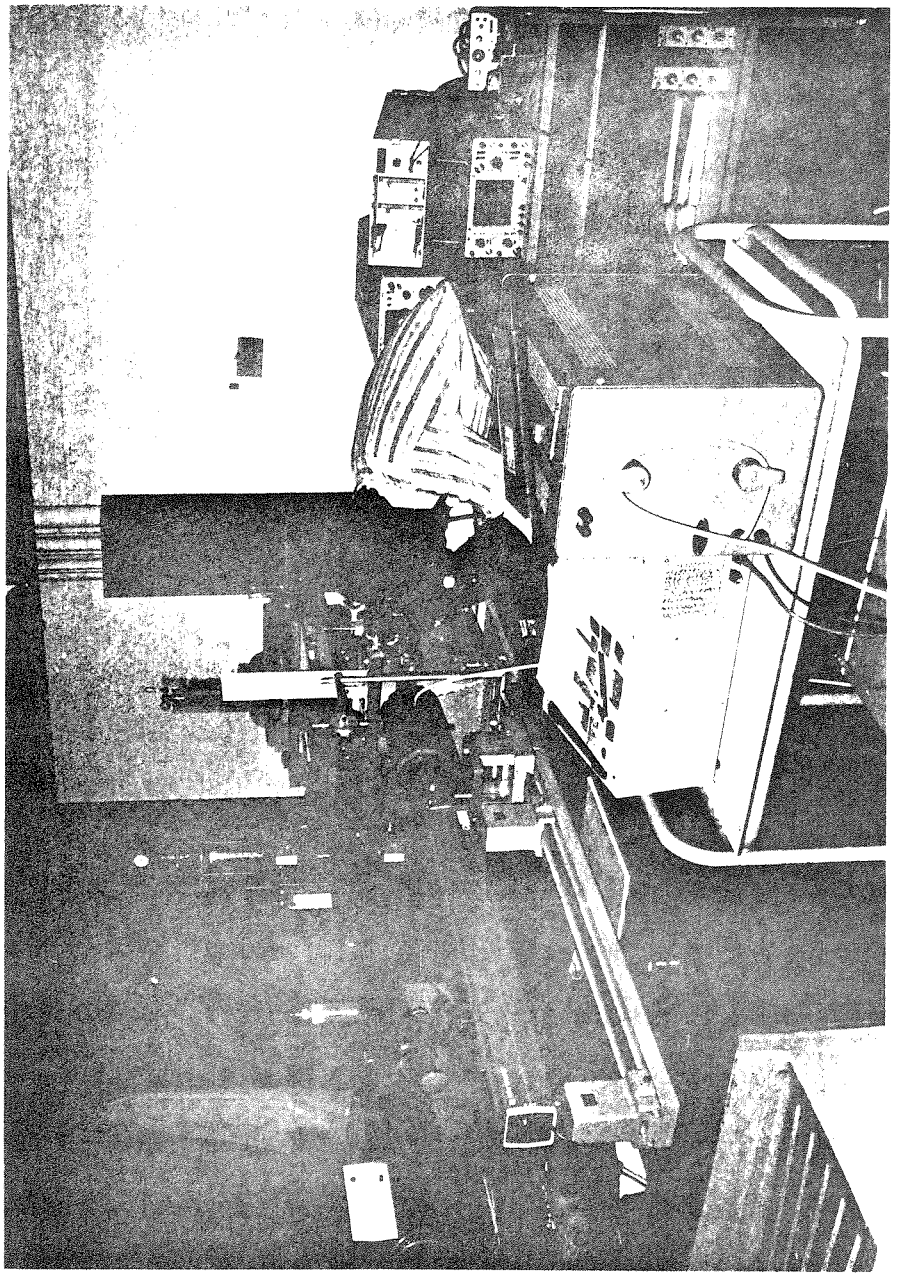

Fig. 11. Photograph of laser-Doppler apparatus

(1) It allows a new output only when the PLL has been "locked on" to the input signal for at least 10 Doppler cycles.

(2) It holds the last signal until a new output signal is accepted.

All of the above functions are required because of the discontinuous nature of the Doppler signal and the occasionally marginal signal-to-noise ratio. The unit can be used over a wide range of particle concentrations which means a wide range of data rates.

The input signal into the tracker is amplified, processed, and validated. The validated signal is displayed on a panel meter as a digital d.c. voltage. An analog d.c. voltage output is also provided, and therefore the instantaneous velocity can be obtained.

3.5.3 Velocity Measuring Technique

A photograph of the experimental apparatus is shown in Figure 11. The LDA transducer was operated with the 120 mm lens at a beam separation of 40 mm. At present this setup gives the smallest possible measuring volume. The photomultiplier was mounted to pick up the forward-scattered light. The scattered light could be picked up over a wide angle because in the dual-beam mode the Doppler frequency is independent of the direction of viewing by the photomultiplier. The 8.25 diopter lens was used in the photomultiplier optics. In order to obtain the sharpest possible image of the crossing on the pinhole of the photomultiplier, the distance from the receiving lens (8.25 diopter) shoulder to the crossing point of the two laser beams should be 120 mm. Because the laser-Doppler anemometer is fixed in position, the point of intersection of the two beams is

also fixed in space. Therefore in order to obtain velocity measurements at different locations in the flow channel, the channel was movable.

The flow channel is mounted on a milling table which has three degrees of freedom. Therefore the flow channel can be moved in three independent directions x, y, and z. Distances traveled in each direction from a fixed origin are accurately determined by use of micrometer-dial indicators which can read to within 0.025 mm. At the beginning of the series of experiments to be discussed the laser beam was aligned so that the two beams that emerged from the optical system of the LDA transducer were separated in frequency by 40 MHz. The traversing mechanism of the milling table was operated to position the channel so that the two beams crossed in the liquid in section "C". Figure 12 is a photograph of the two beams crossing in the channel.

In order to eliminate optical distortion due to the circular cross section of the flow channel, the two beams entered in the horizontal plane through the center of the channel. The flow channel was first moved so that the beams crossed on the outer surface of the outside wall. Then the vertical position (z direction) of the channel was adjusted so that the two incident beams and their reflections coincided. That insured that the incident beams entered in the horizontal plane through the center of the axis. Once this adjustment was made, the position of the channel in the z coordinate was fixed. From then on only the x and y coordinates were adjusted. At every new x coordinate position at which experiments were conducted, it was necessary, however, to check whether the incident beams were entering in the horizontal plane through the center of the channel. A second test was to traverse the channel in the

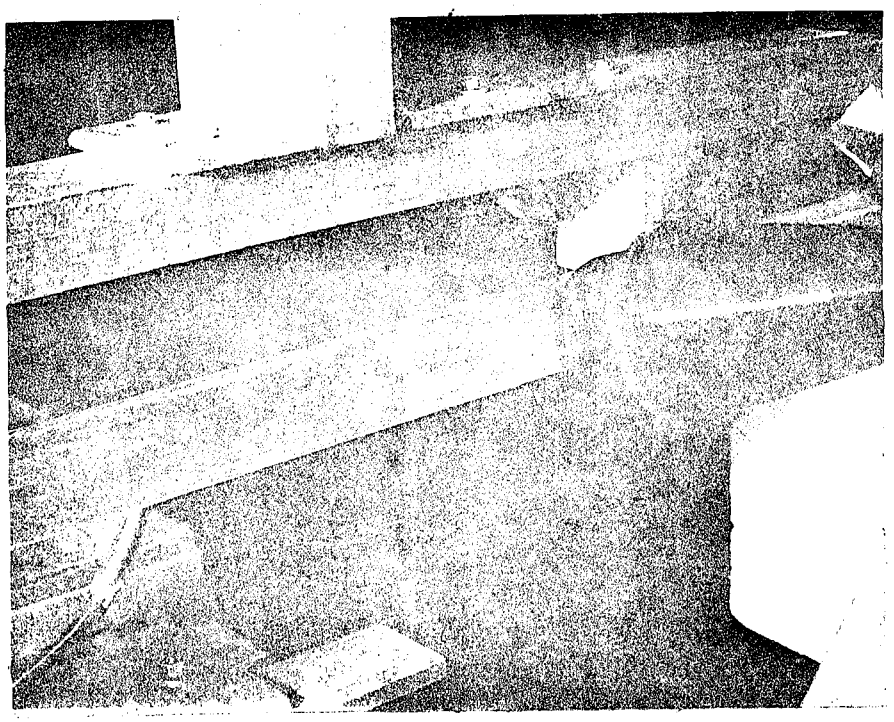

Fig. 12. Photograph of laser beam crossing in a flow channel

y coordinate direction from the outer surface of the outside wall to the outer surface of the inside wall. The distance traveled should be equal to the outer diameter of the channel corrected for refraction by the lucite and the liquid. Once the outer surface of the inside wall had been located, the inner surface of that wall was located by traversing a distance equivalent to the wall thickness of the channel. The outer surface of either wall was located by dusting the surface with cornstarch particles and obtaining a Doppler signal or frequency corresponding to a stationary particle (i.e., zero velocity). The Doppler signal obtained in this case was very "clean". Such a "clean" signal corresponding to a stationary particle could not be obtained on the inner surface because a portion of the measuring volume was in the flowing liquid.

The measuring volume was ellipsoidal in shape. It had a length of 0.72 mm and a width of 0.12 mm. A velocity measurement taken at a point x_1, y_1, and z_1 implies that the center of the measuring volume was at these coordinates. Therefore, the closest possible measuring point in the liquid from the inner wall was at a distance of 0.36 mm (i.e., half the length of the measuring volume). Any closer approach to the wall led to interference of the Doppler signal from the liquid with that from the inner surface wall. This interference was reduced to a large extent by electronically filtering out, with a powerful high-pass filter, the signal caused by the wall. Therefore, it was possible to make velocity measurements at points closer than 0.36 mm from the inner wall. In the present experiments the closest measuring point from the inner wall surface was at a distance of 0.034 mm.

The output signal from the photomultiplier was fed into the frequency translator where it was mixed with the dialed-in frequency of 39.80 MHz. The output from the mixer was fed into a low-pass filter which was set at a cutoff frequency of either 0.5, 1, or 2 MHz and then into a high-pass filter with a cutoff frequency of 0.2 MHz. The cutoff frequency on the low-pass filter depended on the magnitude of the velocity being measured. Output from the high-pass filter was fed into the preamplifier of the tracker, and the amplified signal was monitored on a storage oscilloscope (Tektronix TM 406). The analog output of the d.c. voltage was fed into an integrator where the input signal was averaged for about 20 sec, and the output was displayed on a digital voltmeter (Tektronix TM 504) and printed on a digital printer (Digitec 6130). The frequency-to-voltage converter on the tracker was set at 1V/MHz. A stationary particle (i.e., zero velocity) corresponded to a frequency of 0.2 MHz (= 40.0-39.80) which in turn corresponded with a d.c. voltage of 0.20 volts. Because the subtraction option for the electronic voltage was not used on the tracker, the reading on the digital voltmeter was a voltage proportional to the frequency $(f_D + f_o - f_{lo})$. To obtain the voltage that was directly proportional to f_D, 0.2V was subtracted from the voltmeter reading. For the optical configuration used in these experiments, the voltage-to-velocity conversion factor was 192.5 $(cm)(sec)^{-1}/V$.

In order to obtain the velocity at some position x_1, y_1, z_1 on the horizontal plane through the center of the channel, the traversing mechanism was adjusted so that the measuring volume coincided with that position. The two thumb screws on the photomultiplier were then adjusted so that the pinhole coincided with the image of the beam intersection. If

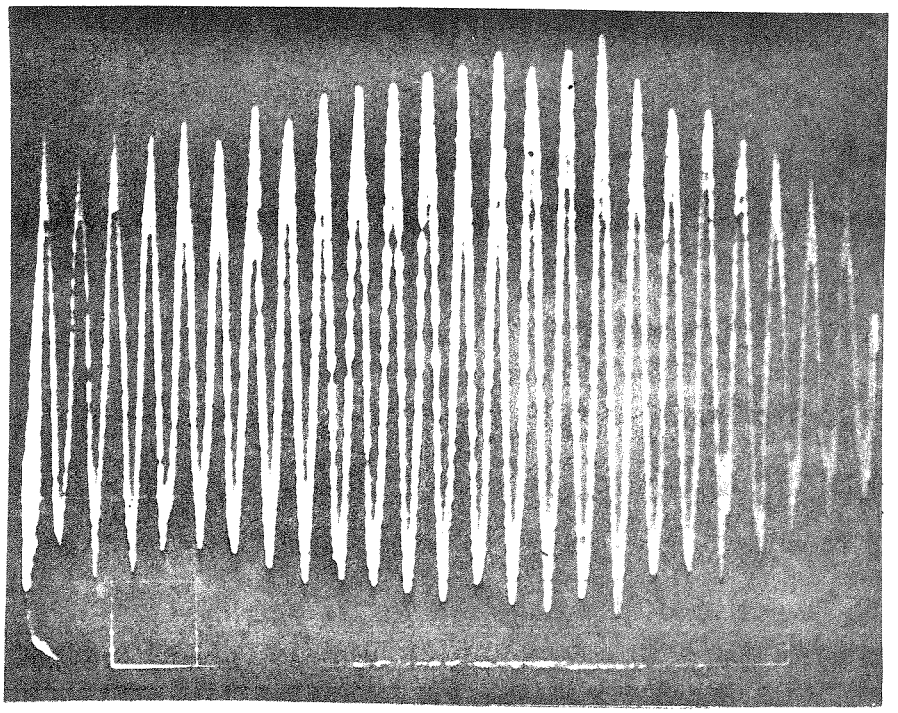

Fig. 13. Photograph of a good quality Doppler signal

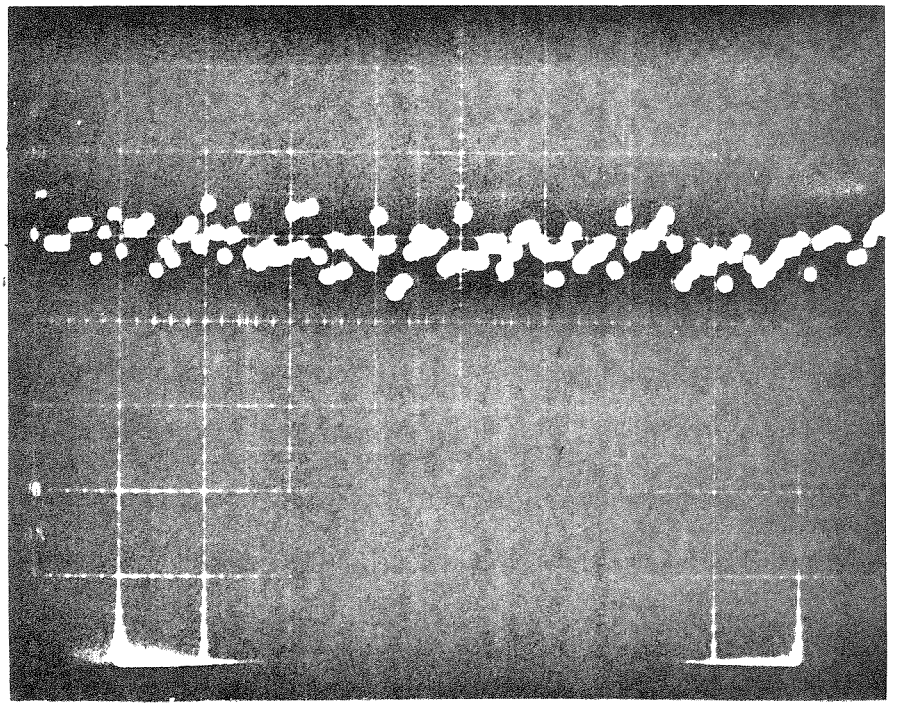

Fig. 14. Photograph of an analog voltage signal from the tracker

the pinhole and the image did not coincide properly, the Doppler frequency signal on the oscilloscope was of poor quality. Finer adjustments for optimizing the coincidence on the pinhole and images were made by monitoring the quality of the signal on the oscilloscope and the sampling rate of the tracker. In order to optimize further the quality of the Doppler frequency signal, the beam crossing was adjusted from the outside of the beam splitter and modulator section by means of an Allen wrench. Figure 13 shows a Doppler signal of good quality, and Figure 14 is a photograph of the analog voltage signal obtained from the tracker. Both figures were photographed from the storage oscilloscope.

All velocity measurements, unless otherwise stated, were made in the horizontal plane through the center of the channel. In section "C" of the flow channel velocity measurements were made from the inside wall to the outside wall as shown in Figure 10 (i.e., wall to wall). In the heart valve chamber (section "B") due to the presence of the sinuses there was a certain amount of optical distortion of the laser beams. This distortion was reduced tremendously by filling the square pot built around the sinuses with glycerine, since glycerine and lucite have almost identical indices of refraction ($\sim$ 1.47). Therefore the effects of optical distortion were negligible when traversing the valve chamber from the inside wall to the center, and accurate measurements were possible in this region. Beyond the center of the channel, however, the optical distortion made it difficult to accurately locate the position of the beam crossing, and therefore velocity measurements were not made beyond the center of the chamber. It was, however, possible to locate the inner

surface of the outside wall, at a point which was almost diametrically opposite the location of velocity measurement close to the inside wall. Therefore it was possible to measure velocities very close to the inner surface of the outside wall (i.e., within 0.034 mm from the wall surface) and obtain an accurate estimate of the wall shear stress on the outside wall in the sinus region. In the heart valve chamber therefore velocity profiles were obtained only from the inside wall to the center of the channel, but it was possible to measure shear stresses on both inside and outside walls.

The liquid used in the experiments was 6 percent-by-weight Pluracol Polyol V-10 (Wyandotte Chemicals) in water. At this low concentration the solution is Newtonian in nature. The solution contained a sprinkling of cornstarch particles which were 10-12 μm in diameter and which were suspended in the liquid so as to scatter light. The concentration of the cornstarch in the liquid was very small. The experiments were conducted at a temperature of about 32°C. At 32°C the Polyol solution had a viscosity of about 0.035 dyne sec/cm^2, a density of about 1.01 g/cm^3 and a refractive index of about 1.33. The temperature of the solution was controlled by blowing temperature-conditioned air over the bucket containing the liquid. The physical properties of the solution were checked every 2 to 3 days.

The aortic prosthesis was placed symmetrically in the heart-valve chamber and the pump was started. Once the flow system was purged of all air, velocity measurements were made. If not otherwise stated, all velocity profiles were obtained in the horizontal plane through the center of the channel. Turbulence intensity levels were measured using

a true RMS voltmeter (HP 3400A). The total flow rate of liquid through the system was controlled by the needle valve and the three bypass valves attached to the pump. Flow rates from 167 cm^3/sec to 417 cm^3/sec (10 liters/min to 25 liters/min) were used in the experiments.

3.6 Brief Description of Aortic Valve Prostheses Used in the Study

3.6.1 Starr-Edwards Ball Valve [30], Model #1260 (Figure 2)

The Starr-Edwards 1260 valves are closed cage silastic ball valves. They are comprised of a polished Stellite alloy 21 cage with a combination of Teflon and polypropylene cloth sewing ring. The cloth on the sewing ring extends to the orifice, leaving no exposed metal on the in-flow face of the valve. The ball is made of silicone rubber and contains 2 percent-by-weight barium sulfate for radiopacity. The radiopacity aids visualization of ball motion on cinefluoroscopy. The 1260 model was first made generally available in July 1969 as a modification of the model 1200 aortic prosthesis.

3.6.2 Model #2320 (Figure 15)

The Starr-Edwards Model 2320 closed caged ball valve prosthesis is comprised of a Stellite alloy 21 cage with completely cloth covered struts and a composite orifice consisting of metal and cloth to form the poppet seating surface. The metallic stops project through the knitted orifice at regular intervals. The cloth covering which is made of Teflon and polypropylene is intended to promote tissue invasion and encapsulation of the valve cage and its orifice. The ball is hollow and made of Stellite alloy 21. It has potentially greater

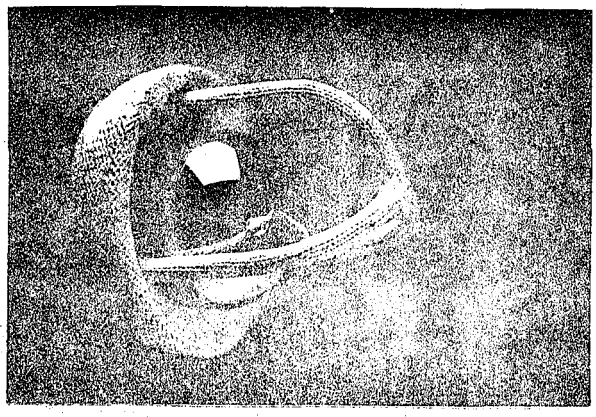

Fig. 15. (a) Starr-Edwards 2320-10A ball valve

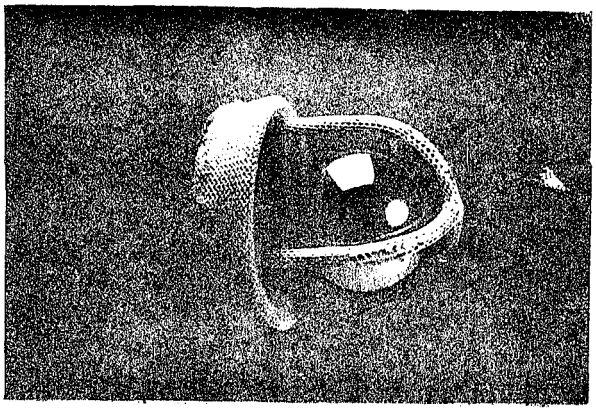

Fig. 15. (b) Starr-Edwards 2400-10A ball valve

resistance to biodegradation as compared with silicone rubber. This model has been on the market since 1968.

3.6.3 Model #2400 (Figure 15)

The Starr-Edwards 2400 closed caged ball valve is known as a composite track valve prosthesis. It is comprised of a partially cloth covered Stellite alloy 21 and a hollow poppet made of the same material. The cage legs are covered with a porous knit polypropylene cloth except for an exposed metal track on the inner aspect which protects the strut cloth from contact by the ball. The orifice is comprised of a composite of cloth and metal stops which protrude through the cloth at regular intervals and protect the orifice cloth from poppet impact. All other surfaces which do not come into contact with the poppet are completely cloth covered.

3.6.4 Björk-Shiley Prosthesis [31] (Figure 2)

The Björk-Shiley valve is a tilting or pivoting disc prosthesis. It consists of a uniquely suspended free-floating disc made of Delrin or pyrolytic carbon, a Stellite cage and struts, and thin Teflon suture rings. The disc has an optimum opening angle of 60°. The newer versions of this valve have a tantalum ring implanted on the outflow face of the disc so that the valve opening may be observed by cinefluoroscopy. The Björk-Shiley valve has been in clinical use since January 1969.

3.6.5 Smeloff-Cutter Prosthesis (Figure 2)

The Smeloff-Cutter Prosthesis is a double-cage full orifice ball valve. It consists of a double open-ended cage which is machined as one unit from commercially pure titanium, and a poppet made from solid

silicone rubber. The suture ring is made of nonreactive Teflon and loops of heavy Dacron suture embedded inside the metal ring, with multiple knots for maximum security. This valve has been on the market since 1966.

3.6.6 Cooley-Cutter Prosthesis (Figure 2)

The Cooley-Cutter prosthesis is also a double-cage open-ended valve, which consists of a biconical (diamond shaped) disc made of pyrolytic carbon as an occluder. It is also a full orifice valve. Even though the Cooley-Cutter is similar in design to the Smeloff-Cutter valve, the length of its cage both on the upstream and downstream end is smaller compared with the Smeloff-Cutter cage. For example, a comparison of the Smeloff-Cutter A5 and Cooley-Cutter A25 valves indicates that the length of the cage of the A5 is about twice that of the A25. The Cooley-Cutter aortic valve has been used clinically since 1971.

Chapter 4

PRESSURE-DROP RESULTS

Evaluation of pressure drops across orifices in a circular channel can be developed from correlated data. Flow past bluff bodies mounted in a channel lead, however, to complicated fluid dynamics which are not yet understood and very sparingly studied. Current designs of artificial heart valves incorporate orifices and bluff bodies in their structure. These lead to extremely complicated fluid dynamics, especially if the flow is turbulent. Numerical analysis of the flow past a bluff body as in an artificial heart valve for steady and unsteady flow is almost impossible because of the large amounts of computation time required. Also, the analysis would require many simplifying assumptions, and results so obtained may not be physically realistic. Therefore, in order to obtain data on pressure drops across prosthetic aortic valves, *in vitro* experiments have to be performed. Experiments were performed on two adjacent valve sizes (sewing ring diameters of 24 to 27 mm) of each of the four designs of prostheses as shown in Table 4. The four types of aortic prostheses tested were the Starr-Edwards ball valve, Björk-Shiley tilting disc valve, Smeloff-Cutter ball valve and the Cooley-Cutter biconical disc valve. The larger size prostheses corresponded with one another, and similarly did the smaller size valves. Prosthetic heart valves are sized according to their sewing ring or tissue annulus diameters, since this is the measurement that is made by the cardiovascular surgeon in the patient's aortic root to determine the appropriate valve size. It is therefore imperative that when comparing valves of different designs, valves of corresponding sewing ring diameters should

be used in the tests. It should be noted that all pressures measured were static pressures. This observation was confirmed by comparing pressure measurements obtained at the center of the channel via the hypodermic needles with those at wall pressure taps.

4.1 Theory

For steady incompressible flow through an orifice of cross-sectional area A_o, the pressure drop across it can be related to the volumetric flow rate Q by the equation

$$Q = C_d \cdot A_o \sqrt{\frac{2(p_i - p_j)}{\rho}} \tag{8a}$$

where C_d is the discharge coefficient and ρ is the density of fluid, which here is taken to be constant. Rearrangement gives

$$p_i - p_j = \frac{\rho}{2C_d^2 \cdot A_o^2} \cdot Q^2 \tag{8b}$$

or

$$p_i - p_j = C_o \cdot Q^2 \tag{8c}$$

where $C_o = \frac{\rho}{2C_d^2 \cdot A_o^2}$. For time-dependent flow across an orifice, the Bernoulli equation along a streamline between stations i and j yields [32]

$$\tilde{p}_i'(t) + \frac{\rho v_i^2}{2} = \tilde{p}_j'(t) + \frac{\rho}{2} V_j^2 + \rho \int_i^j \left(\frac{\partial V}{\partial t}\right) da \tag{9}$$

where $\tilde{p}$ = pressure and prime denotes an ideal quantity, since friction is neglected: V = velocity. The last term in equation (9) represents the unsteadiness of the flow and da is an element of length along the streamline.

If the flow from i to j is assumed to be one-dimensional (i.e., no variation of $\tilde{p}$ or V over a cross section), then V = Q/A,

$$\tilde{p}_i'(t) - \tilde{p}_j'(t) = \frac{\rho}{2}(V_j^2 - V_i^2) + \rho\frac{dQ}{dt}\int_i^j \frac{dx}{A} \tag{10}$$

where dQ/dt is the acceleration of the fluid.

In a real flow the actual pressure drop is larger than the ideal due to frictional effects:

$$\therefore\ \tilde{p}_i(t) - \tilde{p}_j(t) = \frac{\rho}{2}\left(\frac{Q}{A_o C_d}\right)^2 + \rho\frac{dQ}{dt}\int_i^j \frac{dx}{A} \tag{11a}$$

where $\tilde{p}(t)$ is the real time dependent pressure and C_d is the discharge coefficient. It is assumed that the values of C_d obtained from steady flow experiments are applicable to pulsatile flow at corresponding flow rates;

$$\therefore\ \tilde{p}_i(t) - \tilde{p}_j(t) = C_o \cdot Q^2 + \rho\frac{dQ}{dt}\int \frac{dx}{A} \tag{11b}$$

In equation (11b) the first term on the right hand side is the resistive term and the second is the inductive term due to the acceleration of the fluid.

The mean value of $\tilde{p}_i - \tilde{p}_j$ over the systolic ejection period, t_s, can be expressed by the equation

$$\overline{\tilde{p}_i - \tilde{p}_j} = C_o \cdot \overline{Q^2} \tag{12}$$

because the time average of the last term in equation (11b) is zero.

Equations (8) through (12) were developed for steady and unsteady flow across an orifice.

If it is now assumed that the <u>in vitro</u> steady flow pressure drop across a prosthetic aortic valve can be expressed by the equation:

$$p_i = p_j = \Delta p_{ij} = C \cdot Q^2 \qquad (13)$$

where C is a term similar to C_o and is called the overall aortic valve drag coefficient. Equations (8c) and (13) are quite similar, and therefore for pulsatile flow across a prosthetic aortic valve the time dependent pressure drop may be expressed by the equation:

$$\tilde{p}_i(t) - \tilde{p}_j(t) = \Delta\tilde{p}_{ij}(t) = C \cdot Q^2 + \rho \frac{dQ}{dt} \int_i^j \frac{dx}{A} \qquad (14)$$

which is analogous to equation (11b) and is based on the same assumptions. The second term on the right hand side of equation (14) represents the pressure drop due to the acceleration of the fluid (a) through the aortic channel, and (b) through the aortic valve. It is not possible to experimentally separate these two contributions towards the inductive (acceleration) term. If it is assumed that the inductive pressure drop is due primarily to the acceleration of the fluid through the aortic flow channel, then the inductive term may be approximated as $\rho \frac{dQ}{dt} \cdot \frac{L}{A}$. The cross sectional area A is assumed to be constant between pressure measuring stations i and j, and L is the distance between these two stations;

$$\therefore \tilde{p}_i(t) - \tilde{p}_j(t) = \Delta\tilde{p}_{ij}(t) \simeq C \cdot Q^2 + \frac{\rho L}{A} \cdot \frac{dQ}{dt} \qquad (15)$$

For the mean pressure drop across an aortic valve over the systolic ejection time period, t_s, an equation analogous to equation (12) may be obtained

$$\overline{\tilde{p}_i - \tilde{p}_j} = \Delta\bar{p}_{ij} = C \cdot \overline{Q^2} \qquad (16)$$

A comparison of equations (13) and (15) shows that

$$\Delta\tilde{p}_{ij}(t) \simeq \Delta p_{ij} + \frac{\rho L}{A} \cdot \frac{dQ}{dt} \qquad (17)$$

where Δp_{ij} is the steady flow pressure drop across the valve at a flow rate Q. For pulsatile flow across a prosthetic aortic valve the peak systolic pressure drop $\Delta\hat{p}_{ij}$ precedes the peak systolic flow rate Q_{peak}. If $\Delta\hat{p}_{ij}$ occurs at a flow rate $\hat{Q}$, and the acceleration of the fluid at that instant is expressed as $\frac{d\hat{Q}}{dt}$, then from equation (17)

$$\hat{p}_i - \hat{p}_j = \Delta\hat{p}_{ij} \simeq C(\hat{Q})^2 + \frac{\rho L}{A} \cdot \frac{d\hat{Q}}{dt} \tag{18}$$

Now, $C(\hat{Q})^2$ = steady flow pressure drop at a steady flow rate numerically equal to $\hat{Q} = (p_i - p_j)_{\hat{Q}}$

$$\hat{p}_i - \hat{p}_j = \Delta\hat{p}_{ij} \simeq (p_i - p_j)_{\hat{Q}} + \frac{\rho L}{A} \cdot \frac{d\hat{Q}}{dt} \tag{19}$$

A comparison of equations (13) and (16) indicates that

$$\Delta\overline{p}_{ij} = \Delta p_{ij} \quad \text{if} \quad \overline{Q^2} = Q^2 \tag{20}$$

Therefore it should be possible to predict mean systolic pressure drop across the prosthetic aortic valve from pressure drop data for steady flow.

Estimation of Steady-Flow Pressure Drop across a Prosthetic Valve of Orifice Diameter d_2 from Known Data across a Valve of the Same Design of Orifice Diameter d_1:

Consider two valves with orifice diameters d_1 and d_2 $(d_1 > d_2)$. Assume the pressure drop across the valve is entirely due to its orifice. Therefore, steady-flow pressure drop across valve #1 is given by the expression

$$\Delta p_{d1} = \frac{\rho Q^2}{2(C_{d1})^2 \left(\frac{\pi d_1^2}{4}\right)^2} \tag{21}$$

Pressure drop across valve #2 is given by

$$\Delta p_{d2} = \frac{\rho Q^2}{2(C_{d2})^2 \left(\frac{\pi d_2^2}{4}\right)^2} \qquad (22)$$

Combining equations (21) and (22)

$$\Delta p_{d2} = \left(\frac{C_{d1}}{C_{d2}} \cdot \frac{d_1^2}{d_2^2}\right)^2 \cdot \Delta p_{d1} \qquad (23)$$

For a given flow rate Q, Δp_{d1} is experimentally known. Therefore, C_{d1} can be estimated. An exact value of C_{d1} is not, however, necessary to estimate for Δp_{d2}. As can be seen from equation (23) only the ratio of C_{d1} to C_{d2} is required. To obtain this ratio, a plot of orifice discharge coefficient (C_d) vs Reynolds number (Re) [35,36] was used. From this chart, the ratio of C_{d1} to C_{d2} may be obtained at the Reynolds number of interest. Therefore, it is possible to estimate Δp_{d2} from known experimental data of Δp_{d1} by assuming that the pressure drops across prosthetic valves are entirely due to their orifices.

4.2 Typical Pressure-Drop Results

In this section results are shown mainly for two different types of prostheses, namely the Smeloff-Cutter A-5 ball valve and the Björk-Shiley 27 XMBRP tilting disc valve. The observations and comments to be made, however, apply to all ten valves that were studied.

4.2.1 Effect of Viscosity on Pressure Drop

The results obtained indicate that the pressure drops obtained with the Polyol solution and water are the same within experimental error. The above observation holds for both steady and pulsatile flow. The maximum estimated experimental error in a pressure drop measurement was ±667 dyne/cm^2 (± 0.50 mm Hg). Therefore the maximum difference be-

tween two similar (i.e., under identical conditions) pressure drop measurements that could be attributed to experimental error was 1333 dynes/cm^2 (1 mm Hg). The reason for the pressure-drop results for a given valve to be the same at the identical steady of systolic flow rate $\hat{Q}$ for both water and Polyol is because the overall drag coefficient, C, as defined in equation (13) remains more or less constant over the steady (Re_s) or systolic ($Re_{\hat{Q}}$)* Reynolds number regime in which the two experiments were conducted. C is an overall drag coefficient for a particular aortic valve. It includes the discharge coefficient of the orifice and the drag coefficient for the bluff body effect of the superstructure of the prosthetic valve. It should be noted that, for the peak systolic pressure drop as given by equation (18), the contribution of the acceleration term to the overall pressure drop was almost identical for both water and Polyol solution because the density of the two liquids differed by only 1 percent, and that $d\hat{Q}/dt$ was the same. Therefore, for the peak systolic pressure drops to be the same within experimental error at a given flow rate $\hat{Q}$, the overall drag coefficient, C, had to be almost constant over the systolic Reynolds number ($Re_{\hat{Q}}$) regime in which the two experiments were conducted. The Reynolds number between the two experiments differed by a factor of about 3.5, because the only main difference between the two test liquids was their viscosities which differed by a factor of 3.5. The Reynolds number regimes for steady flow were from 4,300 to 21,300 with water, and 1,200 to 6,000 with the Polyol solution. The systolic Reynolds number ($Re_{\hat{Q}}$) regimes for pulsatile flow were from 8,400 to 25,200 with water, and 2,400 to 7,200 with the Polyol solution. The Reynolds numbers were based on the entrance tube ("A") upstream from the valve. If, however,

*$Re_{\hat{Q}}$ = systolic Reynolds number based on a flow rate $\hat{Q}$

the Reynolds numbers were calculated on the basis of the primary orifice diameter of the prosthetic valve, higher numbers would prevail.

The fact that the overall drag coefficient, C, does remain more or less constant over a limited Reynolds number regime is reasonable, and it should be compared with the drag induced by flow around a sphere where the drag coefficient remains almost constant in a Reynolds number regime of 5×10^2 to 2×10^5 [33], and the drag induced by flow past a flat plate plate perpendicular to the direction of the flow, where the drag coefficient remains constant in a Reynolds number regime from 50 to 10^4 [34]. The reason for the drag coefficients in the above cited two examples (sphere and plate) to remain almost constant over limited Reynolds number regions is because in those regions the drag on the body is due entirely to the form drag, or else the form drag predominates over the friction drag. Under these conditions the drag is almost proportional to ρU_∞^2 where U_∞ is the velocity of the fluid approaching the body.

In the flow past the prosthetic aortic valves it is not possible to make a clear-cut statement to the effect that the overall drag coefficient remains constant because the form drag predominates. The problem is far more complex. In the examples of the flow past the sphere and the perpendicular flat plate, there were negligible wall effects (i.e., the sphere or the plate were placed in a wind tunnel which was much larger compared with the size of the body when the experiments were performed). In the case of the flow through prosthetic aortic valves, the size of the flow channel is comparable to the size of the superstructure of the valve. Therefore wall effects become very important. It should also be remembered that flow through a prosthetic valve is a combination of a flow through an orifice and past a bluff body

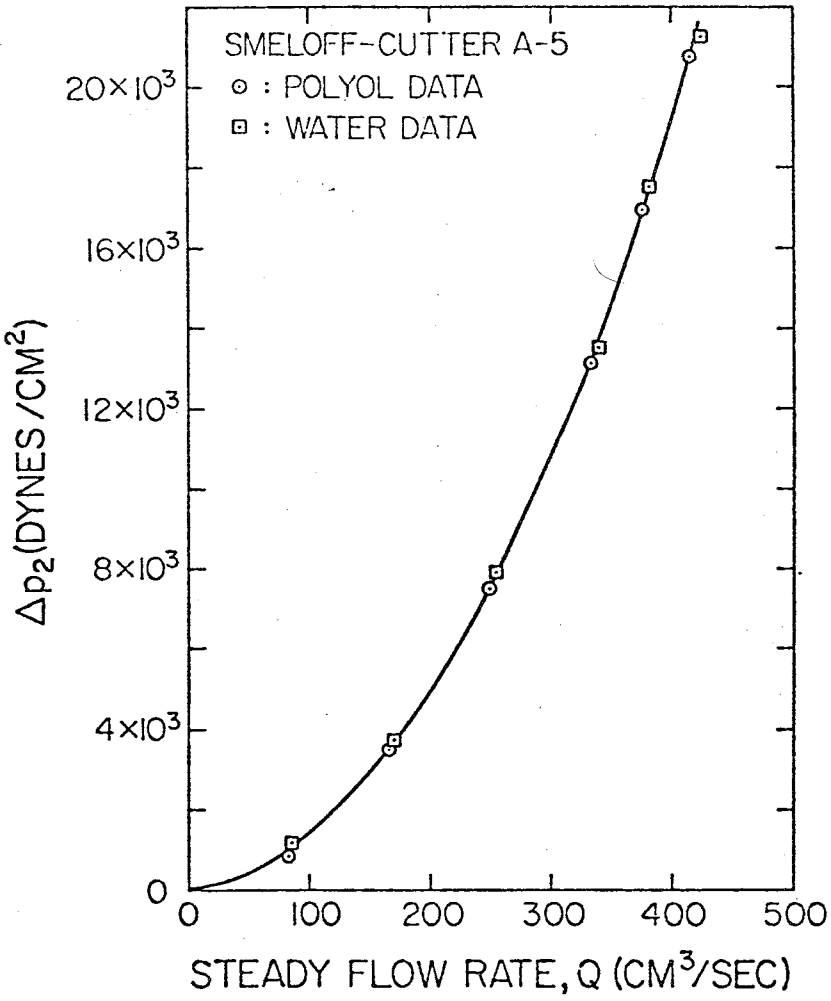

Fig. 16. Steady flow pressure drop across the Smeloff-Cutter A-5 valve

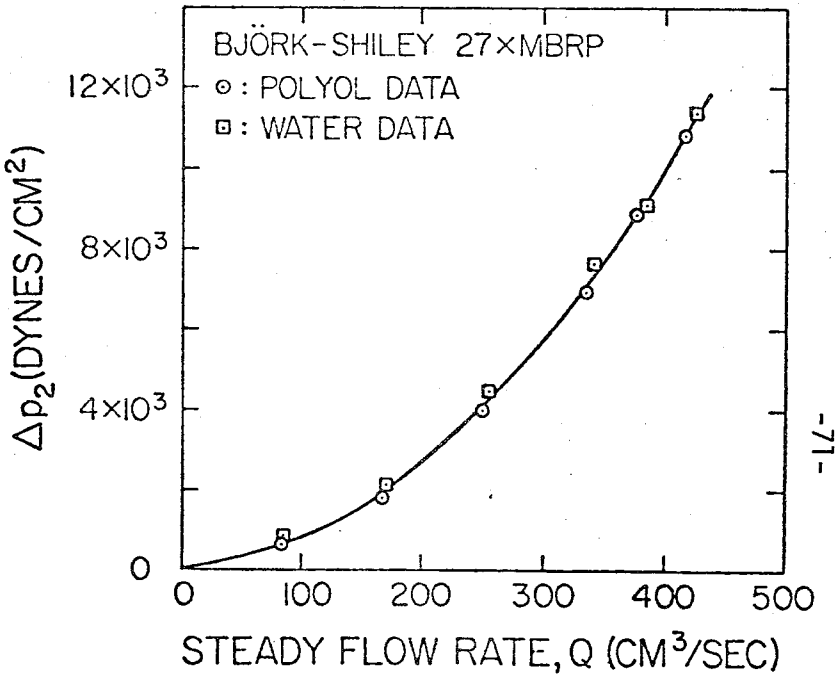

Fig. 17. Steady flow pressure drop across the Björk-Shiley 27XMBRP valve

superstructure. It is therefore not possible to say outright whether the form drag predominates over friction drag. It is only possible to state that the contribution of the form and frictional drags to the overall drag coefficient C, due to the flow through the valve orifice and past the bluff body superstructure of the valve situation in the flow channel, remains more or less constant over limited Reynolds number regimes.

4.2.2 Steady Flow

Pressure-drop measurements were made at six different flow rates of physiological interest, and typical results are shown in Figures 16 and 17 for both water and the Polyol solution. The flow rates used varied from 83 cm^3/sec to 425 cm^3/sec. The maximum flow rate at which the experiments were performed was established by the upper limit of the Brooks rotameter. It should, however, be noted that for a given setting on the rotameter the flow rate of water was larger than the flow rate of the Polyol solution by a factor of 1.02. For example, at a rotameter reading of 100 percent, the flow rate of water was 425 cm^3/sec, while that of the Polyol solution was 417 cm^3/sec. Therefore, there was a factor of 1.02 difference between the corresponding flow rates of the Polyol solution and water. The experiments were conducted at the following rotameter readings: 20, 40, 60, 80, 90 and 100 percent. The results show quite clearly that the pressure drops obtained with the Polyol solution and with water were the same within experimental error. It was also observed that within experimental error the value of the overall aortic valve drag coefficient, C, for

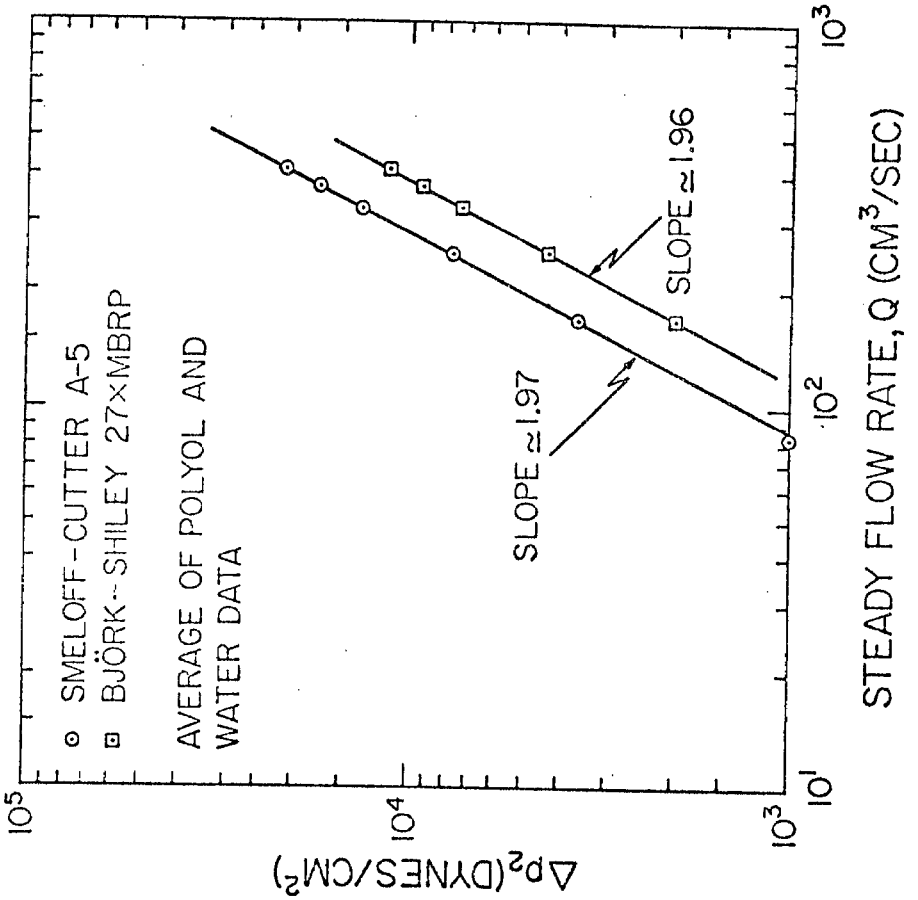

Fig. 18. Steady flow pressure drop across the Smeloff-Cutter A-5 and Björk-Shiley 27XMBRP valves

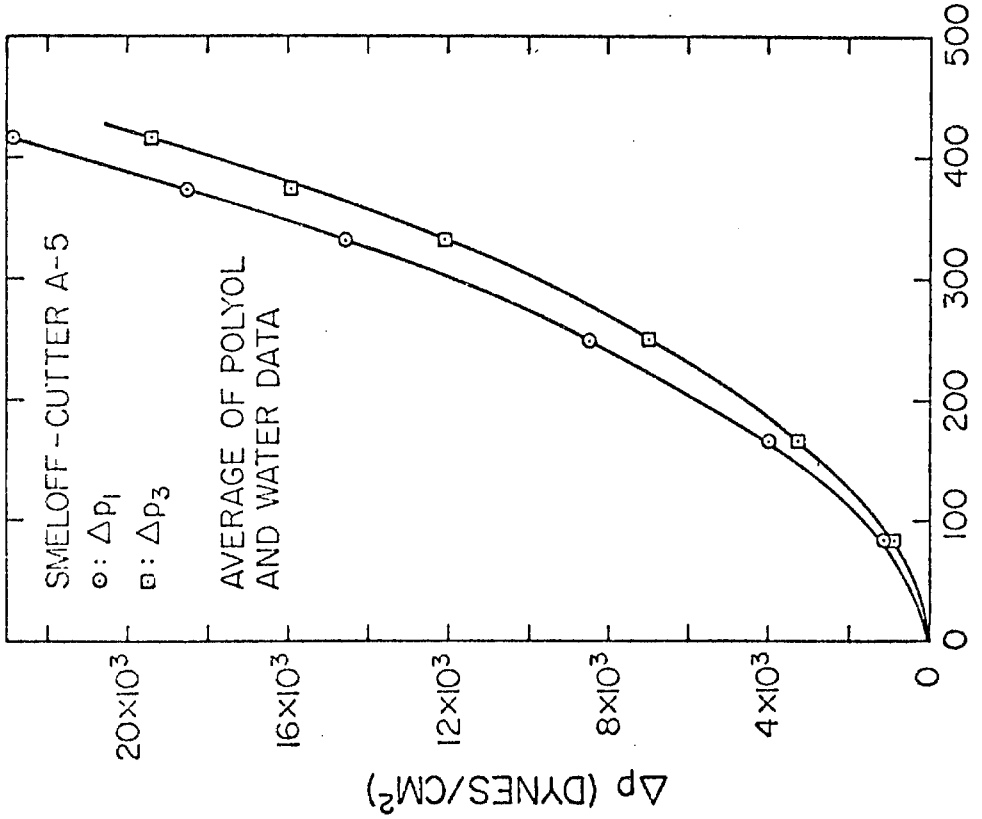

Fig. 19. Steady flow pressure drop across the Smeloff-Cutter A-5 valve

a given valve remained more or less constant over a Reynolds number range of 1,200 to 21,300. This range of Reynolds numbers covers the flow rates of the Polyol solution and water from 83 cm^3/sec to 425 cm^3/sec. The experimental error referred to above was the error in measuring pressure drops across the aortic prosthesis.

Even though Figures 16 and 17 show pressure-drop data obtained across pressure taps I and III (Δp_2), the general remarks made about Δp_2 also apply to the data obtained for pressure drops across taps I and II (Δp_1) and taps I and IV (Δp_3). The distance between taps I and II was 60 mm, between taps I and III was 170 mm, and between taps I and IV was 295 mm. Values of Δp_1, Δp_2, and Δp_3 obtained using Polyol as the test fluid showed correlation coefficients of between 0.99 and 1.0 with the corresponding data obtained using water as the test fluid. Figure 18 shows a plot of pressure drop against flow rate on a log-log scale, which gives a straight line of slope ~ 2. The log-log plots of Δp_1, Δp_2, and Δp_3 against flow rate for all the valves studied gave straight lines of slopes equal to 2 ± 0.2 for Δp in $dyne/cm^2$, and flow rates in cm^3/sec. Therefore, under steady flow conditions the pressure drops of the aortic valve studied may be correlated by the equation

$$\Delta p_{ij} = C \cdot Q^2 \qquad (24)$$

where C is the overall aortic valve drag coefficient.

Figure 19 shows how the pressure drops decrease downstream from the prosthetic aortic valves. The data in Figures 18 and 19 were obtained by averaging together data for water and Polyol. If the data

for Δp_2 were also plotted on Figure 19, they would lie between the data for Δp_1 and Δp_3. The observation that the pressure drop for a given valve decreased with distance downstream from the valve (i.e., $\Delta p_1 > \Delta p_2 > \Delta p_3$) suggests that for all the aortic valves studied, flow separation occurred creating larger pressure drops in the near vicinity of the valve. In almost all cases in which flow takes place around a bluff body, the boundary layer separates from the surface towards the rear of the body. Downstream of the separation point the flow is greatly disturbed by large scale eddies, and this region of eddying motion is usually known as the wake. As a result of the energy dissipated by the highly turbulent motion in the wake, the pressure there is reduced, indicating a large pressure drop across the body. Moving downstream in the wake, some of the pressure loss is recovered, and therefore the pressure drop decreases. When flow separates from a solid surface, however, pressure recovery is never complete. In the case of an aortic prosthesis in a channel, the flow separation and wake created by the bluff body of the valve begin to reattach themselves onto the walls of the channel at some distance downstream from the valve, and some of the pressure loss is recovered. Therefore, as pressure-drop measurements are made farther downstream of the valve, the values obtained get smaller until the entire flow becomes fully reattached. The results obtained in this study indicate that for all ten valves investigated the region of flow separation extended to at least between 150 and 275 mm downstream of the valve. Since pressure measurements were not made farther downstream than 275 mm, it is not possible to predict

if the region of flow separation extended farther than 275 mm. Depending on the configuration of the flow channel, the region of flow separation could be larger or smaller for the same prosthetic aortic valve. Some investigators [5,25] have contended that the downstream pressure should be measured just beyond the point of reattachment of the separated flow. In the average human being, however, the ascending aorta, which is the vessel immediately downstream of the aortic valve, is about 60 to 100 mm in length. After that distance the ascending aorta arches and branch vessels take off from the arch. Therefore, in most instances, in a human being with an implanted aortic prosthesis, the flow never reattaches completely in the ascending aorta. It is, however, of physiological importance to measure the pressure drop across the prosthesis by measuring the pressures in the left ventricle and the ascending aorta. It is therefore of interest to obtain in vitro pressure measurements at a physically realistic distance downstream of the valve. It is not practically possible to obtain accurate pressure measurements extremely close to the valve ($X \simeq 10$ to 30 mm) with instrumentation presently existing in the market. The pressure fluctuations in the close vicinity of the valve ($X \lesssim 30$ mm) are large and rapid, and the time response of the pressure transducers available at present are not rapid enough to accurately measure the pressure in such highly turbulent and disturbed flow regions.

The pressure drop across a given prosthetic aortic valve is affected not only by its orifice but also by the poppet design and the entire superstructure of the valve. The important roles the bluff body shape and size play in the fluid dynamics and the pressure drops across

prosthetic valves are well highlighted in the following two examples. At a flow rate of 417 cm^3/sec, the Björk-Shiley 25XMBRP valve had a Δp_1 of 16,300 dynes/cm^2 and Δp_2 of 12,700 dynes/cm^2, while the Cooley-Cutter A-25 valve had values of 32,500 dynes/cm^2 and 29,700 dynes/cm^2 respectively. Both these valves had almost identical primary orifice diameters (see Table 4). The major difference between these two valves was their poppet design. The Björk-Shiley valve has a tilting disc which, when open, makes an angle of 60° to the vertical plane. The Cooley-Cutter, on the other hand, contains a diamond-shaped disc which is mounted perpendicular to the direction of flow, and is constrained in travel by its cage. For an aortic valve of a given design, the pressure drop across it logically increased as the valve size was decreased. For example, the Smeloff-Cutter A-5 valve showed a value of 22,400 dyne/cm^2 for Δp_1 at a flow rate of 417 cm^3/sec, while the Smeloff-Cutter A-4 had a value of 25,000 dyne/cm^2 at the same flow rate. This increase in pressure drop probably results from the decrease in primary orifice area. In addition, assuming that the pressure drop across the valve is essentially because of its orifice, it is possible to estimate using equation (23) the pressure drop across the Smeloff-Cutter A-4 valve from experimental values obtained from the A-5 valve. A similar calculation may be done between the Björk-Shiley 27XMBRP and 25XMBRP valves. These calculations are tabulated in Tables 5 and 6. The results in these tables indicate that the calculations will yield a larger pressure drop than that experimentally measured. In the case of the Smeloff-Cutter A-4 and Björk-Shiley 25XMBRP valves, the fact that they had smaller size poppets and therefore would have

Table 5. Estimation of Steady Flow Pressure Drops across the Smeloff-Cutter A4 Valve from Experimental Data across the Smeloff-Cutter A5 Valve

Test Fluid: Polyol			Test Fluid: Water		
Q cm^3/sec	Δp_1 dynes/cm^2 Estimated	Experimental	Q cm^3/sec	Δp_1 dynes/cm^2 Estimated	Experimental
83	1665	1120	85	1566	1013
167	5819	4156	170	5386	4039
250	11831	8531	255	11947	9278
333	20081	15596	340	20708	16263
375	25336	19075	383	26316	20288
417	31146	24341	425	32603	25634

Table 6. Estimation of Steady Flow Pressure Drops across the Björk-Shiley 25XMBRP Valve from Experimental Data across the Björk-Shiley 27XMBRP Valve

Test Fluid: Polyol			Test Fluid: Water		
Q cm^3/sec	Δp_2 dynes/cm^2 Estimated	Experimental	Q cm^3/sec	Δp_2 dynes/cm^2 Estimated	Experimental
83	2365	766	85	1956	786
167	6581	2299	170	4071	1953
250	12634	4486	255	8419	4952
333	17291	7851	340	14507	8431
375	21516	9678	383	18221	10351
417	24607	12617	425	21859	13203

Table 7. Estimation of Steady Flow Pressure Drops across the Cooley-Cutter A25 Valve from Experimental Data across the Cooley-Cutter A24 Valve

Test Fluid: Polyol			Test Fluid: Water		
Q cm^3/sec	p_1 dynes/cm^2 Estimated	Experimental	Q cm^3/sec	Estimated	Experimental
83	938	1346	85	1366	1453
167	3858	5279	170	3847	5839
250	8975	10997	255	9239	11797
333	15929	21421	340	16717	21995
375	19945	27260	383	21589	28060
417	24995	32645	425	26295	33565

different fluid dynamic interactions in the heart valve chamber were not taken into consideration at all in the calculations. An attempt to estimate the pressure drops across a larger size prosthesis from known experimental data across a smaller size valve of the same design leads to values which are smaller than the experimentally measured results as shown in Table 7. Until the fluid dynamics of the flow past a bluff body in a circular channel where the bluff body and channel are of comparable size are better understood, it would not be possible to predict theoretically steady-flow pressure-drop data across prosthetic heart valves.

4.2.3 Pulsatile Flow

The experimental results obtained indicate that for all ten prosthetic aortic valves used in the study it was possible within experimental error to predict from equation (19) the peak systolic pressure drops from known steady-flow data. The maximum estimated experimental error in measuring pressure drops was ±667 dynes/cm^2 (± 0.5 mm Hg). The acceleration of the fluid at the instant the peak pressure drop occurs must, however, be known. For the aortic valves studied in the Caltech pulse duplicator, it was experimentally determined that for a heart rate of 70 beats/min and a systolic ejection time period t_s of 300 msec, the acceleration of the fluid at the time $\Delta\hat{p}_{ij}$ occurred could be expressed approximately by the relation

$$\frac{d\hat{Q}}{dt} \simeq \frac{\hat{Q}}{t_s/2} = \frac{2\hat{Q}}{t_s} \tag{25}$$

$\frac{d\hat{Q}}{dt}$ was, however, determined during each experiment. From equation (19) the peak systolic pressure drops across taps I and II ($\Delta\hat{p}_1$) and taps I and III

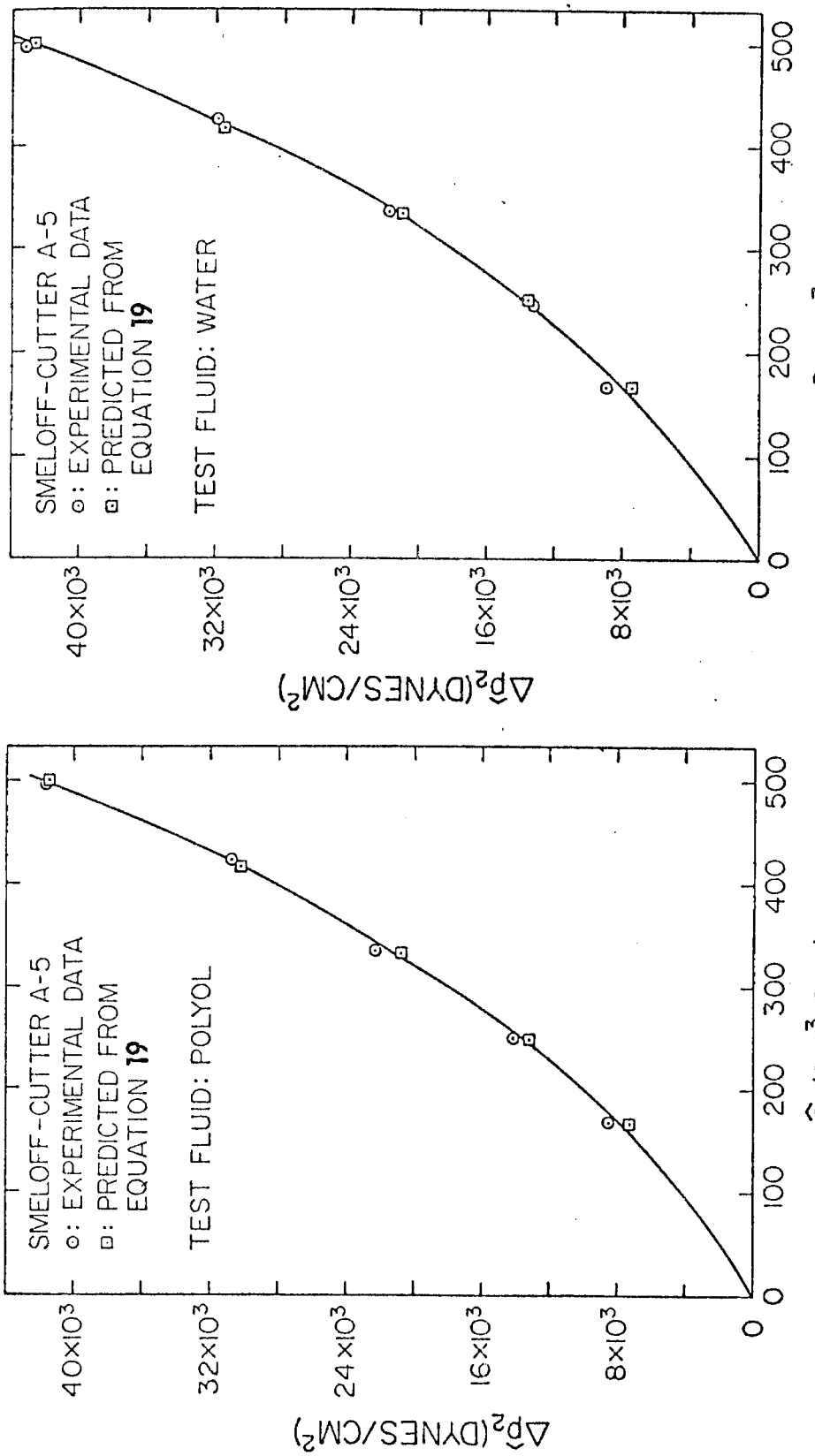

Fig. 20

Fig. 21

Peak systolic pressure drop across the Smeloff-Cutter valve

$(\Delta\hat{p}_2)$ are given by the expressions:

$$\Delta\hat{p}_1 \simeq (p_I - p_{II})_{\hat{Q}} + \frac{\rho L_1}{A_2} \cdot \frac{d\hat{Q}}{dt} \tag{26}$$

$$\Delta\hat{p}_2 \simeq (p_I - p_{III})_{\hat{Q}} + \frac{\rho L_2}{A_2} \cdot \frac{d\hat{Q}}{dt} \tag{27}$$

where A_2 is the cross-sectional area of the inlet and outlet tubes of the flow channel. L_1 and L_2 are the distances between pressure taps I and II, and I and III, respectively.

The contribution of the acceleration term to $\Delta\hat{p}_1$ is smaller than its contribution to $\Delta\hat{p}_2$ because $L_1 < L_2$ as shown in Table 8. In equation (26) it is assumed that the cross sectional area between pressure taps I and II is constant and equal to A_2, even though this section incorporates the sinuses of Valsalva. It was not possible to estimate the cross sectional area of the valve chamber (Section B, Figure 3). The assumptions that were made in order to obtain equations (26) and (27) are either valid or else any errors they introduce seem to nullify each other. That observation is supported by the excellent agreement between the experimental values and predicted values of $\Delta\hat{p}_1$ and $\Delta\hat{p}_2$, which are within experimental error and have correlation coefficients of at least 0.98 (see Figures 60 to 79 and A1 to A20). Typical peak pressure-drop data are shown in Figures 20, 21, 22 and 23. Also, the very good correlation, about 0.99 for both $\Delta\hat{p}_1$ and $\Delta\hat{p}_2$ between the experiments with water and the Polyol solution indicates that within experimental error in the viscosity range of 0.01 dyne sec/cm^2 to 0.35 dyne sec/cm^2 and systolic flow rate $(\hat{Q})$ range of 167 cm^3/sec to 500 cm^3/sec, the peak systolic pressure drops across aortic prostheses are independent of the viscosity of the test fluid.

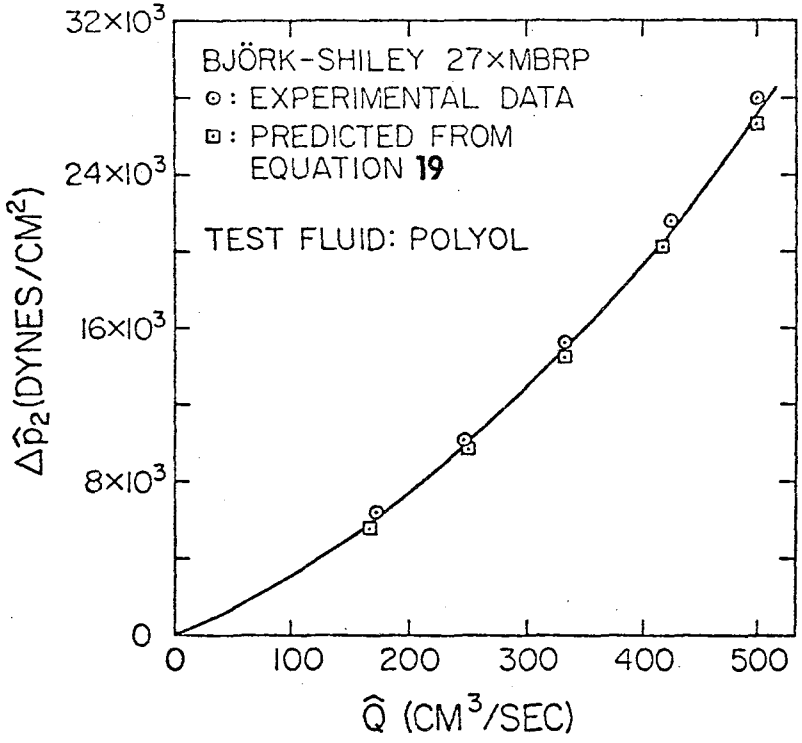

Fig. 22

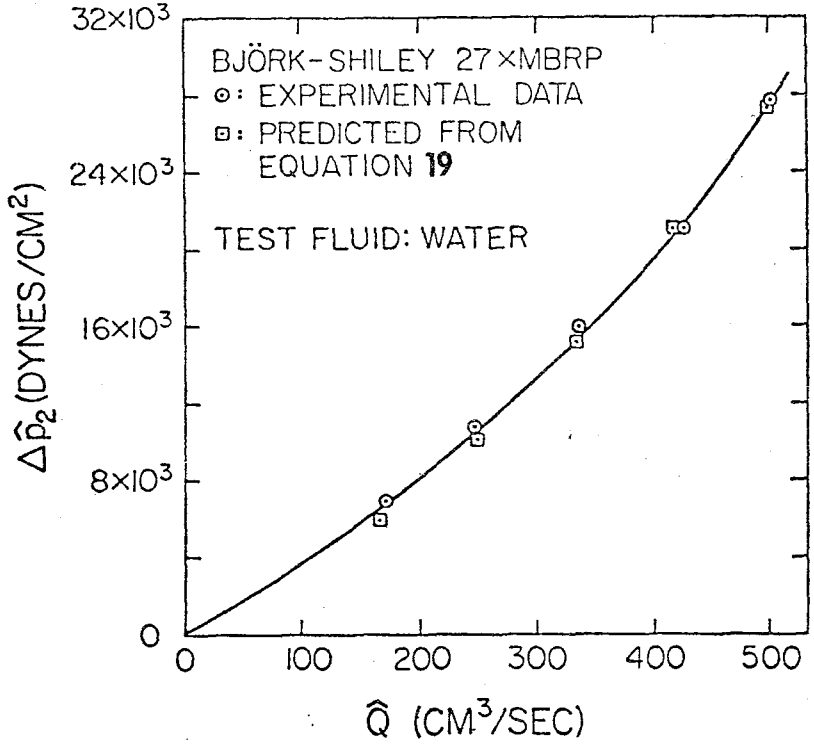

Fig. 23

Peak systolic pressure drop across the Björk-Shiley 27XMBRP valve

Table 8. Calculation of the Pressure Drops Due to the Acceleration Term in Equations (26)* and (27)*

$\hat{Q}$	$\frac{\rho L_1}{A_2}\frac{2\hat{Q}}{t_s}$	$\frac{\rho L_2}{A_2}\frac{2\hat{Q}}{t_s}$
(cm^3/sec)	(dyne/cm^2)	(dyne/cm^2)
166.67	1329	3765
250.00	1993	5648
333.33	2658	7530
416.67	3322	9413
500.00	3987	11295

ρ = 1.01 g/cm^3 for Polyol solution

t_s = 300 msec

L_1 = 60 mm, L_2 = 170 mm

A_2 = 5.067 cm^2

*In equations (26) and (27) the acceleration term has been approximated as

$$\frac{d\hat{Q}}{dt} \simeq \frac{2\hat{Q}}{t_s}$$

The results also tend to indicate that the inductive pressure drop is due primarily to the acceleration of the fluid through the flow channel. Soderlund [5] has also made a similar observation. Therefore, the results obtained suggest that it is possible to predict in vitro peak systolic pressure drops from known steady-flow data, if the acceleration of the fluid at that instant ($d\hat{Q}/dt$) is known.

Typical data for the mean systolic pressure drop are plotted in Figures 24 and 25. It should be noted that the theory developed (equations (12) and (16)) suggests that the mean systolic pressure drop should be plotted against the root-mean-square of the flow rate and not the flow rate. Under the pulsatile flow conditions of our experiments, it was experimentally observed that

$$\frac{\sqrt{\overline{Q^2}}}{Q_{peak}} \simeq .65 \tag{28}$$

where Q_{peak} is the peak flow rate during systole. The value of $\sqrt{\overline{Q^2}}$ was determined during each individual experiment. Because the steady and peak pressure-drop experiments showed no difference within experimental error between the Polyol solution and water, the mean pressure-drop experiments were only conducted with the Polyol solution. Results shown in Figures 24 and 25 indicate that there was very good correlation, about 0.99, between the experimental values and the values predicted from equation (20). It was possible to predict the experimental results to within at least 667 dynes/cm^2 (0.50 mm Hg) or better. Equations (12) and (16) are derived on the assumption that

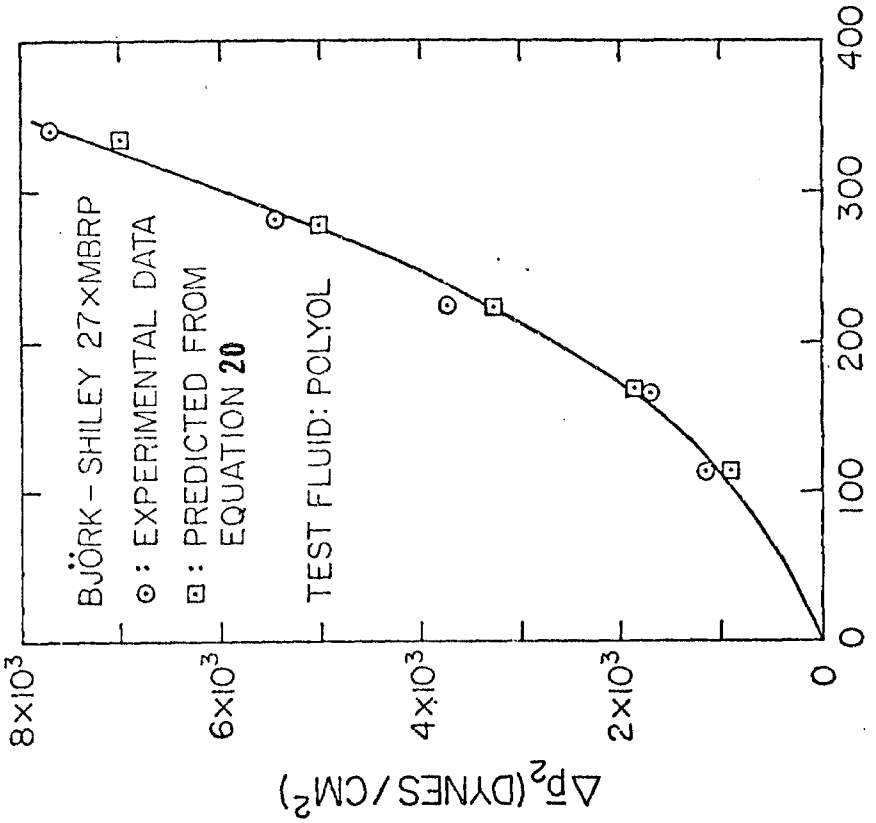

Fig. 25. Mean systolic pressure drop across the Björk-Shiley 27XMBRP valve

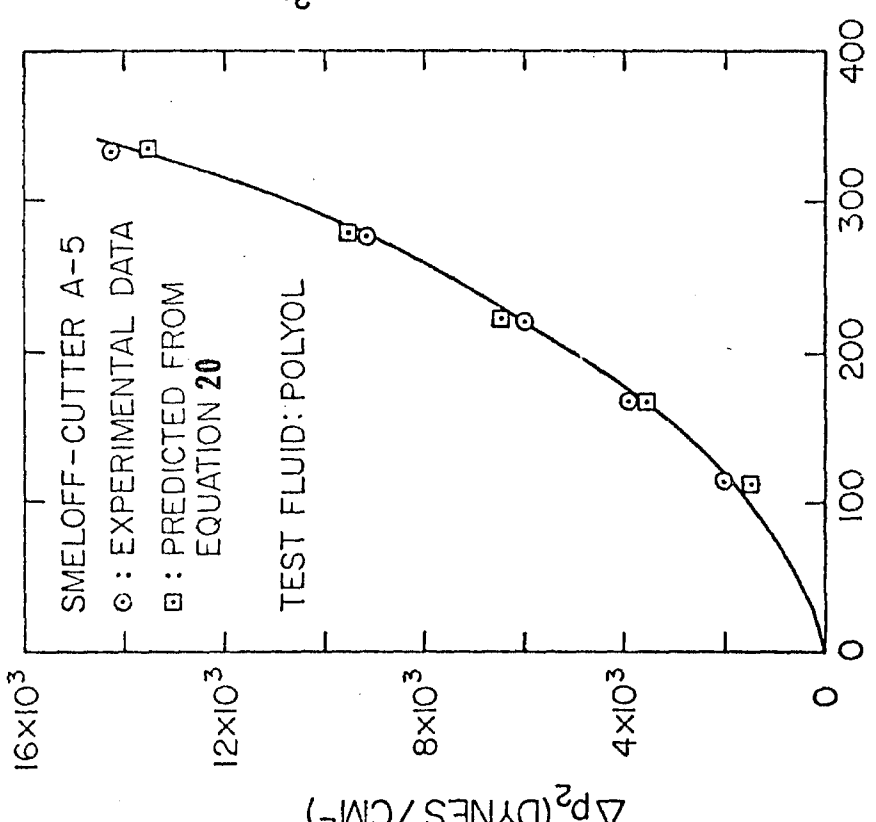

Fig. 24. Mean systolic pressure drop across the Smeloff-Cutter A-5 valve

the fluid acceleration term in equation (11b) integrates out to zero over the systolic ejection period t_s. The experimental results bear out this assumption. The results obtained for $\Delta\bar{p}_1$ and $\Delta\bar{p}_2$ are in very good agreement with the values predicted from the theory (equation (20)), with correlation coefficients of about 0.99. Therefore, the results indicate that it is possible to predict within experimental error the mean systolic pressure drop from known steady-flow data (see Figures 80 to 99).

4.3 Comparison of Pressure Drops across the Different Prostheses

In this section the pressure-drop results obtained across all ten aortic prostheses are discussed in a comparative manner. Results obtained for the pressure drop between pressure taps I and II are presented graphically (Figures 26 through 99) for all valves, under both steady and pulsatile flow, for both test fluids. The mean systolic pressure-drop results are presented for both $\Delta\bar{p}_1$ and $\Delta\bar{p}_2$. Results not presented graphically in this section are given in appendix A-1. Please note that in Figures 26 through 99 the length of the Y-axis is longer than that of the X-axis even though the figures are log-log plots. In the steady-flow pressure drop plots if there is no data point for a flow rate of 83 cm^3/sec, it is because the pressure drop at that flow rate was less than 1000 $dyne/cm^2$. The average value of the overall drag coefficient, C, over a steady flow Reynolds number range of 1,200 to 21,300 for each aortic prosthesis is given in Table 9. The value of C given in the table is for the equation

$$\Delta p_1 = C_1 \cdot Q^2 \qquad (29)$$

and is obtained by averaging appropriately the steady-flow data for water and Polyol.

Before comparing the pressure-drop characteristics of the different valves, the hydrodynamic instability of the poppets of the Starr-Edwards caged ball aortic valves requires some discussion. The following discussion on the Starr-Edwards ball valves pertains to conditions of steady flow. Of all the valves studied under steady flow conditions,

it was initially observed that the results of the four Starr-Edwards ball valves, namely the 1260-12A, 1260-10A, 2400-10A and 2320-10A, were the hardest to reproduce; under steady-flow conditions at times the results were observed to differ by almost a factor of two. It was observed from the very beginning that the poppets of these valves became hydrodynamically unstable at a flow rate of about 133 cm^3/sec for both test liquids. The instability of the poppet caused it to oscillate and rotate at different positions in the cage. Such hydrodynamic instability of the ball of the Starr-Edwards caged ball valves has also been observed by other investigators [5,14,15]. These investigators, however, did not realize or notice that the ball could oscillate and spin at different positions in the cage. During this study it was observed that the ball could oscillate at three different positions, namely, top (apex) of the cage, middle of the cage, and bottom of the cage. Depending on the position of oscillation of the ball of a given Starr-Edwards valve, the pressure drops obtained were observed to differ by as much as a factor of two. During a given experiment the ball would oscillate at any three of these locations, and it could change its position of oscillation during the middle of the experiment. It was, however, possible to maintain the oscillating position of the ball at a given location during an experiment with a great deal of care. This was accomplished by squeezing by hand the rubber hosing downstream and upstream from the flow channel, and also by increasing or decreasing the flow rate in the flow system in a gradual manner. Steady-flow pressure-drop experiments were conducted with the 1260-12A and the 2400-10A valves with the ball oscillating at the three different

Table 9. Overall Aortic Valve Drag Coefficient Defined by the Equation $\Delta p_1 = C_1 Q^2$

Valve		Position of Ball in Cage	C_1 (dynes $sec^{-2} cm^{-8}$)
Björk-Shiley	27XMBRP		0.083
Björk-Shiley	25XMBRP		0.095
Smeloff-Cutter	A5		0.134
Smeloff-Cutter	A4		0.145
Cooley-Cutter	A25		0.193
Cooley-Cutter	A24		0.206
Starr-Edwards	1260-12A	At top	0.133
Starr-Edwards	1260-12A	At middle	0.187
Starr-Edwards	1260-12A	At bottom	0.245
Starr-Edwards	1260-12A	Tied at top	0.107
Starr-Edwards	1260-10A	At top	0.135
Starr-Edwards	2320-10A	At top	0.137
Starr-Edwards	2400-10A	At top	0.138
Starr-Edwards	2400-10A	At middle	0.184
Starr-Edwards	2400-10A	At bottom	0.250

locations. Experiments with the 1260-10A and 2320-10A were conducted with the ball oscillating at the top of the cage. It was observed from the experiments with the ball oscillating at the top of the cage that the pressure-drop results obtained for the 1260-10A, 2400-10A and 2320-10A prostheses were almost the same within experimental error. It was therefore decided that the results obtained with the 2400-10A with the ball oscillating at the middle and bottom of the cage would be applicable to the 1260-10A and 2320-10A prostheses with the poppet at the same positions. It should be remembered that the 1260-10A, 2400-10A and 2320-10A Starr-Edwards prostheses have the same sewing ring diameter and almost the same primary orifice area. For a given Starr-Edwards ball valve, as the position of oscillation of the ball moves from the apex (top) of the cage to the bottom of the cage, the area of central flow available to the fluid is reduced, and the fluid is forced to flow peripherally around the ball in a shorter distance from the orifice, leading to larger pressure drops.

Comparison of the pressure-drop data, steady and pulsatile, obtained across the different designs of prostheses, namely Starr-Edwards, Björk-Shiley, Smeloff-Cutter and Cooley-Cutter, indicate without a doubt that the Björk-Shiley prosthesis creates the lowest pressure drop. As stated before, the larger size prosthesis of the four different designs correspond with each other and so did the smaller size prostheses. A comparison of the steady-flow pressure drops across the larger of the two sizes of each type of prosthesis gives the following ranking in order of increasing pressure drop:

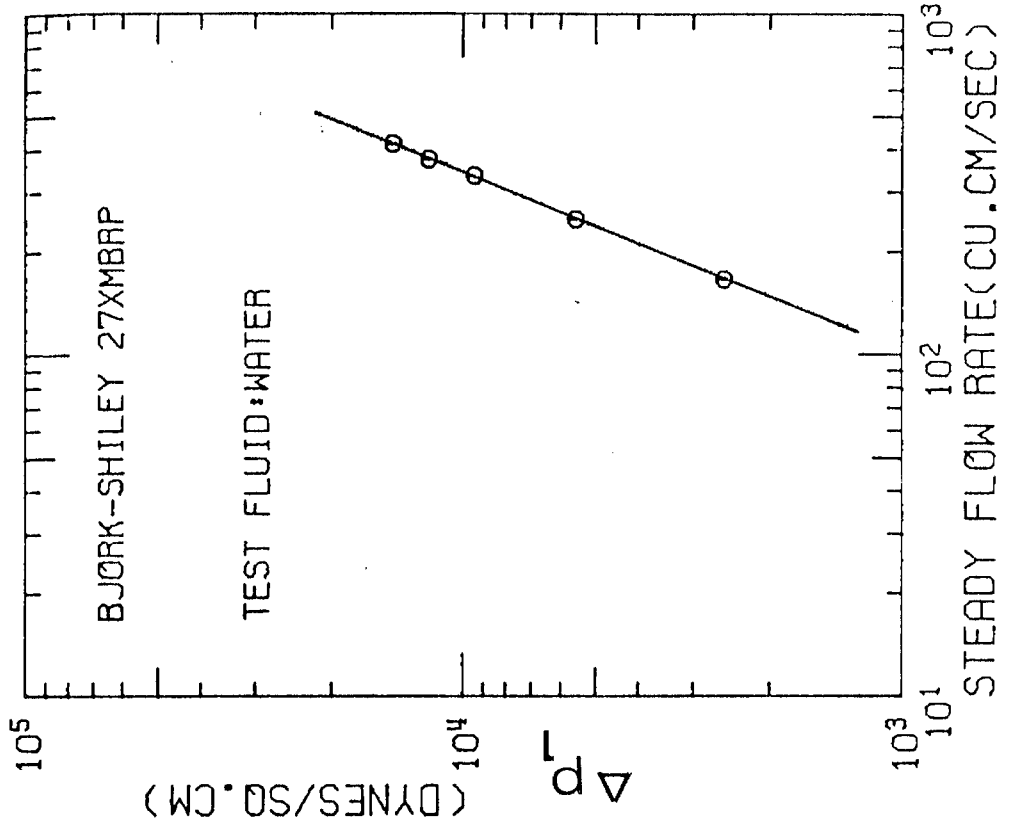

Fig. 27

Steady flow pressure drop across the Björk-Shiley 27XMBRP valve

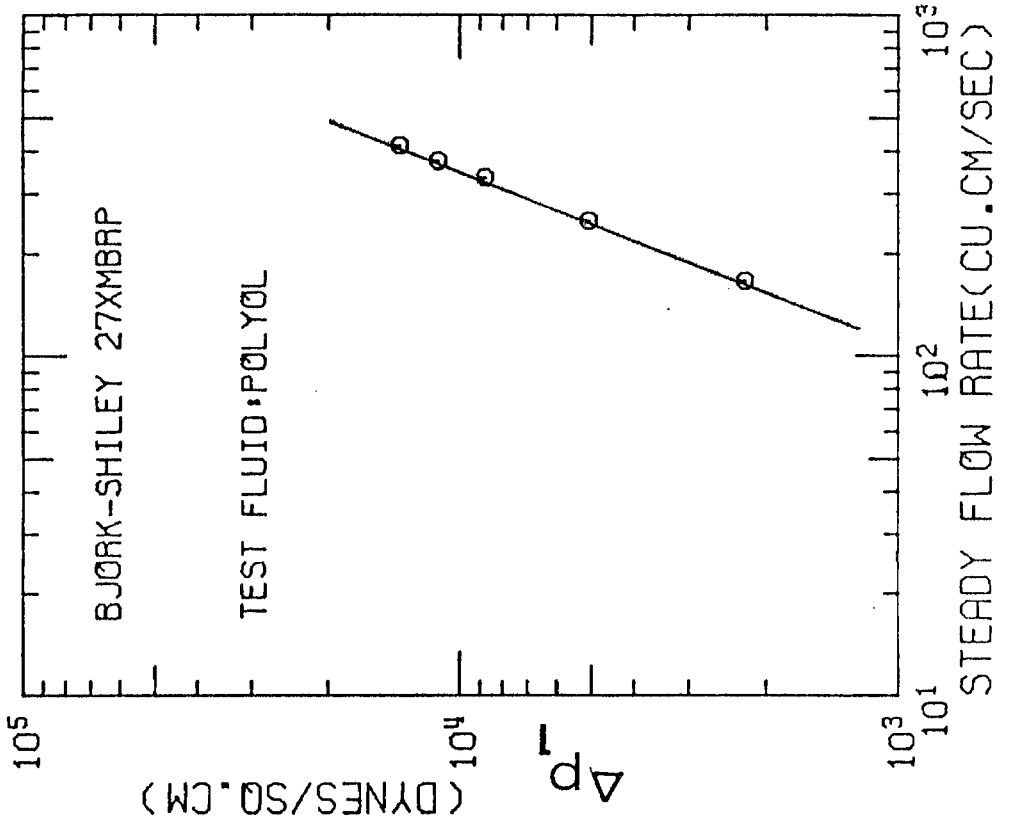

Fig. 26

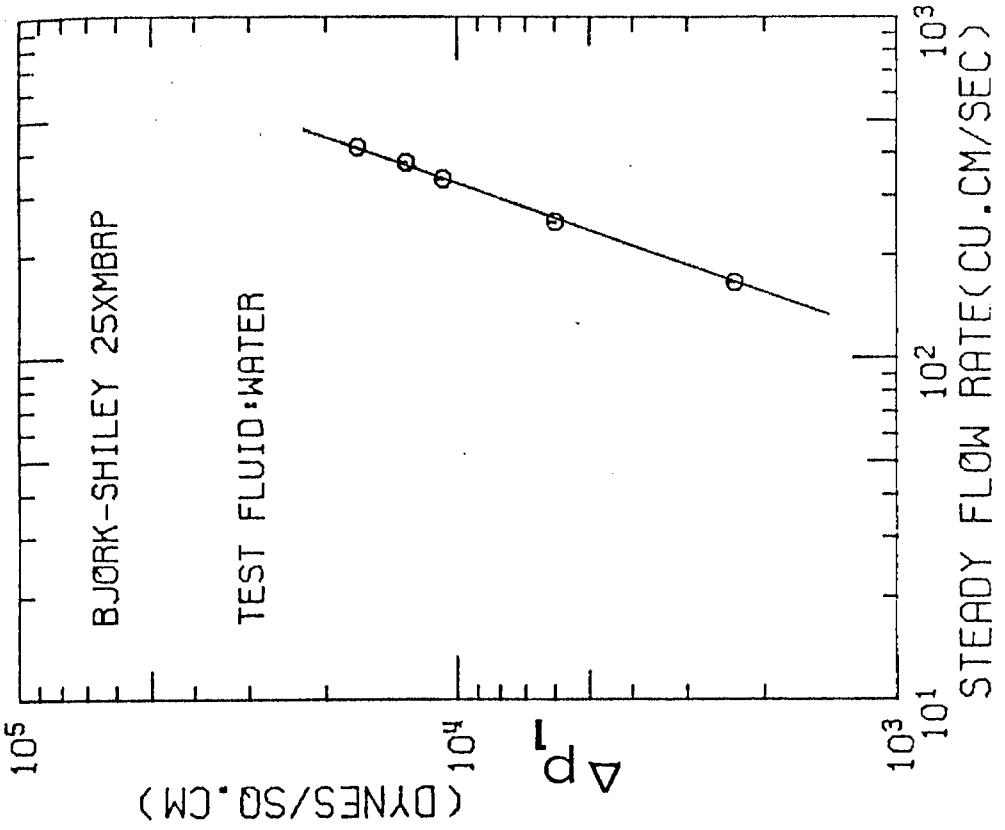

Fig. 29

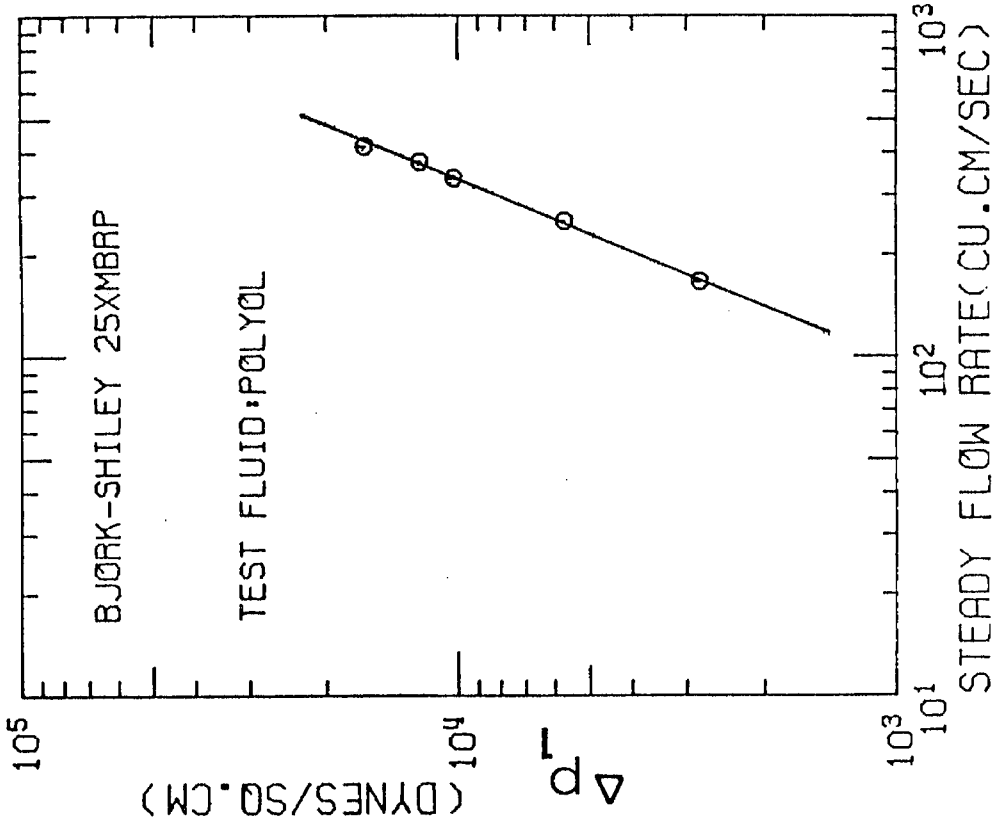

Fig. 28

Steady flow pressure drop across the Björk-Shiley 25XMBRP valve

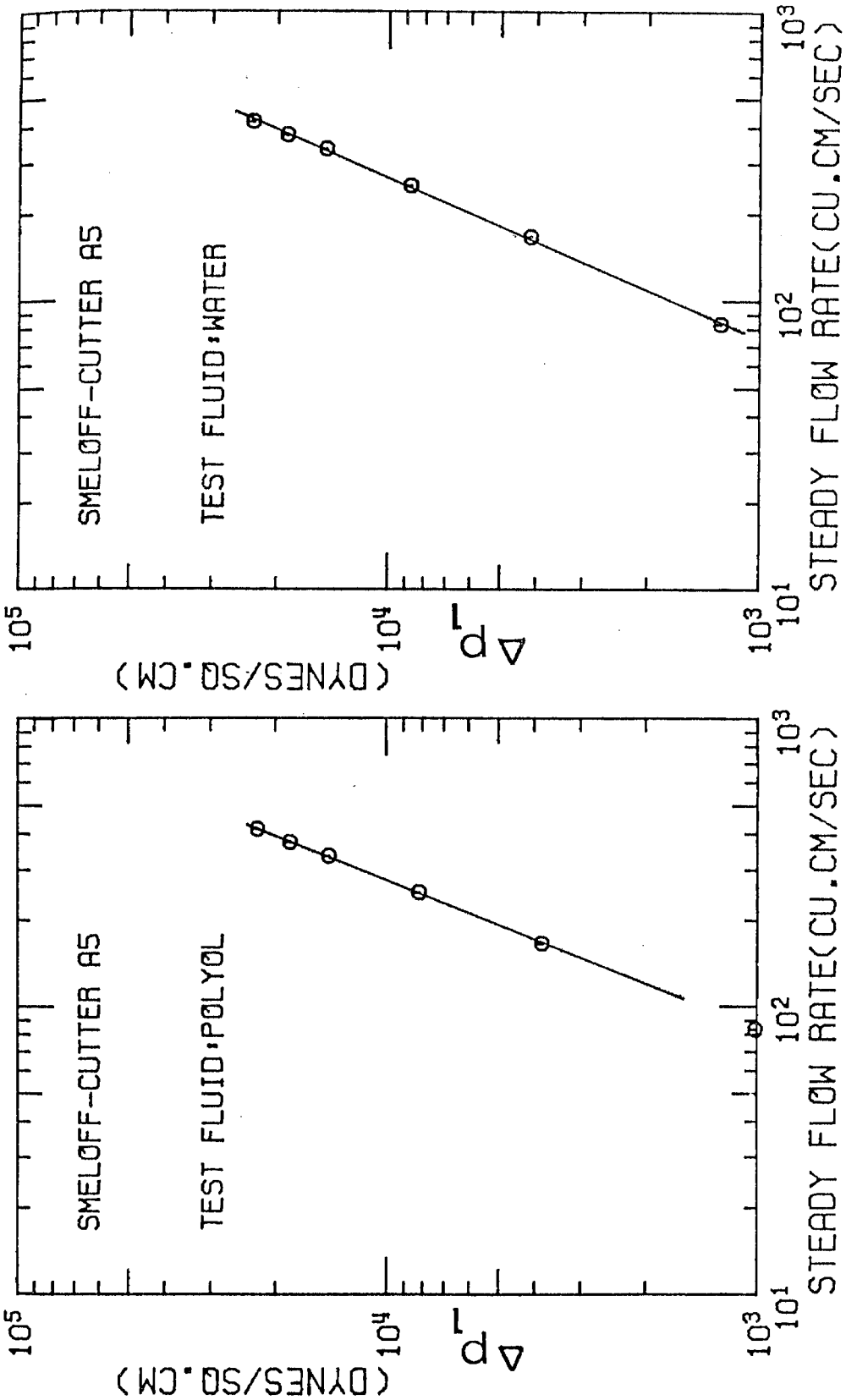

Fig. 30

Fig. 31

Steady flow pressure drop across the Smeloff-Cutter A-5 valve

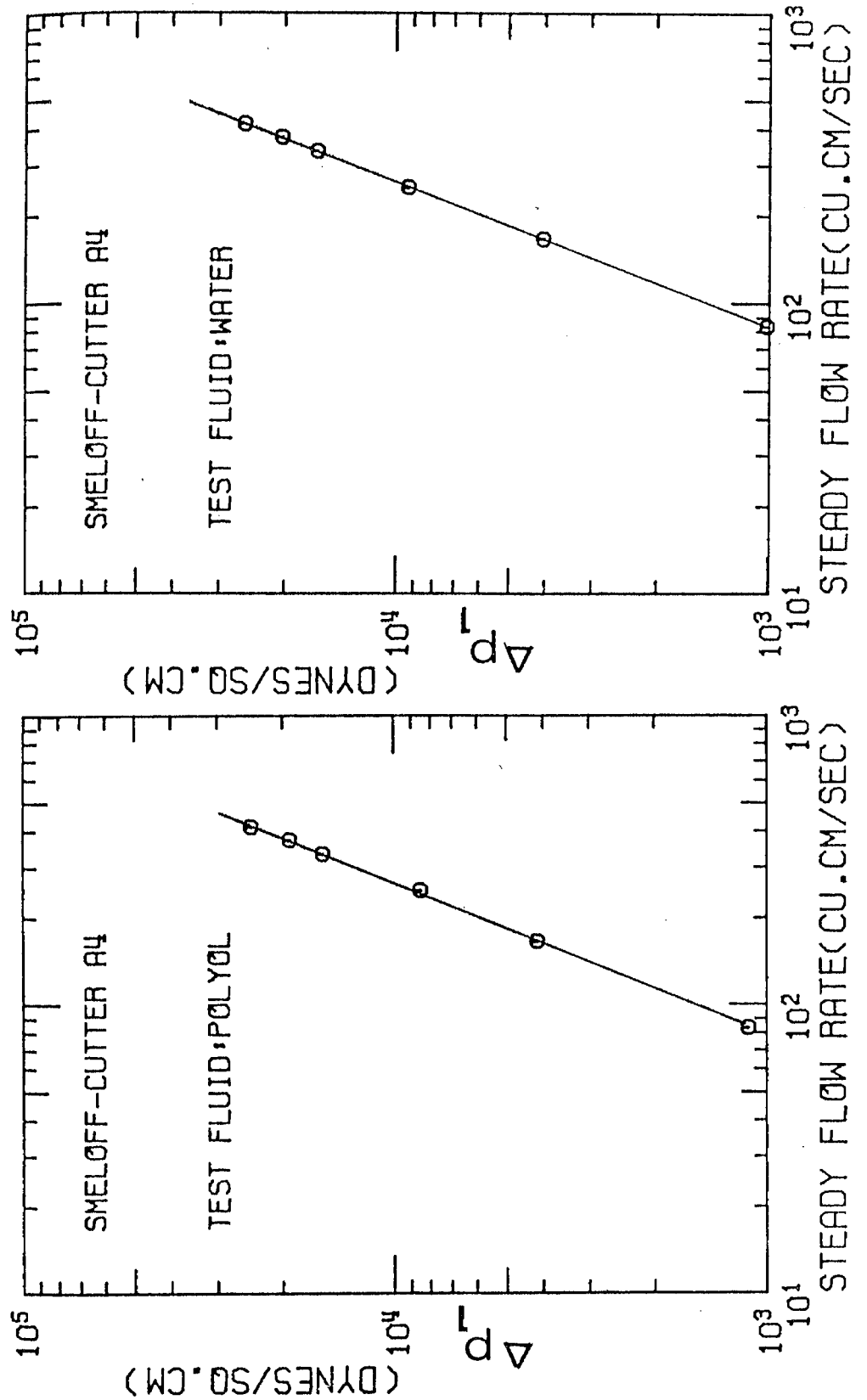

Fig. 32

Fig. 33

Steady flow pressure drop across the Smeloff-Cutter A-4 valve

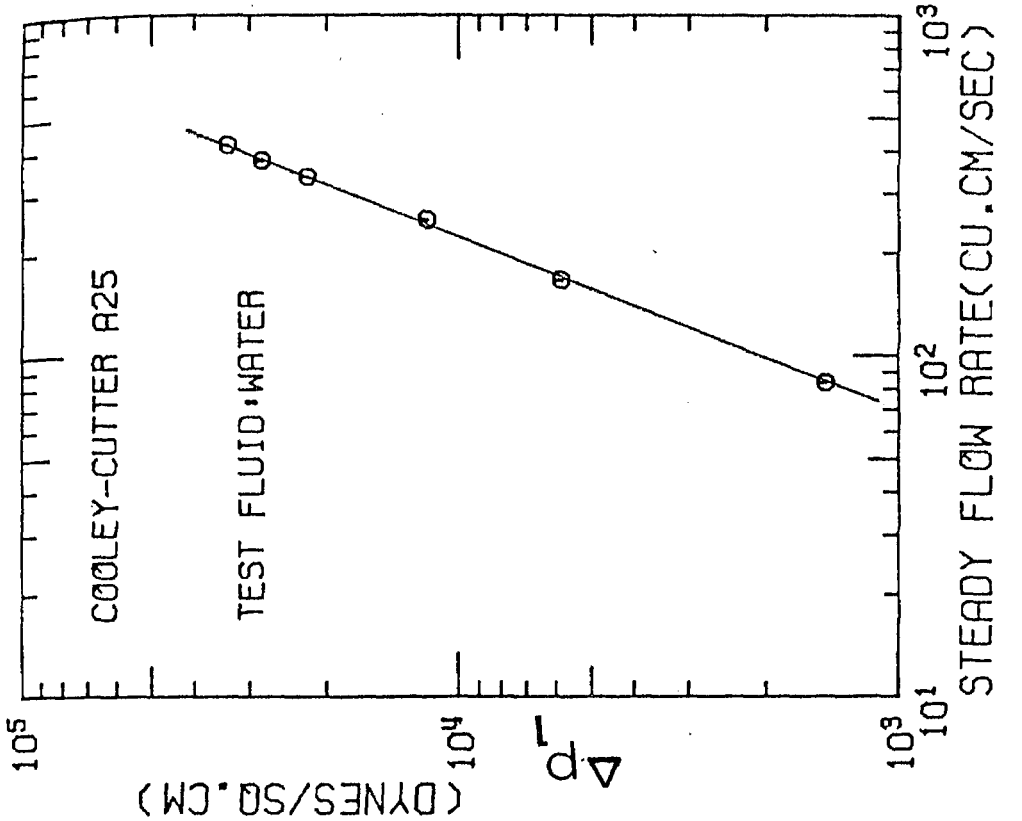

Fig. 35

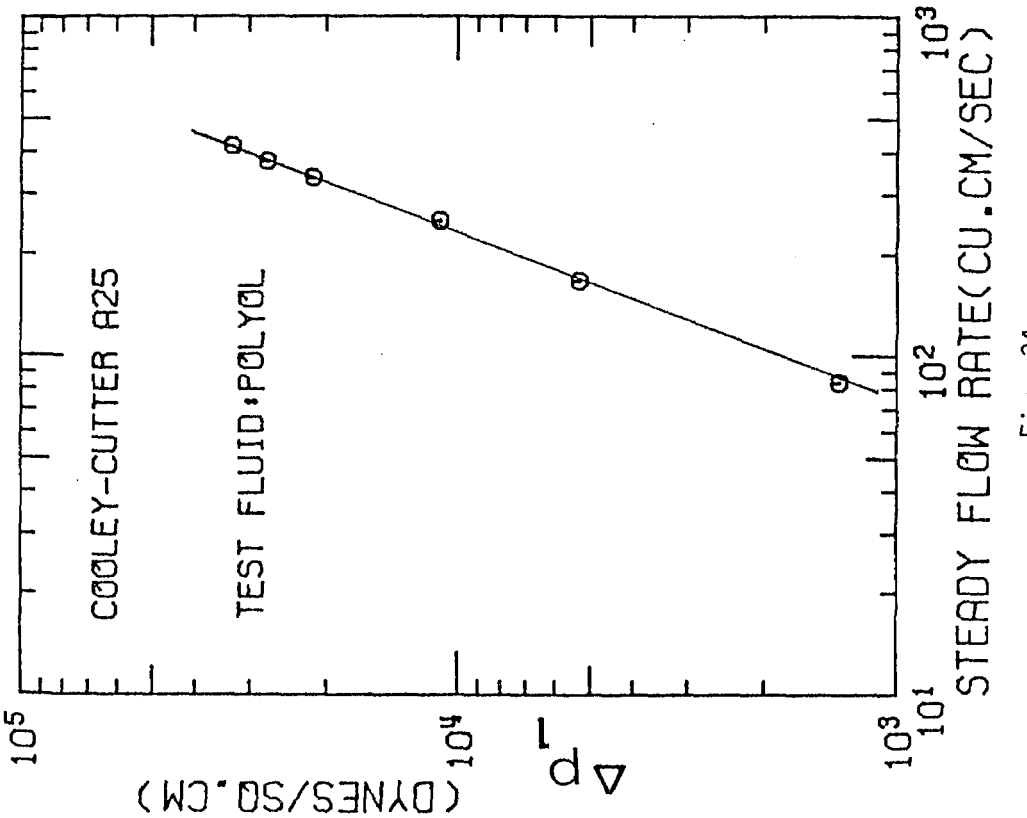

Fig. 34

Steady flow pressure drop across the Cooley-Cutter A-25 valve

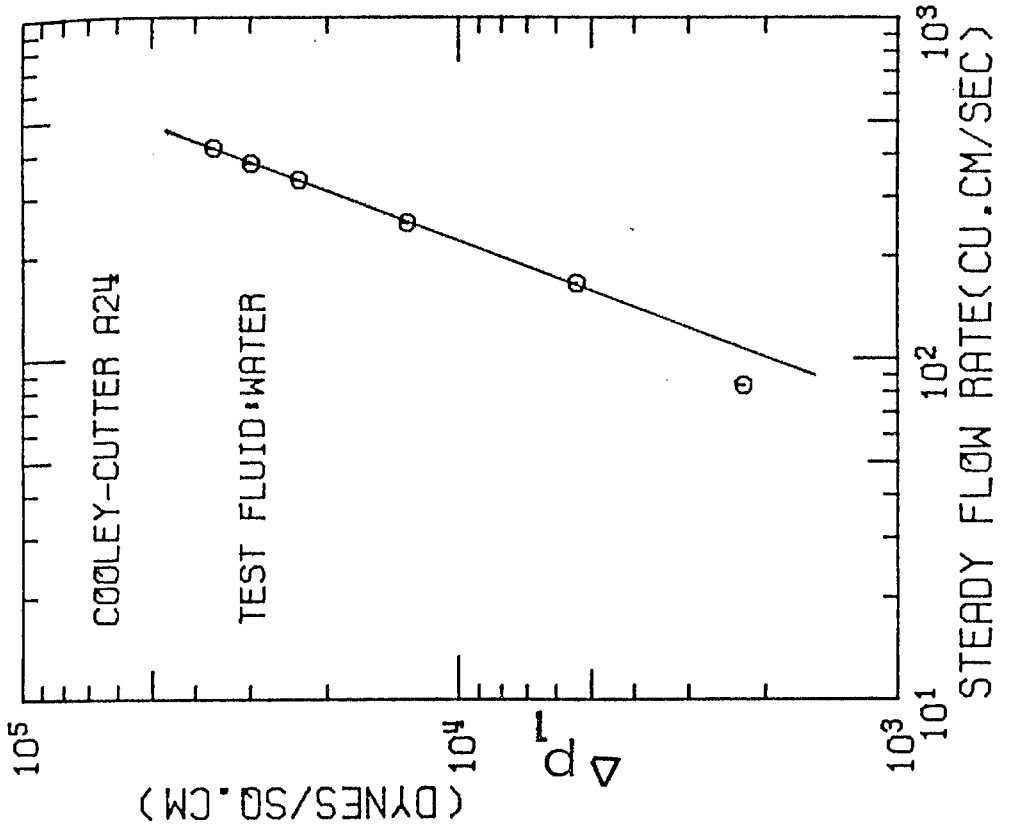

Fig. 37

Steady flow pressure drop across the Cooley-Cutter A-24 valve

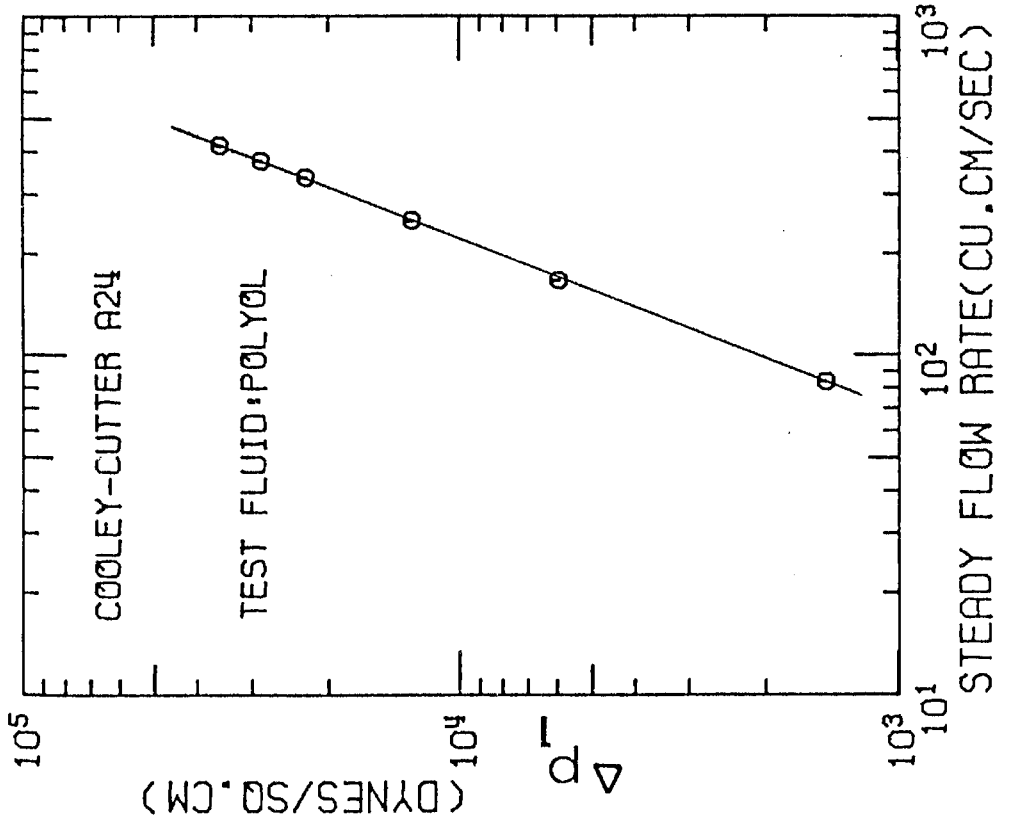

Fig. 36

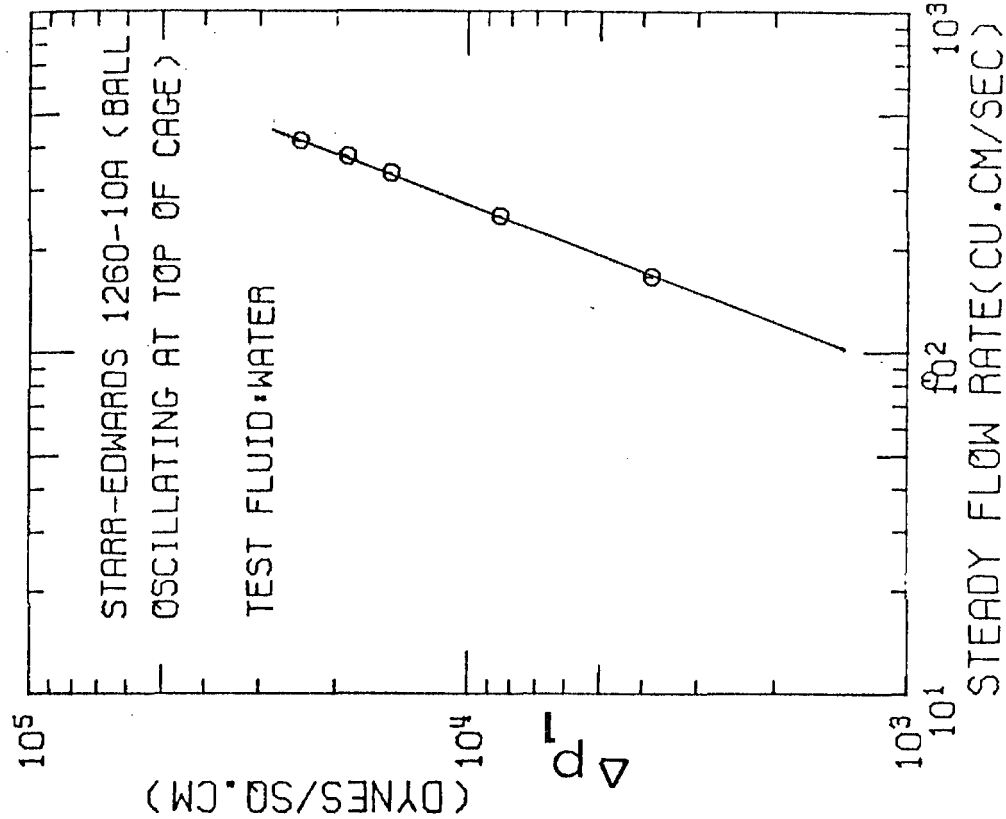

Fig. 39

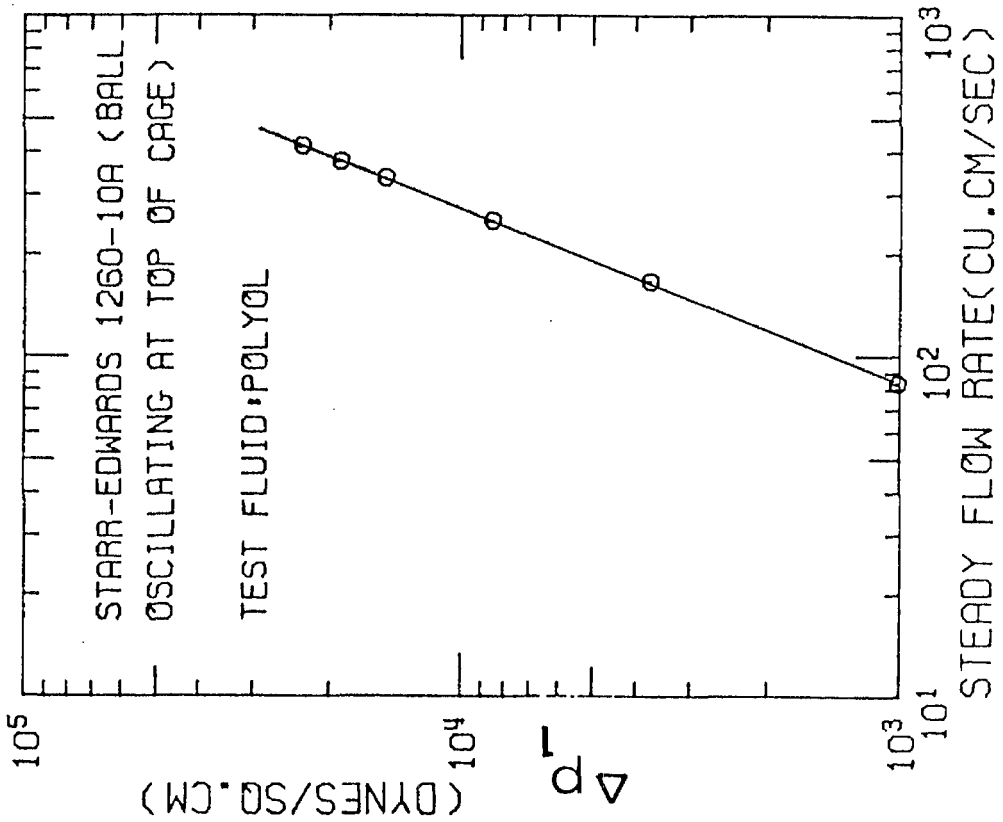

Fig. 38

Steady flow pressure drop across the Starr-Edwards 1260-10A valve (ball at top)

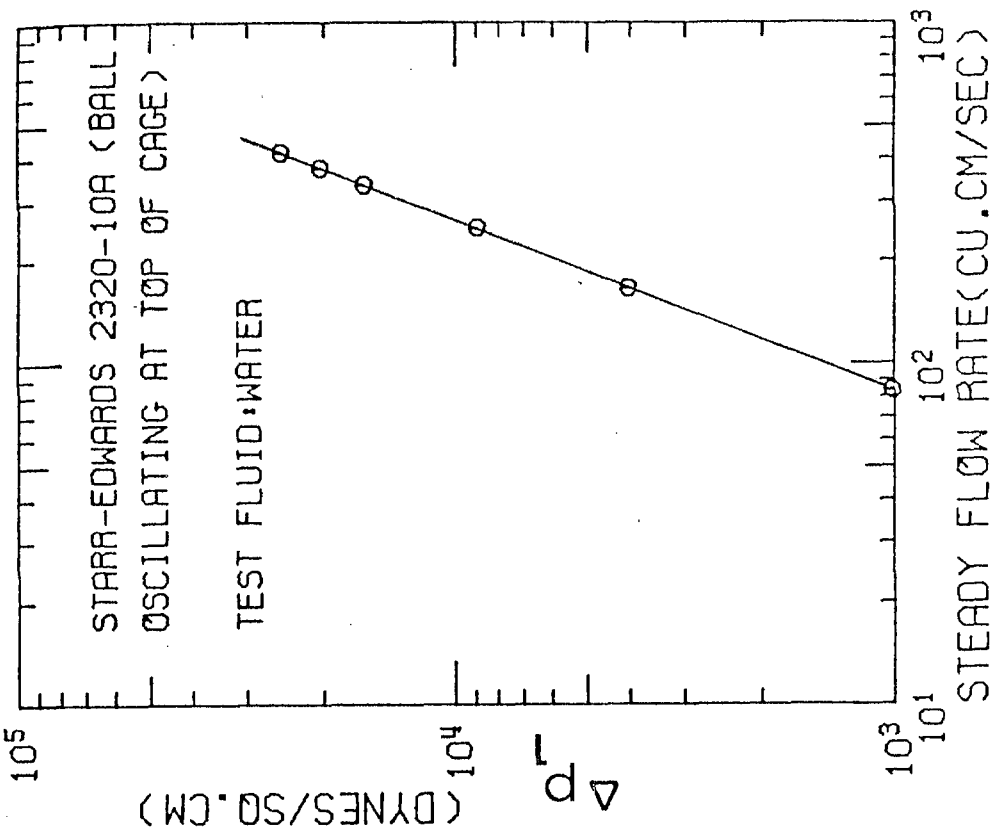

Fig. 41

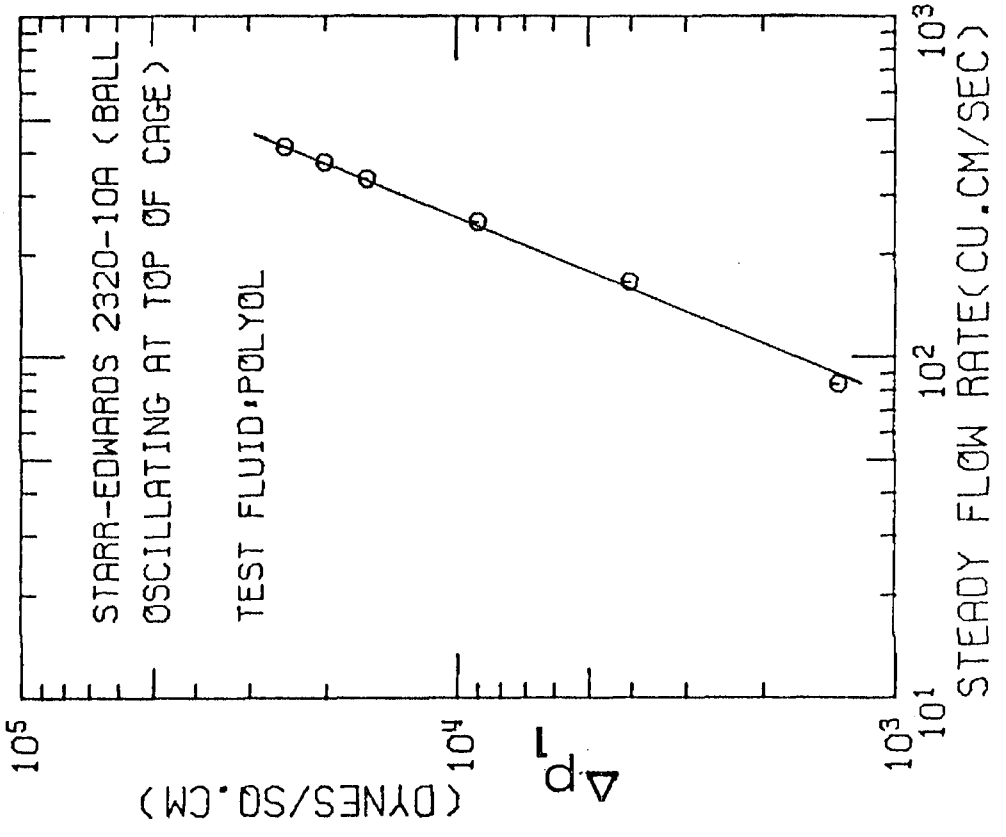

Fig. 40

Steady flow pressure drop across the Starr-Edwards 2320-10A valve (ball at top)

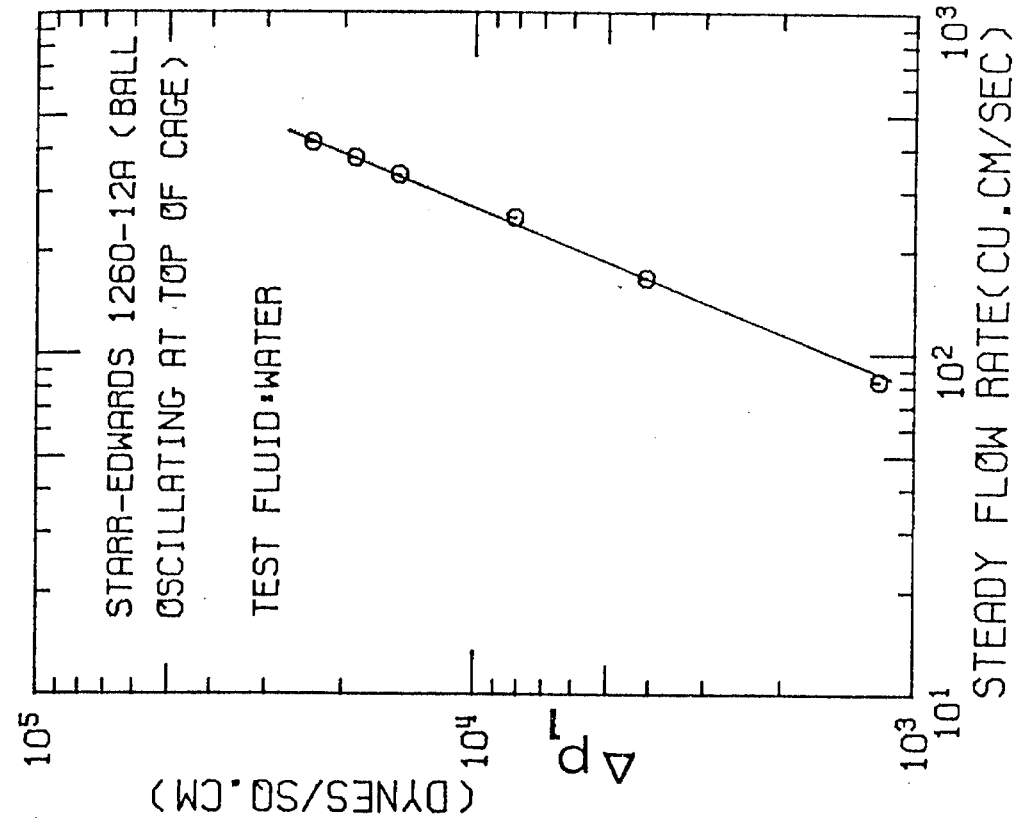

Fig. 43

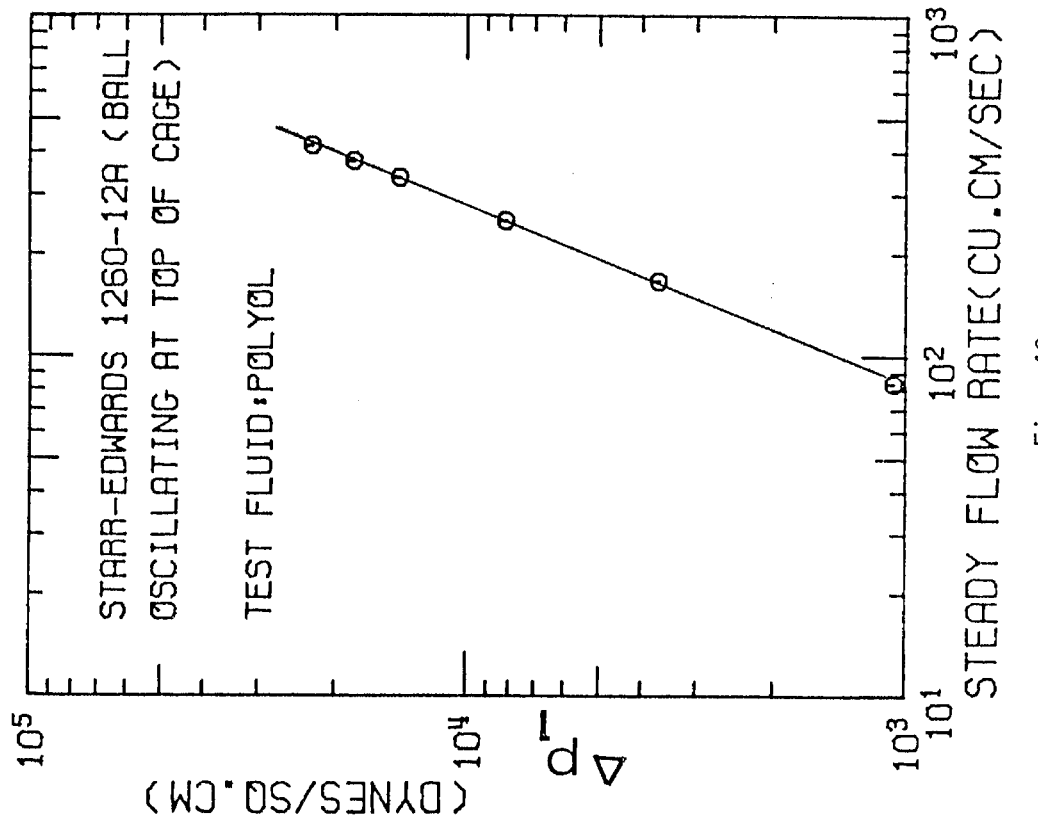

Fig. 42

Steady flow pressure drop across the Starr-Edwards 1260-12A valve (ball at top)

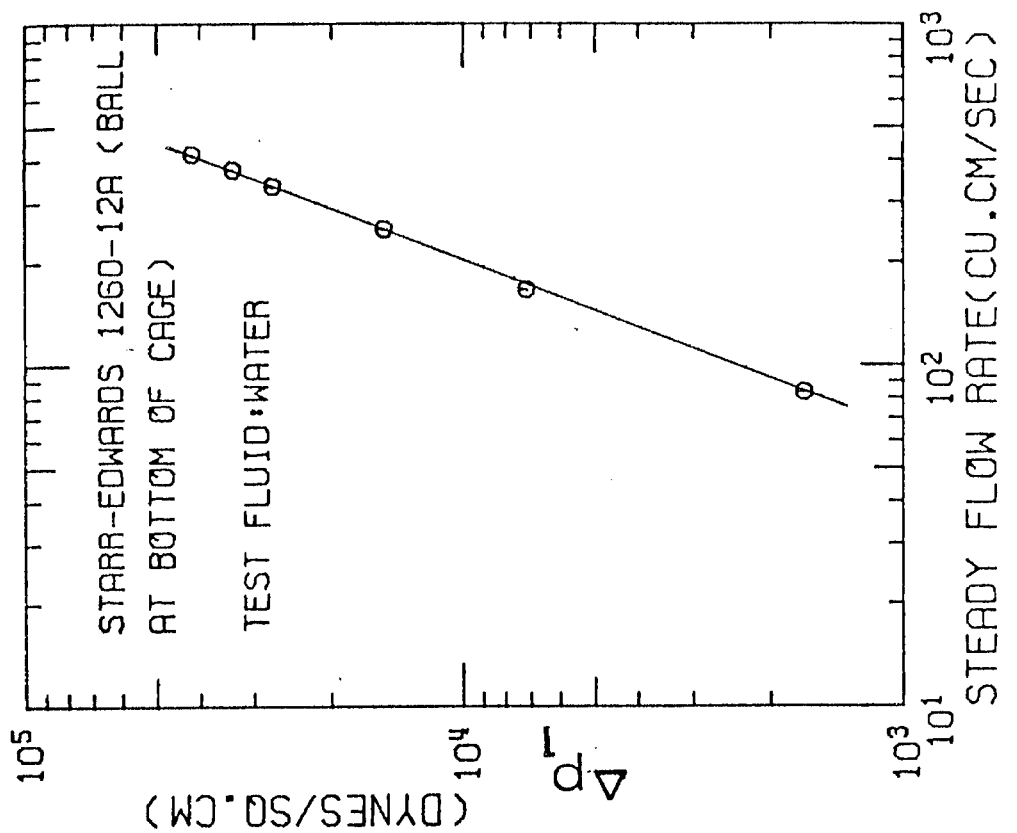

Fig. 45

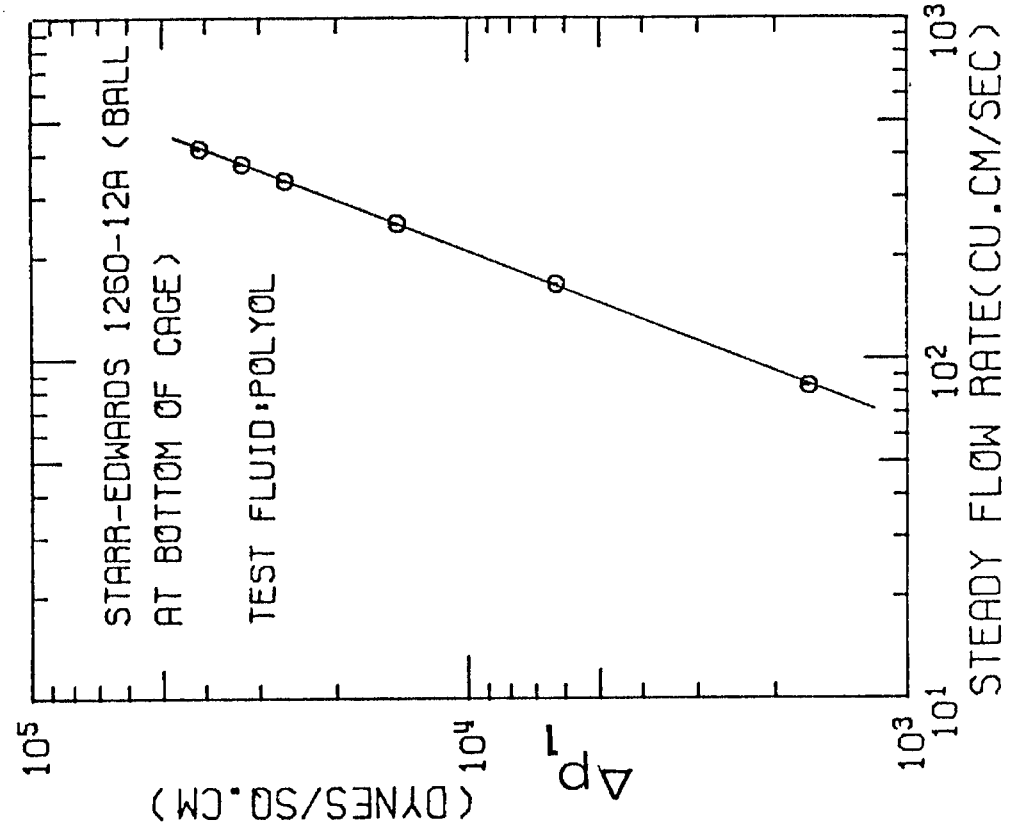

Fig. 44

Steady flow pressure drop across the Starr-Edwards 1260-12A valve (ball at bottom)

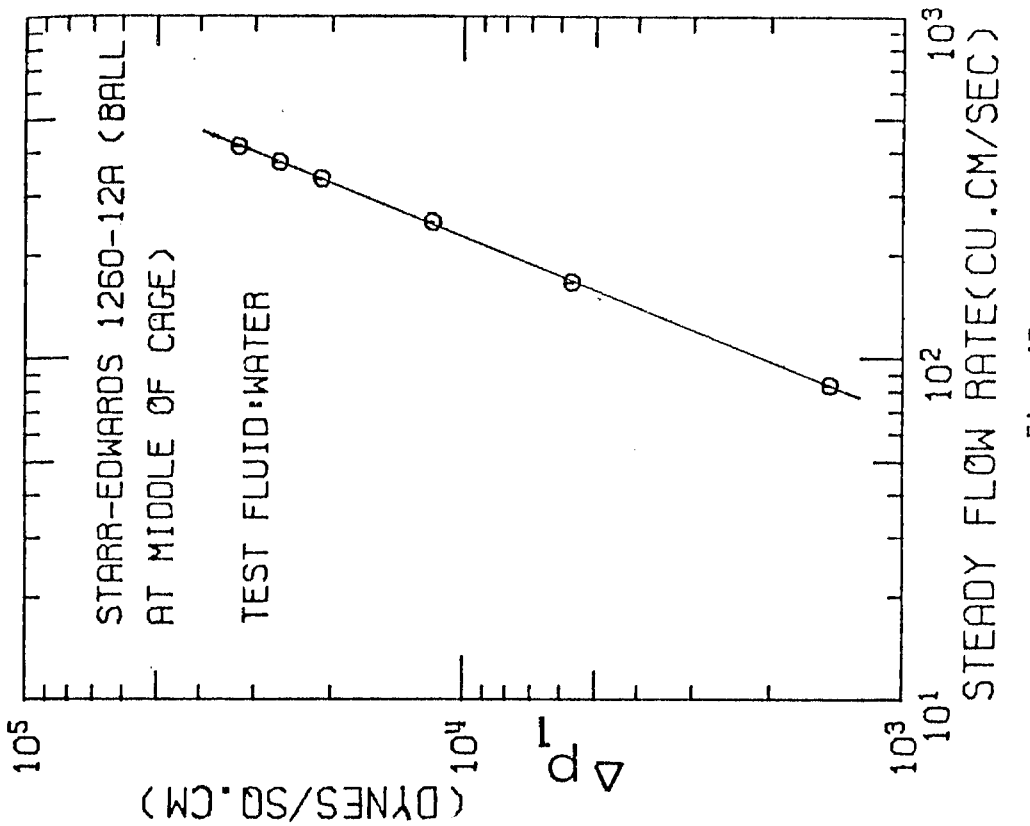

Fig. 47

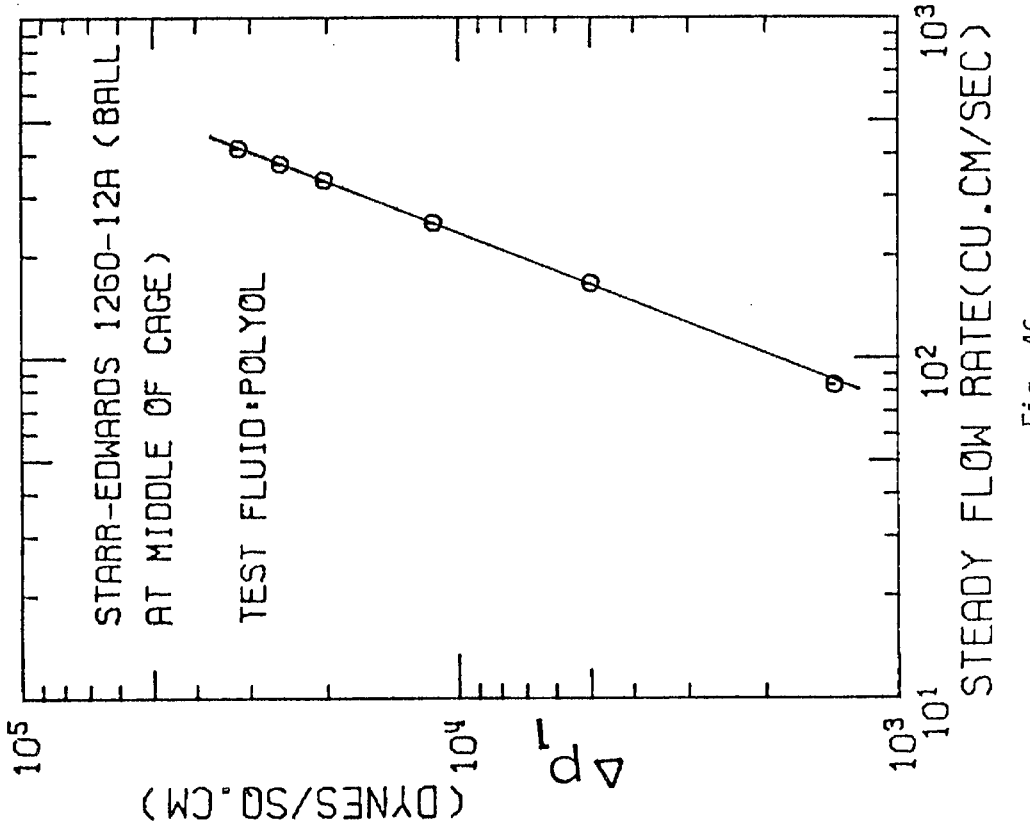

Fig. 46

Steady flow pressure drop across the Starr-Edwards 1260-12A valve (ball at middle)

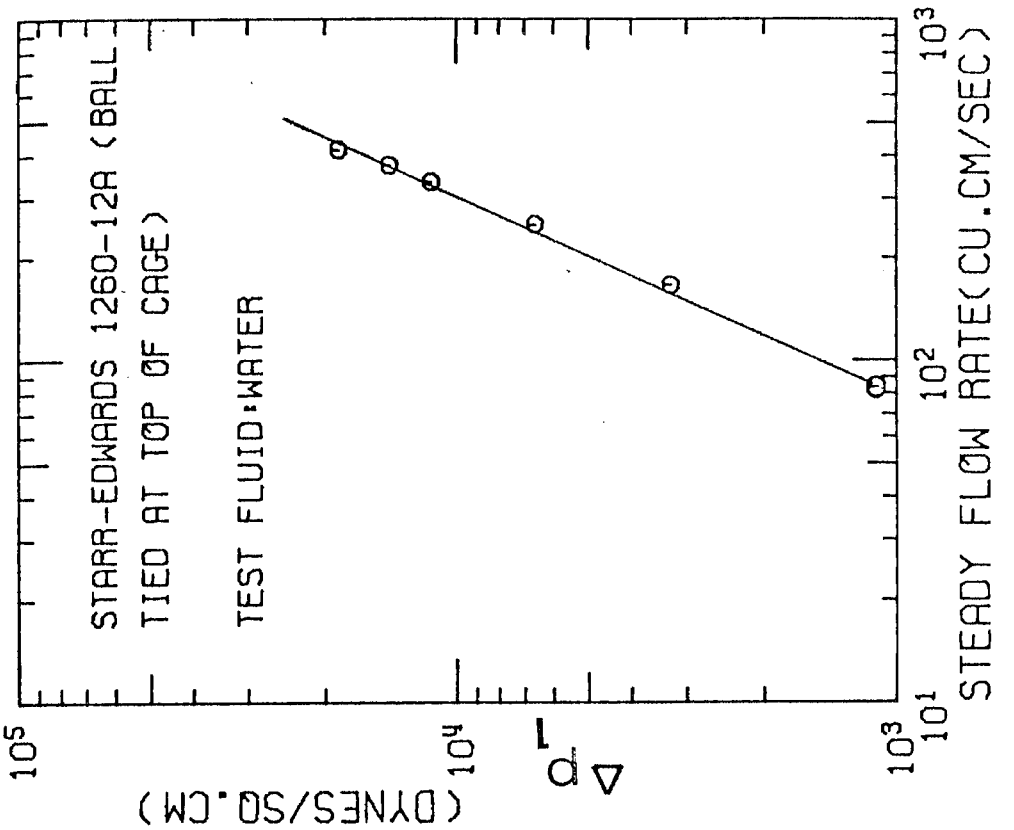

Fig. 49

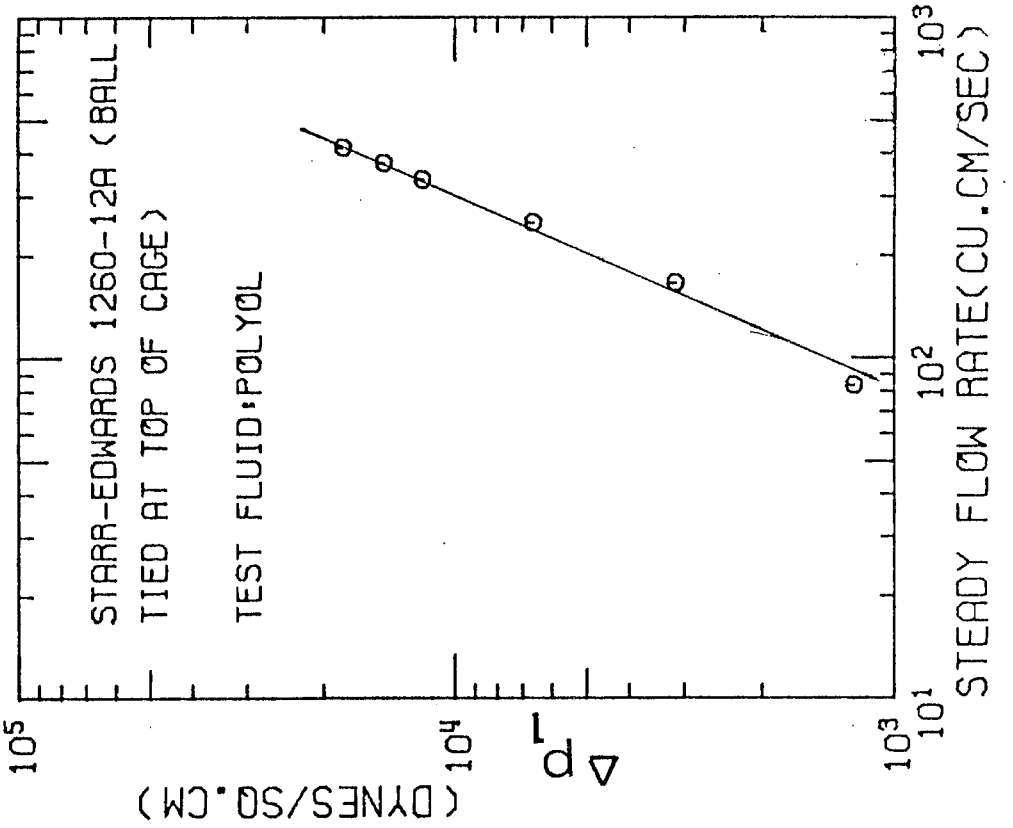

Fig. 48

Steady flow pressure drop across the Starr-Edwards 1260-12A valve (ball tied at top)

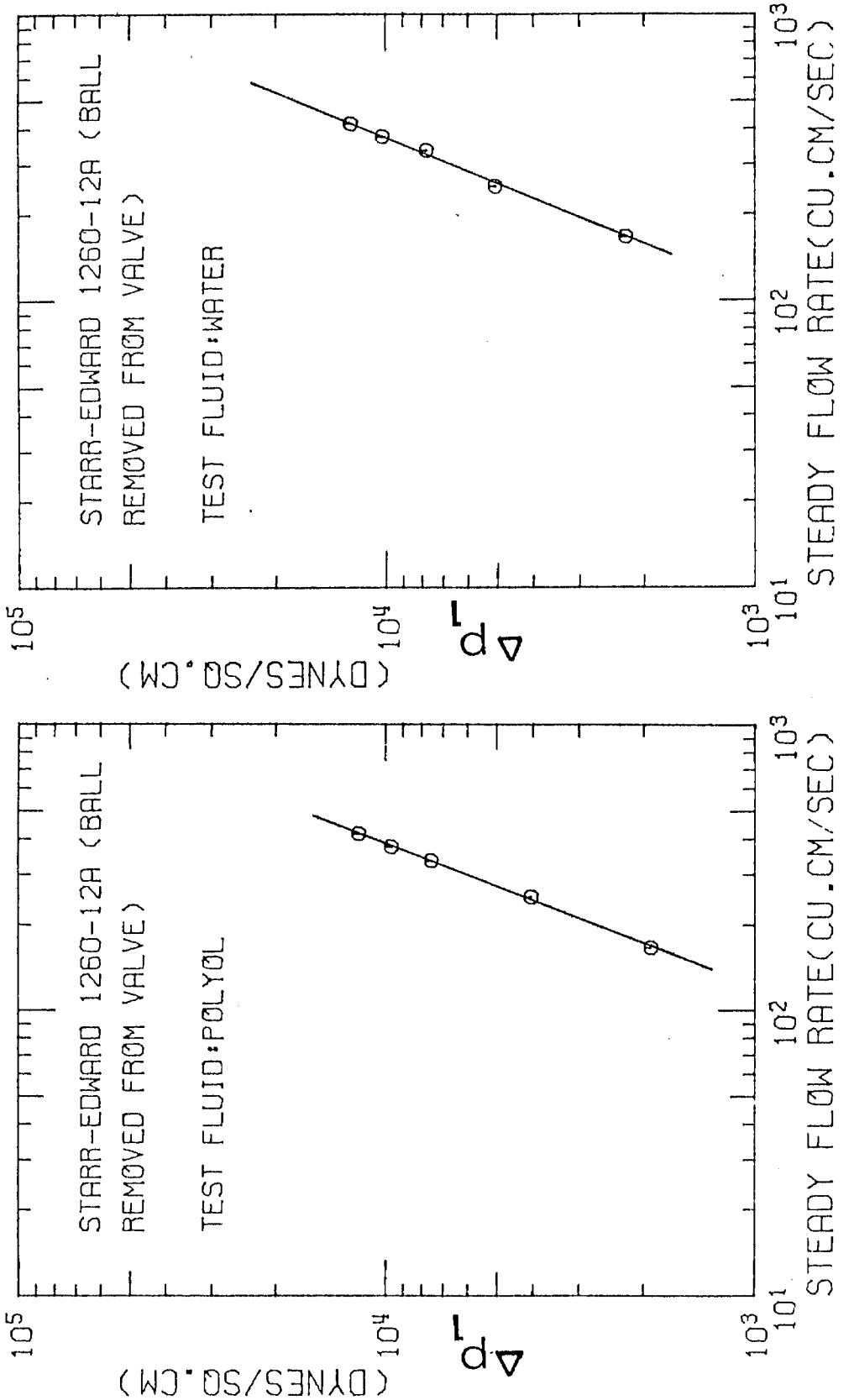

Fig. 51

Fig. 50

Steady flow pressure drop across the Starr-Edwards 1260-12A valve (ball removed)

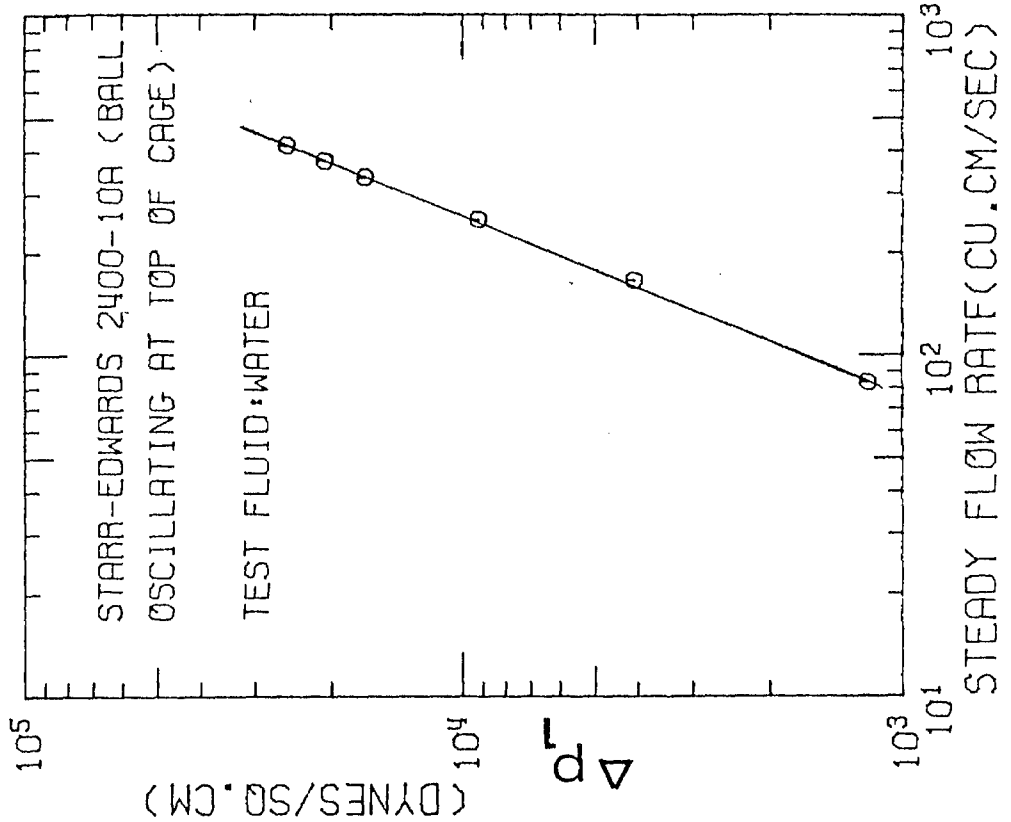

Fig. 53

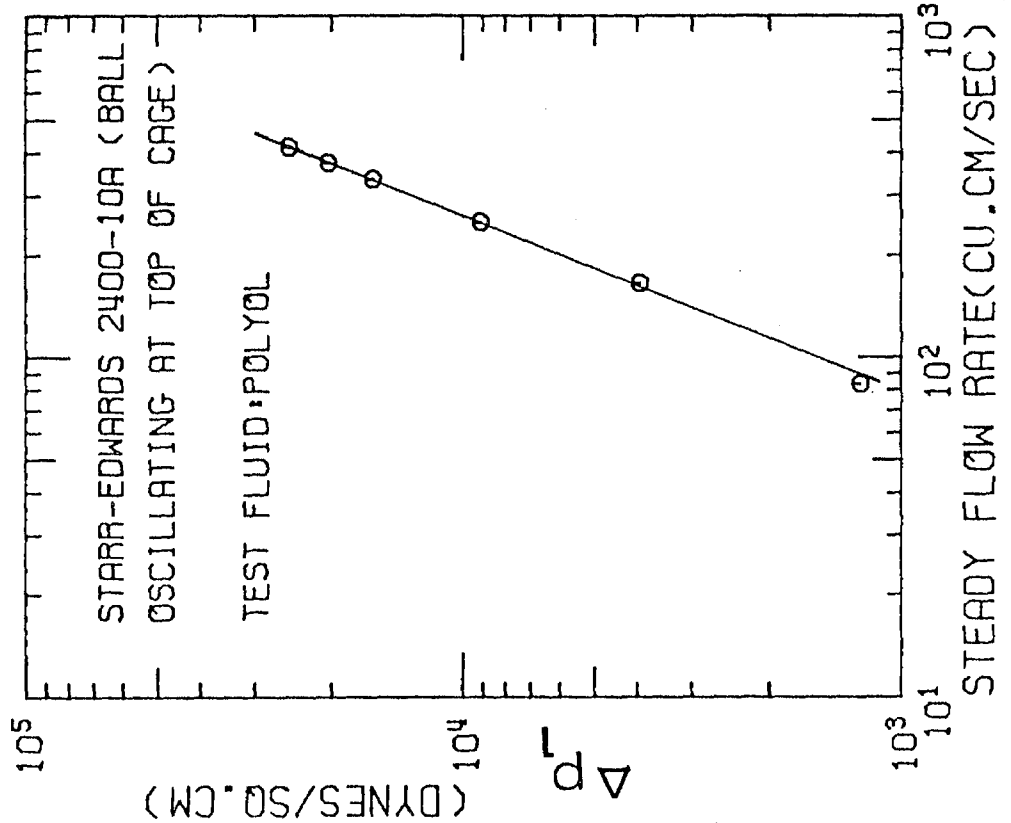

Fig. 52

Steady flow pressure drop across the Starr-Edwards 2400-10A valve (ball at top)

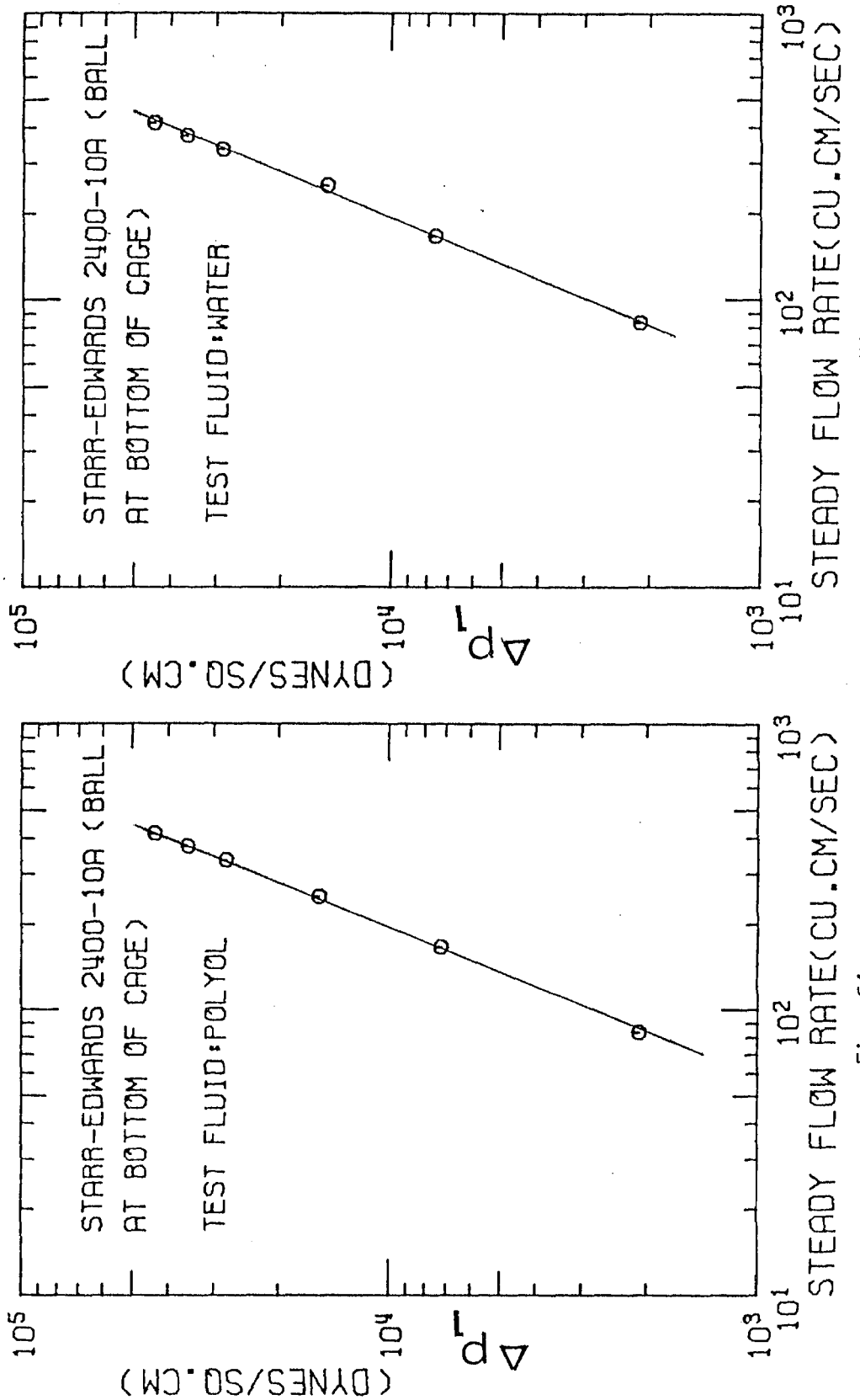

Fig. 54

Fig. 55

Steady flow pressure drop across the Starr-Edwards 2400-10A valve (ball at bottom)

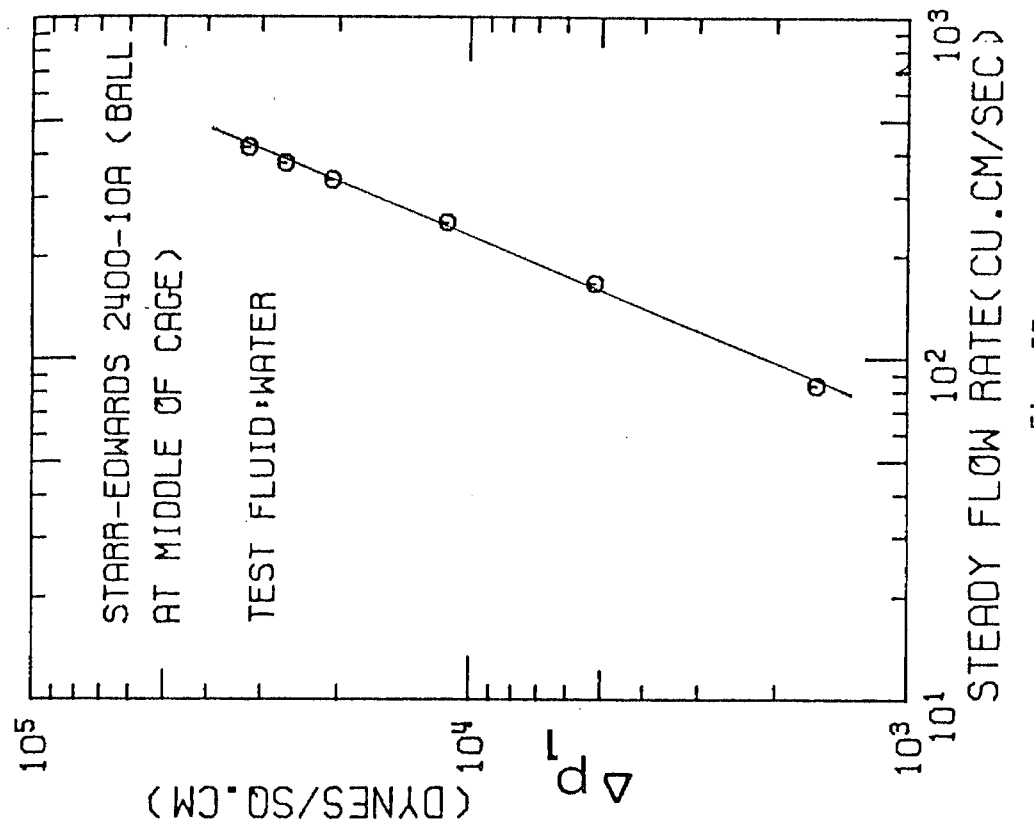

Fig. 57

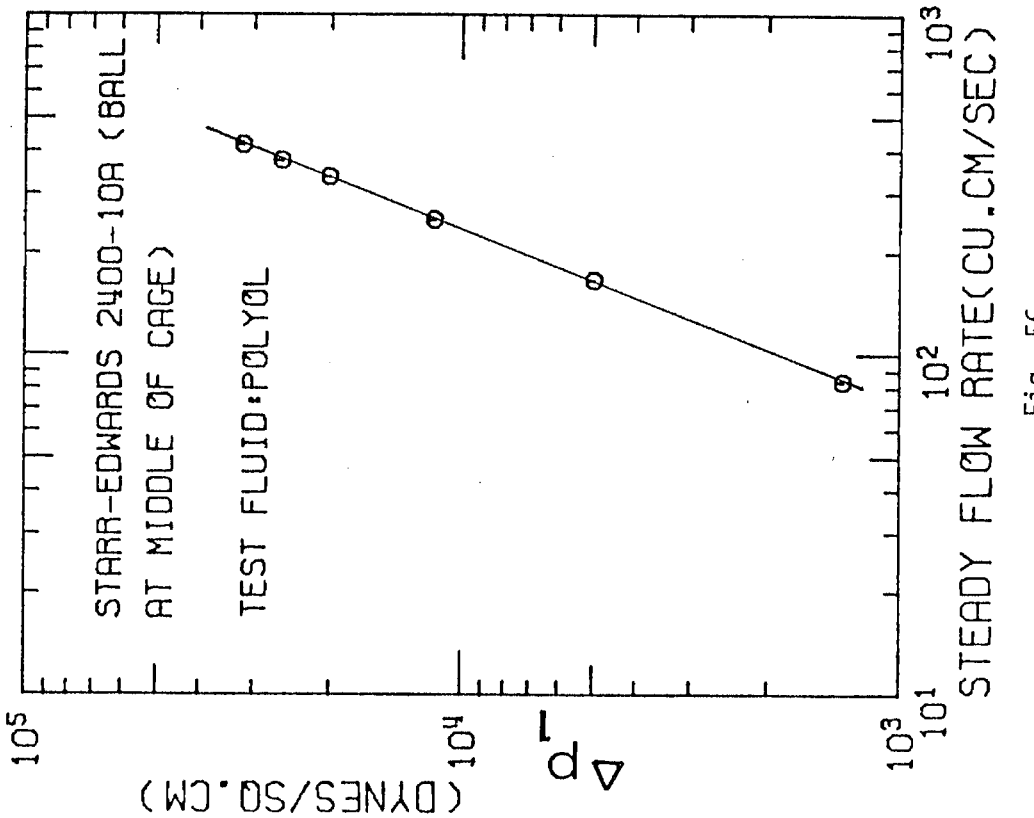

Fig. 56

Steady flow pressure drop across the Starr-Edwards 2400-10A valve (ball at middle)

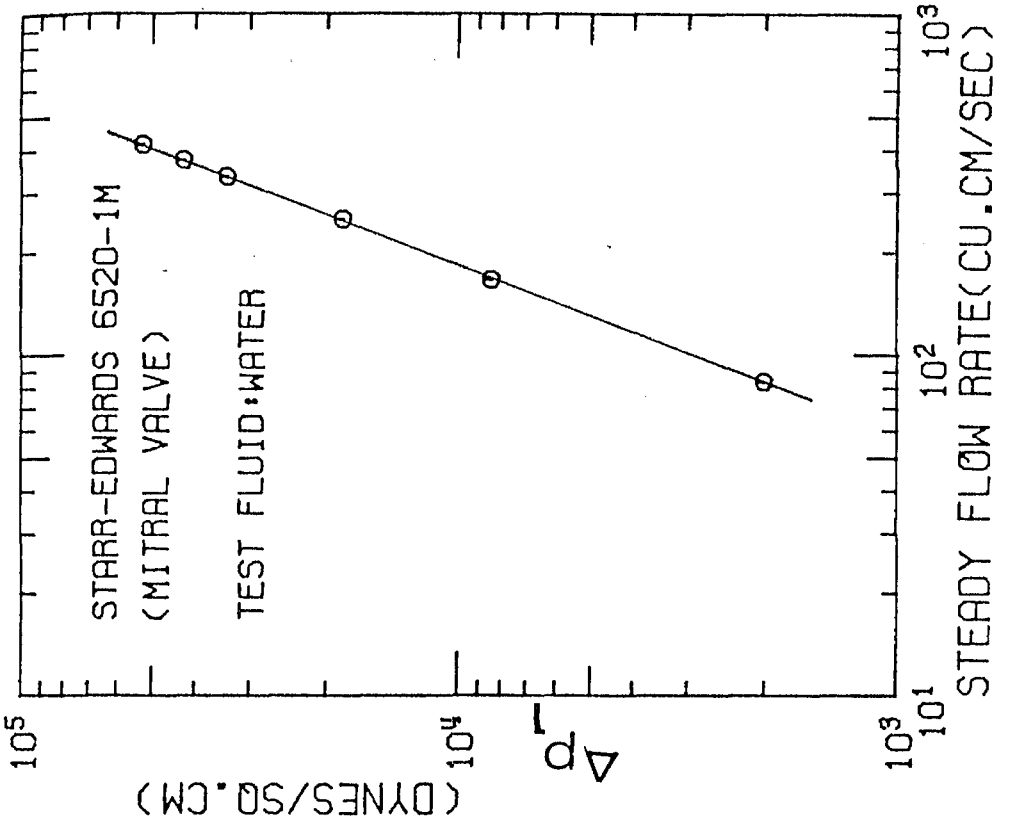

Fig. 59

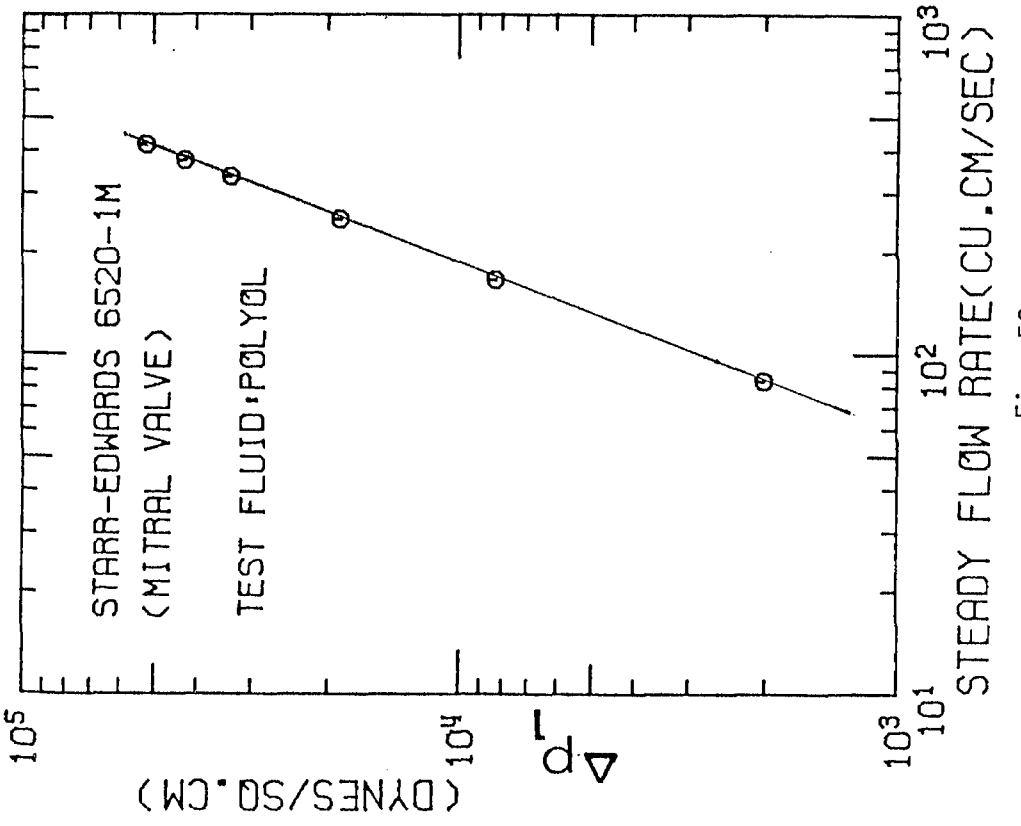

Fig. 58

Steady flow pressure drop across the Starr-Edwards 6520-1M mitral valve

1	Björk-Shiley	27XMBRP
2	Starr-Edwards	1260-12A (ball tied at top of cage)
3	Smeloff-Cutter	A5
	Starr-Edwards	1260-12A (ball oscillating at top)
4	Starr-Edwards	1260-12A (ball oscillating at middle)
	Cooley-Cutter	A-25
5	Starr-Edwards	1260-12A (ball oscillating at bottom)

Note: A double ranking indicates that within experimental error the pressure drops across both valves were almost indentical. A similar ranking of the peak-systolic and mean-systolic pressure-drop data gives:

1	Björk-Shiley	27XMBRP
2	Smeloff-Cutter	A5
3	Starr-Edwards	1260-12A
	Cooley-Cutter	A25

A ranking of the smaller size valves under steady flow conditions gives:

1	Björk-Shiley	25XMBRP
2	Starr-Edwards	1260-10A (ball oscillating at top)
3	Starr-Edwards	2320-10A (ball oscillating at top)
4	Starr-Edwards	2400-10A (ball oscillating at top)
5	Smeloff-Cutter	A4
6	Starr-Edwards	2400-10A (ball oscillating at middle)
7	Cooley-Cutter	A24
8	Starr-Edwards	2400-10A (ball oscillating at bottom)

Under pulsatile flow conditions:

1	Bjork-Shiley	25XMBRP
2	Smeloff-Cutter	A5
3	(Starr-Edwards	1260-10A
	(Starr-Edwards	2320-10A
	(Starr-Edwards	2400-10A
4	Cooley-Cutter	A24

It was observed that in order to predict the peak-systolic and mean-systolic pressure drops (equations (19) and (20)) across the Starr-Edwards ball valves, the steady-flow data of the balls oscillating at the middle of their cages were required. These observations strongly suggest that the poppets of the Starr-Edwards ball valves stay at the middle of their cages during the major part of systole instead of staying at the top of the cage as was envisioned when originally designed. During the opening phase of the valve the ball strikes the apex (top) of the cage and bounces back to the middle of cage, where it seems to attain an equilibrium position. The above observations have not, to my knowledge, been reported in the literature. The observations made of the Starr-Edwards ball valve in this study under pulsatile flow may not always occur in every in vitro test performed, or in every patient who has such a valve. The reasons for the hydrodynamic instability of the ball are due to complex fluid dynamic interactions of the fluid with the superstructure of the valve and the walls of the heart valve chamber. No hydrodynamic instability of the ball was observed with the Smeloff-Cutter valves under steady flow conditions. Therefore, possible

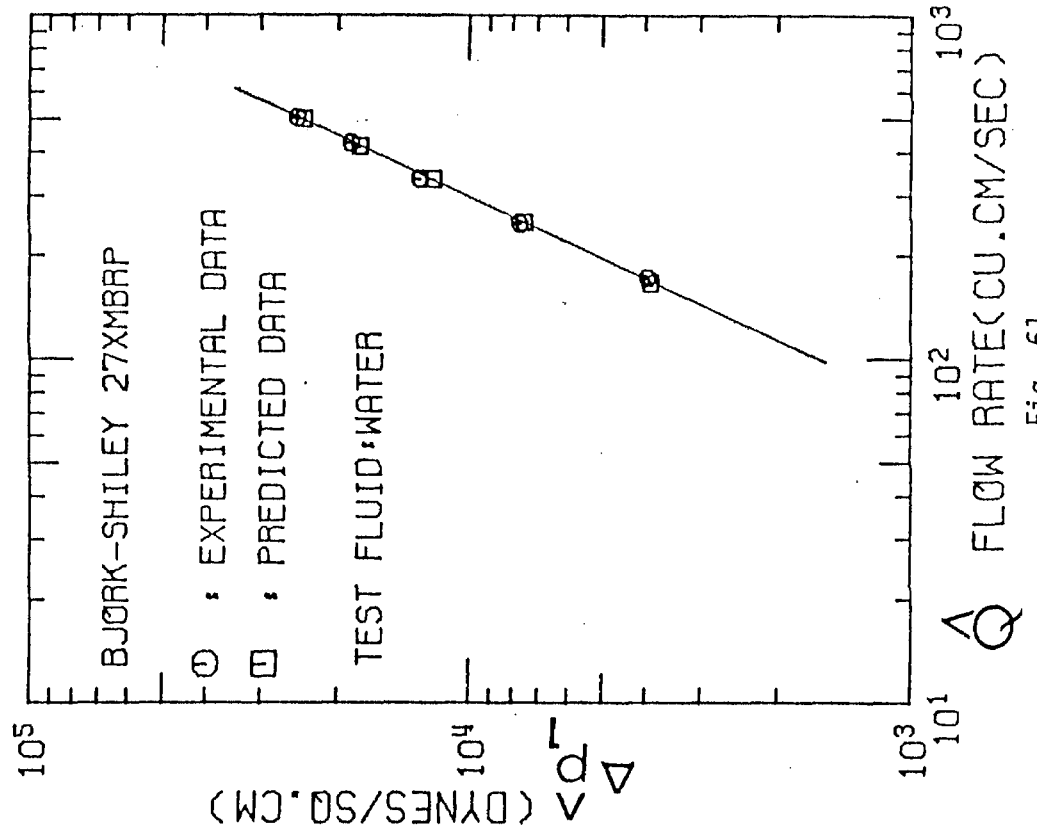

Fig. 61

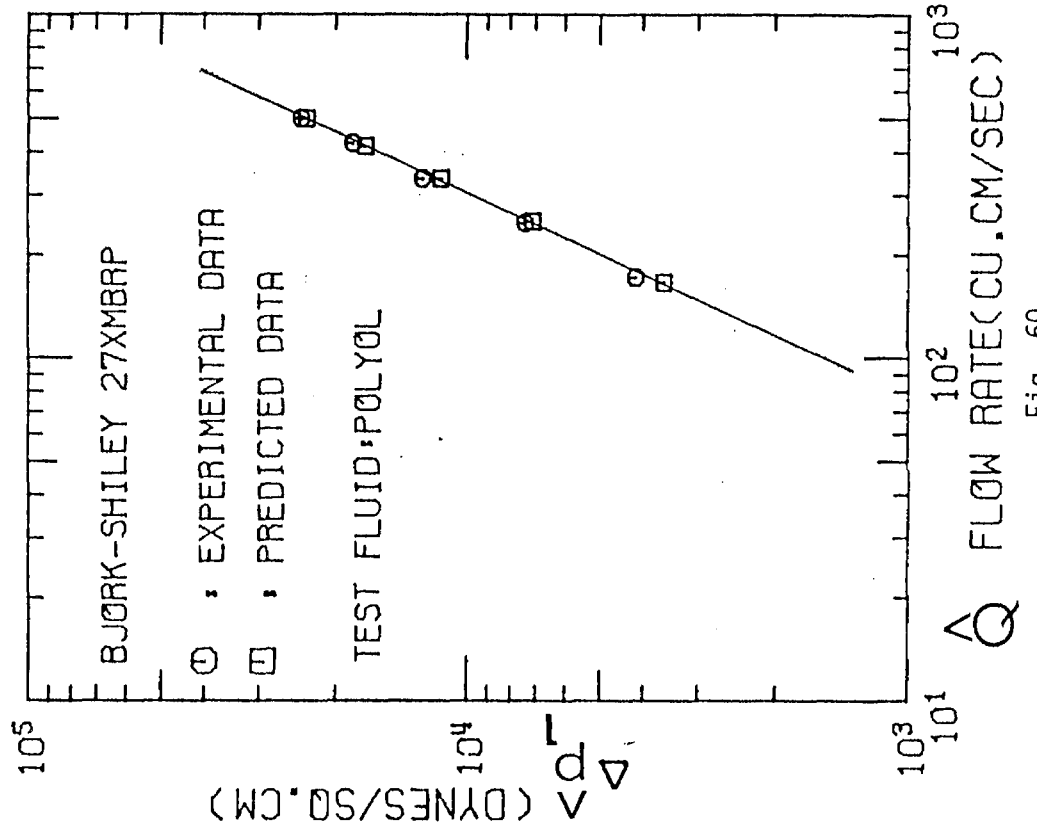

Fig. 60

Peak systolic pressure drop across the Björk-Shiley 27XMBRP valve

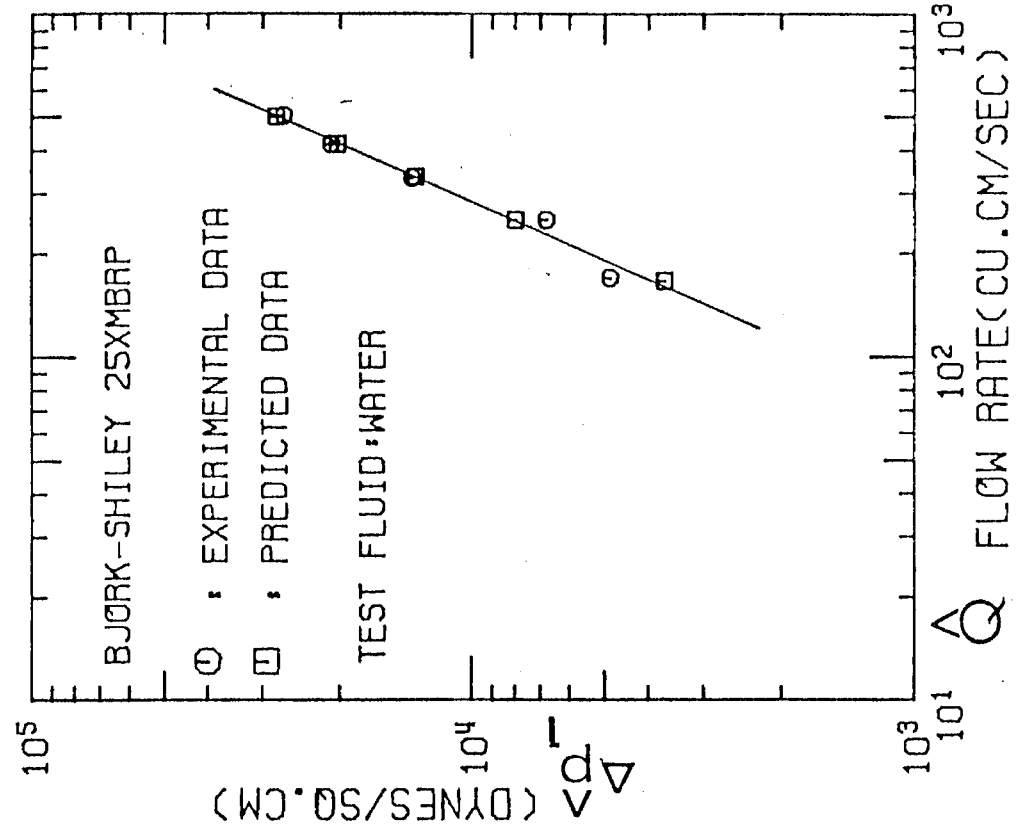

Fig. 63

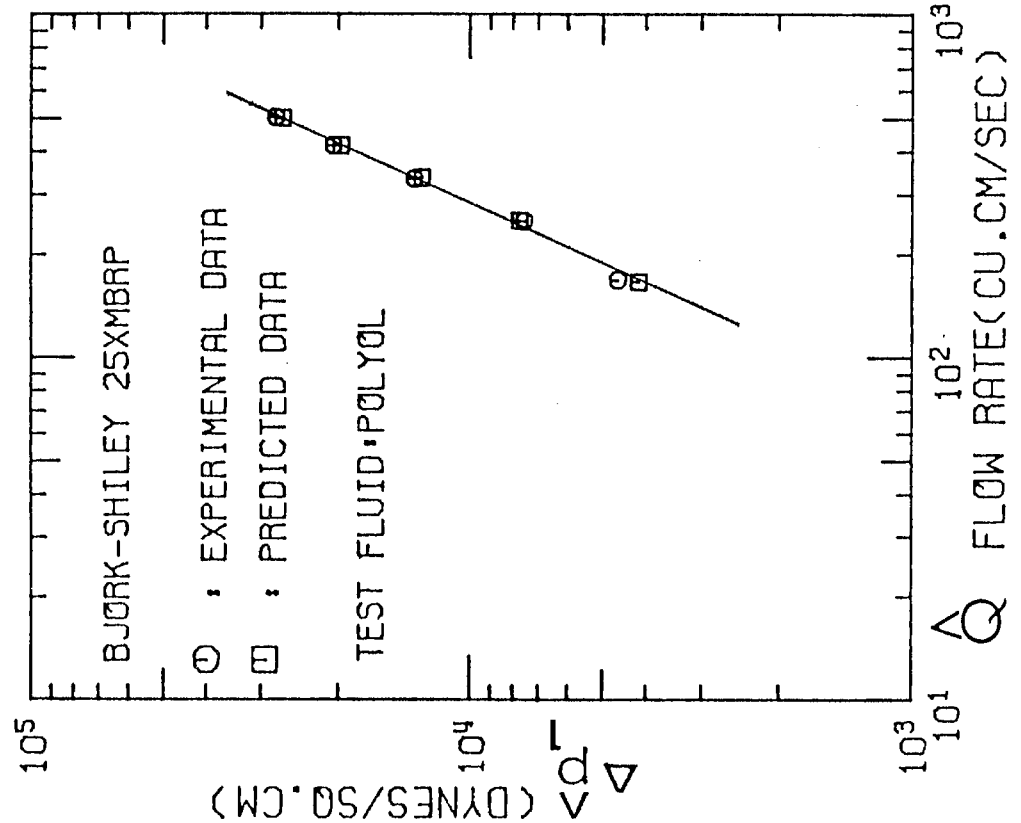

Fig. 62

Peak systolic pressure drop across the Björk-Shiley 25XMBRP valve

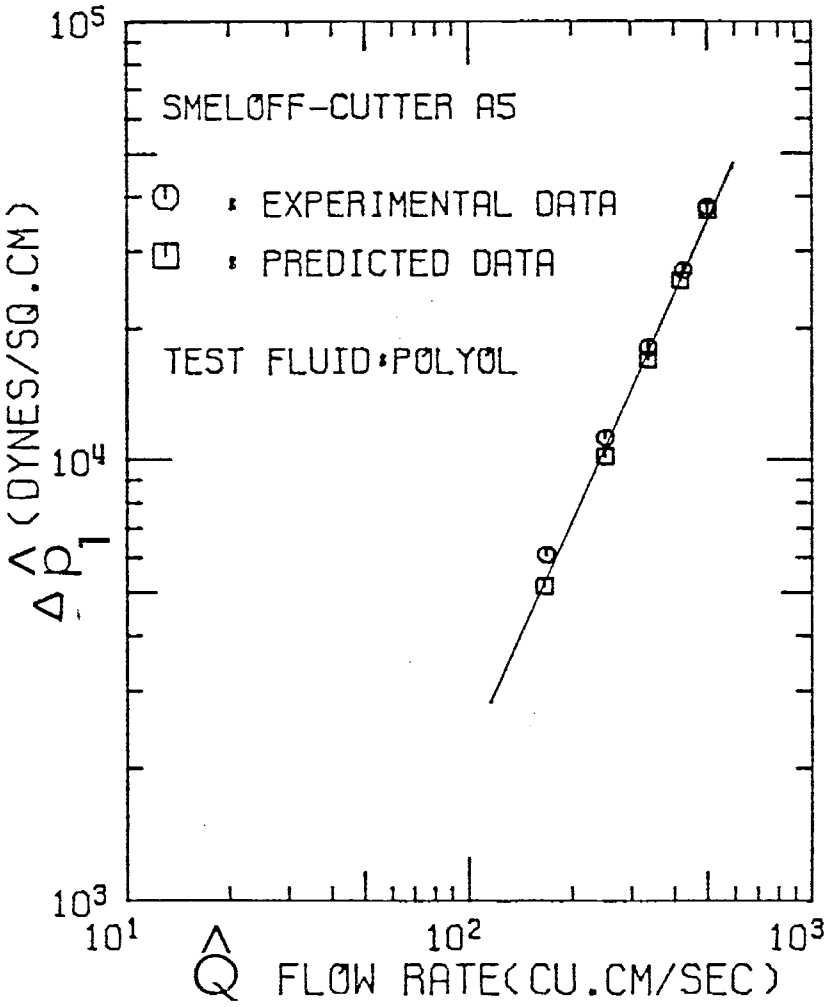

Fig. 64

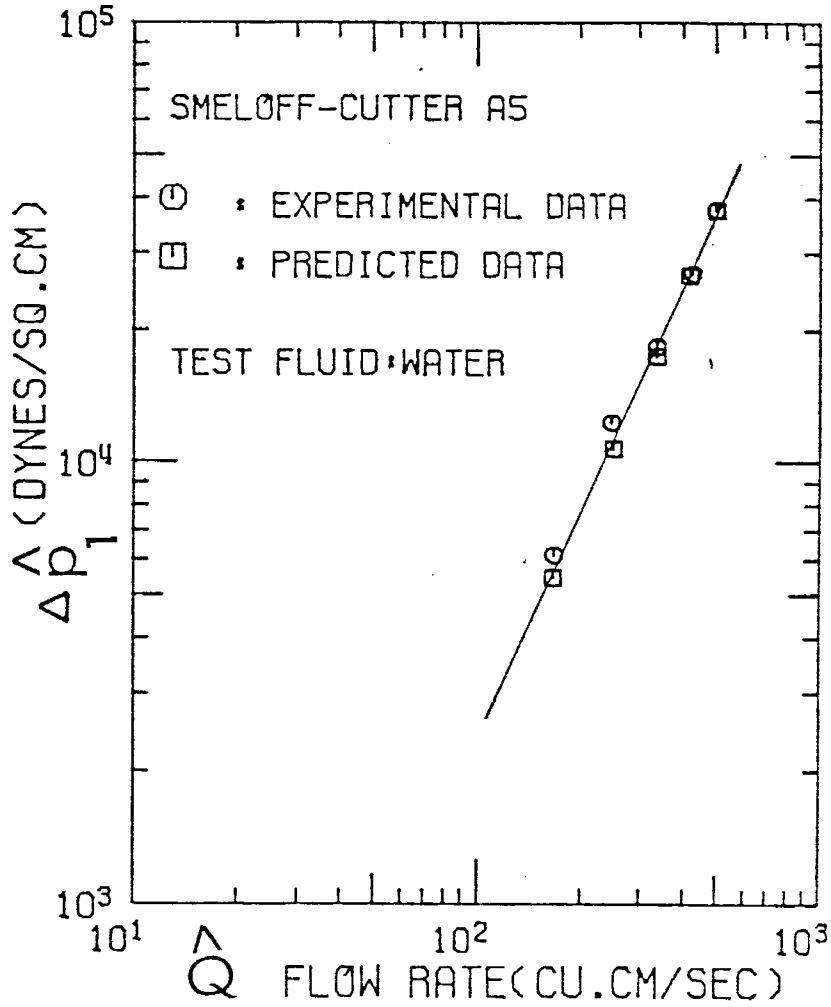

Fig. 65

Peak systolic pressure drop across the Smeloff-Cutter A-5 valve

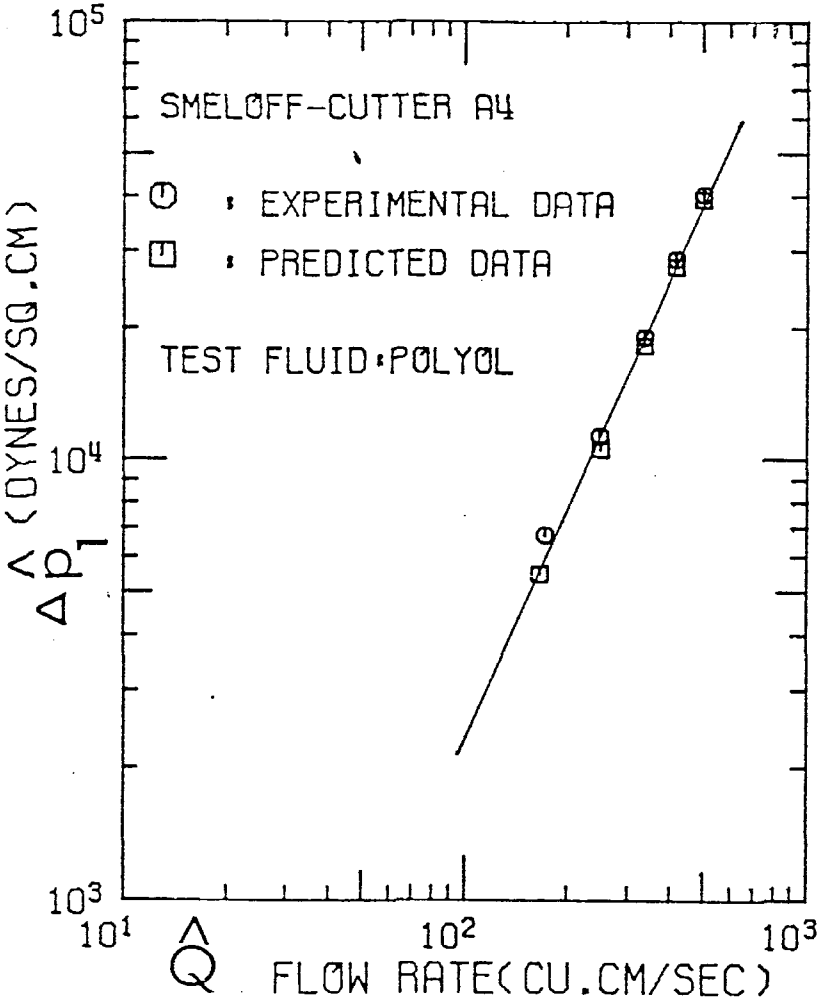

Fig. 66

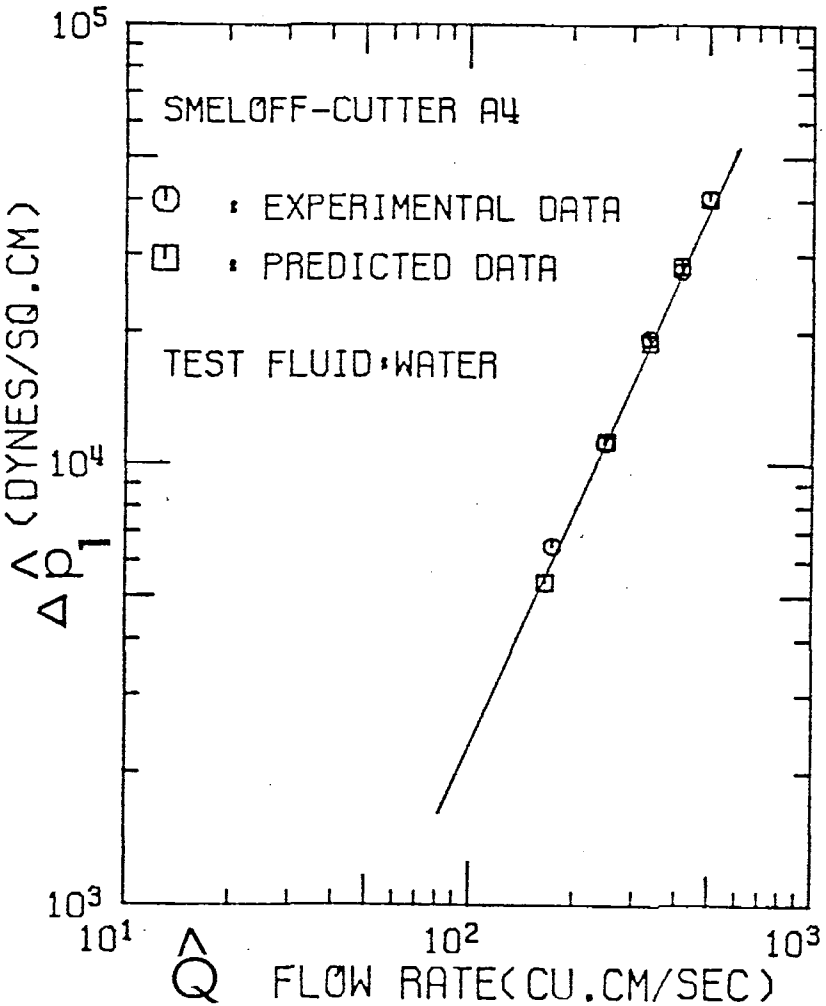

Fig. 67

Peak systolic pressure drop across the Smeloff-Cutter A4 valve

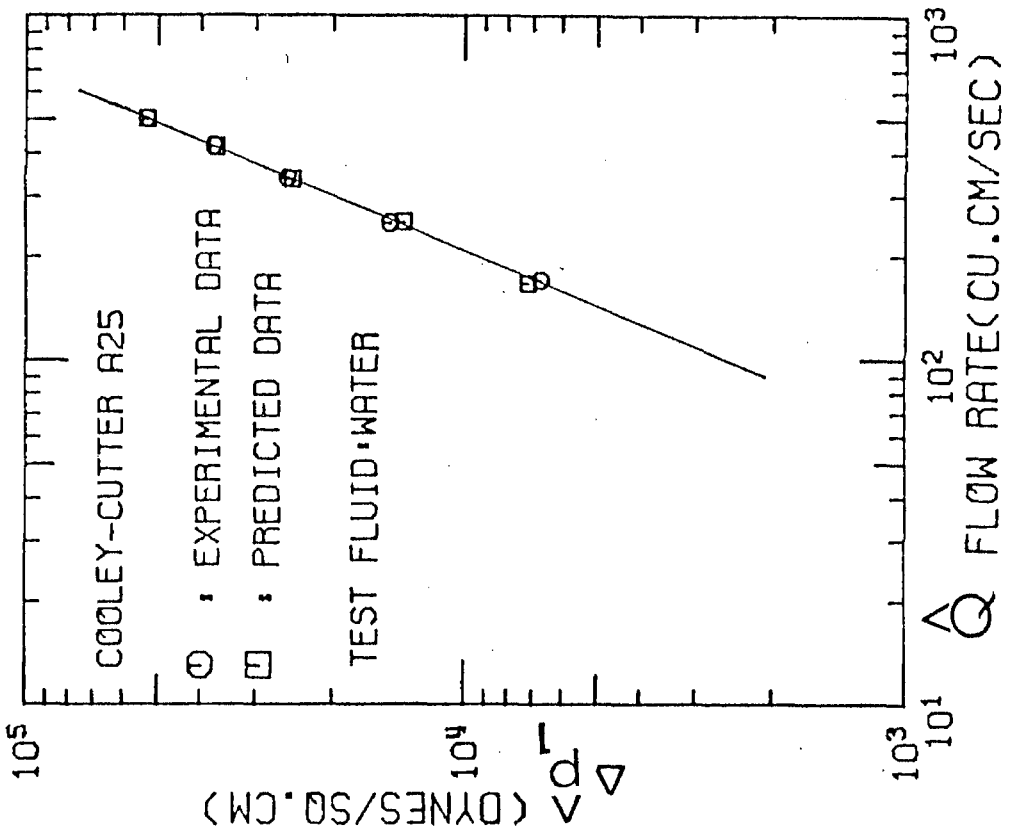

Fig. 69

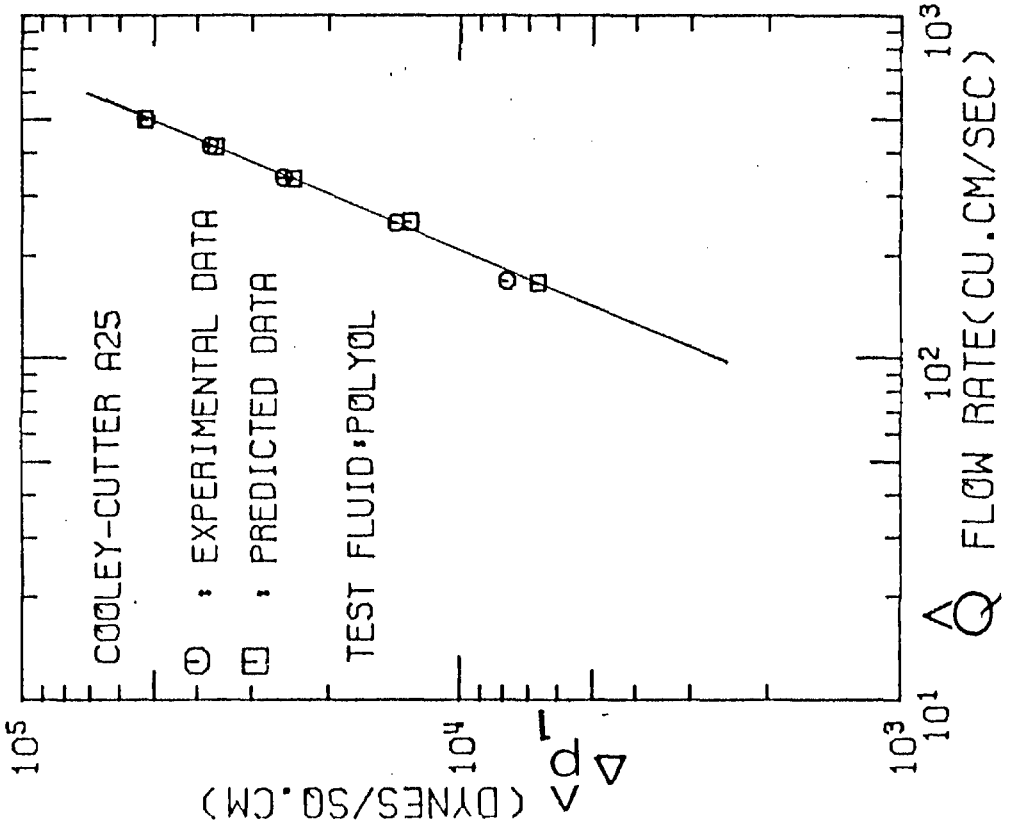

Fig. 68

Peak systolic pressure drop across the Cooley-Cutter A-25 valve

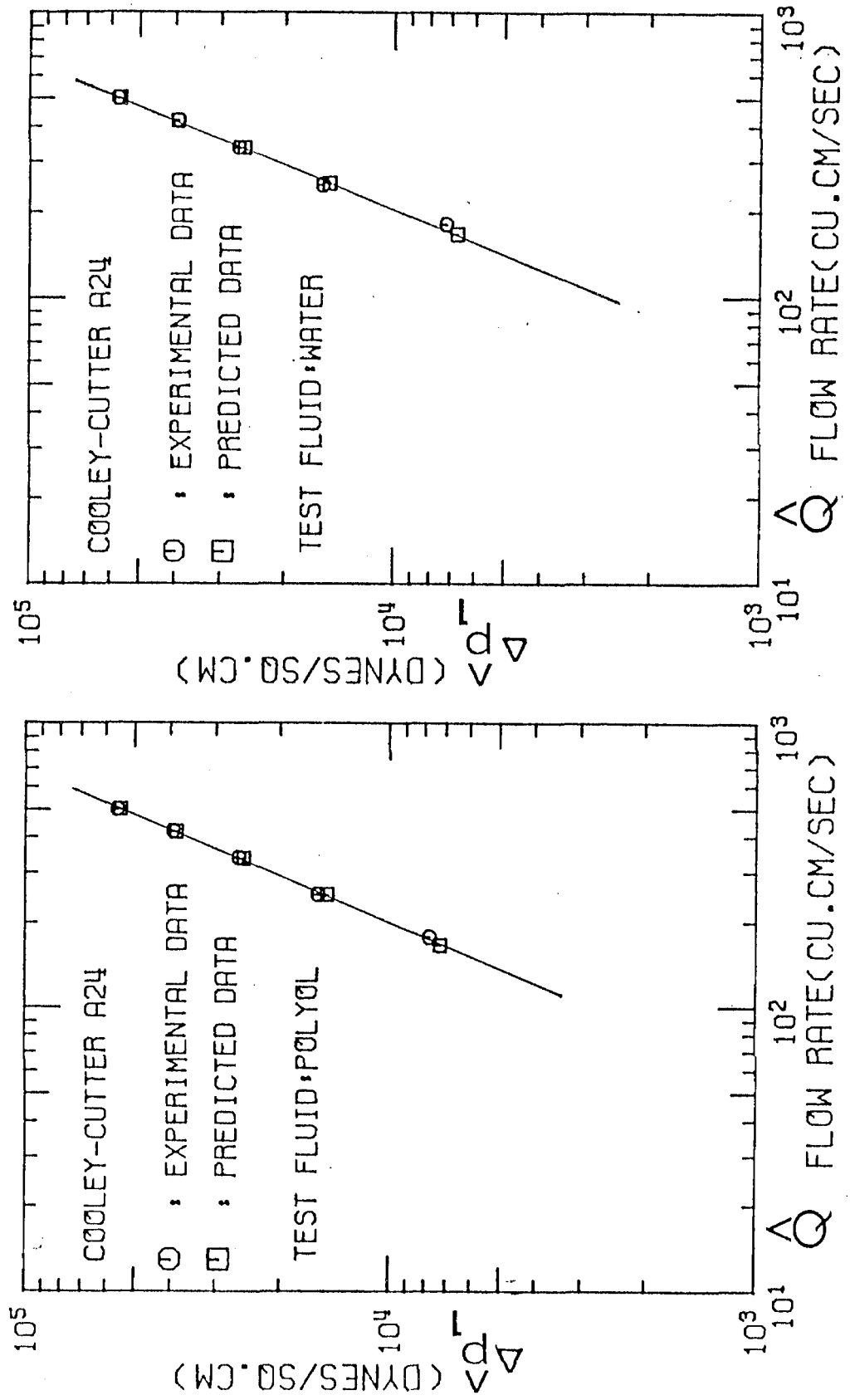

Fig. 70

Fig. 71

Peak systolic pressure drop across the Cooley-Cutter A-24 valve

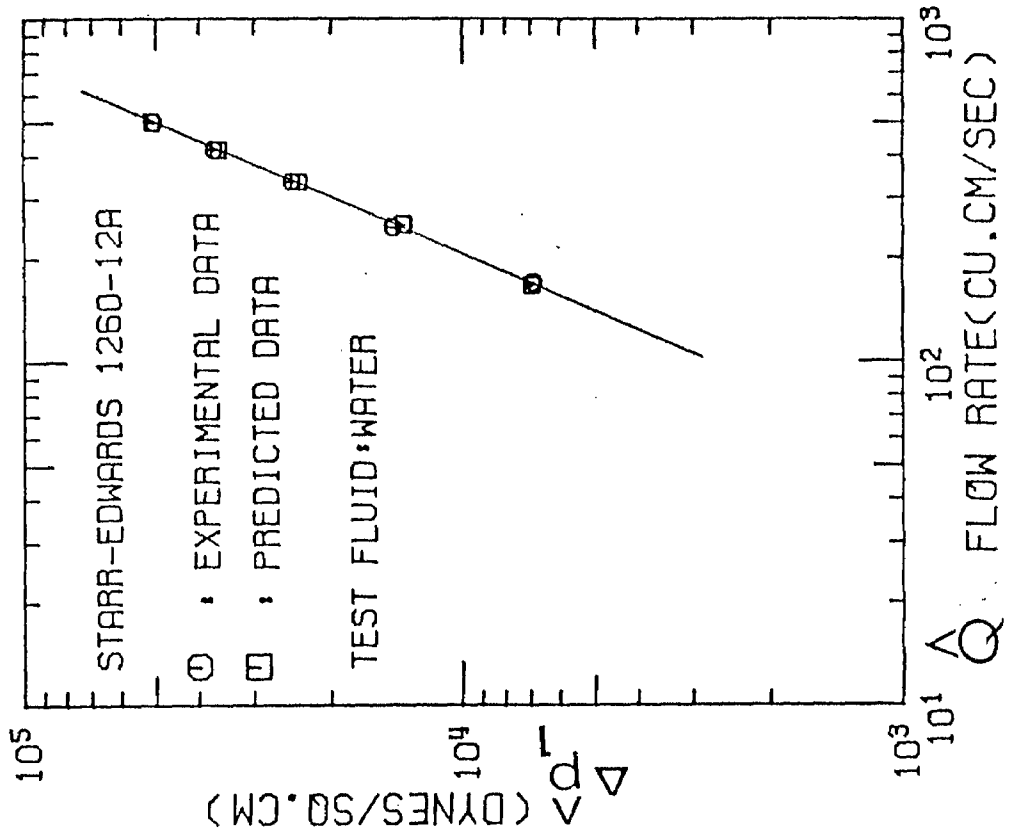

Fig. 73

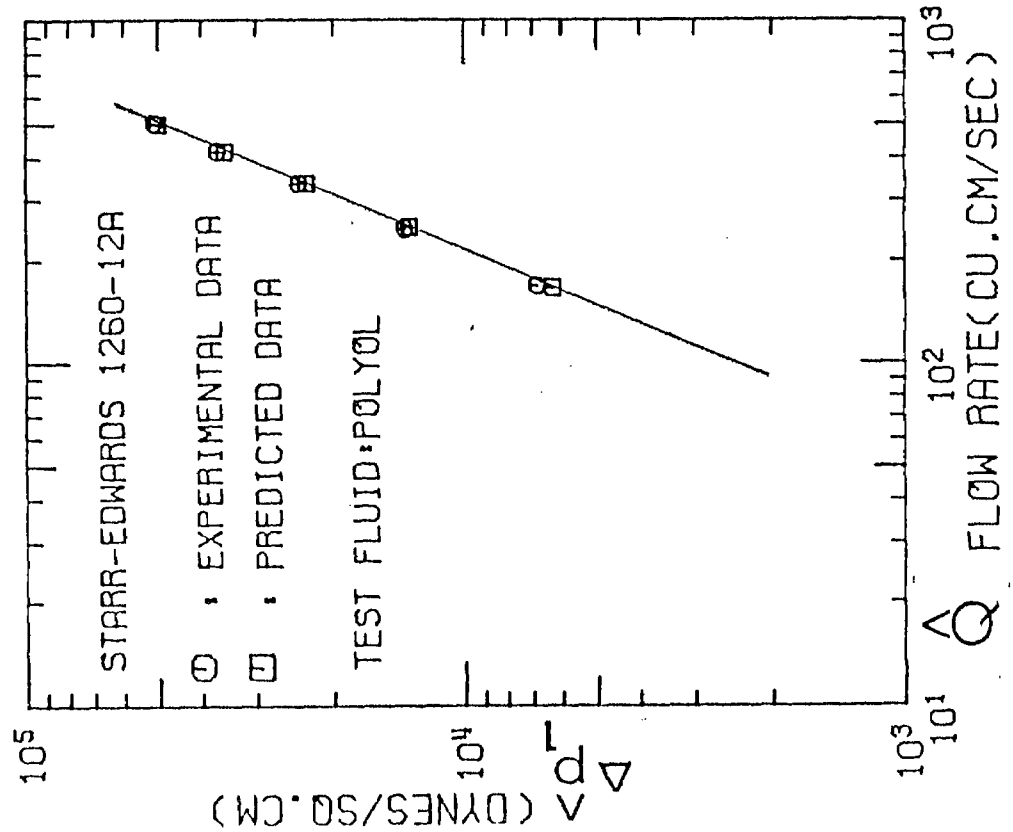

Fig. 72

Peak systolic pressure drop across the Starr-Edwards 1260-12A valve

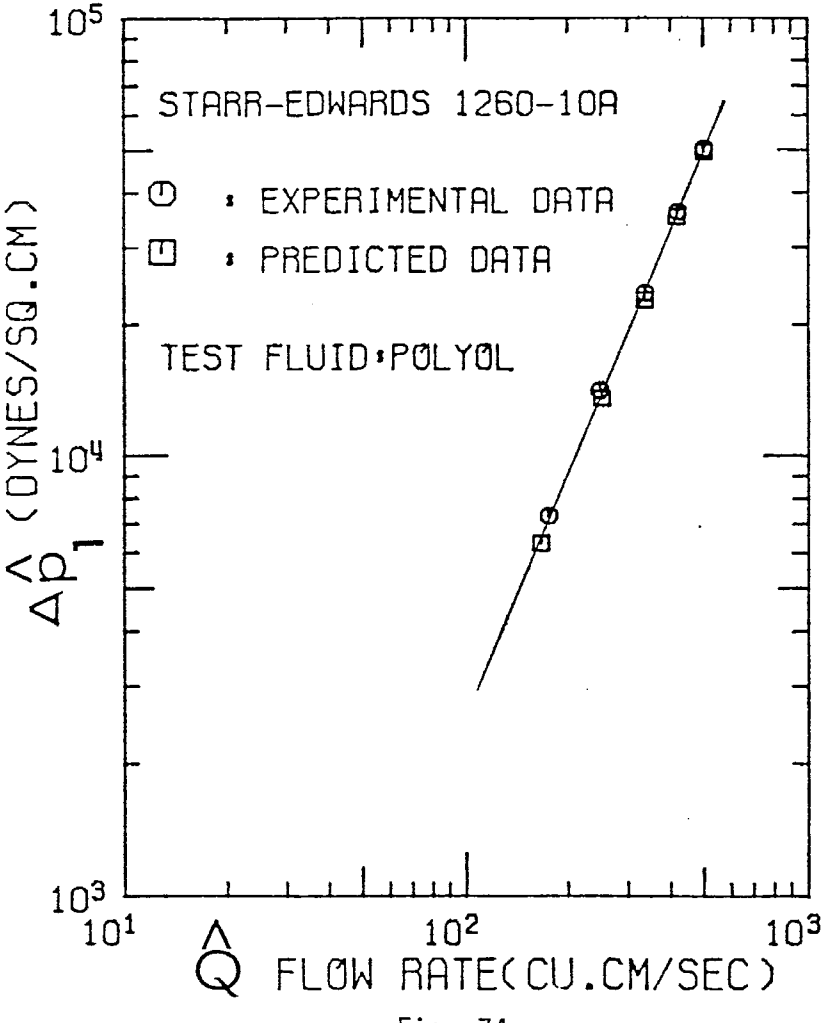

Fig. 74

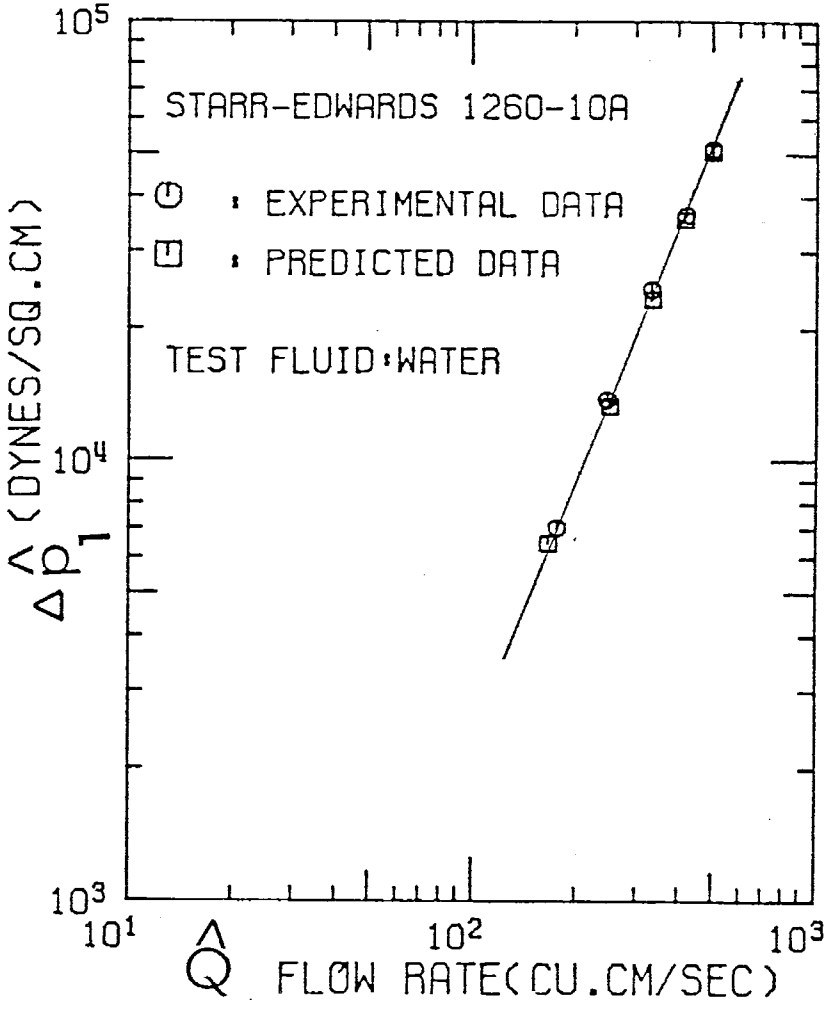

Fig. 75

Peak systolic pressure drop across the Starr-Edwards 1260-10A valve

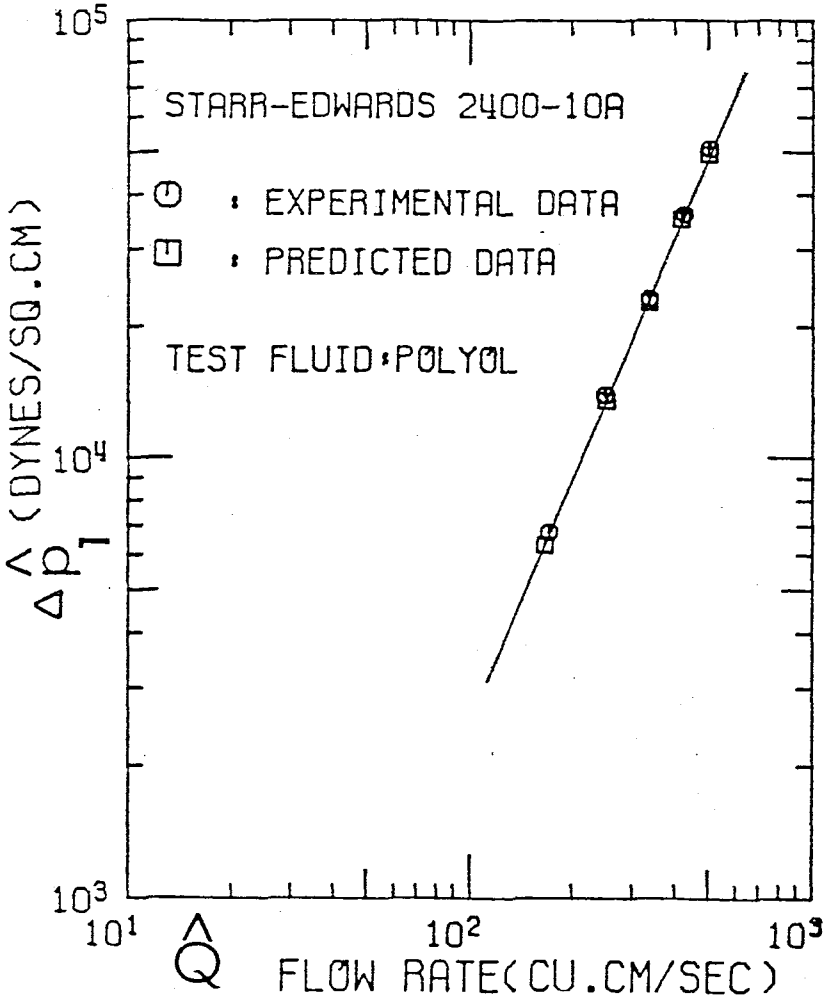

Fig. 76

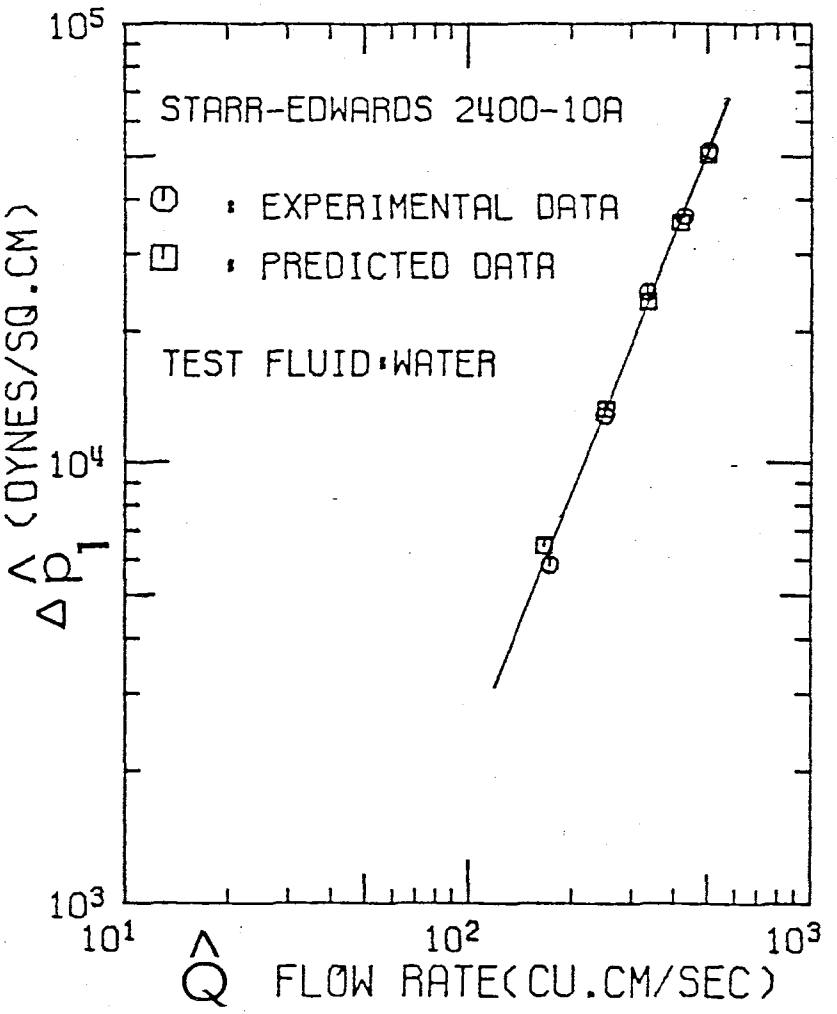

Fig. 77

Peak systolic pressure drop across the Starr-Edwards 2400-10A valve

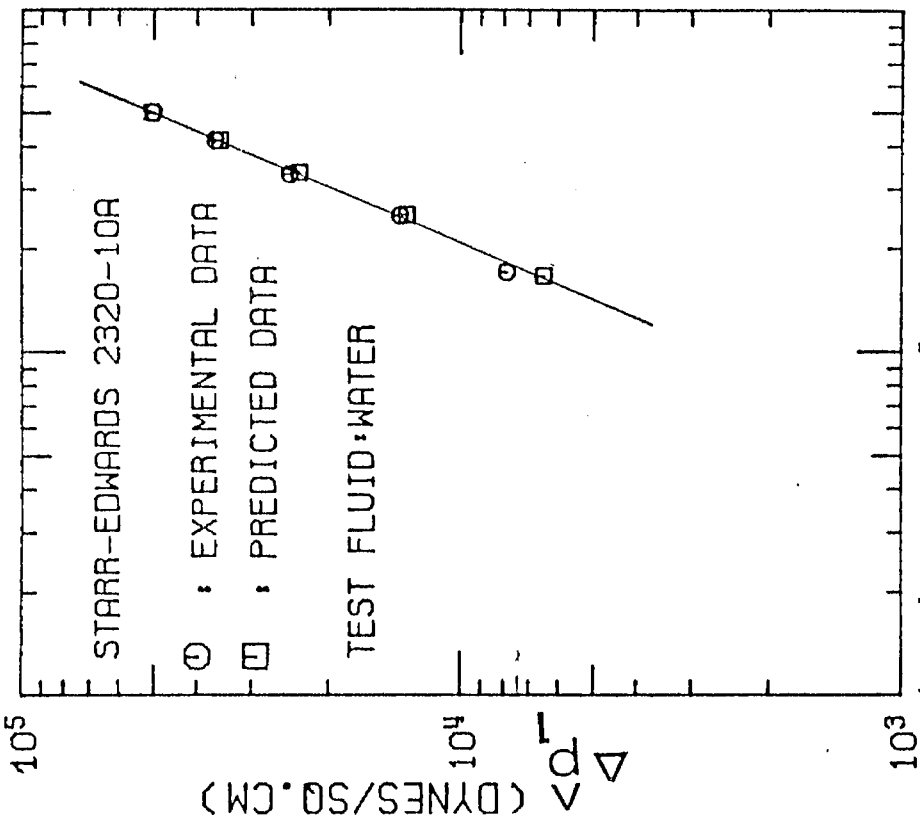

Fig. 79

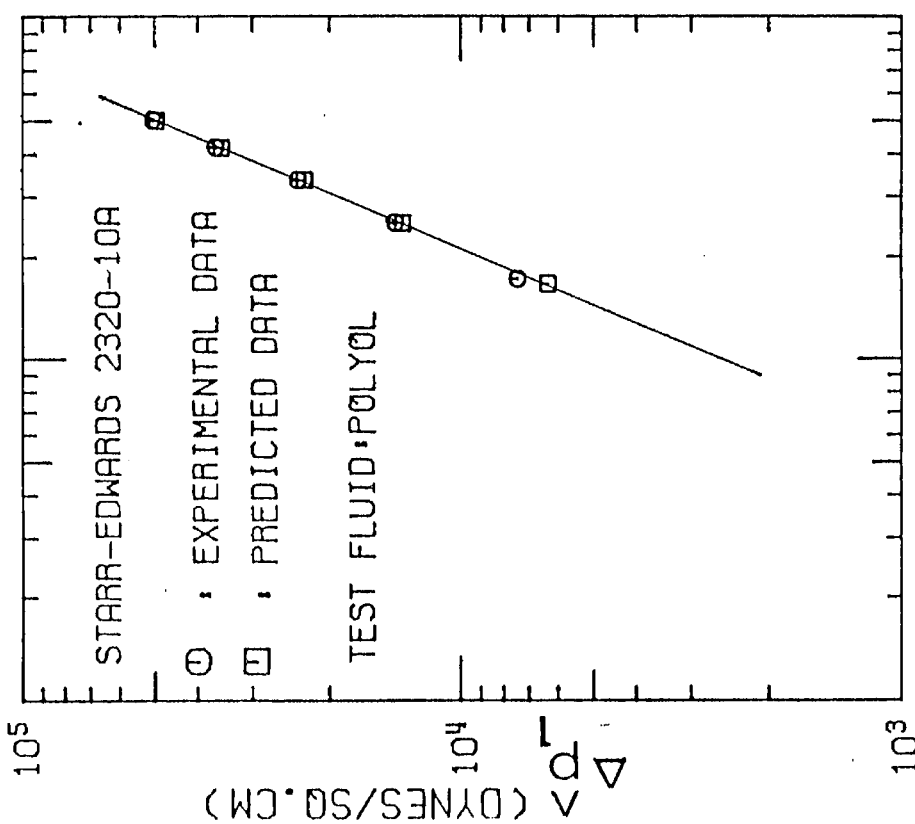

Fig. 78

Peak systolic pressure drop across the Starr-Edwards 2320-10A valve

reasons for the hydrodynamic instability of the ball in the Starr-Edwards valve could be due to its closed cage structure, smaller orifice area and larger ball diameter compared with the Smeloff-Cutter valve of corresponding size.

Figures 42, 43, 48 and 49 show steady-flow pressure-drop results for the Starr-Edwards 1260-12A valve with the ball tied at the top of the cage, and with the ball oscillating at the top of the cage. It can be observed from these two plots that the pressure drops across the tied ball are smaller than those measured across the oscillating ball. This observation is not unusual and has been observed in flow past stationary and oscillating circular cylinders. When the sphere or ball oscillates, the width of the wake and the pressure drag increase, leading to a larger pressure drop. If the poppet of the Starr-Edwards 1260-12A prosthesis was stable, the pressure drops across it under steady flow would be very similar to those obtained with the ball tied, which are less than those obtained across the Smeloff-Cutter A5 valve. Therefore, under pulsatile flow the Starr-Edwards 1260-12A would be ranked next to the Björk-Shiley 27 XMBRP if its ball was hydrodynamically stable. The above discussion indicates the importance of having a hydrodynamically stable poppet.

Placing a lucite disc with a 27 mm orifice in the aortic valve seating area instead of the prosthesis, the pressure gradient measured across it was about 78 dyne cm^{-2}/cm at a steady flow rate of 417 cm^3/sec. This experimental situation is similar to having a fully open, normally functioning aortic valve in the heart valve chamber. This indicates

without any doubt that a normally functioning natural aortic valve creates the least possible pressure drop in the system.

For the Björk-Shiley, Smeloff-Cutter and Cooley-Cutter prostheses the pressure drops increased as the valve size decreased. In the case of the Starr-Edwards valves, however, the pressure drops across the size 12A valve were fairly similar to those of the size 10A valves under steady and pulsatile flow. The instability and therefore the motion and the position of the poppets of the Starr-Edwards valves were probably responsible for these findings.

As stated before, of the four designs of valves studied, for a given size of prosthesis the Björk-Shiley valve has the smallest pressure drop across it for both steady and pulsatile flow. Correspondingly, it seems the Cooley-Cutter has the largest pressure drop. As an additional piece of experimentation the pressure drops across a Starr-Edwards 6520-1M disc valve were measured under steady-flow and the results are shown in Figures 58 and 59. This valve is at present clinically used in the mitral position, but a valve of very similar design was used in the aortic position in the mid-sixties. The results in Figures 58 and 59 show that this valve has the highest pressure drops across it under steady-flow conditions compared with the other four designs of valves. The Starr-Edwards 6520-1M mitral valve had a sewing ring diameter of 26 mm and a primary orifice diameter of 16.307 mm. The disc valve contains a disc which is mounted perpendicular to the direction of the axial flow and constrained in travel by a short cage.

The use of a disc valve for the aortic position in the mid-sixties indicates that in the early designs of heart valve prostheses, fluid

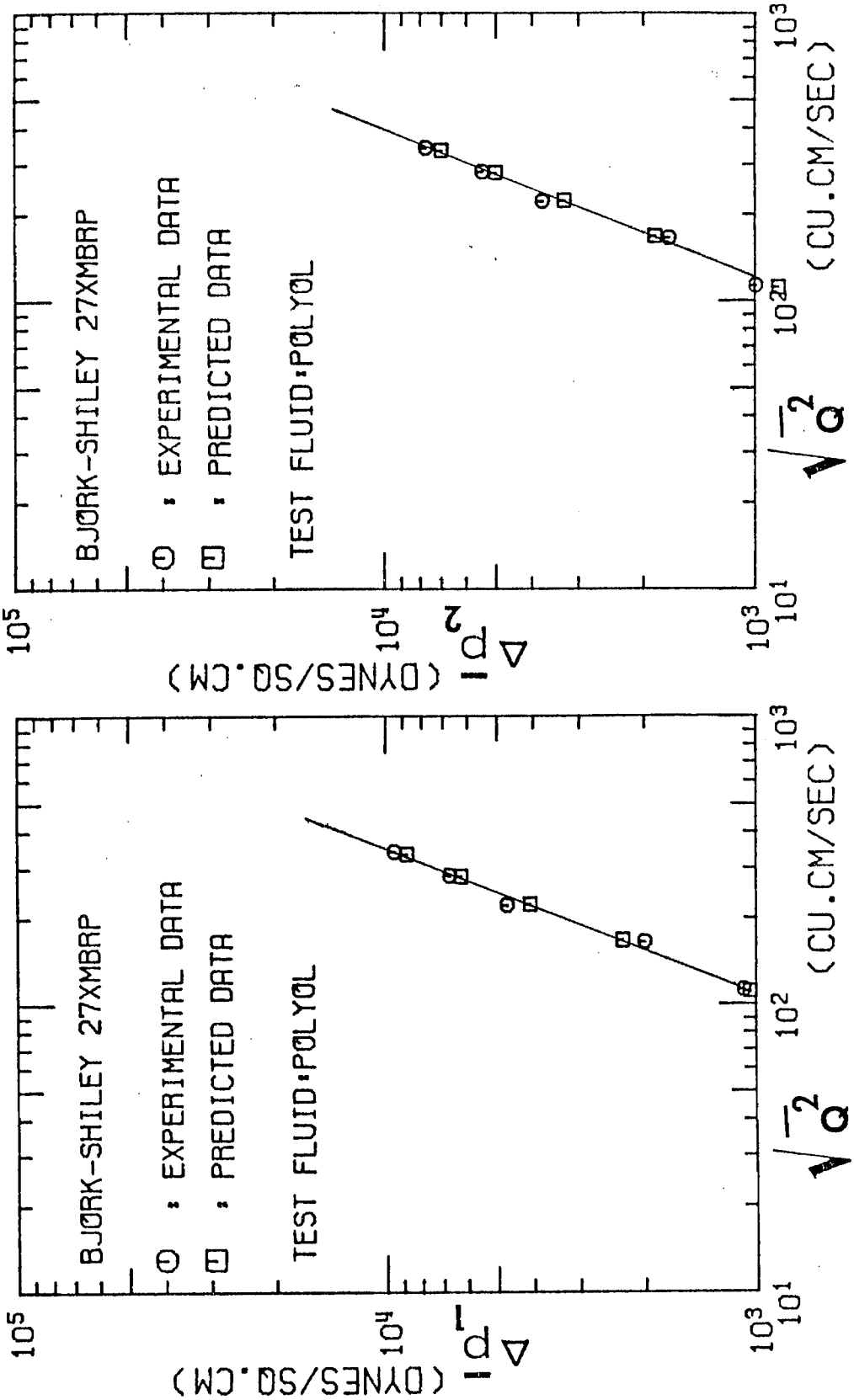

Fig. 80

Fig. 81

Mean systolic pressure drop across the Björk-Shiley 27XMBRP valve

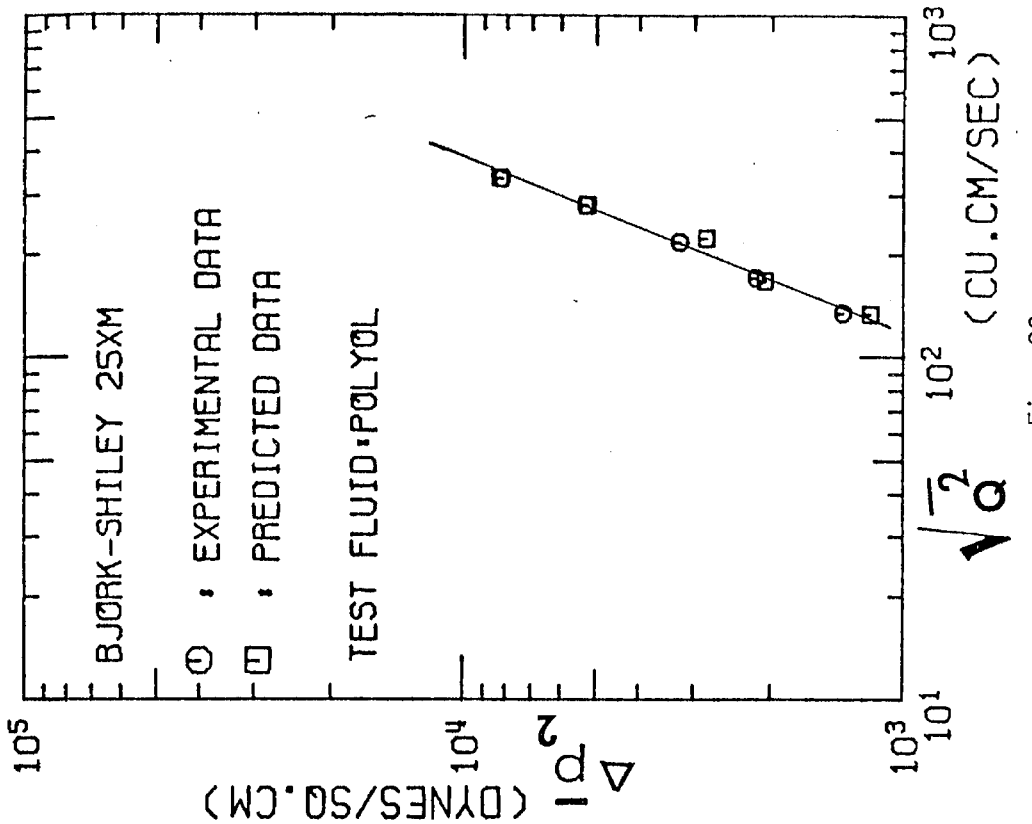

Fig. 82

Fig. 83

Mean systolic pressure drop across the Björk-Shiley 25XMBRP valve

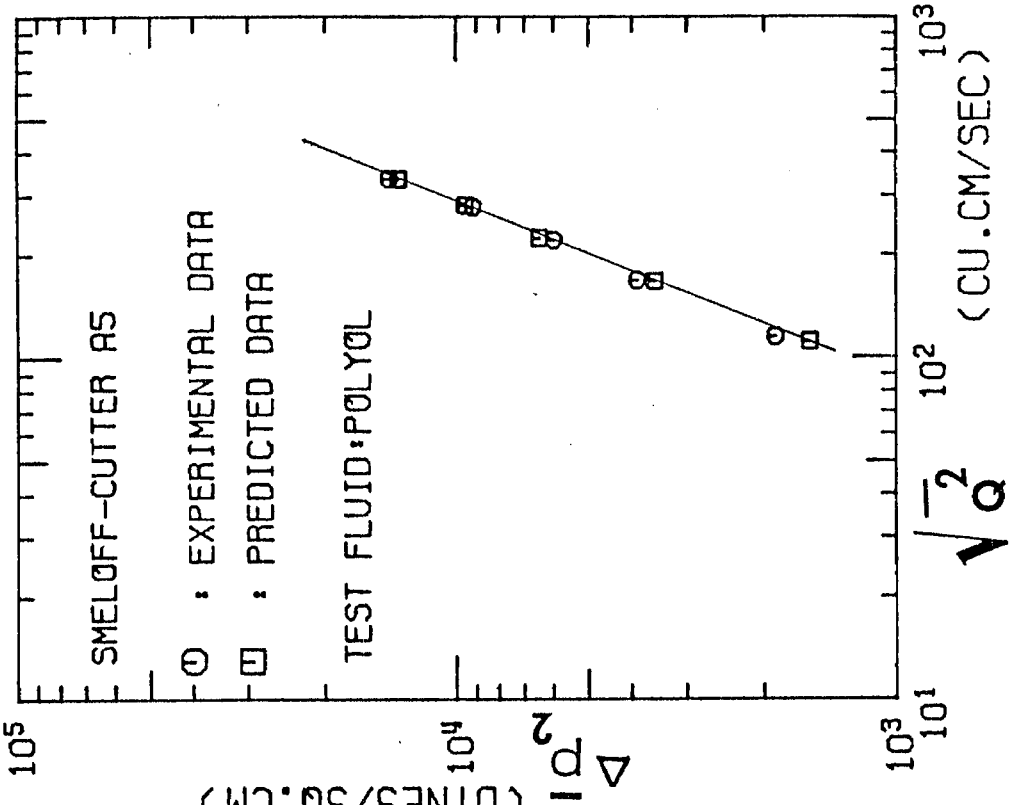

Fig. 85

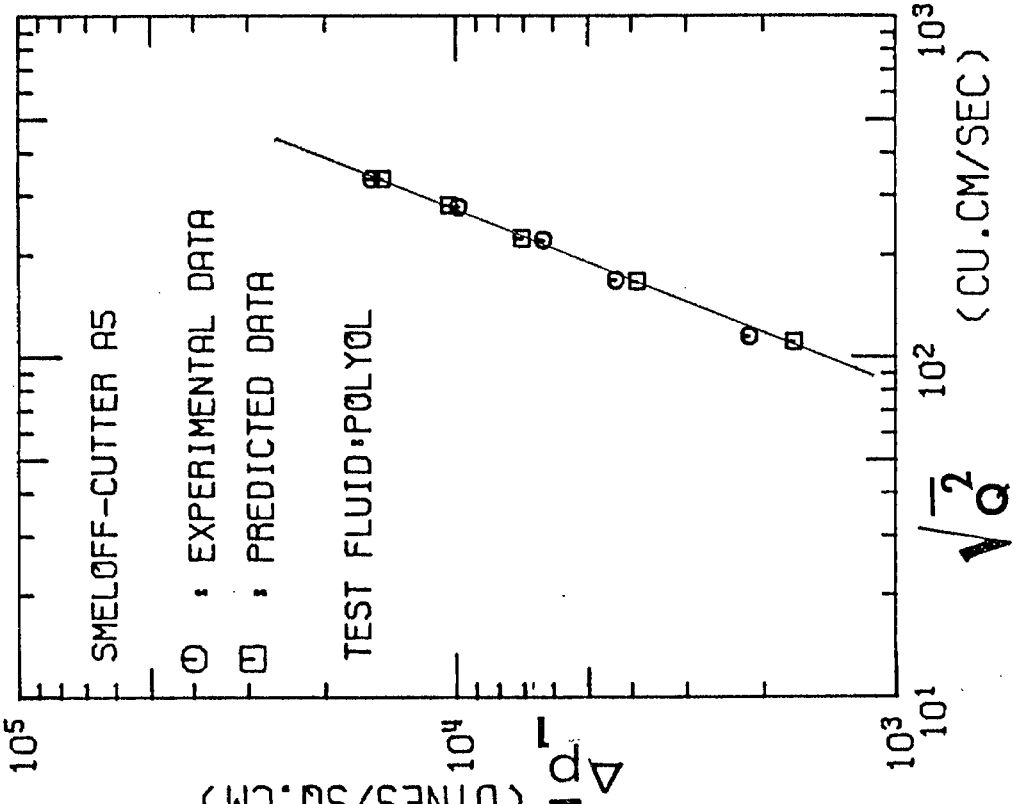

Fig. 84

Mean systolic pressure drop across the Smeloff-Cutter A-5 valve

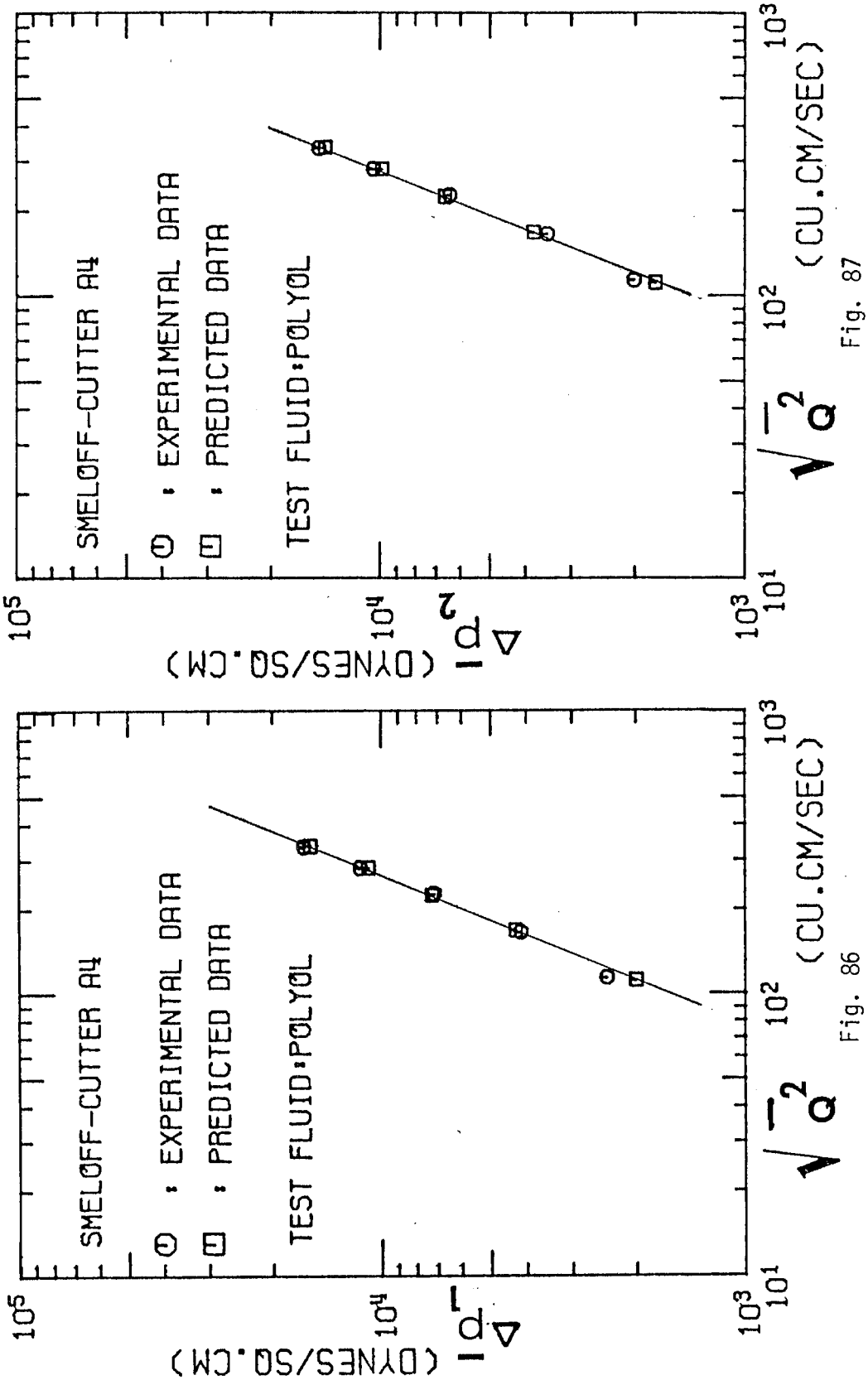

Fig. 86

Fig. 87

Mean systolic pressure drop across the Smeloff-Cutter A-4 valve

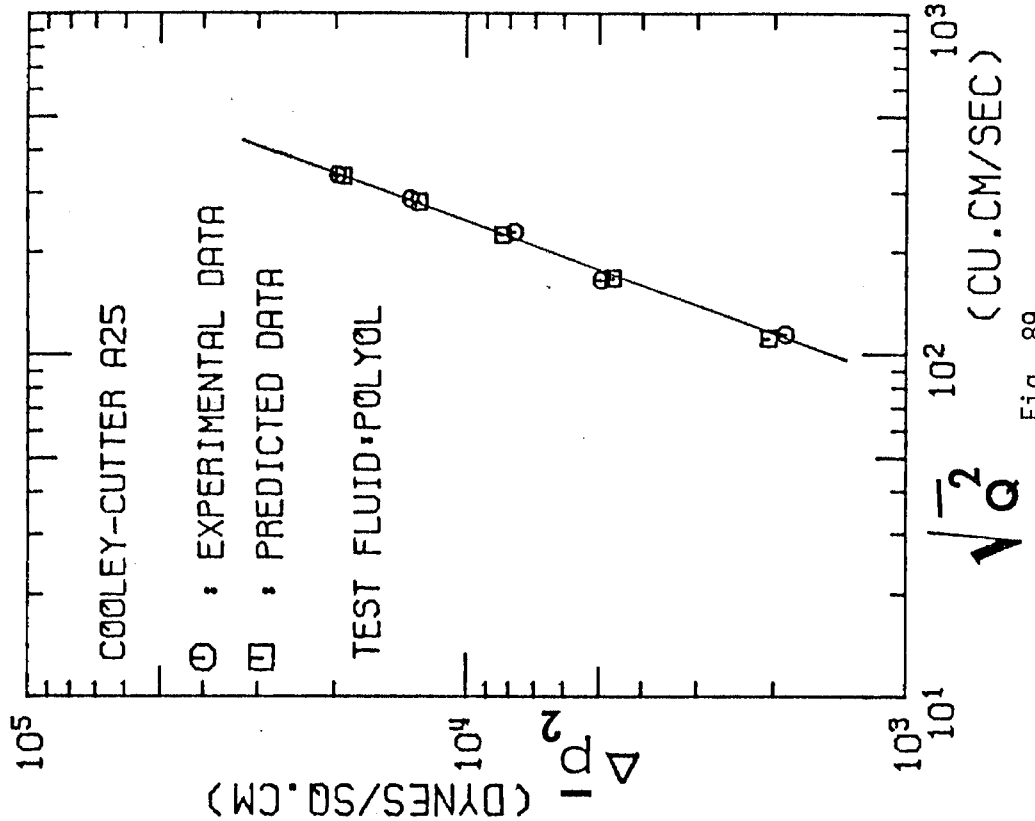

Fig. 88

Fig. 89

Mean systolic pressure drop across the Cooley-Cutter A-25 valve

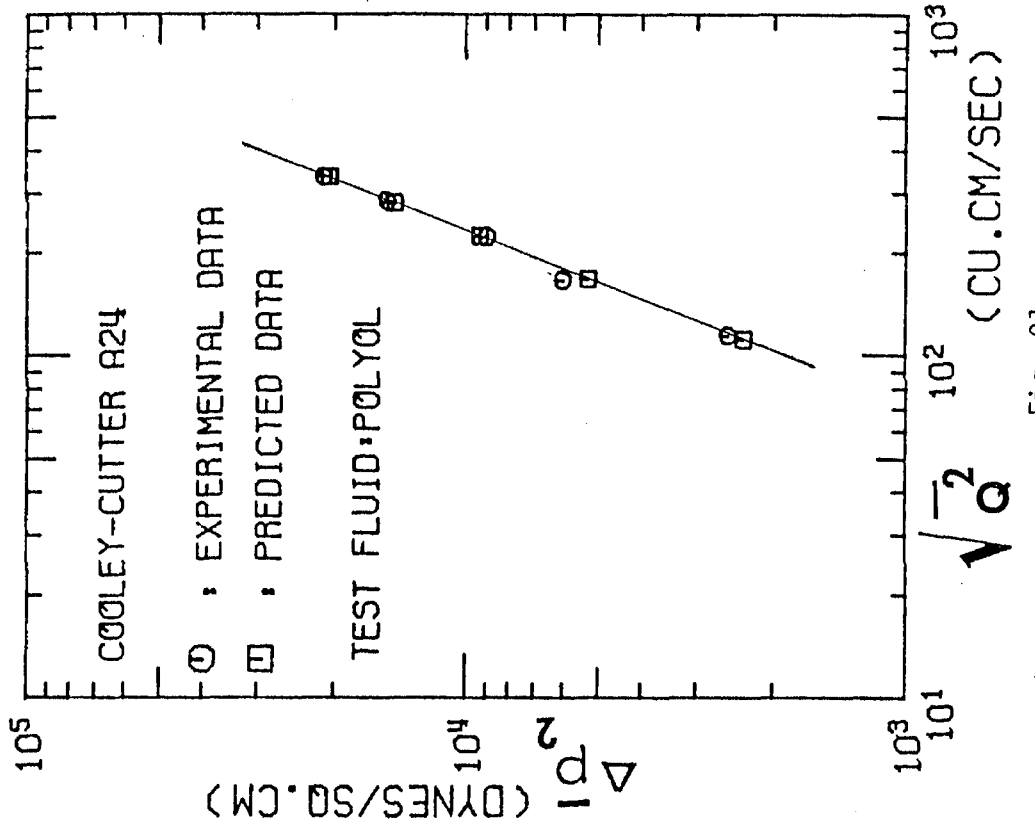

Fig. 90

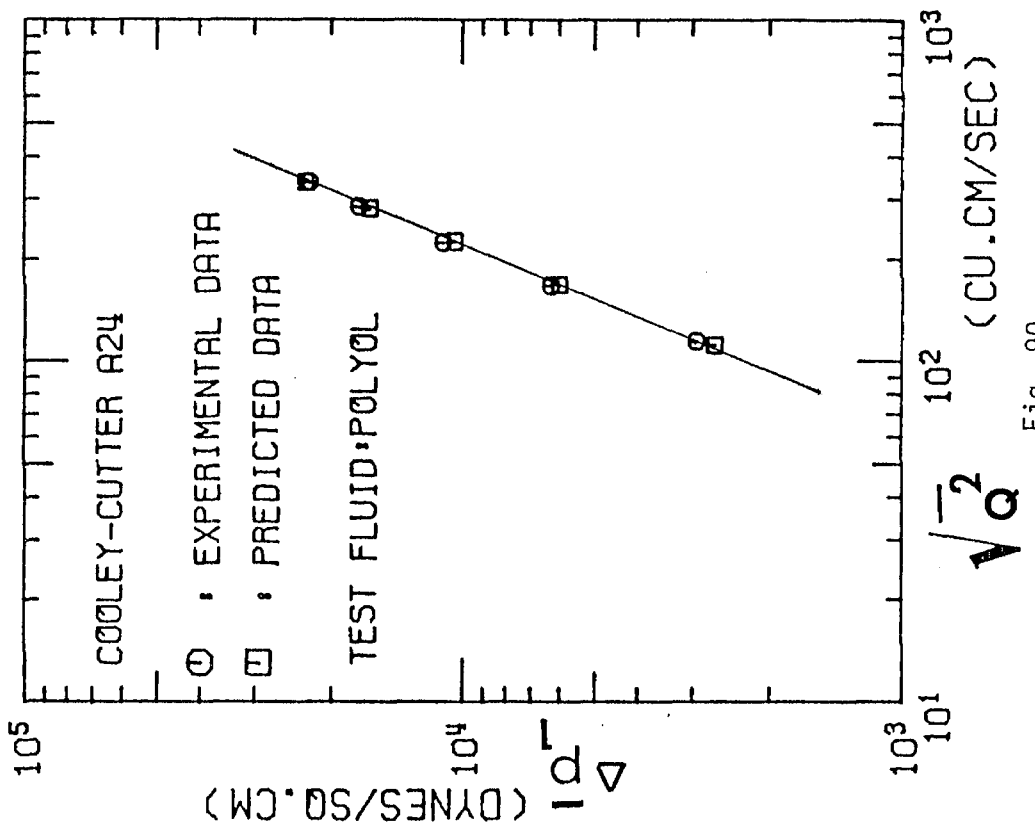

Fig. 91

Mean systolic pressure drop across the Cooley-Cutter A-24 valve

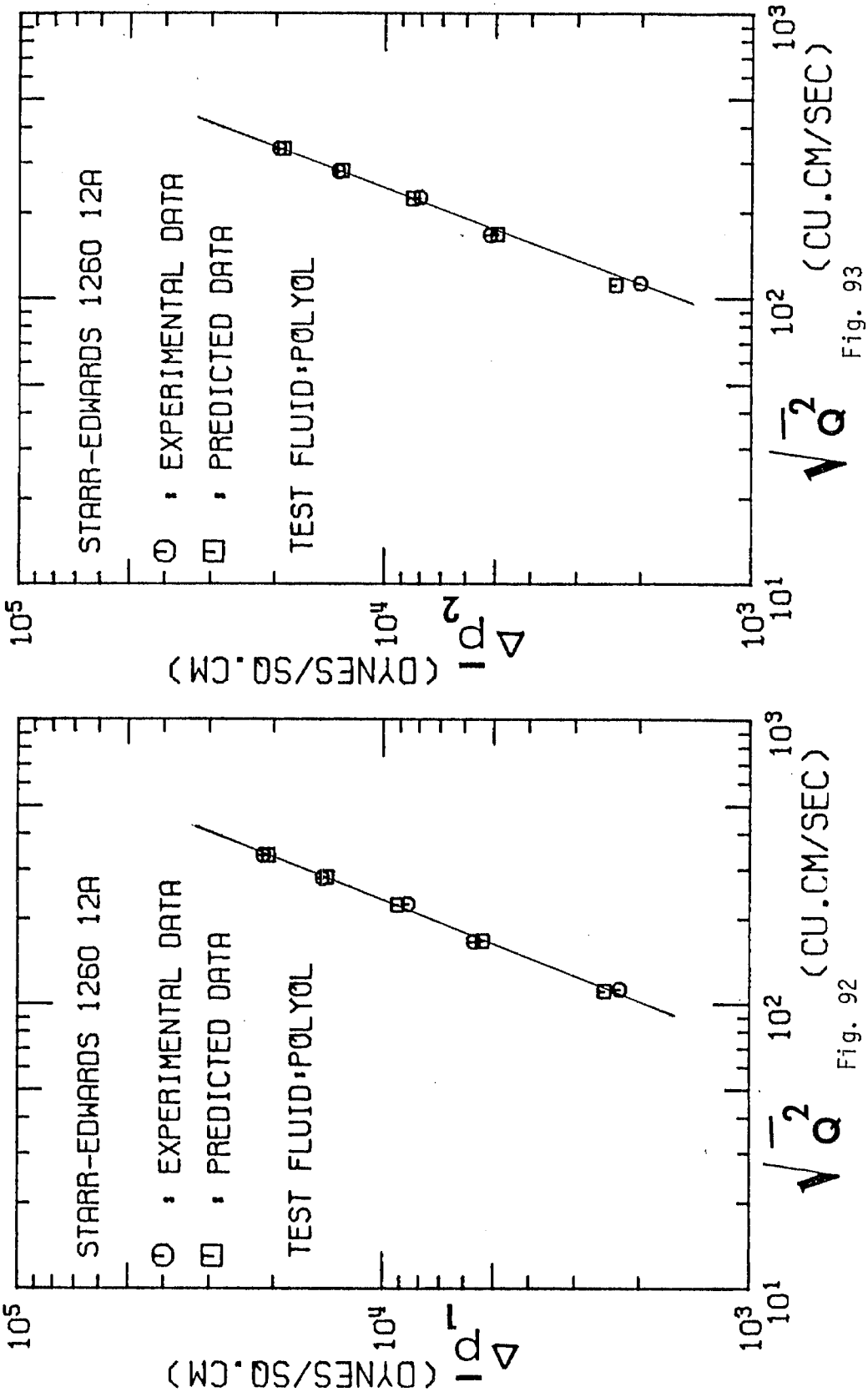

Fig. 92

Fig. 93

Mean systolic pressure drop across the Starr-Edwards 1260-12A valve

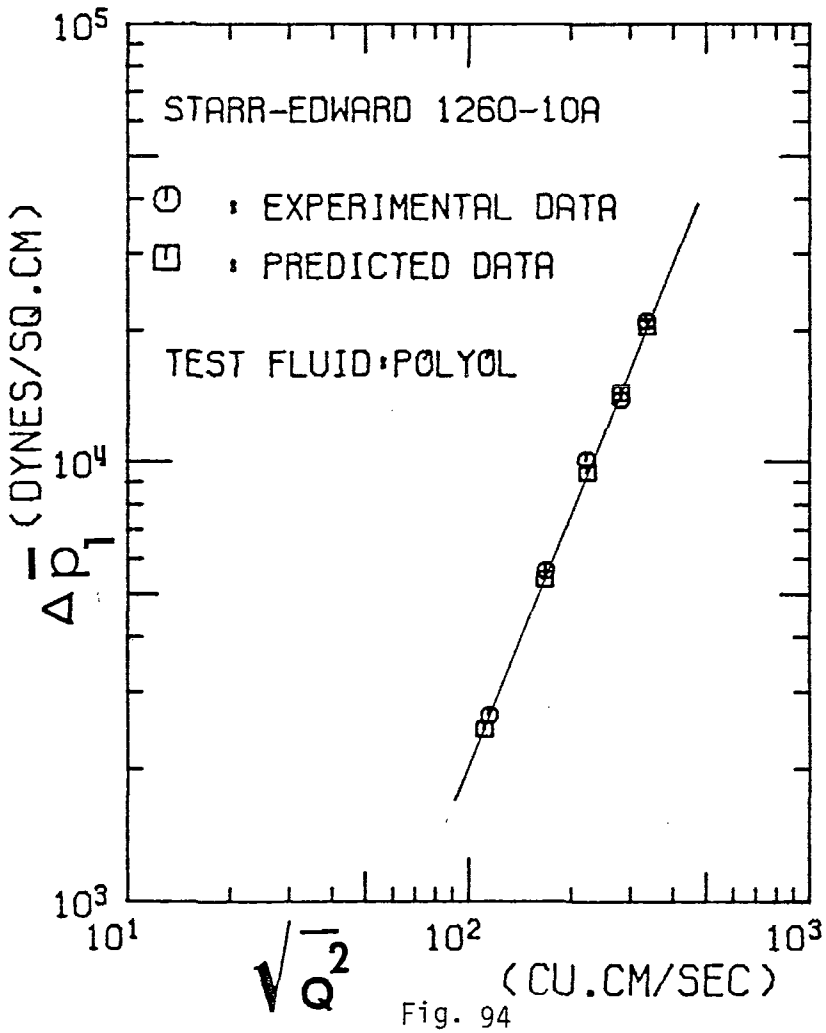

Fig. 94

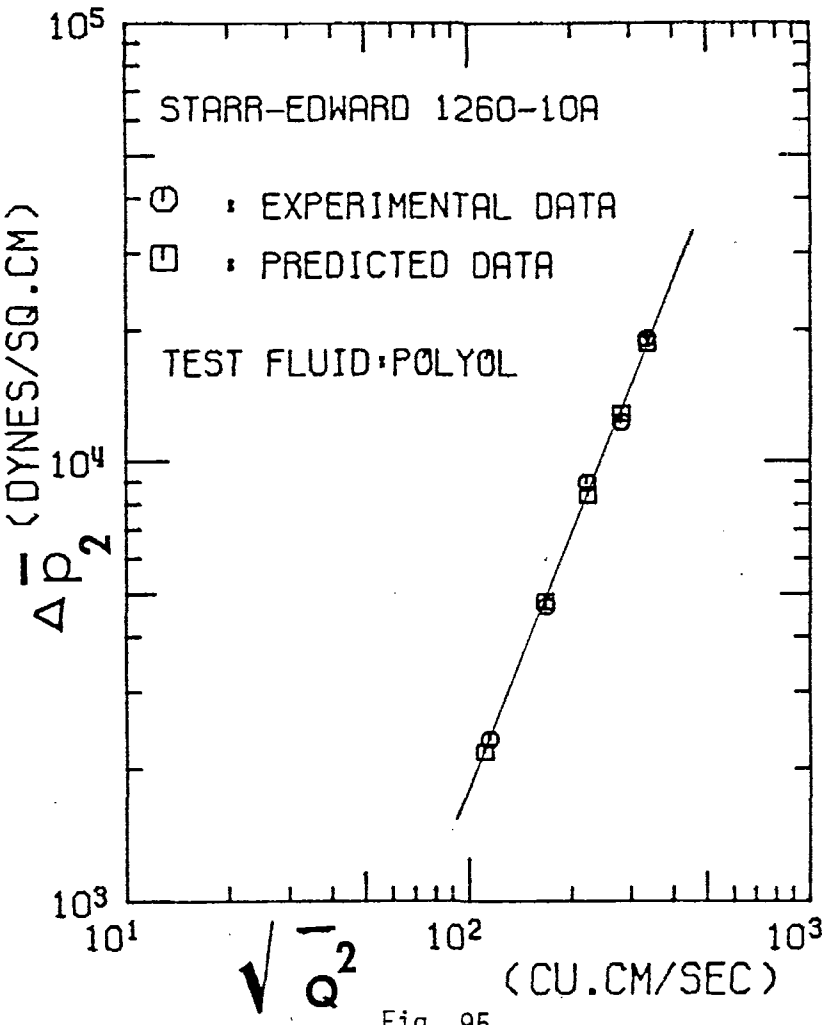

Fig. 95

Mean systolic pressure drop across the Starr-Edwards 1260-10A valve

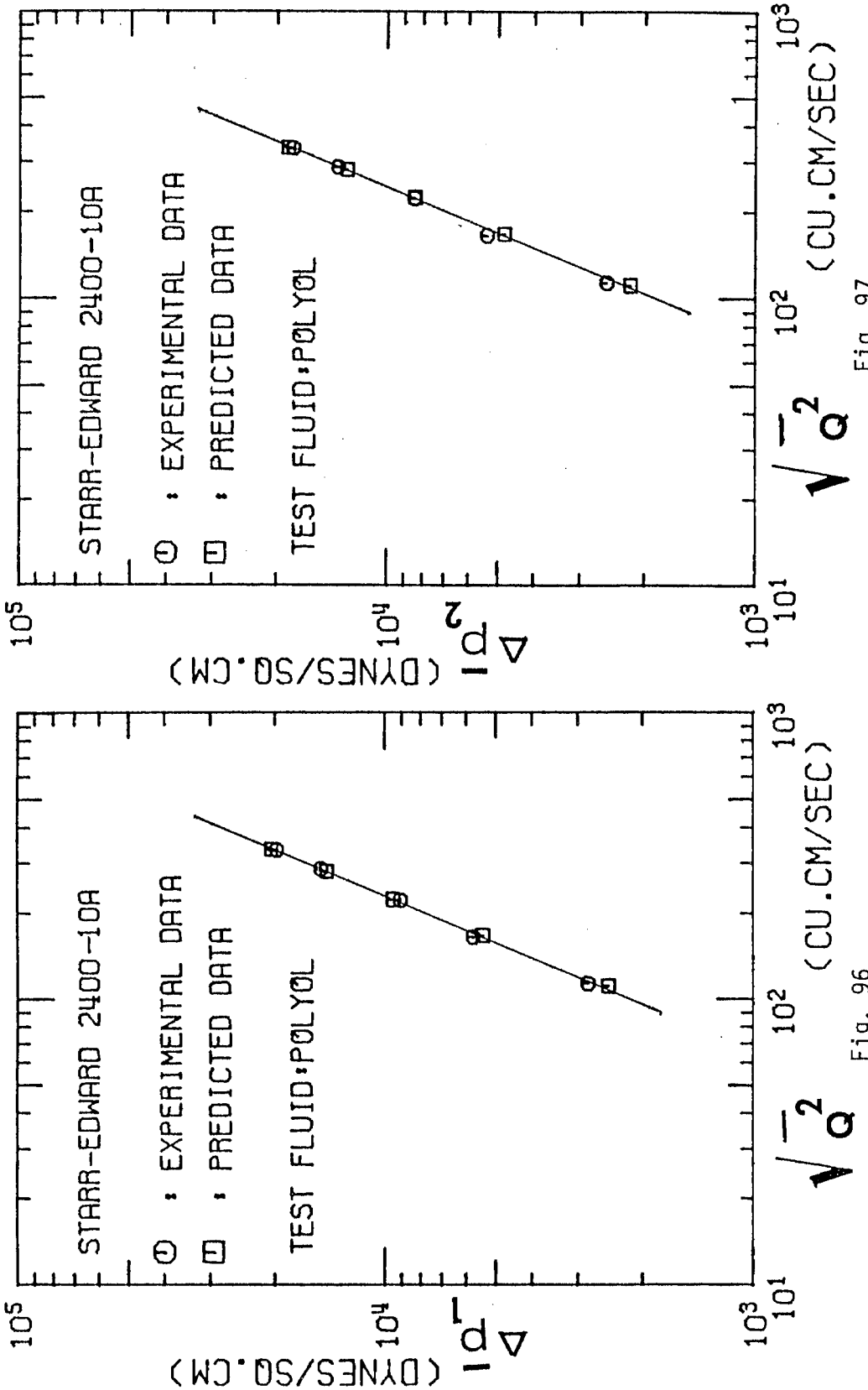

Fig. 96

Fig. 97

Mean systolic pressure drop across the Starr-Edwards 2400-10A valve

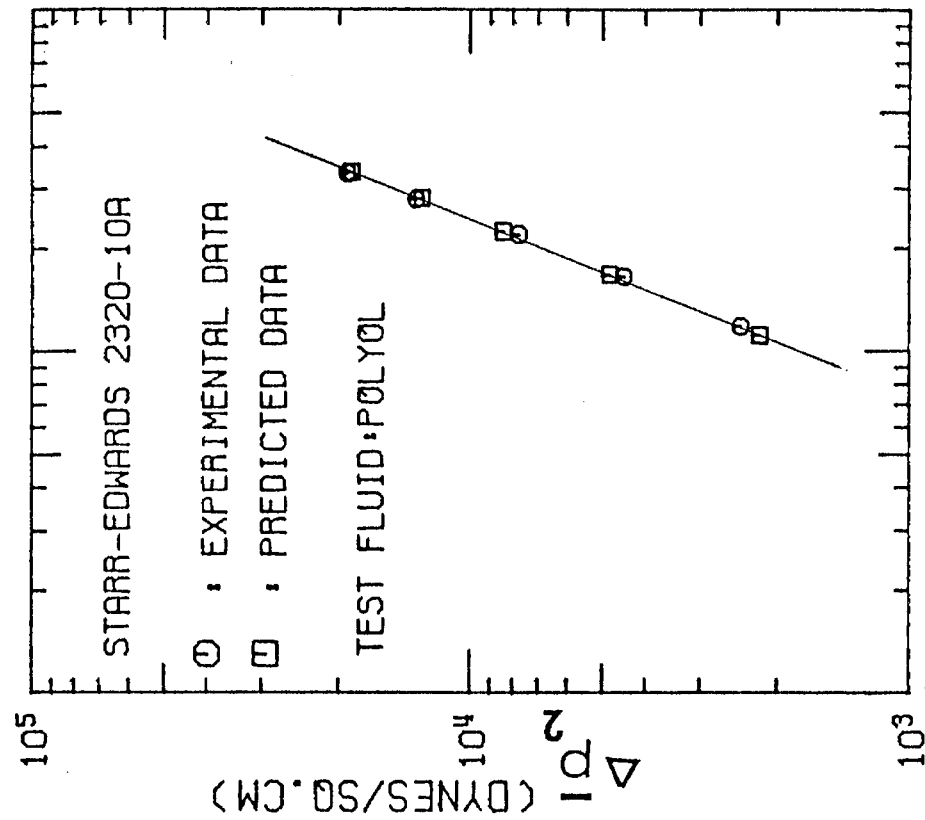

Fig. 99

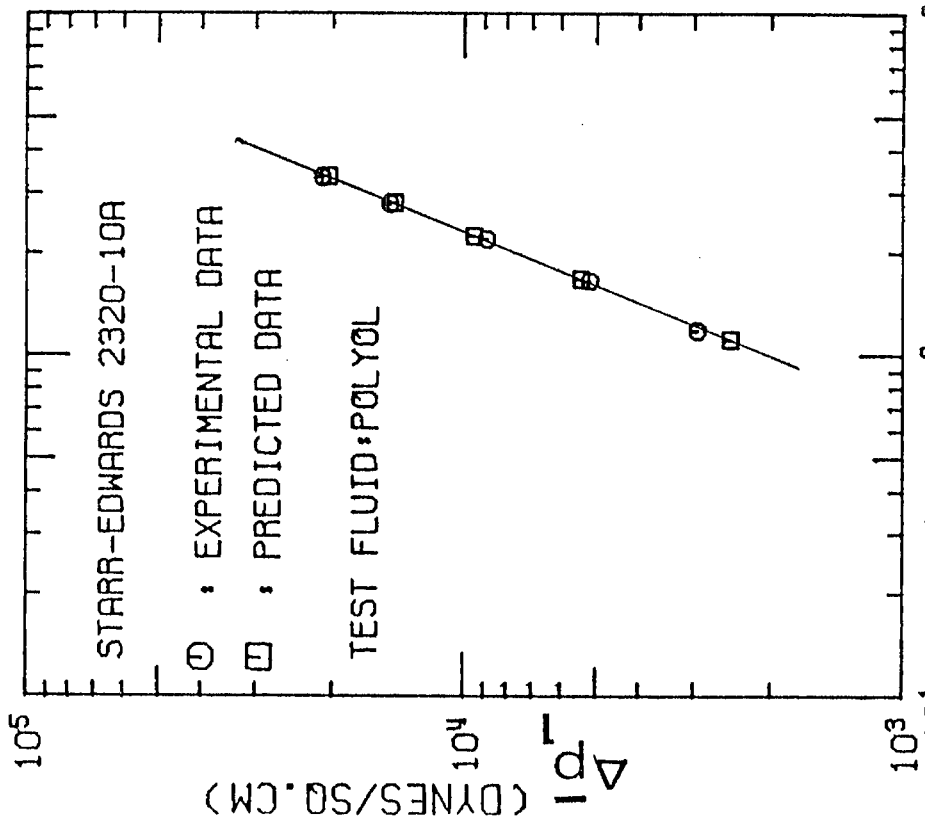

Fig. 98

Mean systolic pressure drop across the Starr-Edwards 2320-10A valve

dynamic aspects of design were not taken into serious consideration. It is well documented in the fluid mechanic literature that a disc placed perpendicular to the direction of flow creates a very large drag and therefore a large pressure drop would occur across a prosthesis which used such a disc as its poppet. For example, in a Reynolds number regime of 1,000 to 25,000 the drag coefficient for flow past a circular disc placed perpendicular to the direction of flow is about 1.12 [38], while for flow past a sphere it is about 0.44 [33]. The Cooley-Cutter biconical or diamond-shaped disc valve creates larger pressure drops than a Smeloff-Cutter ball valve of the corresponding size. The reason for this is probably twofold. First, since the biconical disc design originated from a flat disc placed perpendicular to the flow, it probably creates a larger drag compared with a sphere in the same Reynolds number regime. Second, for valves of comparable sewing ring diameter, the size of the biconical disc is larger than the ball, and also the cage of the Cooley-Cutter valve is smaller than the Smeloff-Cutter valve. Due to the shorter cage the flow is forced peripherally around the biconical disc in a shorter distance from the orifice, and due to the larger size poppet there are probably more complex interactions of the fluid with the valve superstructure and the walls of the heart valve chamber, leading to a larger overall drag coefficient compared with the Smeloff-Cutter valve of corresponding size.

The main reason the Björk-Shiley tilting disc prosthesis has the least pressure drops of the four designs of prostheses is because it has the largest area available for open flow. The Björk-Shiley valve has

the largest ratio of primary orifice diameter to sewing ring (tissue annulus) diameter as shown in Table 4. Also, it has a tilting disc which, when fully open, makes an angle of $\sim 30°$ to the direction of flow, and the drag coefficient on a disc at that angle in the Reynolds number range of 1,000 to 25,000 is about 0.35 [38,39] compared to 0.44 for a sphere and 1.12 for a circular disc perpendicular to the direction of flow.

4.4 Nomenclature

A = area of cross section

A_o = primary orifice area of aortic valve

A_2 = area of cross section of flow section "C" (Figure 3)

C_d = orifice discharge coefficient

C_o = orifice constant

C = overall aortic valve drag coefficient

L = distance between pressure taps

L_1 = distance between pressure taps I and II

L_2 = distance between pressure taps I and III

$\Delta p_{ij} = p_i - p_j$ = steady-flow pressure drop between taps i and j

Δp_1 = steady-flow pressure drop between taps I and II

Δp_2 = steady-flow pressure drop between taps I and III

Δp_3 = steady-flow pressure drop between taps I and IV

$(p_i - p_j)_{\hat{Q}}$ = steady-flow pressure drop between taps i and j at a steady flow rate numerically equal to $\hat{Q}$

$\Delta \tilde{p}_{ij}(t) = \tilde{p}_i(t) - \tilde{p}_j(t)$ = pressure drop between taps i and j for time dependent flow

$\hat{p}_i - \hat{p}_j$ = peak systolic pressure drop between taps i and j

$\Delta \hat{p}_1$ = peak systolic pressure drop between taps I and II

$\Delta \hat{p}_2$ = peak systolic pressure drop between taps I and III

$\Delta \bar{p}_{ij} = \overline{p_i - p_j}$ = mean systolic pressure drop between taps i and j

$\Delta \bar{p}_1$ = mean systolic pressure drop between taps I and II

$\Delta \bar{p}_2$ = mean systolic pressure drop between taps I and III

Q = flow rate (cm^3/sec)

$\hat{Q}$ = systolic flow rate at the instant $\Delta \hat{p}_{ij}$ occurs

$\sqrt{\overline{Q^2}}$ = root mean square flow rate during systole

Q_{peak} = peak systolic flow rate

$\frac{dQ}{dt}$ = acceleration of fluid (cm^3/sec^2)

$\frac{d\hat{Q}}{dt}$ = acceleration of fluid at the instant $\Delta\hat{p}_{ij}$ occurs

Re = Reynolds number

$Re_{\hat{Q}}$ = systolic Reynolds number based on a flow rate $\hat{Q}$

t_s = systolic time

Greek Letters

ρ = fluid density

μ = fluid viscosity

Chapter 5

PROBLEMS CREATED BY THE FLUID MECHANICS OF PROSTHETIC AORTIC VALVES

As stated in Chapter 2, two of the more serious problems and complications associated with aortic heart valve prostheses are red-cell destruction and thrombus formation. A third problem not mentioned in Chapter 2 is the damage to the endothelium of the ascending aorta. These three problems are directly related to the fluid dynamics and mainly to shear stresses at and near the wall in the vicinity of the valve. In the next three sections the current knowledge on these three pathological problems will be summarized.

5.1 Red-Cell Destruction

Destruction of red blood cells (RBC) is generally referred to as hemolysis. Hemolysis can be subdivided into intra- and extra-vascular hemolysis. Intra-vascular hemolysis is defined [40] as loss from the circulation of erythrocytes (RBC) that are sufficiently damaged to destroy the integrity of the membrane and cause spillage of hemoglobin into the blood plasma. Extra-vascular hemolysis is the loss of RBCs that are damaged but not lysed in the vascular tree, and subsequently are removed by the reticuloendothelial system and catabolized.

Hemolytic disease due to intra-vascular RBC destruction is well documented in patients with prosthetic heart valves and valvular heart disease [41,42,43,44,13]. Hemolysis leads to the reduction in RBC life span. The average RBC has a mean life span of approximately 120 days or a half-life of about 27 days before being filtered out in the kidney.

A vast majority of the patients with prosthetic aortic valves have reduced RBC life spans. Bone marrow, where new RBCs are formed, therefore, becomes overworked due to the reduced life span of the RBCs. The bone marrow can compensate to a large extent to supply the body with RBCs so that the patient may not become anemic. However, if the combination of intra- and extra-vascular hemolysis is such that the RBC life span is about 1/5 the normal value of 120 days, anemia results [45]. RBCs which showed shortened life spans in a patient with a prosthetic valve had a normal life span when transfused into a compatible normal person [46,47].

Brodeur et al. [44] in their study of 20 patients with aortic or multiple Starr-Edwards ball valve prostheses found that the half-life (T/2) of the RBCs ranged from 9 to 25 days. A majority of these patients had T/2 of about 20 days. They also studied 21 patients with aortic-valve disease, and the majority of these patients had T/2 of about 20.7 days. Crexell et al. [41] studied 208 patients with different valve prostheses. Of the 208 studied, 140 (67.3 percent) showed clear signs of intra-vascular hemolysis. Of these 140 patients, 47 had severe hemolysis. Crexell and his coworkers estimated the degree of hemolysis from RBC survival times obtained by $^{51}Cr_{21}$ tests. They correlated mild hemolysis with a RBC T/2 of 15 to 24 days and severe hemolysis with T/2 less than 15 days. Five percent of their patients had chronic hemolytic anemia. A similar finding was obtained by Rodgers and Sabiston [42]. Crexell et al. also observed that the incidence and degree of hemolysis was greater with the cloth-covered struts and Stellite ball of the Starr-Edwards valves as compared with uncovered struts and silicone ball. Roberts [13] in his excellent review article states that caged-ball

valves (Starr-Edwards, Magovern, Smeloff-Cutter, etc.) hemolyze RBCs more frequently and more severely after aortic replacement than after mitral-valve replacement. He also states that the cloth-covered strut models hemolyze more frequently and more severely than the non-cloth-covered models. The caged-disc prostheses (Kay-Shiley, Cooley-Cutter, etc.) according to Roberts cause universal hemolysis. In one of his studies [48] he observed that 13 of 16 patients with disc-type prostheses had renal hemosiderosis, indicating that mild to severe intravascular hemolysis had occurred. The Björk-Shiley tilting disc valve creates relatively mild hemolysis [49]. Wallace et al. [40] found in their study that red-cell destruction not only increased intra-vascular but also extra-vascular hemolysis. They also observed that malfunctioning valve prostheses and valvular disease led to increased intra- and extra-vascular hemolysis. Another important finding was the discovery [46,47,50] of hemoglobin-filled RBC fragments or cells of drastically altered appearance in patients with heart-valve prostheses. These cells or fragments are known as pyknocytes. They are seen in normal blood and represent 0.20 to 0.27 percent of the total cell population. In one study [50] of prosthetic valve patients, pyknocytes constituted about 20 to 30 percent of the red cells, and they occurred at above normal levels in nearly all heart valve patients.

Many clinicians [40,41,43] have observed that the degree of hemolysis that occurs in the majority of the patients with normally functioning aortic prostheses is generally mild, but the incidence of chronic hemolysis is high. As Roberts [13] states, hemolysis at present is rarely a major clinical problem with any design of prosthetic valve

because the bone marrow is capable of replacing the destroyed RBCs without the development of anemia or thrombocytopenia. Hemolytic anemia occurs when severe hemolysis is present. About 5 percent of the patients with valve prostheses have hemolytic anemia. The long-term effects of chronic hemolysis have, however, not yet been completely established. As pointed out by Roschke and Harrison [51], mild, chronic, mechanical hemolysis may not be innocuous because it could lead to other complications such as gallstone formation. They observed an overall prevalence of gallstones in a group of 46 patients with prosthetic valves and attributed it to mild mechanical hemolysis and bilirubin production. Mercendino and Manhas [52] also observed a marked increase in the prevalence of gallstones in a group of 39 prosthetic valve patients. Another long-term effect of mild chronic hemolysis could be impairment of renal or kidney function. RBC contents when released intravascularly can saturate the kidney. Bernstein et al. [53] have shown that the limit of tolerance of the kidney is about 0.1 mg of hemoglobin per 100 cc of blood. This is approximately equivalent to halving the RBC life span.

The hemolysis that occurs with prosthetic heart valves is due to mechanical forces, because the materials developed for use in prosthetic valves are sufficiently inert to rule out chemical interaction. There are three main mechanical forces which may cause injury to RBCs as they flow through a prosthetic valve. These are: (i) pressure or normal forces, (ii) impact due to crushing of RBCs between solid surfaces, and (iii) shearing forces. Hellums and Brown [54] have shown that the first two physical forces mentioned above cause

negligible damage to RBCs. Red blood cell destruction occurs due to elevated shearing stresses.

Over the past 10 years or so, a large amount of research has been done to study in vitro the effects of shear forces on RBCs. Hellums and Brown [54] summarize the findings of this research. Numerous variables tend to affect the mechanical hemolysis in the near vicinity of the prosthetic valve. In vitro studies suggest that when hemolysis occurs where there are no surface effects it depends on the level and duration of the shear stress. Blackshear and coworkers [45,55,56] have found in in vitro testing with a jet nozzle, that RBCs lyse at a shear stress of about 40,000 dynes/cm^2, with exposure times on the order of 10^{-5}sec. The exposure time in jet experiments is far shorter than the usual exposure time of a RBC passing through a prosthetic valve. On the other hand, Hellums and coworkers [54,57,58] have found in rotating viscometer studies that RBCs lyse at laminar shear stresses of 1500 dynes/cm^2 with exposure times of 120 sec. Sutera and Mehrjardi [59] investigated the effects on RBCs of turbulent-shear stresses of 100 to 4,500 dynes/cm^2. They found that significant hemolysis began to occur at about 2000 to 2500 dynes/cm^2. The exposure time in the experiments was 240 sec. The hemolysis and the fragmentation of the red cells occurred in the bulk of the fluid and not at surfaces. They also observed that the RBCs began to lose their biconcave shape at a shear stress of about 500 dynes/cm^2, and a majority of them assumed an almost prolate ellipsoidal shape at shears above 1500 dynes/cm^2. Roschke and Harrison in their paper [51] show a plot of shear stress vs duration of stress exposure for in vitro tests, and indicate a region of incipient in vitro hemolysis.

In a theoretical study Richardson [60] has attempted to predict the approximate time for hemolysis when a RBC is subjected to an arbitrary shear stress of τ . He predicts that the upper bound for the hemolysis time is given by

$$t_c = \frac{3.4 \times 10^6}{K^2} \text{ sec} \qquad (30)$$

where t_c = time to hemolysis

K = shear rate

According to equation (30) the approximate predicted time to hemolysis in the turbulent jet test is 9×10^{-7} sec and in the concentric cylinder viscometer test is 2×10^{-3} sec. Hellums and Brown [54] observed that significant morphological changes may occur at stresses which produce relatively small amounts of plasma hemoglobin. They have also observed that pathological RBCs differ in shear resistance from normal cells and may be ordered in increasing resistance: sickle cell anemia, iron deficient, thalassemia minor, normal and hereditary spherocytosis. Blackshear contends [61] that prosthetic valves tested *in vitro* produce hemolysis at a lesser rate than that measured *in vivo*. He attributes the difference to the fact that *in vivo* the RBCs are more sticky and are therefore more apt to stick onto surfaces which leads to surface dominated hemolysis.

The foregoing discussion on the *in vitro* testing of shear stress vs RBC hemolysis pertains to effects that occur in the bulk of the fluid. Surface or wall effects are considered to be negligible or non-existent. As shown in Figure 13 in Roschke and Harrison's article [51] there is,

however, a range of shear stresses (< 10^3dynes/cm^2) at which surface effects dominate. Blackshear [45,61] is of the opinion that most of the hemolysis that occurs in the vicinity of prosthetic valves is due to surface effects. In vivo and in vitro tests have been conducted at shear stress loads of the order of 10 to 10^2dynes/cm^2 in the presence of surfaces [55, 56,62,64,65,66]. The fact that the hemolysis in such experiments was associated with wall contact is highlighted by the evidence that the hemolysis was virtually eliminated by siliconizing or albuminating the vessel walls. These tests indicate that in the presence of a surface to which a RBC may attach itself, hemolysis could occur at shear stresses on the order of 10^2dynes/cm^2 or less. The RBC that sticks to a wall or a surface is pulled downstream by the flow, but remains fixed to the surface by a tether. According to Blackshear [61] such a cell flies from the wall like a kite. Eventually when the tether gets stretched to some limiting point the cell snaps off. If this process occurs quickly the entire cell may lyse, producing fragmented cells similar to those observed in patients with prosthetic valves. A slower process, perhaps in an area of weaker flow, would cause the tether to break off, leaving the remainder of the cell basically intact. The opening in the cell membrane so formed would allow the cytoplasm to diffuse into the plasma forming a ghost cell. Kochen [67] postulates that in the stretching process the pores in the RBC membrane enlarge allowing all but the largest molecules such as hemoglobin and proteins to diffuse through. This may also lead to water entering the cell and causing it to swell. Najappa et al. [62] have observed that when RBCs are subjected to shear stresses of less than

100 dynes/cm^2 they become osmotically fragile. In these experiments surface effects dominated. Similar observations have been made by Rand [63]. Wallace et al. [40] suggest that once the RBC becomes osmotically fragile it becomes more permeable to water, causing it to swell. Such swelling causes the RBC to take on an abnormal shape. Sublethal shear may also affect the flexibility of the RBC. Therefore, as the red cell travels through the systemic circulation and reaches the microcirculation where vessel size and cell size are of the same order, the abnormal shape, fragility and/or reduced flexibility of the RBC may lead to further damage of the cell and hemolysis could occur in the microcirculation. Wallace et al. [40] state that the cells with abnormal shapes would be removed from the circulation by the reticuloendothelial system. Rand has shown [63] that if the tether is slowly stretched the membrane may pinch off where the tether is attached to the cell, forming two new cellules. This could explain the formation of pyknocytes which are observed in aortic heart valve patients.

Blackshear [45,56] proposes a relatively simple model for the lysis of a tethered cell due to the flow field adjacent to the surface. The model presented here is much the same as that given by Blackshear, but contains a few simple modifications. Assume that a cell is firmly anchored at a site on the surface by a tether as shown in Figure 100, and that the balance of the cell at the end of the tether is a sphere of radius R.

a = radius of tether

b = distance of center of RBC sphere from surface

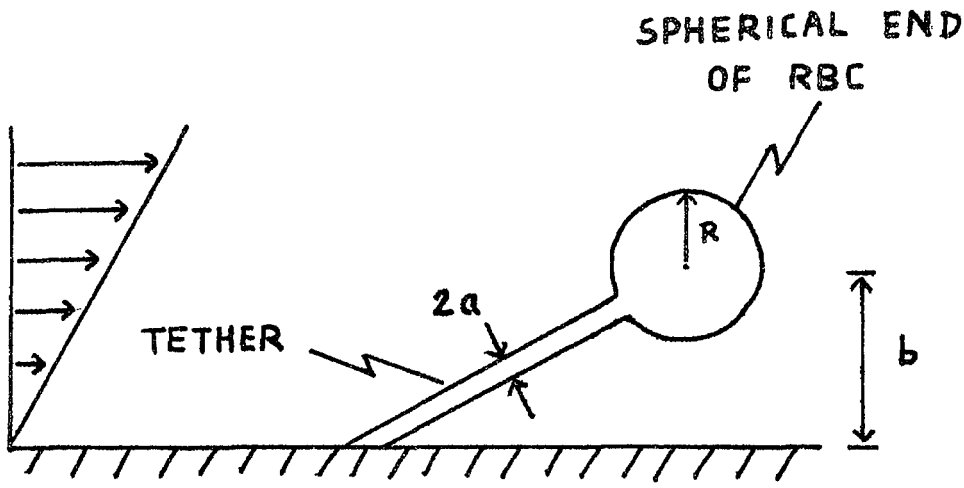

Fig. 100. Schematic of tethered red cell

In order that the spherical end does not break off from the tether, a force balance gives:

drag force of spherical part of RBC < surface tension force (31)

Therefore for the spherical end of RBC to break off from the tether and cause lysis

drag force acting on sphere $\geq$ surface tension force (32)

If $Re_{RBC} \leq 2$, then

$$\text{drag force} = 6\pi\mu V_1 R \tag{33}$$

where V_1 is the velocity of blood approaching the spherical part of the RBC; Re_{RBC} is the Reynolds number based on the spherical part of the RBC; and μ is the viscosity of blood. Assuming a uniformly distributed tension on the RBC membrane

$$\text{surface tension force} = 2\pi a\, \sigma_c \tag{34}$$

where σ_c is the critical surface tension at which the tether and the spherical end separate.

Rand [63] has measured σ_c to be between 15 and 30 dynes/cm. Therefore for lysis,

$$6\pi\mu V_1 R \geq 2\pi a\, \sigma_c \tag{35}$$

If the velocity gradient at the wall $(dV/dr)_{r=0}$ is uniform close to the wall, then the mean velocity at the sphere, V_1, will be $b(dV/dr)_{r=0}$.

$$\therefore \quad 6\pi R\mu b\left(\frac{dV}{dr}\right)_{r=0} \geq 2\pi a\, \sigma_c \tag{36}$$

$$\therefore \quad \tau_\omega \geq \frac{1}{3} \cdot \frac{a}{b} \cdot \frac{\sigma_c}{R} \tag{37}$$

where τ_ω is the wall shear stress. If $2 < Re_{RBC} \leq 500$, then

$$\text{drag force} \simeq \pi R^2 \cdot \frac{1}{2} \rho v_1^2 \frac{18.5}{Re_{RBC}^{3/5}}$$

$$= \frac{\pi R^2}{2} \rho v_1^2 \frac{18.5}{(\rho v \frac{2R}{\mu})^{3/5}}$$

$$= \pi R^{7/5} (\mu V_1)^{7/5} \mu^{-4/5} \rho^{2/5} \cdot 6.1 \qquad (38)$$

For lysis

$$\text{drag force} \geq \text{surface tension force}$$

$$\pi R^{7/5} \mu^{-4/5} \rho^{2/5} (\mu V_1)^{7/5} \cdot 6.1 \geq 2\pi a \sigma_c \qquad (39)$$

$$\pi R^{7/5} \mu^{-4/5} \rho^{2/5} (b \cdot \tau_\omega)^{7/5} \cdot 6.1 \geq 2\pi a \sigma_c \qquad (40)$$

$$\tau_\omega \geq \left(\frac{a^5 \sigma_c^5 \mu^4}{\rho^2} \right)^{1/7} \frac{1}{2.22 bR} \qquad (41)$$

It should be noted that the velocity gradient at the wall may not be uniform. As observed in the velocity measurements in this study, in the near vicinity of valves the velocity gradient at the wall was not uniform even over a distance of 400 μm from the wall. Therefore, it is better not to approximate for V in equations (35) and (39). Therefore for lysis equation (35) gives

$$V_1 \geq \frac{1}{3} \frac{a \sigma_c}{\mu R} \qquad (42)$$

Equation (39) gives

$$V_1 \geq \left(\frac{a^5 \sigma_c^5}{\mu^3 \rho_c} \right)^{1/7} \frac{1}{2.22R} \qquad (43)$$

Consider the following two examples. The dimensions used for the tethered RBC are experimentally observed values [45,61,67,68].

Case I: Short tether length with large tether diameter:

$R = 3.0$ μm; $a = 1.60$ μm, $b = 30$ μm

$\sigma_c = 30$ dynes/cm; $\mu = 0.035$ dynes sec/cm^2

For $Re_{RBC} \leq 2$, for lysis to occur

$\tau_\omega \geq 1777$ dynes/cm^2

$V_1 \geq 152$ cm/s

Case II: Long tether length with small tether diameter:

$R = 3.0$ μm; $a = 0.16$ μm; $b = 100$ μm

$\sigma_c = 30$ dynes/cm; $\mu = 0.035$ dynes sec/cm^2

For $Re_{RBC} \leq 2$, for lysis to occur

$\tau_\omega \geq 53$ dynes/cm^2

$V_1 \geq 15$ cm/sec

The foregoing two examples illustrate the fact that if a RBC gets attached onto a surface the shear required to lyse the cell is less than that required for in-bulk lysis. In Case I even if the velocity or the

wall shear in the vicinity of the tethered cell were not as high as 152 cm/sec or 1800 dynes/cm^2 respectively, a smaller velocity or stress acting on the cell for a relatively long period of time could weaken the connection between the tether and rest of the cell and make the cell more vulnerable to lysis.

In blood flow through tubes of diameter 100 μm or less, investigators have observed a cell-free layer near the wall. The cell-free layer known as the skimming layer is about 1000 Å in size. This dimension, however, is very hard to measure. Phibbs and Burton [69] and Keller [70] have observed in tubes of 1000 to 3000 μm diameter that some cells appear to come into contact with the vessel wall. In the above studies the shear flow was well defined. In the flow past prosthetic aortic valves the shear flow is completely broken up, creating a very turbulent and disturbed flow field in the downstream vicinity of the valves. Therefore RBCs and the other formed elements in blood could quite easily contact the vessel wall in the near vicinity of prosthetic aortic valves. Blackshear [61] has shown that the diffusion of cells towards a vessel wall or prosthetic surface is proportional to the velocity gradient at the surface. Turbulent flow increases the velocity gradient near the vessel wall. Therefore, since the prosthetic aortic valves create very turbulent and disturbed flow fields in their near vicinity, some RBCs will in all probability come into contact with the walls of the ascending aorta. In order that Van der Waals forces become effective between cells and vessel wall or prosthetic surface, the separation distance between them should be about 100 Å or less. In general, if a smooth cell is

thrust through the skimming layer towards a smooth vessel wall, the cell is protected from the wall by a lubricating layer of plasma greater than 100 Å in thickness. Even if the RBC and vessel wall do come into contact, due to their smooth surfaces, the RBC will not stick to the wall. Also, the RBC and the intact endothelial lining of vessel wall have the same surface charge. If, however, roughness elements of cell size or smaller exist on the vessel wall or on the cell, the lubricating layer between the wall and the RBC may be sufficiently thin for Van der Waals or surface forces to be large enough to bond the RBC to a site of the vessel wall. Blackshear [61] contends that roughness elements of the size of about 0.1 μm or larger are sufficient to trap a RBC to a surface. He also states that in general the roughness element is a blood originated deposit.

In a normal human being the ascending aorta is smooth due to the endothelial lining on the vessel wall. There are also no prosthetic surfaces present in the human aortic valve. Therefore in a normal healthy person, RBCs which flow past the aortic valve will not stick onto the vessel walls and consequently no hemolysis will occur due to cell-wall interaction. In the case of a patient with aortic valvular heart disease or with a prosthetic aortic valve, the wall of the ascending aorta will contain rough and/or sticky sites due to non-endothelialization of the wall, the deposition of platelets, blood cells, and/or fibrin on the non-endothelialized vessel wall or a combination of these effects. Therefore, a RBC which encounters the ascending aorta wall will in all probability stick to the wall. Any rough surfaces of the prosthetic aortic valve which do not become endothelialized would be ideal

surfaces for RBCs to get stuck onto. Once the RBC gets stuck to the vessel wall or a prosthetic valve surface, depending on the shear stresses or velocities adjacent to the tethered cell, the RBC could be damaged to varying extents. In the worst case the RBC would be lysed and hemoglobin would be released into the plasma.

5.2 Thrombus Formation

Thrombus formation is probably the major problem associated with prosthetic heart valve replacement. If a patient does not receive anticoagulation therapy after aortic valve replacement, or if he stops the therapy for some time period, he may develop a thromboembolic complication. The thromboembolic complication could be fatal. At present the majority of physicians maintain their prosthetic aortic valve patients on strict anticoagulant therapy.

At present the area of controversy or debate is the factor or factors by which thrombus formation is initiated and propagated. There are three factors by which the thrombus formation associated with prosthetic aortic valves could be initiated. These are (a) blood vessel damage, (b) hemolysis of red blood cells, and (c) mechanical trauma of platelets due to shear. The three factors are interrelated and at present it is not possible to state which of the three factors predominates.

Platelets do not adhere to intact endothelial cells but they do adhere to subendothelial connective tissue composed of collagen and other materials. The main point in the factor involving vessel damage [80,81,82] is that platelets have access to collagen fibers once the

endothelial lining of a vessel wall is damaged or eroded off. The adhesion of platelets to the damaged vessel leads to the subsequent release of ADP and the platelet factor 3 (PF-3), which initiates both aggregation and coagulation of platelets and ultimately leads to thrombus formation.

RBCs contain ADP and a clot-promoting factor known as erythrocytin. Both these substances are released from a RBC into the plasma when the RBC is hemolyzed [83,84,85,86]. When the ADP and the erythrocytin are released into the plasma, both platelet adhesion-aggregation and coagulation may be initiated, resulting in thrombus formation.

The third factor suggests that when platelets undergo relatively high shear stresses (100-500 dynes/cm^2) denaturing of the platelet occurs. The platelets when damaged by shear release ADP which could initiate adhesion and coagulation of the platelets and lead to thrombus formation [77,78,79].

There are many articles in the medical literature pertaining to the clinical observation of thrombus formation in patients with prosthetic aortic valves [9,12,13,48,71,72]. Platelet studies in patients with prosthetic valves have shown shortened survival times [73,74,75,76]. In vitro studies conducted in rotating viscometers by Hellums and coworkers [54,77, 78] and by Hung et al. [79] indicate that platelets could be damaged by shear stresses of the order of 100 to 500 dynes/cm^2. Hung et al. [79] state that human platelets had a threshold tolerance to shear stress which was approximately 10 times lower than that obtained for RBCs in the same viscometer under identical conditions. Brown et al. [77] observed in their

studies that at a shear of about 50 dynes/cm^2 the platelets appeared swollen, and ATP and ADP were released into the blood plasma. At shear stresses of about 150 to 250 dynes/cm^2 platelet fragments and distorted platelets were observed. It has also been observed that at shears of 100 to 200 dynes/cm^2 platelet counts drop. The behavior of platelets to shear has not, however, been studied as extensively as the behavior of RBCs, and more in vitro work is required in order to understand more clearly the threshold shears above which platelets undergo various degrees of damage.

Nose et al. [87] observed in in vitro experiments that thrombi formed only in areas of turbulence and/or statis, and at junctions where geometric imperfections disrupted established flow patterns. Thrombus formation and build-up in areas of stagnation of stasis have been observed by many investigators [9,88,89,90,91]. Kingsley et al. [90] state that thrombus formation occurs in areas of boundary layer separation and turbulence. Madras et al. [92] state that areas of high flow and turbulence can either lead to increased or decreased thrombus formation in a given area, depending on which of one of two mechanisms is dominant. High flow

and turbulence lead to high shear stresses at a surface, and any blood elements which are loosely attached to the surface may be detached, either before an actual thrombus is formed, or the thrombus may embolize leaving a clean surface. Another explanation is that high flow implies shorter contact time between the blood elements and a surface. Complex biochemical reactions are required to cause platelet aggregation or to activate the coagulation sequence. The shorter the residence time of the blood elements in the near vicinity of the surface, the less time is available for the biochemical reactions to occur. Therefore, little or no thrombi may occur on the surface under these conditions. The second mechanism is that high flow and turbulence would increase the rate at which platelets are brought to the surface. If the surface is such that the platelets will adhere onto the surface on arrival, the high flow and turbulence would lead to a more rapid accumulation of platelets and thrombus formation on the surface. Therefore, areas of high flow and turbulence can lead to either increased or decreased thrombosis. The large surface shears associated with high flow can also cause embolization of thrombi formed on a surface and lead to thromboembolic complications. The effects of turbulence and high flow on thrombus formation require further investigation.

Thrombus formation that has been observed on the superstructure of recovered aortic prostheses is seen not only in areas of stagnation or low flow, but also in areas of relatively high flow where turbulence occurs. Roberts [72] has observed that the thrombus formation on the Starr-Edwards ball valve was not localized at the apex of the cage (area of stasis), but was also seen on the sides of the struts and on the

metallic orifice ring. The struts and the metallic orifice ring are in areas of relatively high flow. Once it originates, thrombus formation spreads out. For example, thrombi which originate in an area of stagnation can spread towards areas of high or turbulent flow, or vice versa. Thrombus formation on the Björk-Shiley valve has been observed in an area of stagnation or low flow, and will be discussed in more detail in Chapter 7. The thrombus formation observed on recovered valves contains platelets that are enmeshed in a fibrin network. It is also observed that red cells get trapped in the fibrin network and are hemolyzed.

5.3 Damage to the Endothelial Lining of the Wall of the Ascending Aorta

The damage to the endothelial lining of the wall of the ascending aorta is in my opinion a very important consequence of the use of prosthetic aortic valves. Damage to the vessel wall as stated in Section 5.2 could lead to thrombus formation.

Fry [94,95] conducted two studies on the effects of wall shear on the endothelial lining of the aortic wall. He found that the endothelial cells on the vessel wall could be damaged at wall shear stresses of about 400 dynes/cm^2 and could be eroded off the vessel wall at shear stresses of about 950 dynes/cm^2. He observed that when the endothelial surface was exposed to shearing stresses above some critical value (400 dynes/cm^2) the cells began to suffer structural and chemical changes. The critical stress is known as the "yielding" stress. If a shearing stress above the critical value is applied for a long enough time period, the yielding process continues until the cells become mechanically unstable and are

washed away from their moorings to the basement membrane in total or by progressive erosion of cell substance. As the eroded vessel wall surface is exposed to the flowing blood, deposition of blood elements and thrombotic materials occur. Fry [95] found that the deposited material consisted of fibrous tissue, platelets, blood cells, and other unidentified debris. He states that such deposition could lead to intimal thickening of the vessel wall. Woolf and Carstairs state [96] that the fibrous tissue observed on the aortic wall due to the intimal thickening owes its presence to either infiltration or thrombus formation, or a combination of these two factors.

William C. Roberts, probably one of the leading cardiac pathologists in the U.S.A., has studied hundreds of recovered aortic prostheses of varying designs. In his studies he has observed the conditions of the walls of the aortic root. His findings are well documented [13,48, 72,93]. He has found in many cases that there was intimal thickening in the aortic roots including the area of the coronary arterial ostia. The thickening was produced by the deposition of fibrous tissue on the internal elastic membrane of the proximal ascending aorta. The degree of intimal proliferation varied from minimal to extremely severe. In some cases the intimal thickening involved not only the ascending aorta and proximal coronary arteries, but also the entire coronary bed. Roberts made his initial findings in 1967 [72,92], and he attributed the intimal proliferation to the localized turbulent flow created by the prosthetic aortic valves. He also stated that the intimal fibrosis in the aortic root and in very near vicinity may be a previously

unrecognized consequence of aortic valve replacement. In his recent review article [13] he once again refers to the problem of intimal proliferation of the proximal ascending aorta and states that it is a potential problem with all the peripheral flow type aortic prostheses.

It therefore seems that high wall shear stresses (> 400 dynes/cm^2) could damage the endothelial lining of the wall of the proximal ascending aorta and lead to intimal thickening in that area. The effects of high wall shear stresses and turbulence on the wall of the ascending aorta, however, require further investigation.

Chapter 6

VELOCITY MEASUREMENTS

A patient with an aortic prosthesis has an average cardiac output of about 58 cm^3/sec to 92 cm^3/sec (3.5 to 5.5 liters/min) and a peak systolic flow rate of about 250 to 417 cm^3/sec (15 to 25 liters/min). With these flow rates in mind the velocity measurements were conducted at steady flow rates in the range of 167 cm^3/sec to 417 cm^3/sec. The measurements were performed at the following fixed locations downstream from the front end of the valve seat: (i) X = 42.0 mm, (ii) X = 55.0 mm, (iii) X = 67.4 mm, (iv) X = 92.8 mm, and (v) X = 118.2 mm. These five downstream locations are in section 'C' (see Fig. 3), and the velocity profiles were measured from the inside to the outside wall as shown in Figure 10 (i.e., wall to wall). In the sinus or heart valve chamber region (section 'B', Fig. 3) which is surrounded by the lucite pot filled with glycerine, velocities were obtained at different X coordinates depending on how close to the valve measurements they could be made without obstructing the paths of the laser beams. In this region velocity measurements were made from the inside wall to about the center of the channel. As discussed in the experimental section, it was possible to obtain wall shear measurements on both the inside and outside walls. In the velocity profile plots presented in this thesis the data points which appear to lie on the vertical axes correspond to velocity measurements made at distances of 0.034 mm from the vessel wall.

6.1 Velocity Measurements Upstream of the Heart Valve Chamber

Figures 101 and 102 show velocity profiles obtained upstream from the heart valve chamber at X = -110.0 mm and X = -33.5 mm (i.e., in section 'A' of the flow channel). These profiles are independent of the type of valve placed in the valve chamber. Comparing Figures 101 and 102 it can be seen that the profiles are identical, indicating that the flow has reached a steady state (i.e., independent entrance conditions). Knowing that the flow at X = -33.5 has reached a steady state and that it is axisymmetric, the five velocity profiles in Figure 102 were integrated across their area of cross section. The resulting volumetric flow rates as given in Table 10 were within at least ±1.5 percent of the flow rates measured during the experiments.

Table 10. Comparison of Measured and Calculated Flow Rates at X = -33.5 mm

Measured Flow Rate cm^3/sec	Calculated Flow Rate cm^3/sec
166.7	168.7
250.0	247.2
333.3	329.5
375.0	374.0
416.7	419.8

All experiments were conducted in a Reynolds number range of 2,400 to 6,000 based on the tube diameter of 25.4 mm. Therefore, the flow region was turbulent. Velocity profiles in Figures 101 and 102 can be fitted by an empirical 1/6th power-law equation,

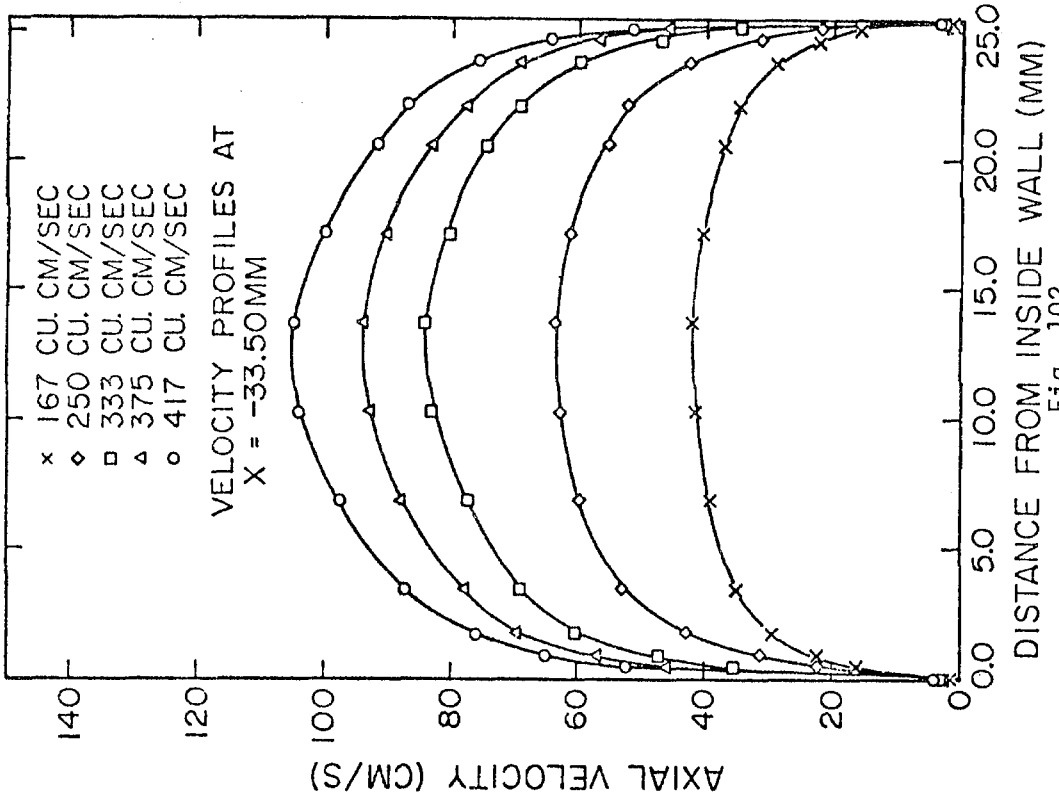

Fig. 102

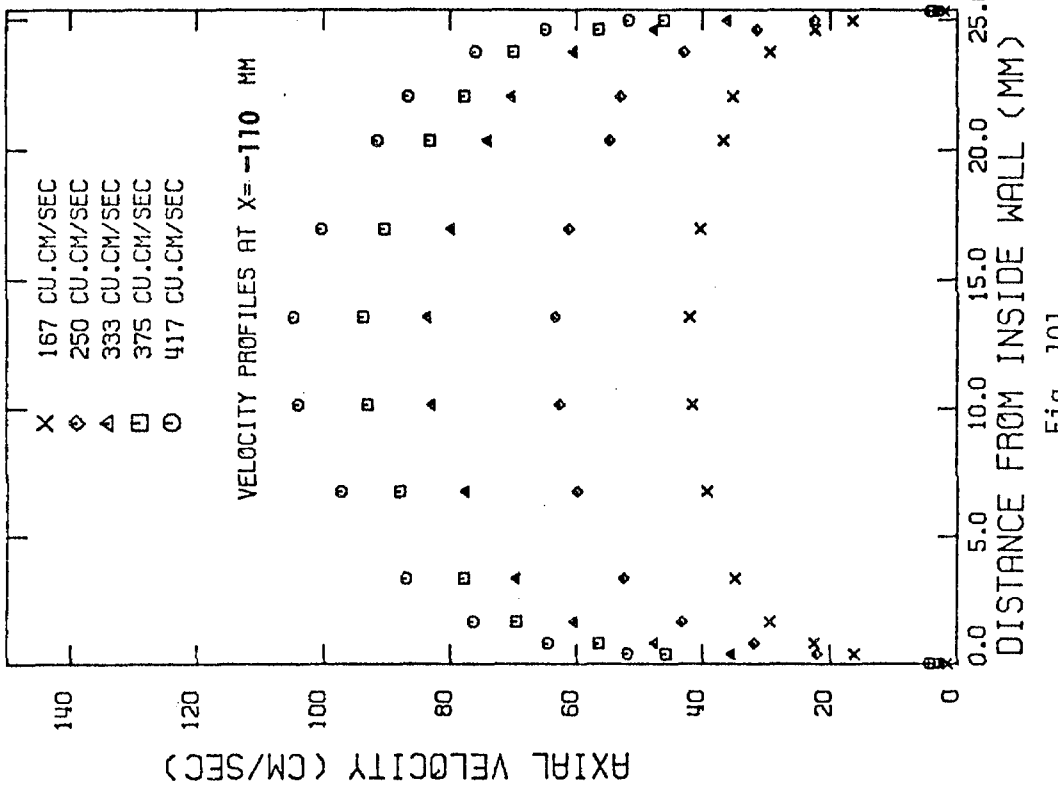

Fig. 101

Velocity profiles upstream from the heart valve chamber

$$\bar{v}_x(r) = \bar{v}_{x,max}\left(1 - \frac{r}{r_o}\right)^{1/6} \tag{44}$$

which further indicates that the flow was turbulent [97]. The wall shear stresses measured at the various flow rates at X = -33.5 mm compare very favorably with those estimated from pressure drop measurements in section 'A' as shown by the values in Table 11. The calculated values are obtained from the equation

$$\tau_w = \frac{\Delta\bar{p}}{L} \cdot \frac{d_o}{4} \tag{45}$$

where

τ_w = wall shear stress

d_o = internal diameter of channel

$\frac{\Delta\bar{p}}{L}$ = mean pressure drop across a length L of the flow channel

Table 11. Comparison of Measured and Calculated Wall Shear Stresses at X = -33.5 mm

Flow Rate cm^3/sec	Measured Wall Shear Stress ($dynes/cm^2$)	Calculated Wall Shear Stress ($dynes/cm^2$)
167	14	14
250	20	21
333	30	28
375	39	38
417	45	43

Turbulent intensity-level measurement I_x, as defined by equation (46) in the axial direction indicated values of about 5 to 8 percent in section 'A' of the flow channel.

$$I_x = \frac{\sqrt{\overline{v_x'^2(r)}}}{\overline{v}_x(r)} \times 100 \qquad (46)$$

The reliability and accuracy of the laser-Doppler anemometer are demonstrated by the results obtained upstream (X = -33.5 mm) from the heart valve chamber. Flow rates obtained from the velocity profile measurements compare very well with the measured flow rates. Results for the wall shear also compare extremely well with the wall-shear stresses estimated from the pressure-drop measurements. The wall-shear stresses indicated that the velocity measurements very close to the wall (0.034 mm from the wall) are accurate.

In the following sections the velocity profiles obtained with the different types of prosthetic valves are shown graphically. The profiles by themselves convey a larger amount of information than can be described in words. Table 12 gives the measured wall shear stresses in the sinus region ($X \leq 37$ mm) and at X = 118.2 mm at a flow rate of 417 cm^3/sec, and Table 13 gives the measured wall shears at the same locations at a flow rate of 167 cm^3/sec. The wall-shear stresses at the other flow rates studied will lie between the values obtained at these two flow rates (417 and 167 cm^3/sec). Wall-shear stress was measured by assuming that the velocity increased linearly from the wall to the point of measurement closest to the wall (i.e., 0.034 mm from the wall). It should be noted that all velocity profiles were obtained in the axial direction in the horizontal plane through the center of the channel. Also the two locations of measurement very close (within 0.034 mm) to the inside and outside walls in the sinus region were not exactly diametrically opposite each other. This was due to the distortion of the laser beams in passing

through the heart valve chamber (section 'B').

6.2 Velocity Measurements Downstream from the Prosthetic Valves

6.2.1 27 mm Lucite Disc

The experiments conducted with the 27 mm orifice diameter lucite disc in the heart valve chamber are almost analogous to having a fully open, normally functioning human aortic valve in the valve chamber. Figures 103, 104, 105, 106 and 107 show the velocity profiles downstream of the lucite orifice. These sets of experiments indicated that the inlet velocity profiles were only slightly disturbed. The profiles emerging from the heart valve chamber were still turbulent in shape, and and reached a steady state within a downstream distance of about X = 67.4 mm. The turbulence intensity levels ($I_x \simeq 5$ to 10 percent) were no higher than those measured upstream from the valve chamber at X = -33.5 mm. The measured wall shear at a flow rate of 417 cm^3/sec was about 60 dynes/cm^2 in the sinus region and about 50 dynes/cm^2 in section 'C' of the flow channel. The estimated wall shear, calculated from pressure drop measurements, yielded an average value of about 50 dynes/cm^2 at a flow rate of 417 cm^3/sec. The measured wall shears were not much larger than those measured upstream at X = -33.5 mm. These results tend to indicate that the fully open, normally functioning natural human aortic valve creates very minimal flow disturbances and relatively low wall shear stresses both in the sinus region (section 'B') and in the downstream section 'C' . Integration of velocity profiles at X = 67.4 mm across their area of cross section gave volume flow rates which were within at least ±1.5 percent of the measured values.

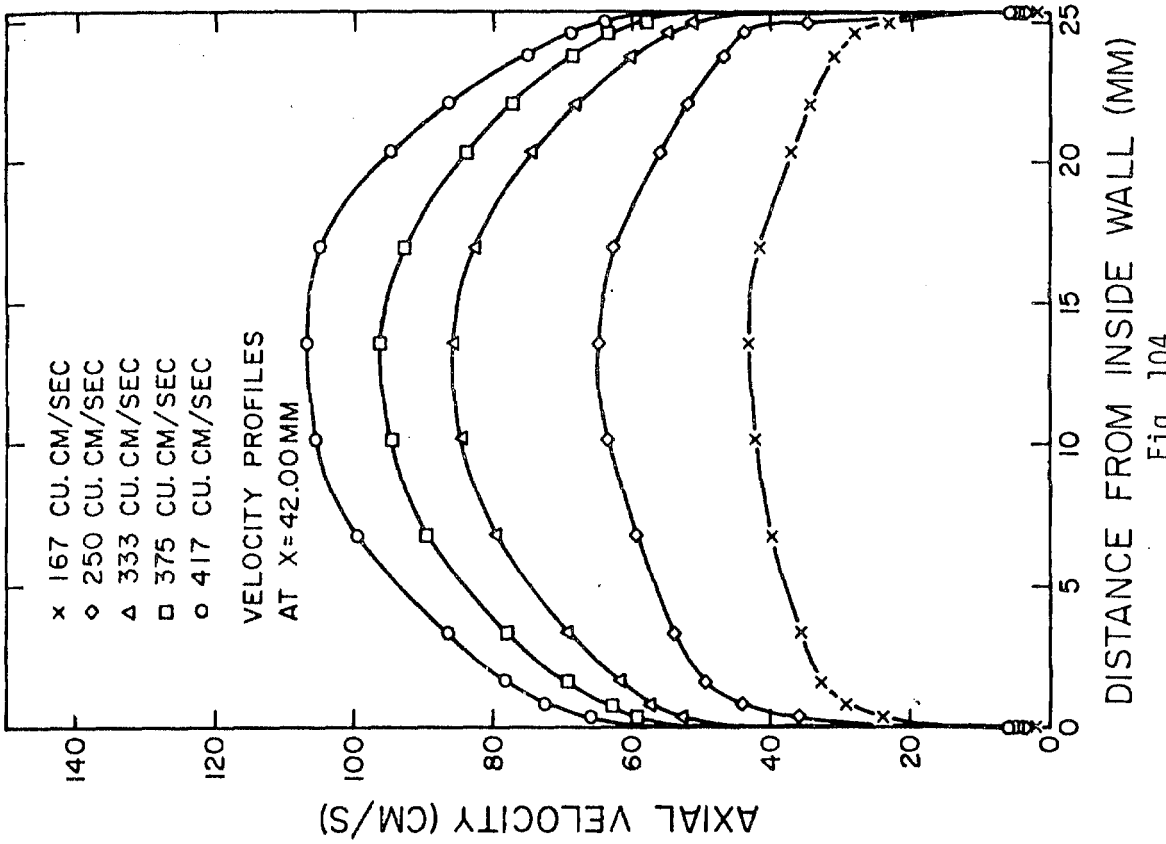

Fig. 104

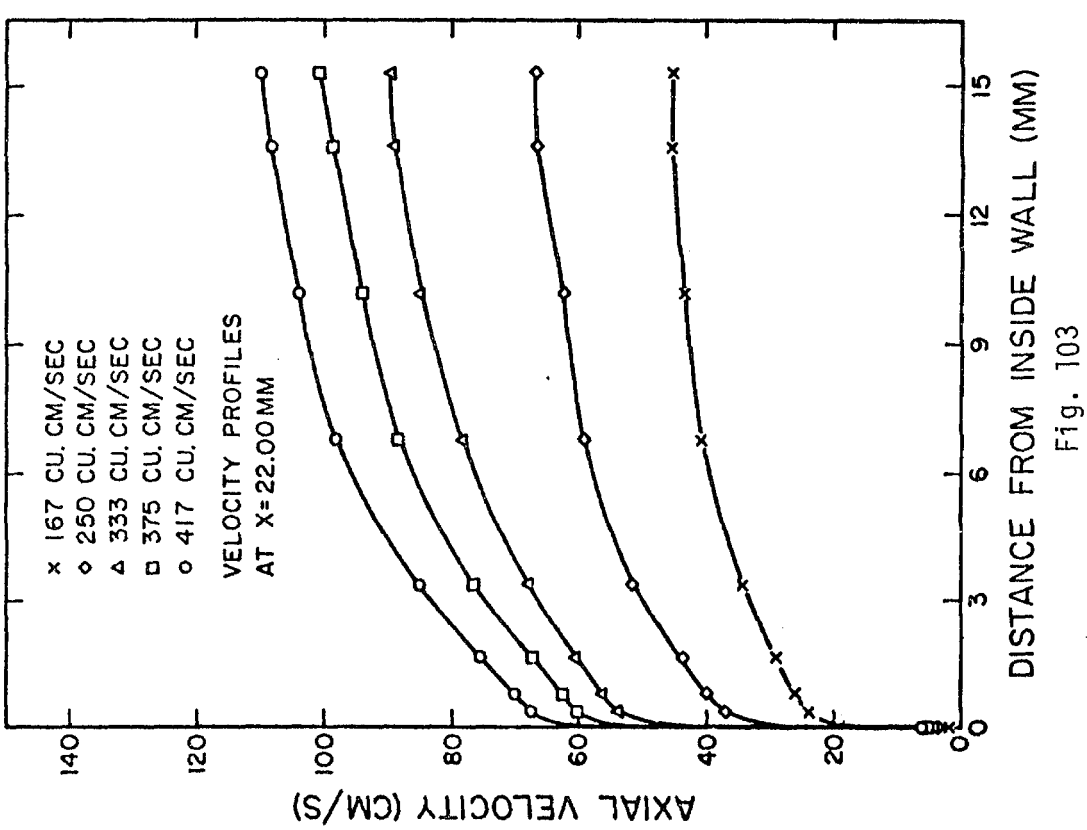

Fig. 103

Velocity profiles downstream from the lucite disc

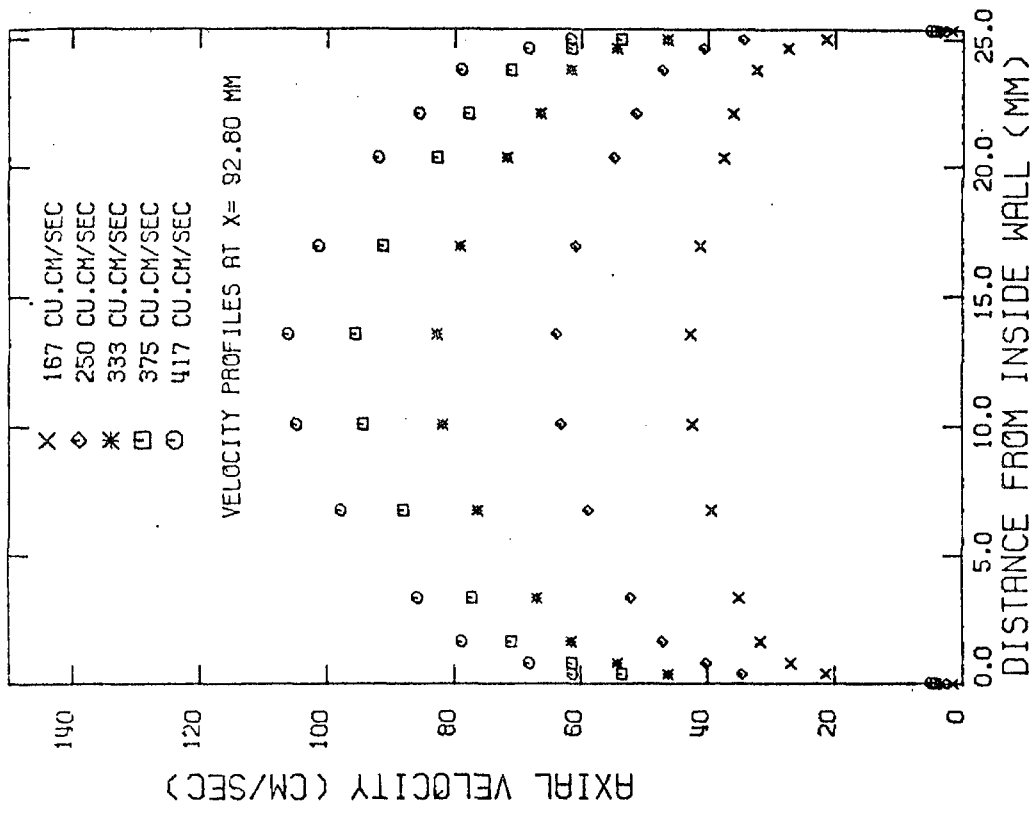

Fig. 106

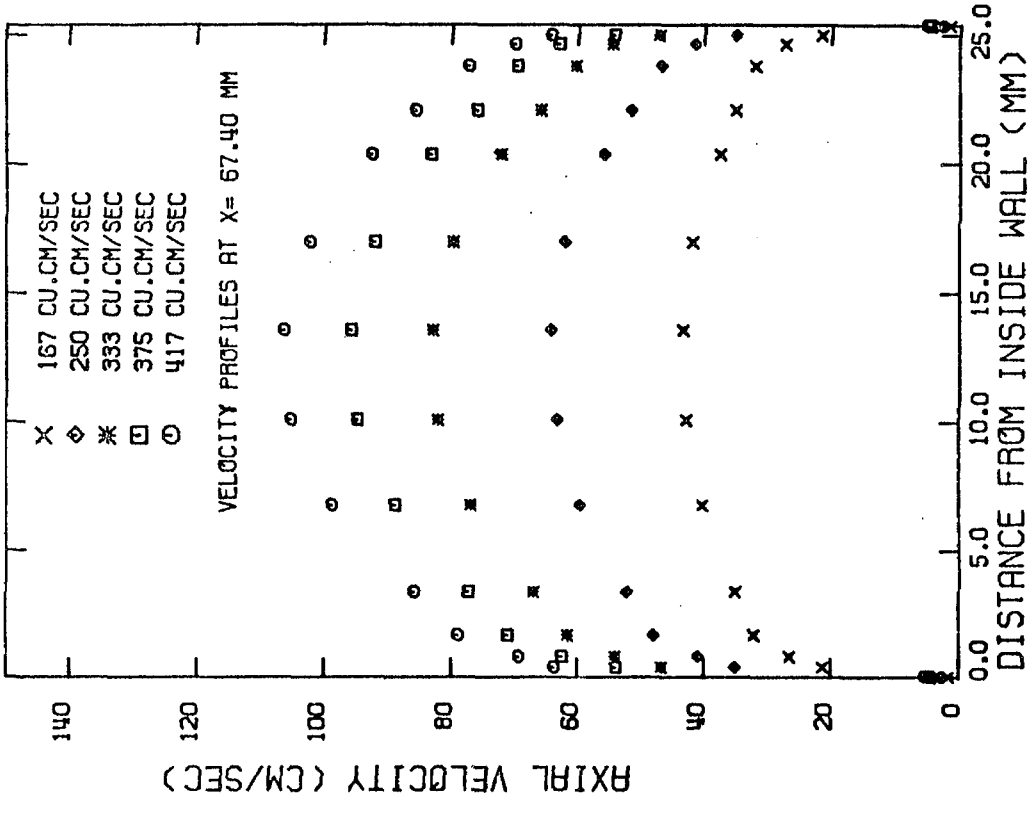

Fig. 105

Velocity profiles downstream from the lucite disc

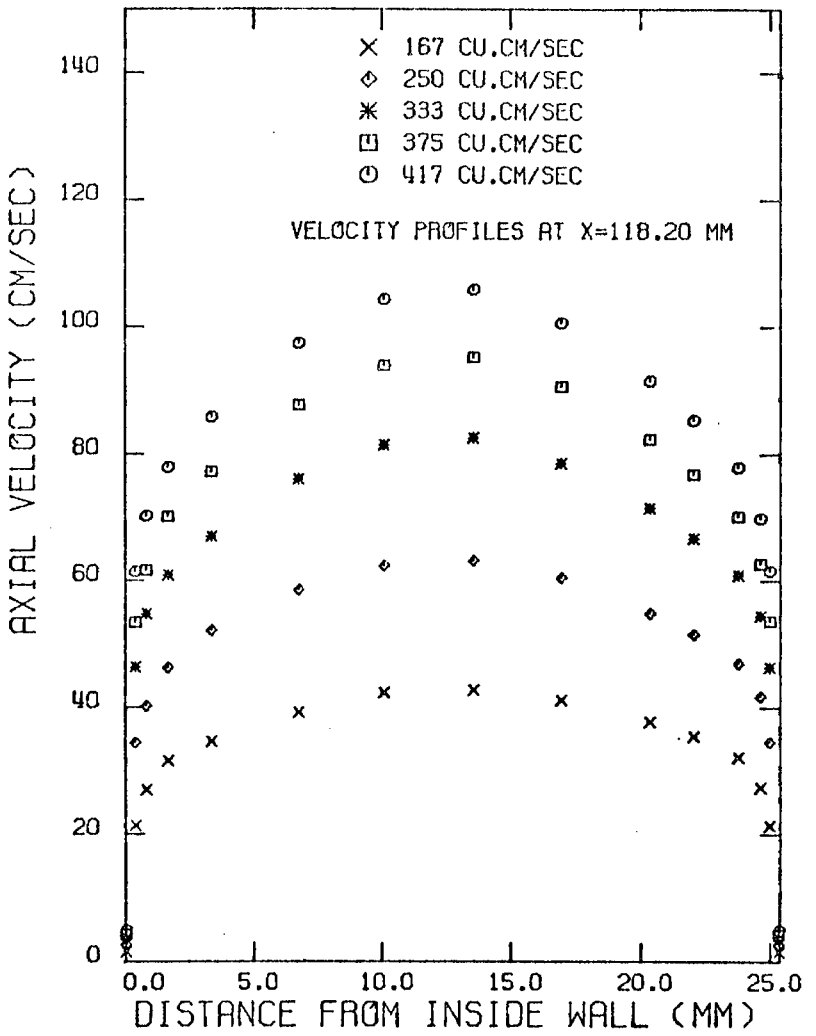

Fig. 107. Velocity profiles downstream from the lucite disc

6.2.2 Starr-Edwards 1260-12A

Two sets of experiments were performed with the Starr-Edwards ball valve. The first set was made with the ball tied at the apex of the cage with sewing thread. When the ball was free it went into random oscillations and rotations due to hydrodynamic instability at a flow rate of about 133 cm^3/sec. The random oscillations were hard to control and made velocity measurements difficult. It should be noted that in order to obtain velocity profiles at a given downstream location the flow channel had to be moved back and forth in the Y-direction. The movement of the flow channel would sometimes alter the position and nature of the oscillations of the ball. Therefore to simplify the experiment the ball was tied. A second series of experiments were conducted with the ball free and oscillating at the top (apex) of the cage.

Figures 108 to 113 show the velocity profiles obtained with the ball tied. The fact that the ball was tied is illustrated by the profiles in Figure 108, which show an area of zero flow in the very near vicinity of the stationary ball. The location X = 22 mm is about 2 to 3 mm downstream from the apex of the cage. The wall shear stresses measured on the inside and outside walls are presented in Tables 12 and 13.

Figures 114 to 119 show the velocity profiles for the experiments conducted with the ball untied and oscillating at the apex of the cage. At X = 42.0 and 55.0 mm (Figs. 115 and 116) the velocity profiles obtained at the flow rates of 167 and 250 cm^3/sec are quite different in shape from those obtained at 333, 375 and 417 cm^3/sec. The reason for the change in shape of the profiles is probably associated with some

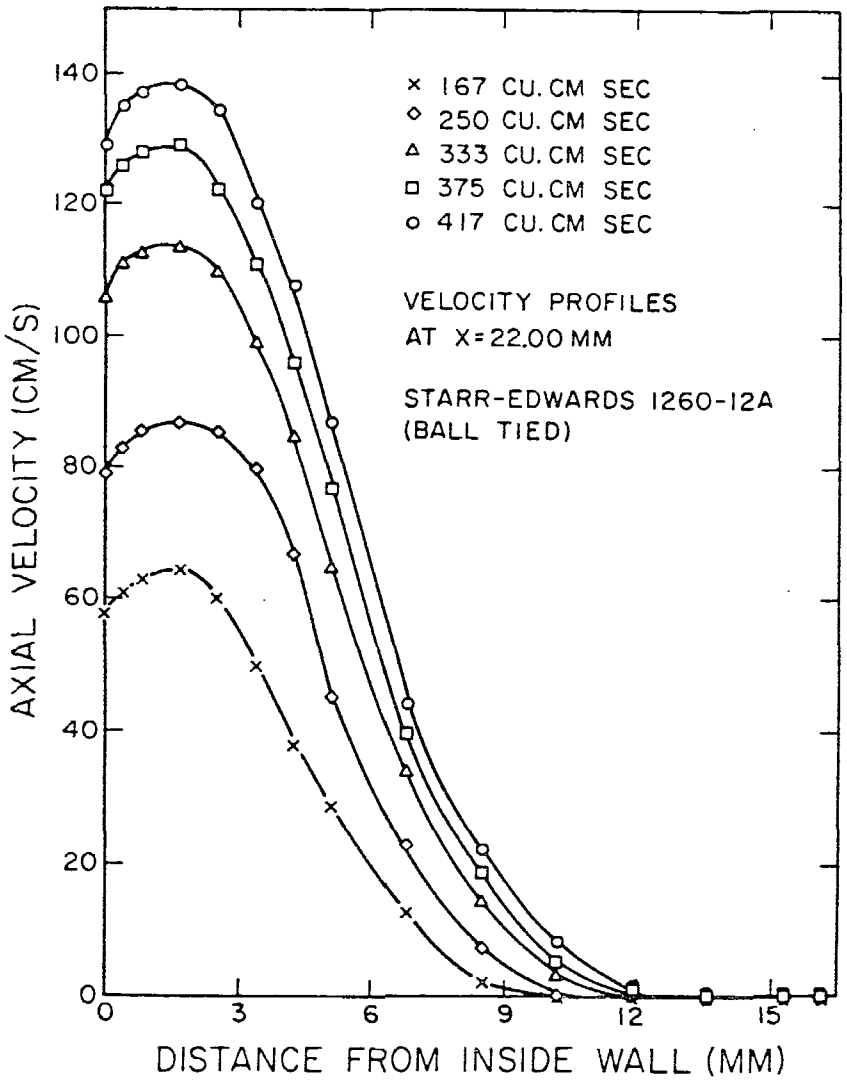

Fig. 108

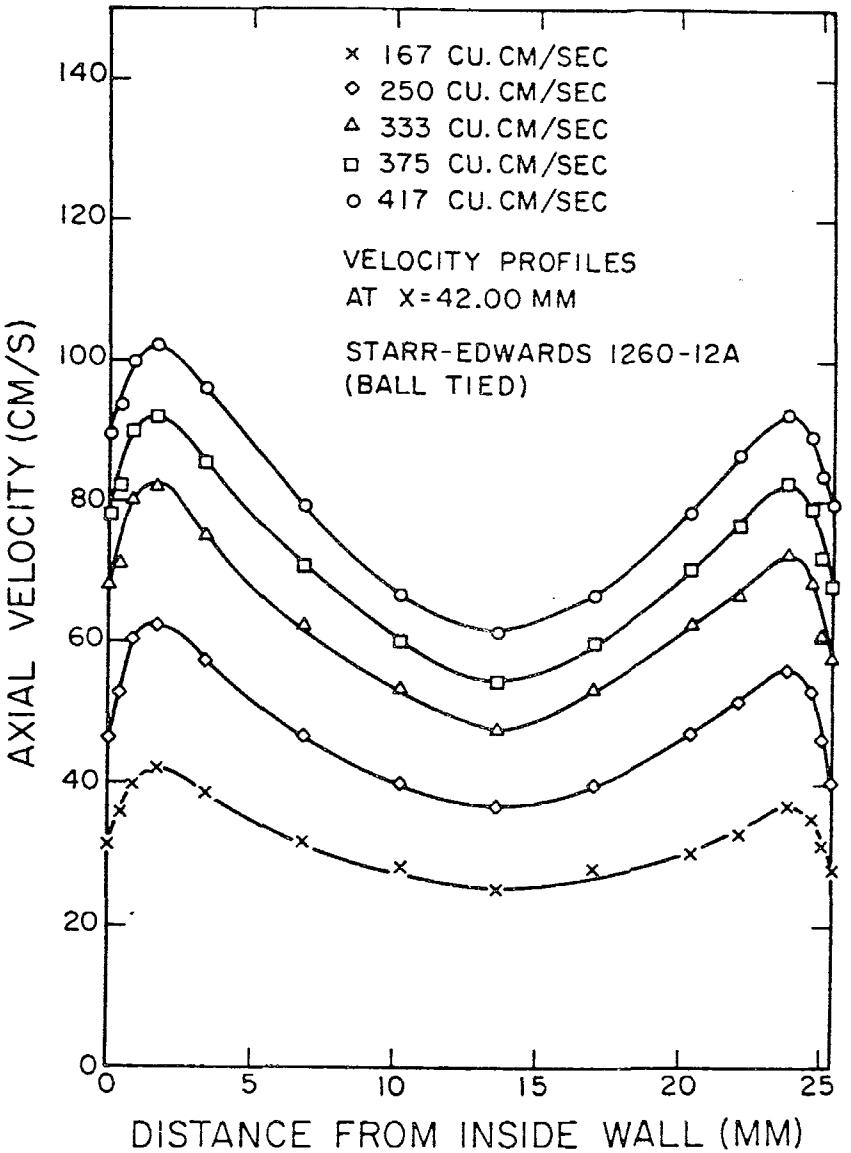

Fig. 109

Velocity profiles downstream from the Starr-Edwards 1260-12A valve (ball tied)

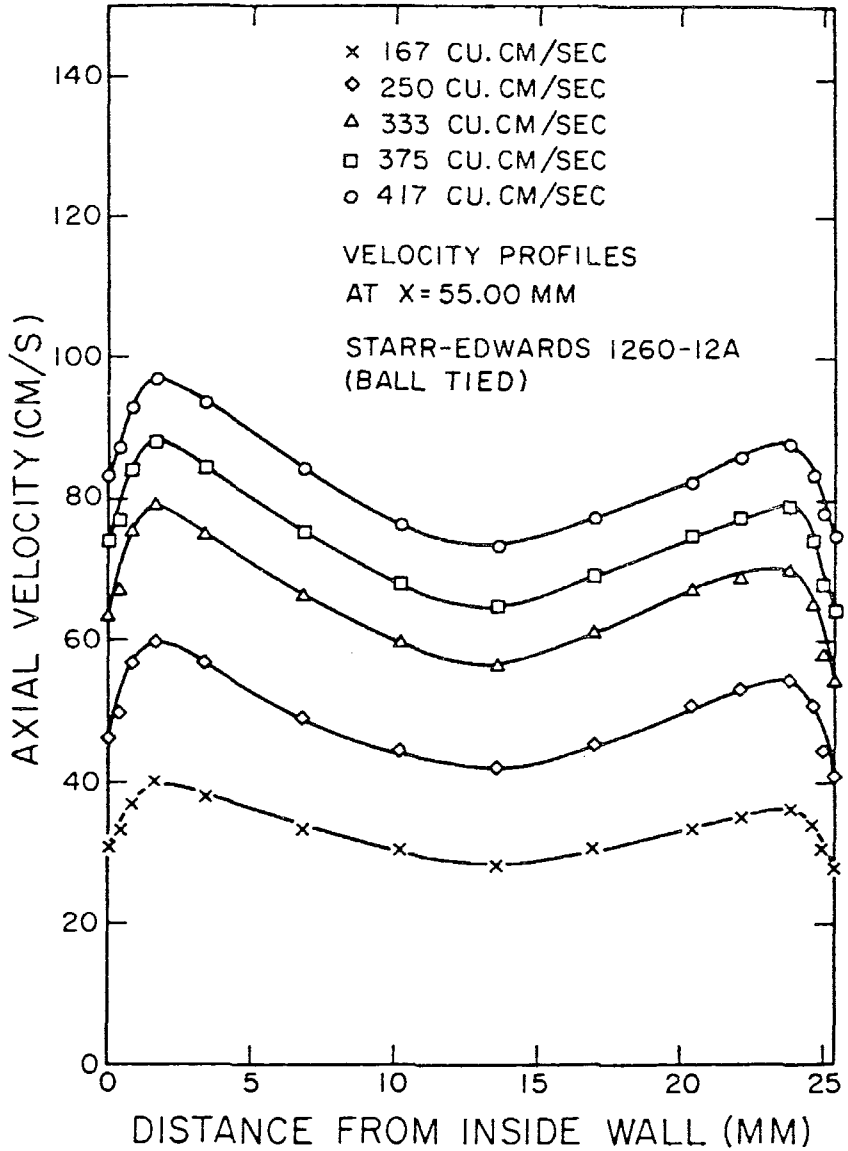

Fig. 110

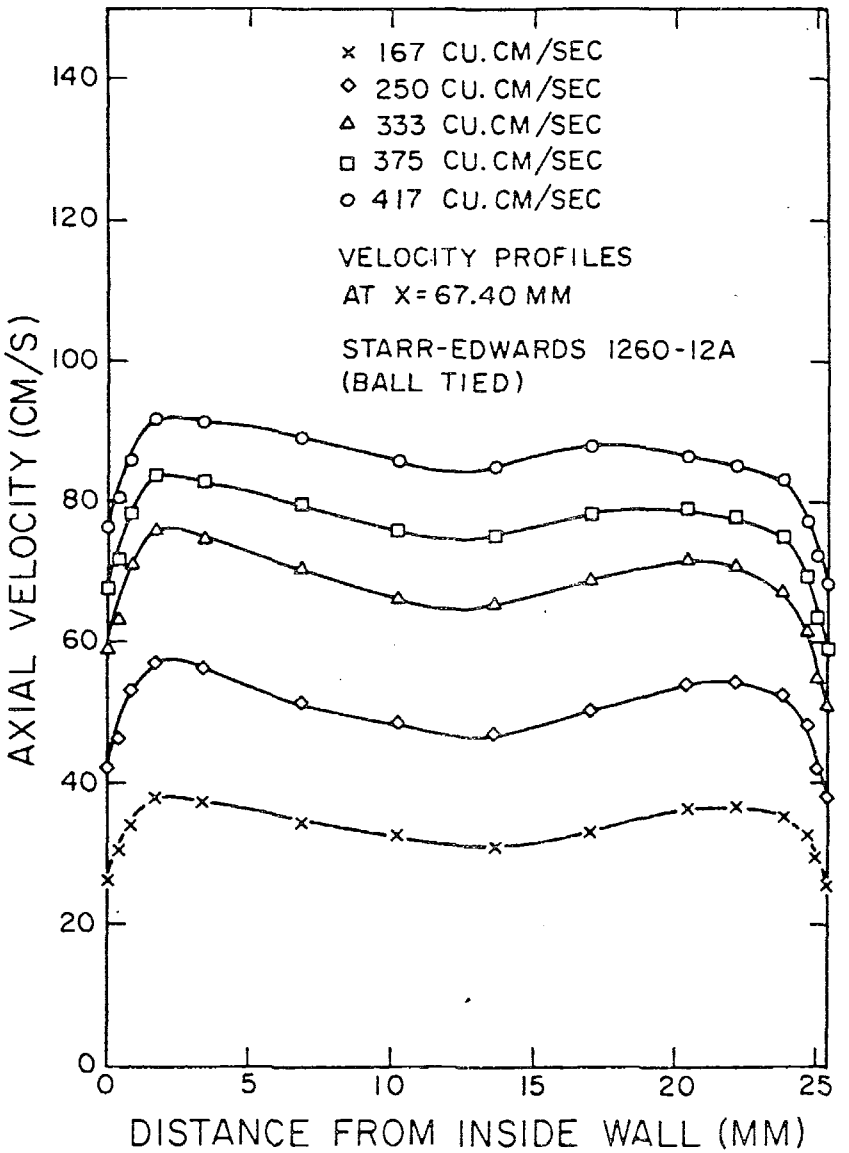

Fig. 111

Velocity profiles downstream from the Starr-Edwards 1260-12A valve (ball tied)

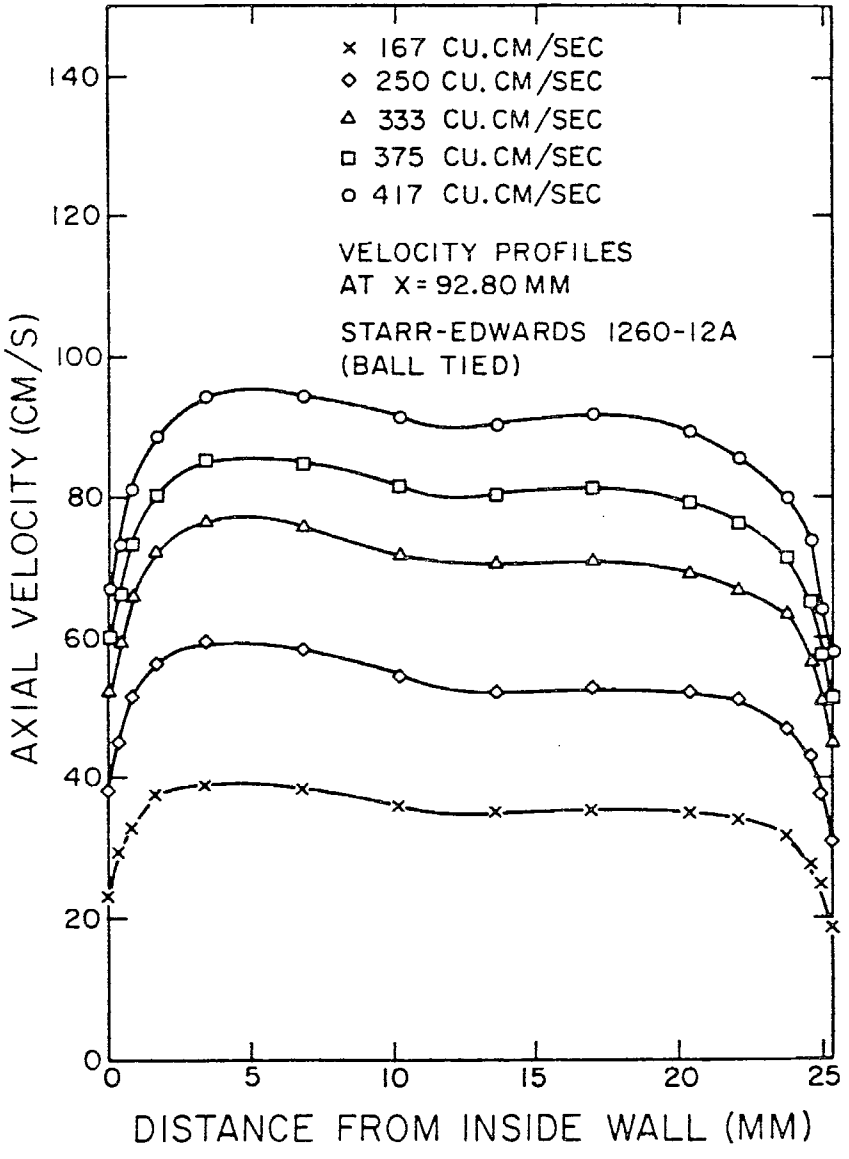

Fig. 112

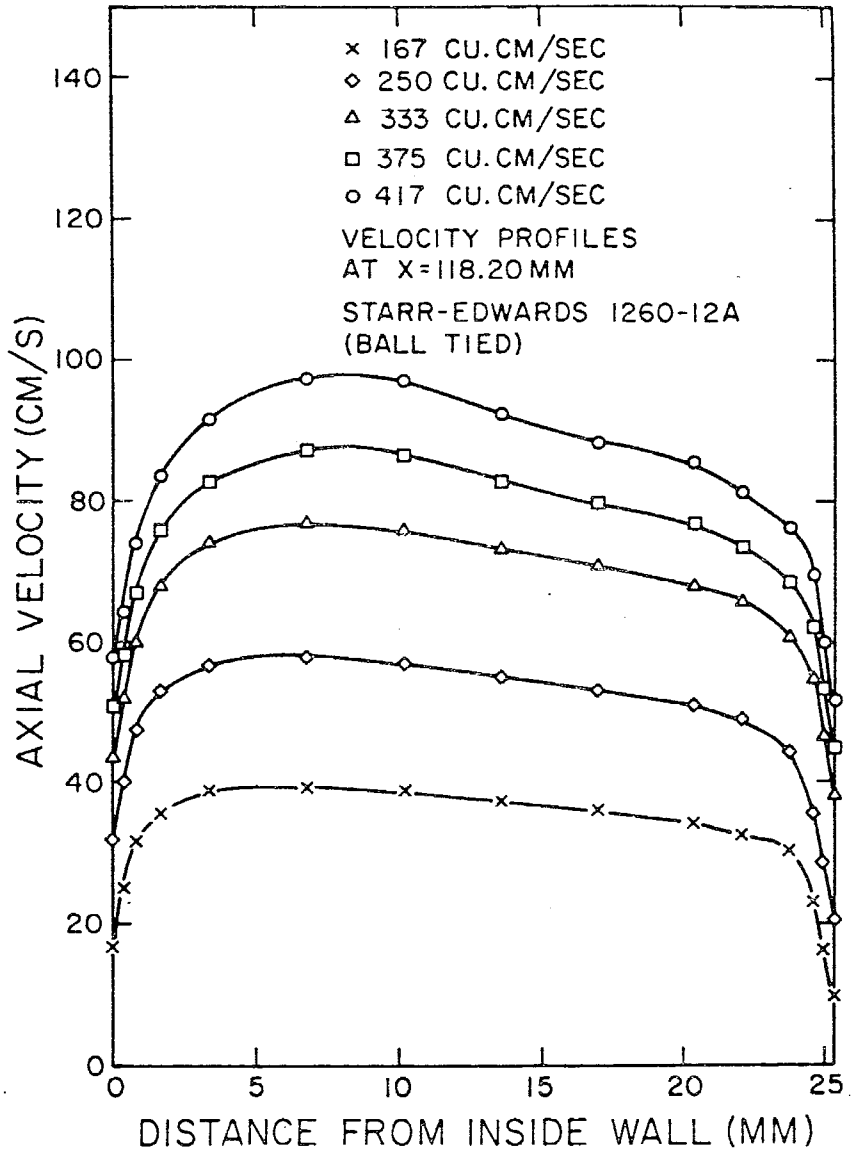

Fig. 113

Velocity profiles downstream from the Starr-Edwards 1260-12A valve (ball tied)

change in the nature of the oscillations and rotations of the ball at the apex of the cage. In the near vicinity of the valve ($X \leq 55$ mm), there are differences in the profiles obtained with the ball tied and untied. The area of stagnation at X = 22 mm is smaller in the case of the untied ball and is confined more towards the apex of the cage, and not the entire area occupied by the top surface of the ball as was observed with the tied ball. It should be noted in Figures 108 and 114 that the velocities in the stagnation zone are plotted as zero velocity. In the experiments, however, the velocities in both stagnation zones oscillated between ±2.0 cm/sec. The velocity profiles at X = 55.0 mm and 67.4 mm tend to indicate that the profiles of the untied ball tend to return to turbulent pipe flow profiles somewhat faster than the profiles of the tied ball. The velocity profiles of the tied ball create a larger velocity defect (i.e., dip in the center of the velocity profile) phenomenon at X = 55.0 and 67.4 mm compared with the untied ball, because of the larger stagnation effect created by the stationary ball. Wall shear stress measurements indicate that the wall-shear in the sinus region is larger for the case of the untied ball.

Figure 114 shows clearly, as stated previously, the stagnation zone formed near the apex of the cage of the Starr-Edwards ball valve (ball untied). At X = 22.0 mm and at flow rate of 417 cm^3/sec the size of the stagnation zone was approximately 5 to 6 mm in diameter, and approximately 12 mm in diameter at a flow rate of 167 cm^3/sec. At a distance of X = 20.5 mm downstream of the untied ball valve the diameter of the stagnation zone was observed to be approximately 7 to 8 mm

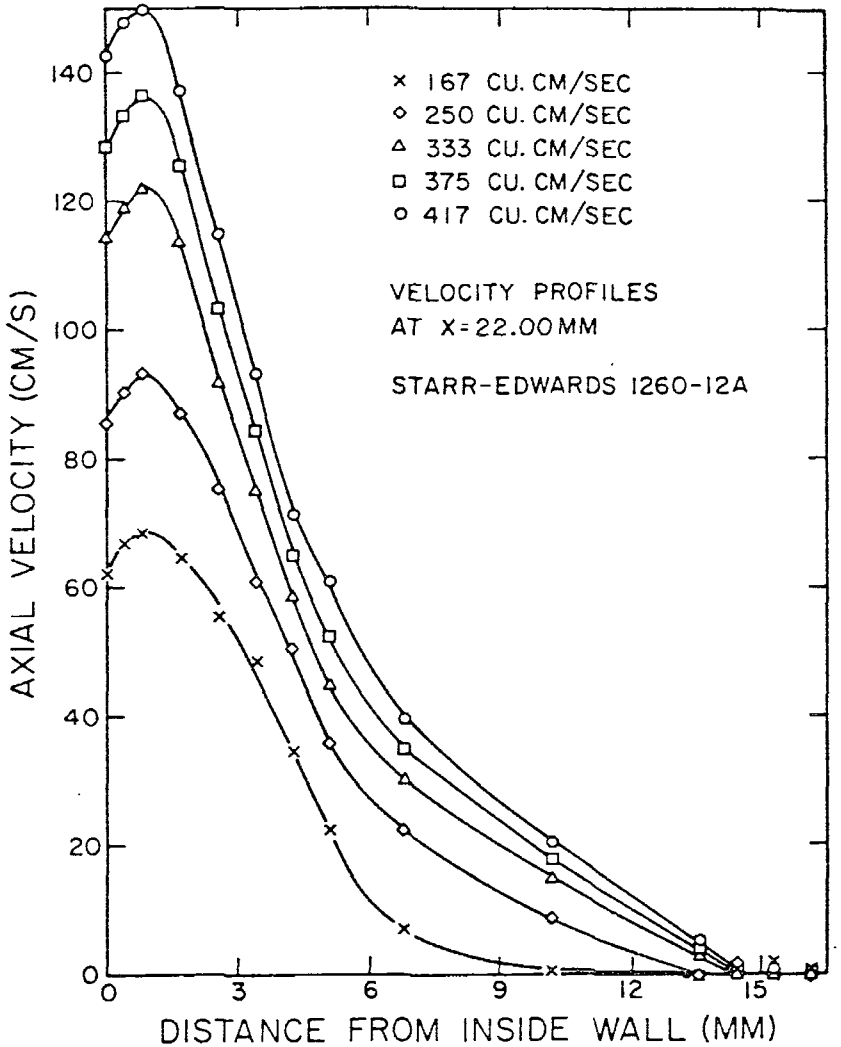

Fig. 114

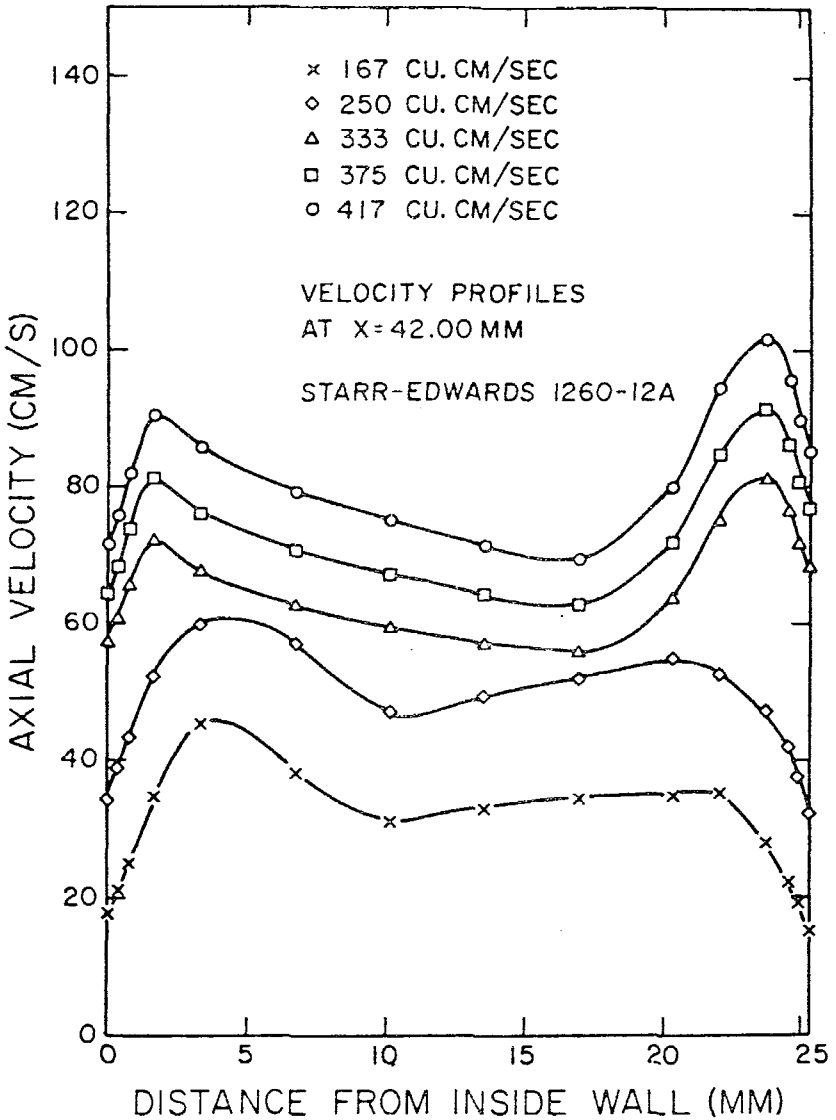

Fig. 115

Velocity profiles downstream from the Starr-Edwards 1260-12A valve

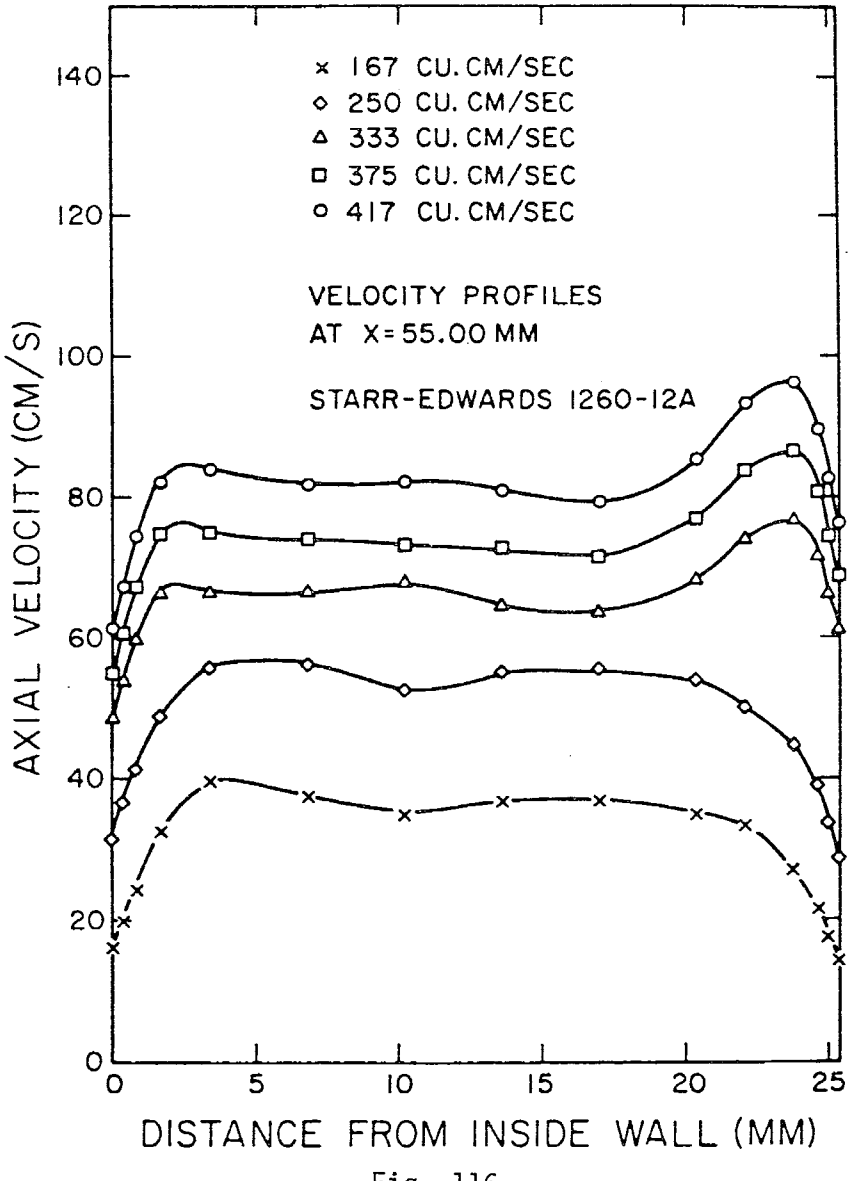

Fig. 116

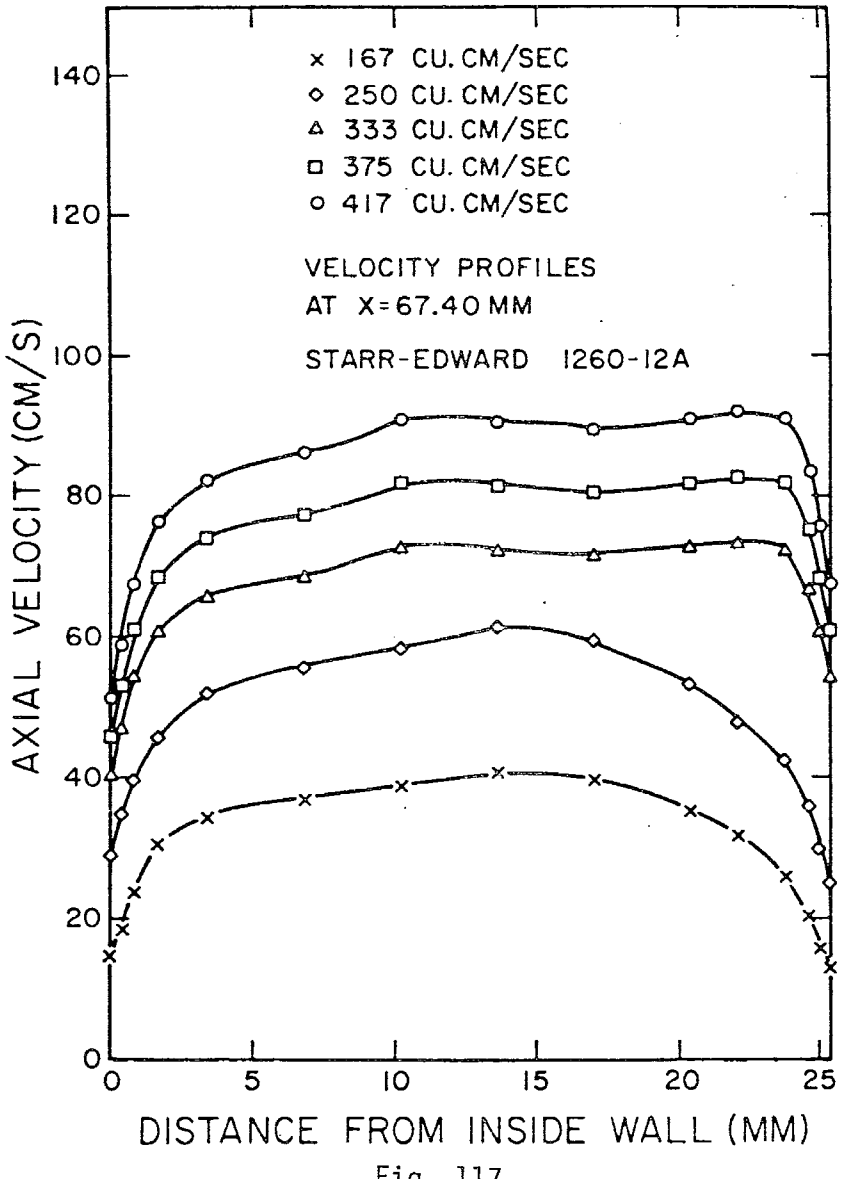

Fig. 117

Velocity profiles downstream from the Starr-Edwards 1260-12A valve

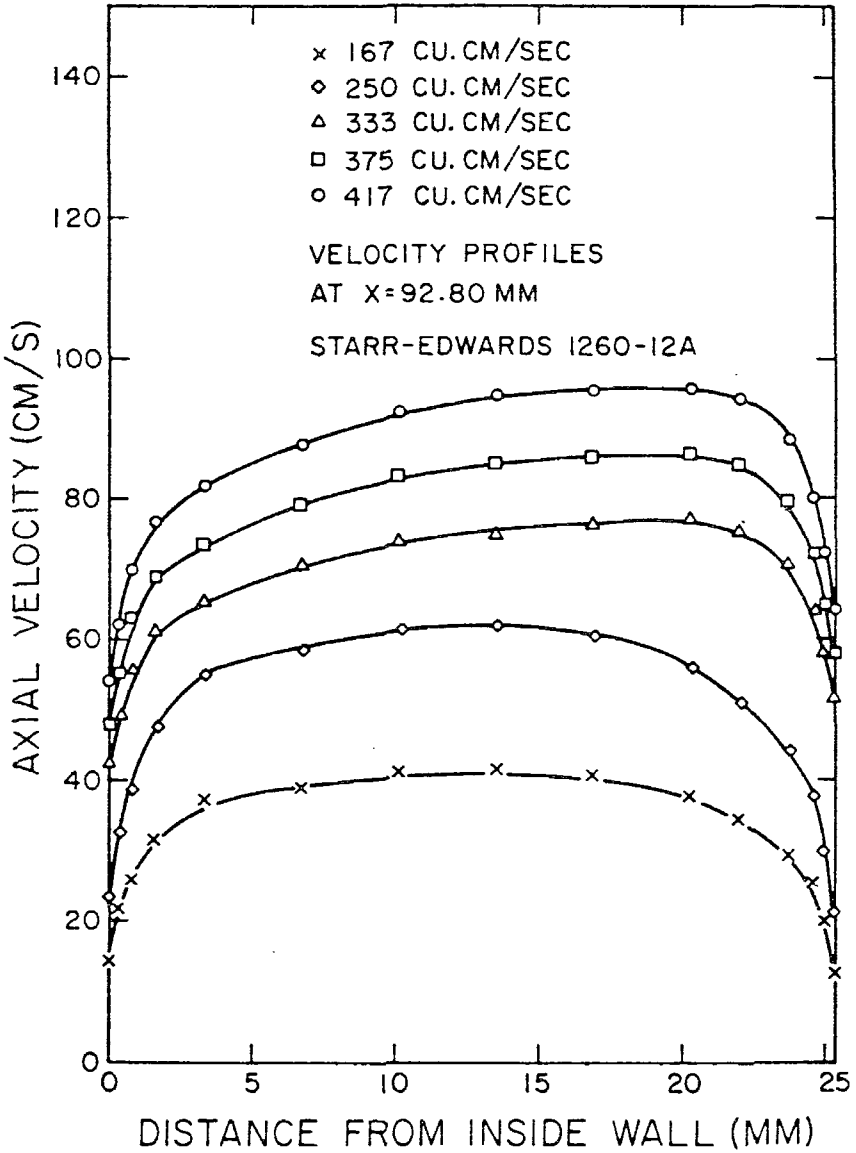

Fig. 118

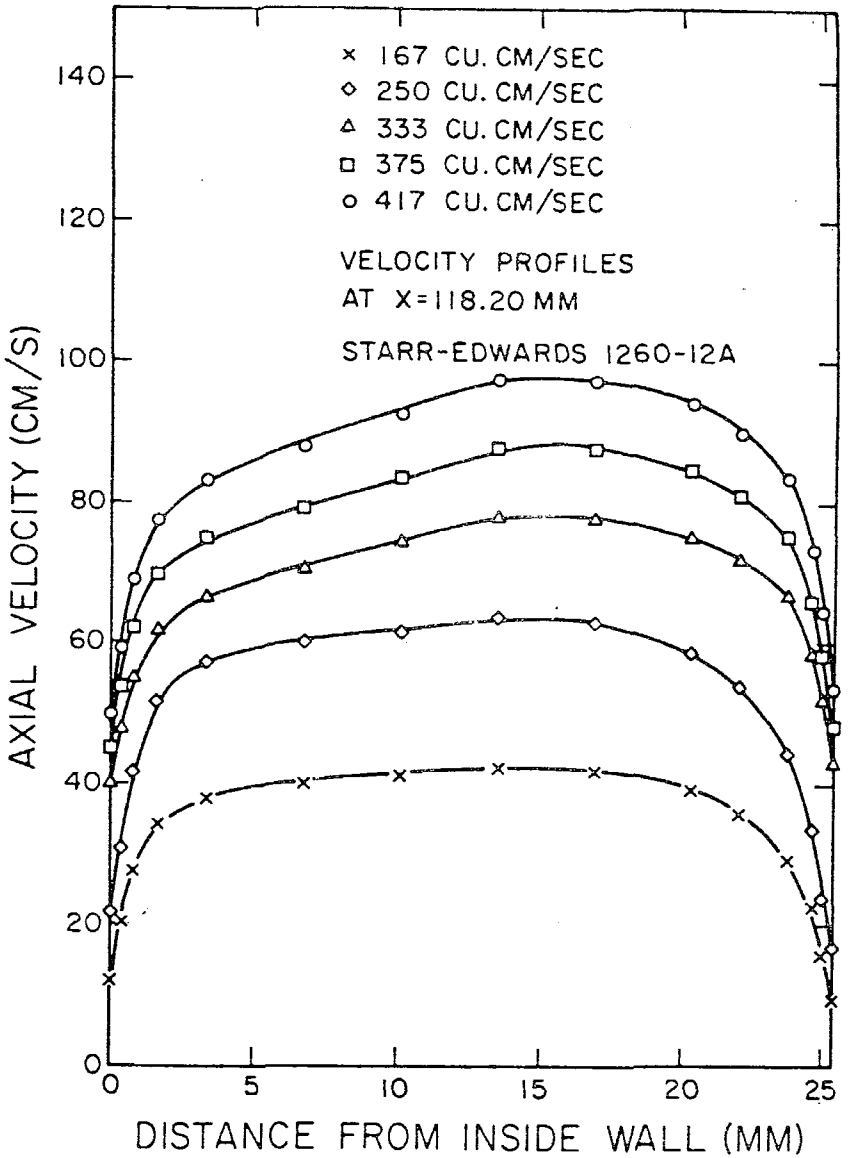

Fig. 119

Velocity profiles downstream from the Starr-Edwards 1260-12A valve

at a flow rate of 417 cm^3/sec and about 12 mm at a flow rate of 167 cm^3/sec. At the same downstream distance (X = 20.5 mm) from the tied ball valve the stagnation zone had a diameter of approximately 10 mm at a flow rate of 417 cm^3/sec and about 15 mm at a flow rate of 167 cm^3/sec. The stagnation zone has been qualitatively observed by others [14,16] but has not been quantitatively measured before. It is well known that areas of stagnation in the very near vicinity of a structure lead to the deposition of thrombus material on that structure. Therefore, the area of stagnation immediately downstream ($\sim$ 2 to 3 mm) from the apex of the cage could lead to thrombus formation at the location where the struts of the valve cross. Such thrombus formation has been clinically observed [9,13,72].

The fact that the oscillations of the ball decrease the size of the stagnation zone is illustrated by Figures 108 and 114. The oscillations, however, tend to increase the velocity of the fluid in a region close to the vessel wall (distance from inside wall $\leq$ 3.5 mm) as illustrated in Figures 108 and 114. It is therefore valid to assume that the velocities in the annular region between the vessel wall and the surface of the ball would increase as the speed of the oscillations of the ball increased. It was observed during the pressure drop experiments that, as the speed of the oscillations increased, the location of the oscillations moved from the top to the back of the cage. For example, with the ball oscillating at the top (apex) of the cage, at X = 22 mm the velocity very near the wall was about 145 cm/sec at a flow rate of 417 cm^3/sec; with the ball oscillating at the back of the cage, however, the velocity measured was about 190 cm/sec. As the

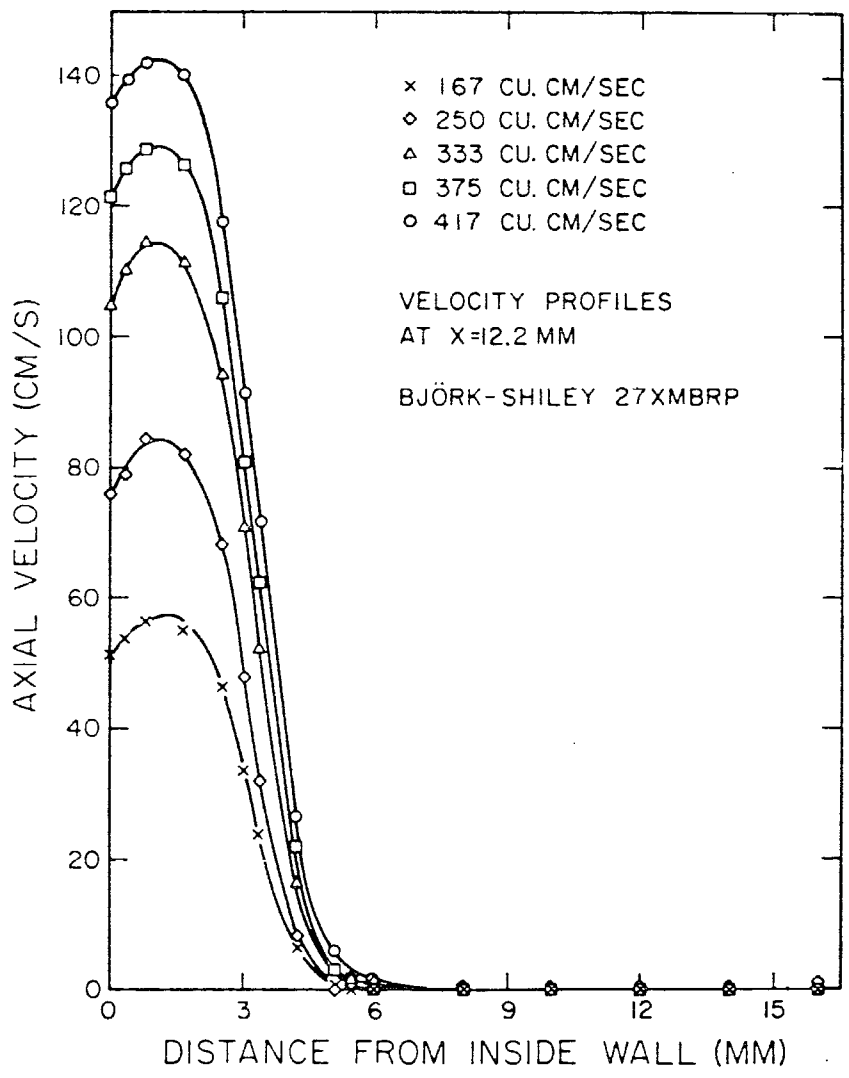

Fig. 120

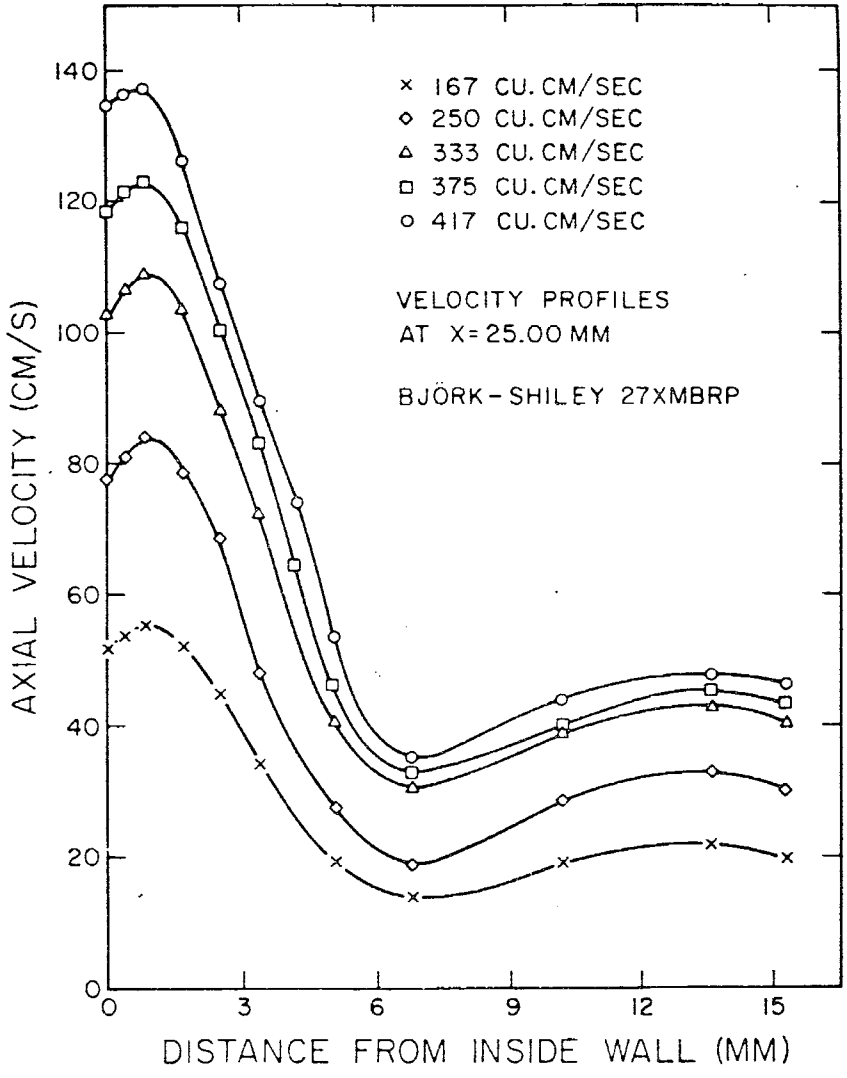

Fig. 121

Velocity profiles downstream from the Björk-Shiley 27XMBRP valve

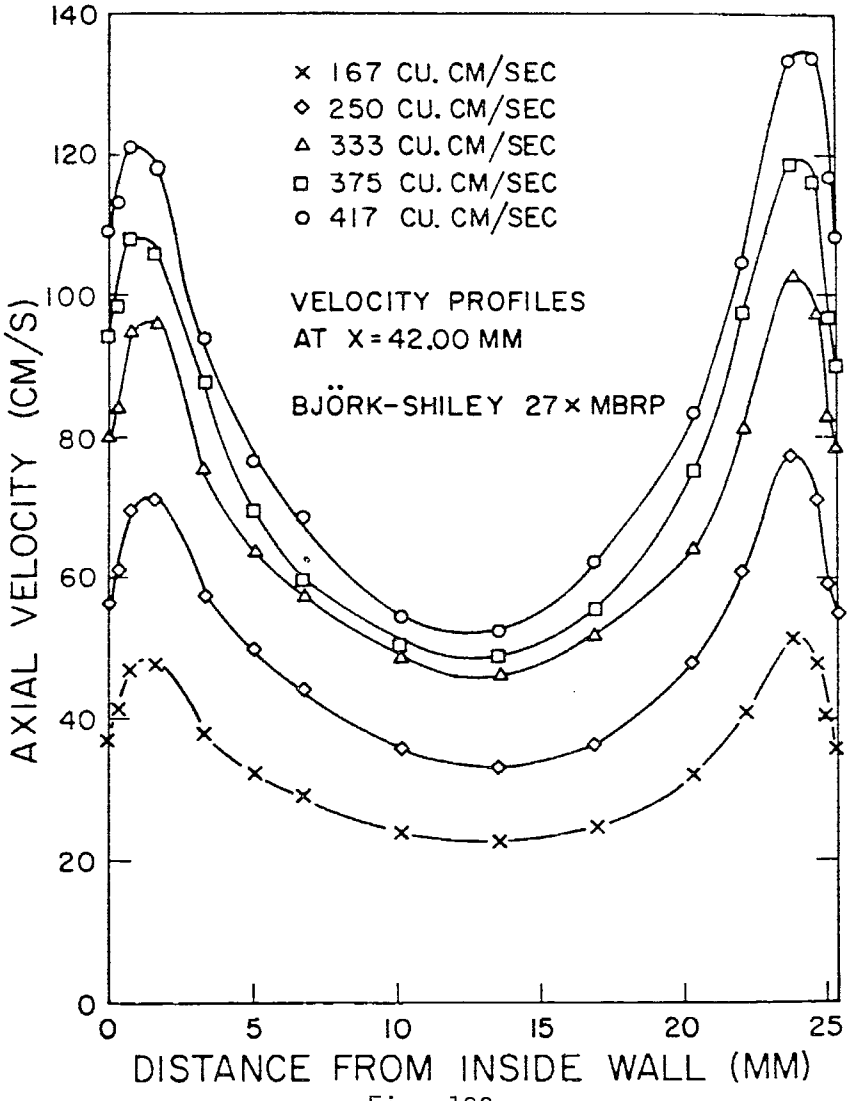

Fig. 122

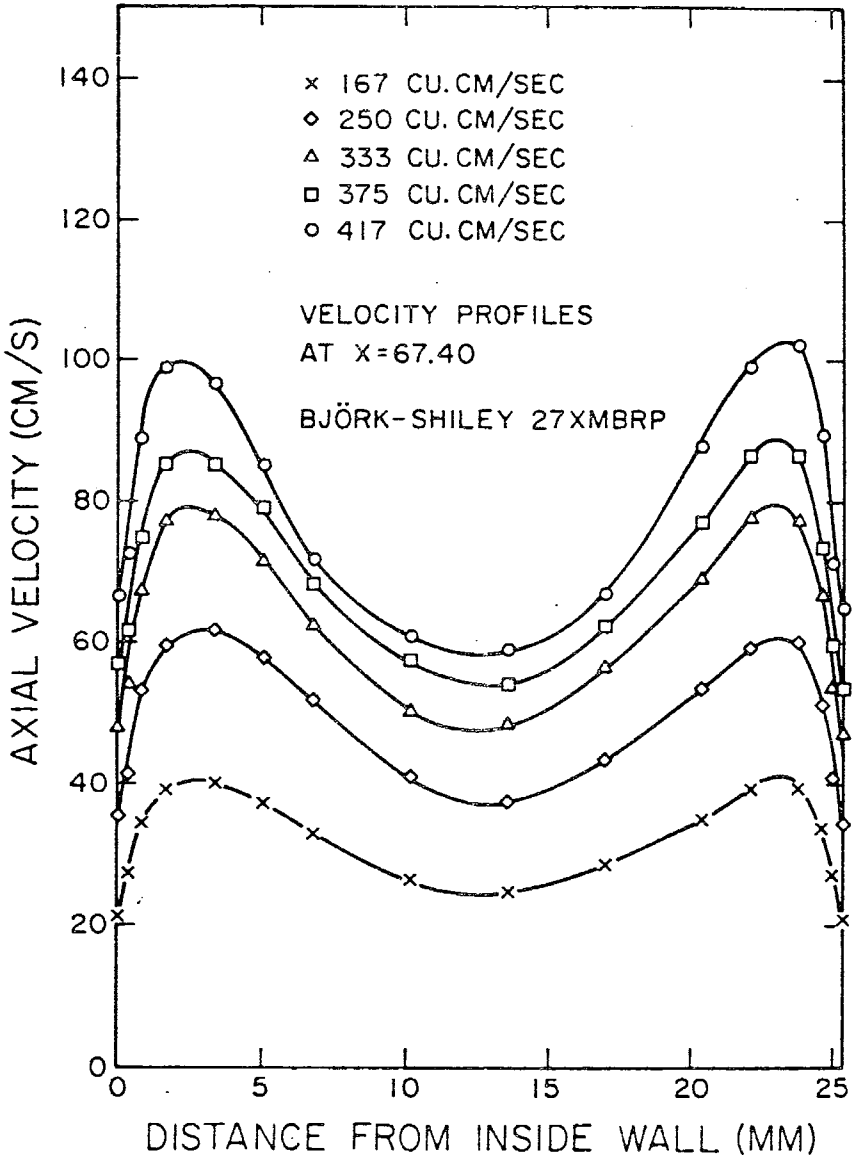

Fig. 123

Velocity profiles downstream from the Björk-Shiley 27XMBRP valve

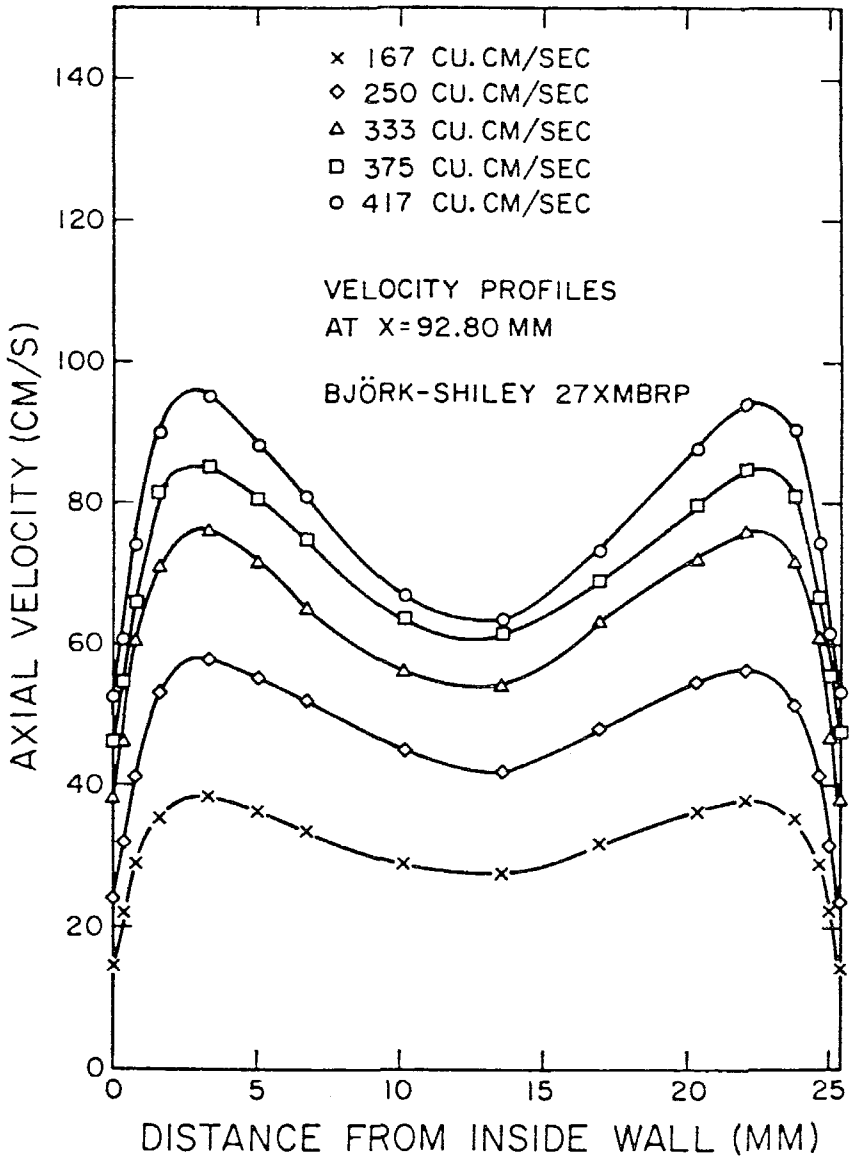

Fig. 124

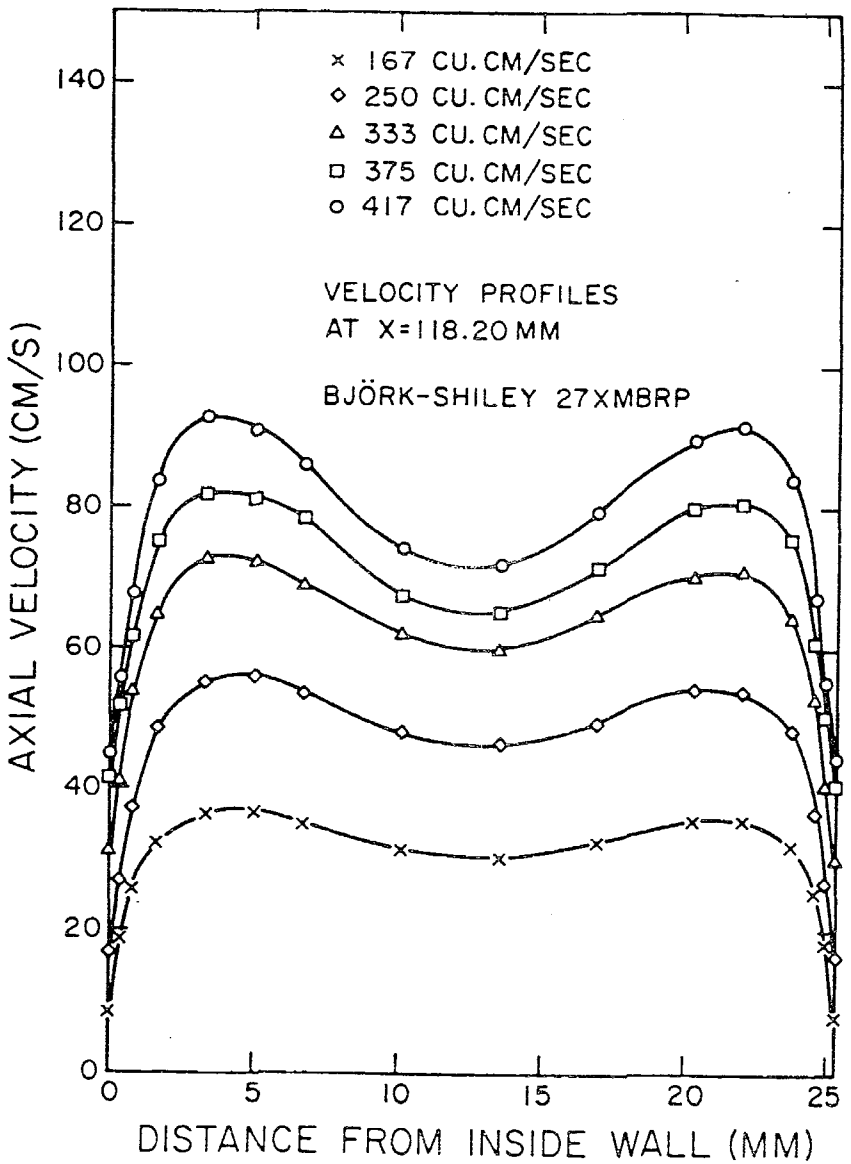

Fig. 125

Velocity profiles downstream from the Björk-Shiley 27XMBRP valve

velocities along the vessel wall in the sinus region increase, the wall shear in the very near vicinity of the valve also increases. Also, the increase in velocity in the annular region leads to increased shear (wall and bulk) in that region. Therefore, even though the oscillations of the ball lead to a smaller area of stagnation, the speed of the oscillations tend to increase the shear in the very near vicinity of the valves. As discussed in Chapter 4, as the location of oscillation of the ball moves from the top (apex) to the bottom of the cage, the pressure drop across the valve almost doubles. The pressure drop and velocity measurements indicate that to obtain optimum performance with the Starr-Edwards ball valves the ball should oscillate at the top (apex) of the cage. The pulsatile flow pressure drop experiments, however, suggest that the ball spends a majority of its time during systole at the middle of the cage.

6.2.3 Björk-Shiley 27XMBRP

The velocity profiles obtained with the Björk-Shiley valve are shown in Figures 120 through 125. The Björk-Shiley valve creates a large zone of stagnation ($\sim$ 20 mm wide in the Y direction) in the very close vicinity of the disc, and that is well illustrated in Figure 120. In this region the velocities oscillate between $\pm$2 cm/sec, which indicates the existence of small recirculation cells. At all four locations of measurements in section 'C' of the flow channel the velocity profiles at all flow rates studied exhibit the velocity defect phenomenon. Even at X = 118.2 mm (Fig. 125), none of the profiles have returned to a turbulent pipe flow profile. Therefore, the effects of

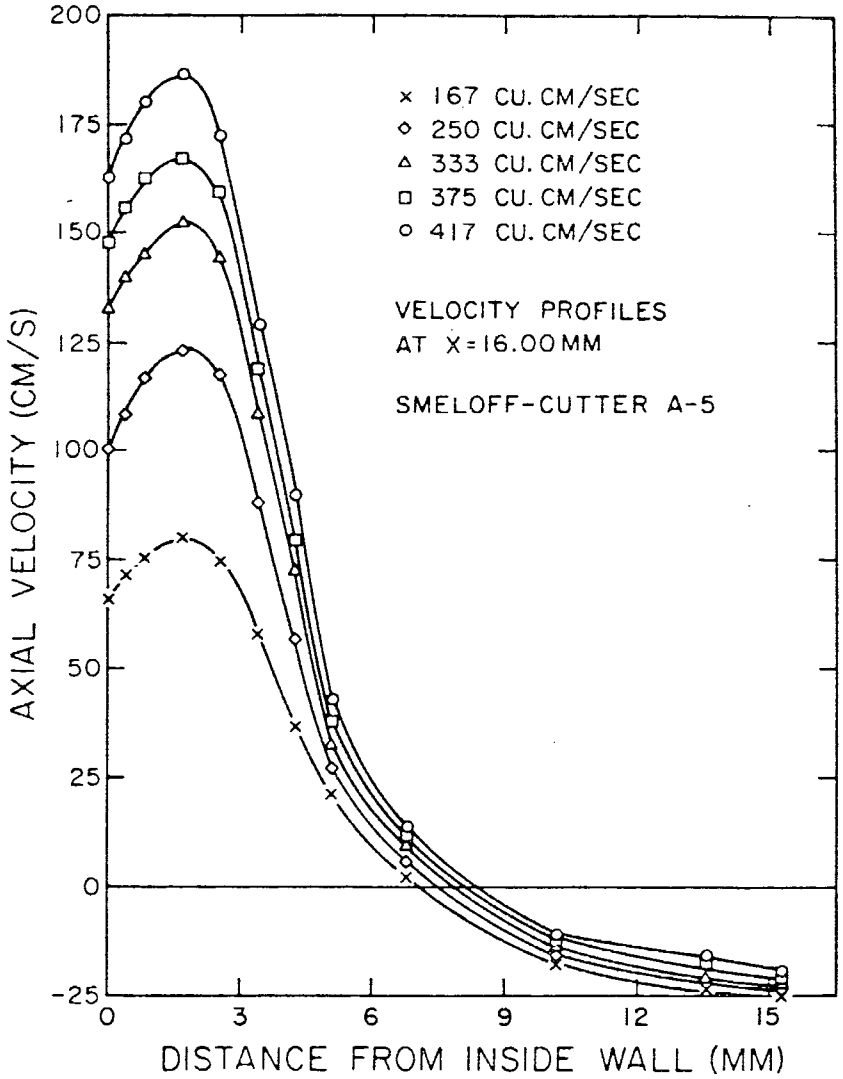

Fig. 126

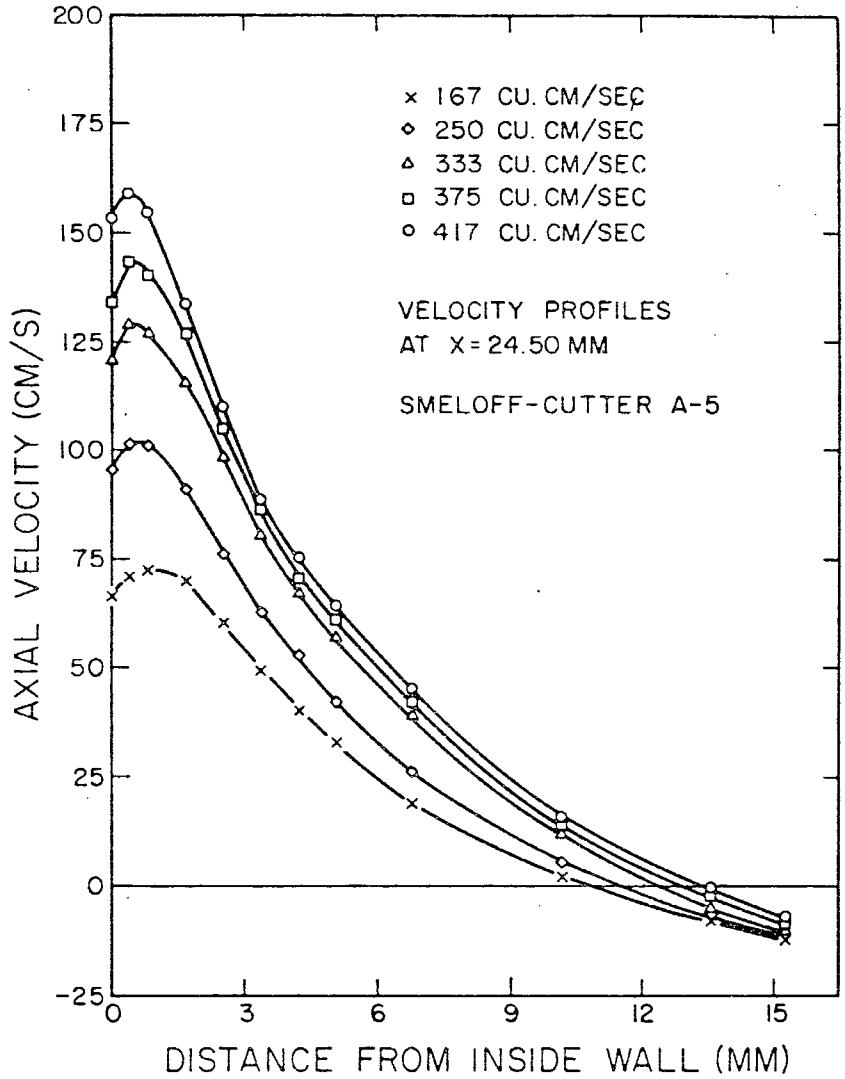

Fig. 127

Velocity profiles downstream from the Smeloff-Cutter A5 valve

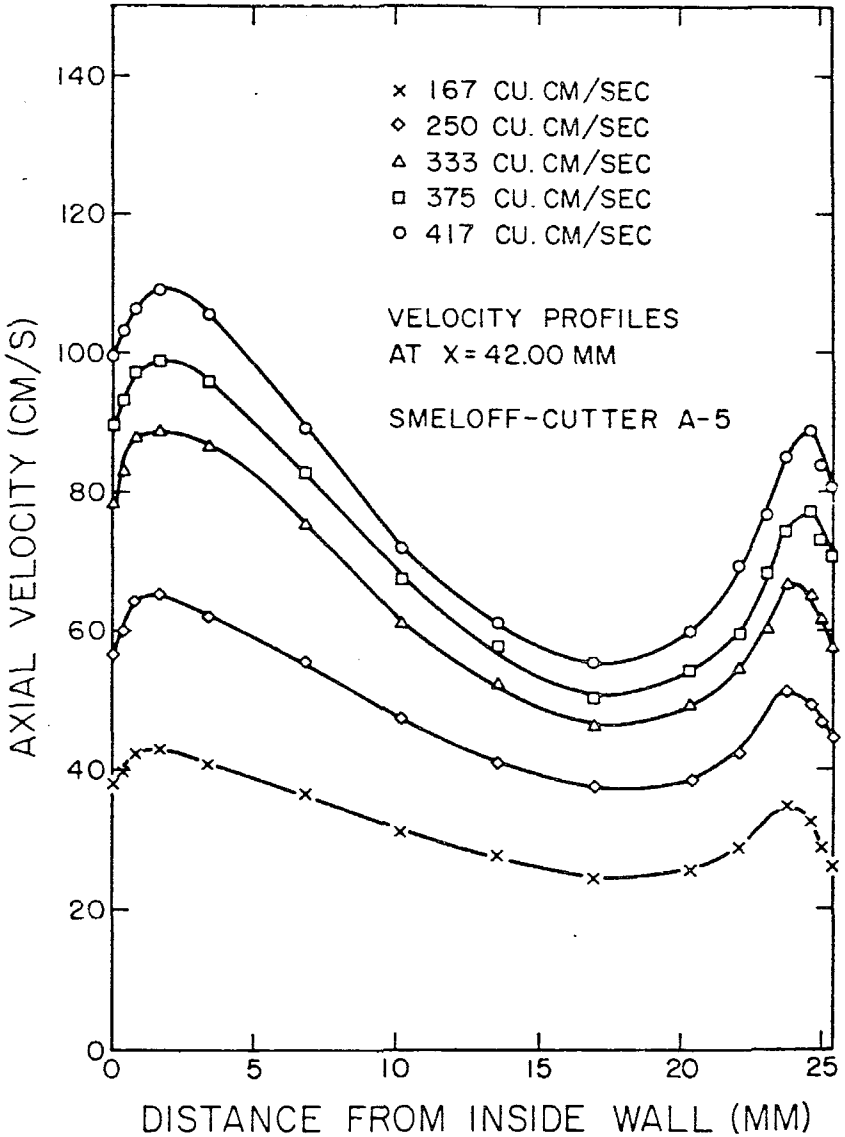

Fig. 128

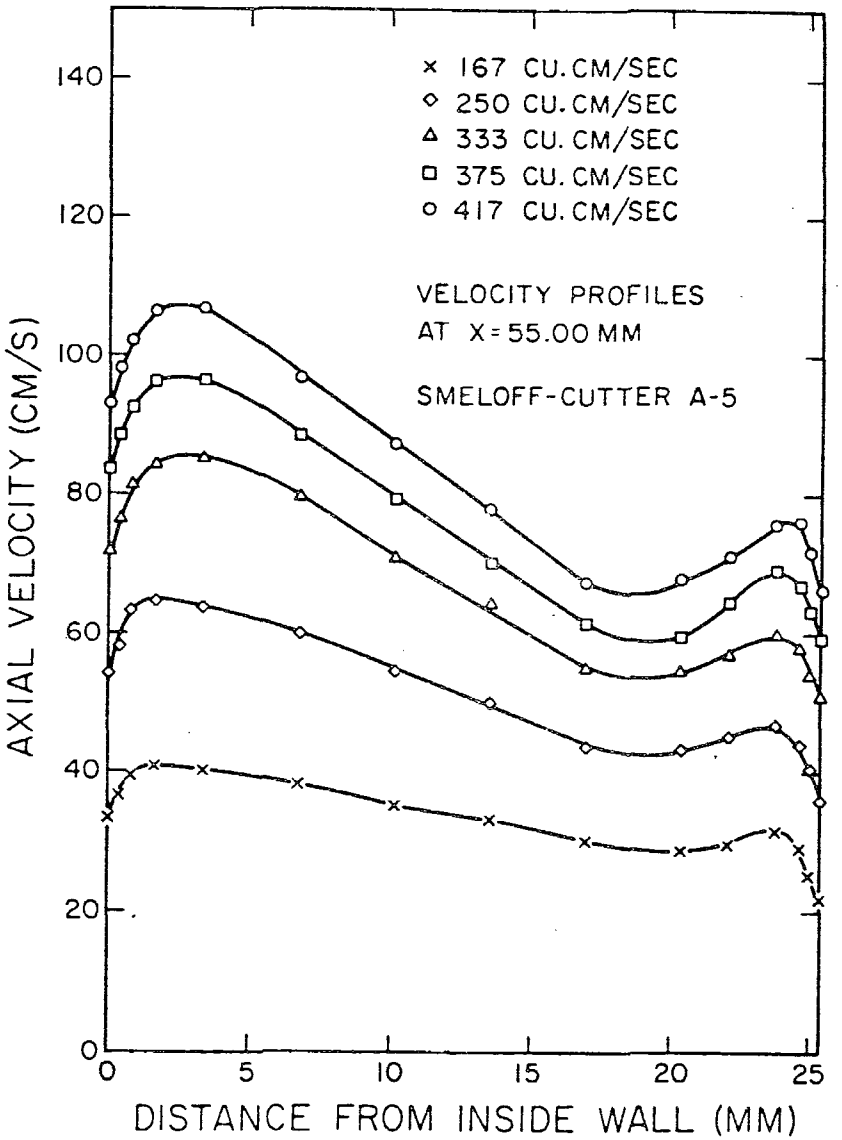

Fig. 129

Velocity profiles downstream from the Smeloff-Cutter A5 valve

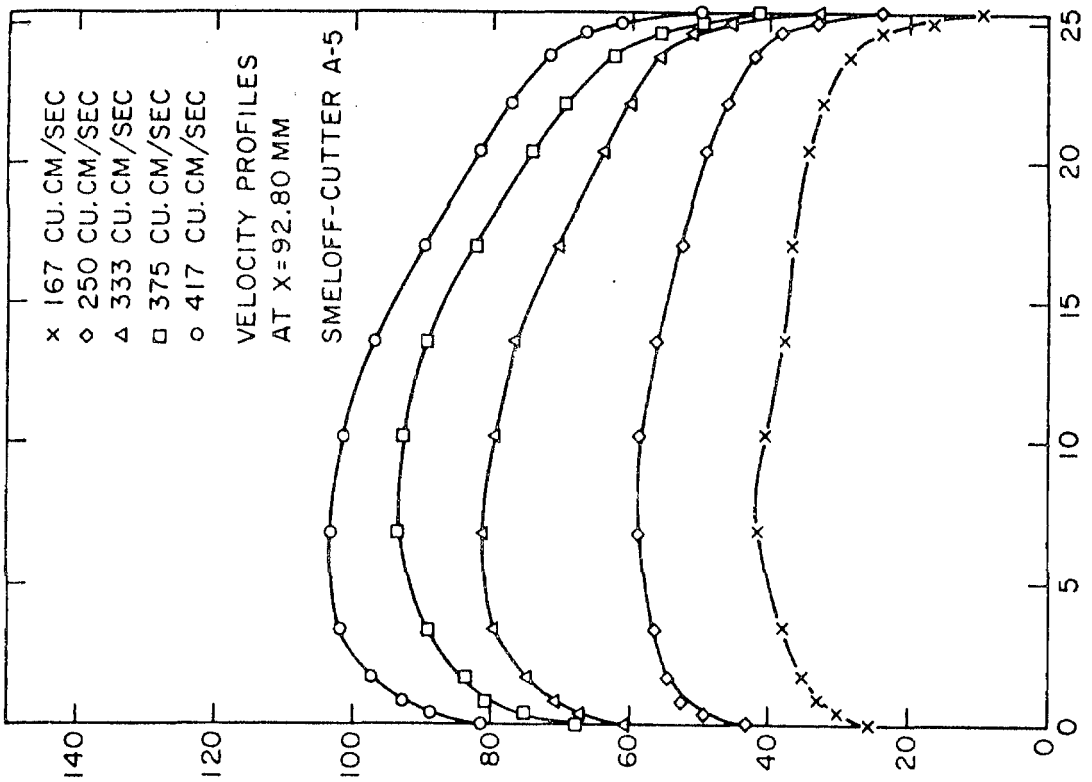

Fig. 131

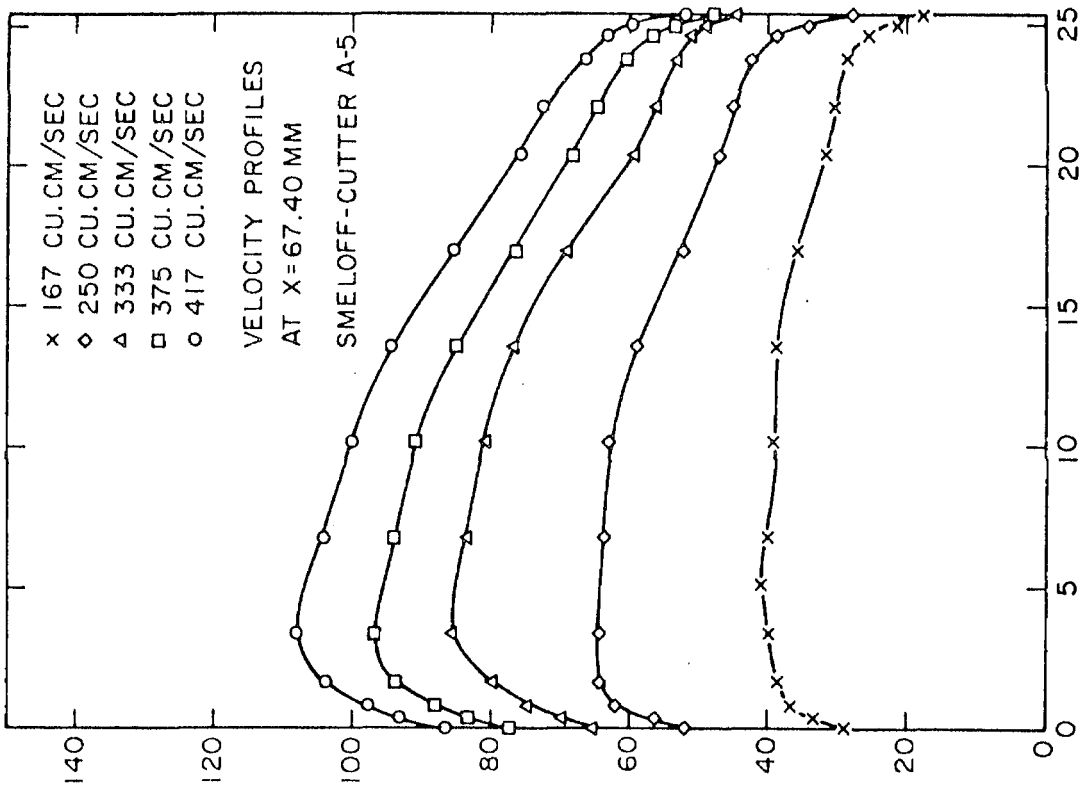

Fig. 130

Velocity profiles downstream from the Smeloff-Cutter A5 valve

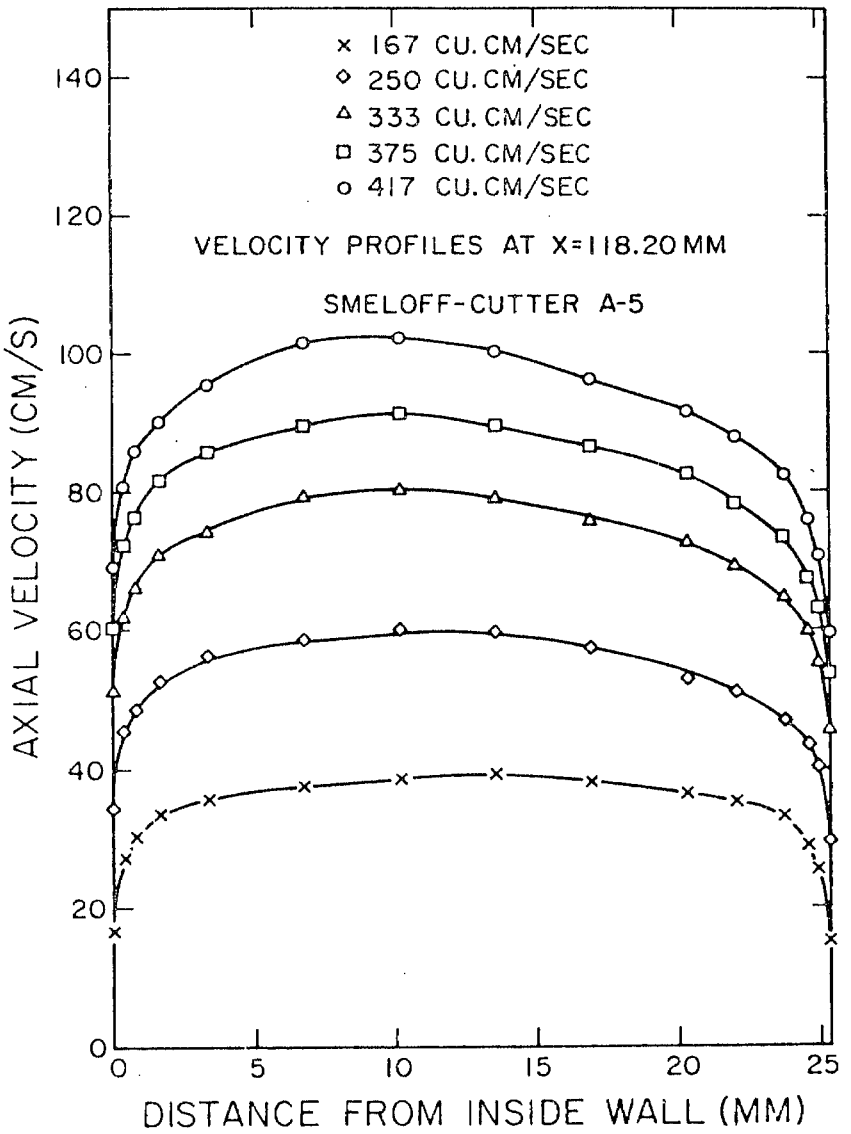

Fig. 132. Velocity profiles downstream from the Smeloff-Cutter A5 valve

the stagnation zone created by the Björk-Shiley valve could be observed even 118 mm downstream from the valve.

The stagnation zone created immediately downstream ($\sim$ 1 mm) from the disc indicates that the Björk-Shiley valve will be prone to thrombus formation. The effects of the stagnation zone on thrombus formation and its complications relating to the Björk-Shiley aortic prosthesis are discussed in detail in Chapter 7.

6.2.4 Smeloff-Cutter A5

Figures 126 through 132 illustrate the velocity profiles obtained with the Smeloff-Cutter A5 ball valve. At the flow rates studied the ball rotated somewhat at the top of the cage, but this rotation did not affect the velocity measurements as did the oscillations of the ball in the Starr-Edwards ball valve. As shown in Figure 126, the velocities near the top of the cage were negative and on the order of -10 to -25 cm/sec. The measurements at location X = 16 mm were about 2 mm downstream from the top of the cage.

6.2.5 Cooley-Cutter A25

The results obtained with the Cooley-Cutter biconical (diamond shaped) disc valve are shown in Figures 133 through 139. The Cooley-Cutter A25 valve has a sewing ring diameter of 25 to 26 mm. The next larger size available at present (A28) has a sewing ring diameter of 28 to 29 mm. It was found that the A28 was a little too large to fit into the heart valve chamber used in this study. It was therefore decided to study the Cooley-Cutter A25 valve with other designs of aortic prostheses having sewing ring diameters of 26 to 27 mm. Under

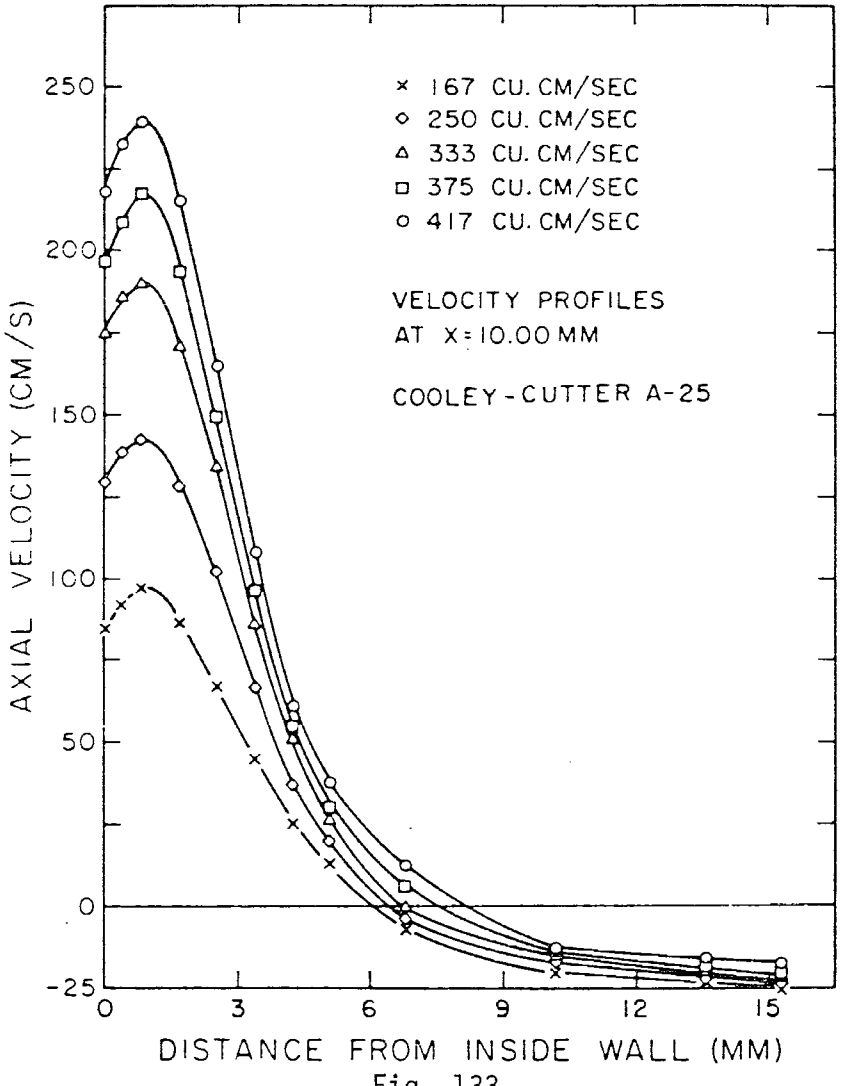

Fig. 133

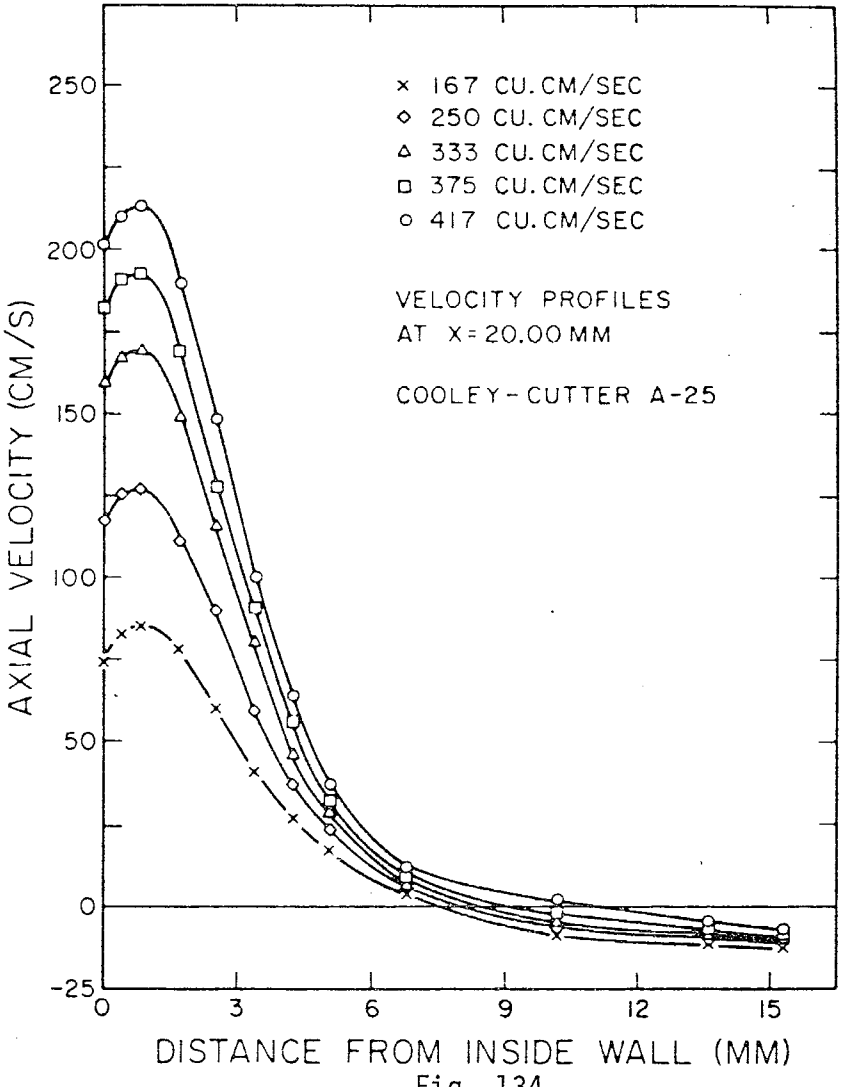

Fig. 134

Velocity profiles downstream from the Cooley-Cutter A25 valve

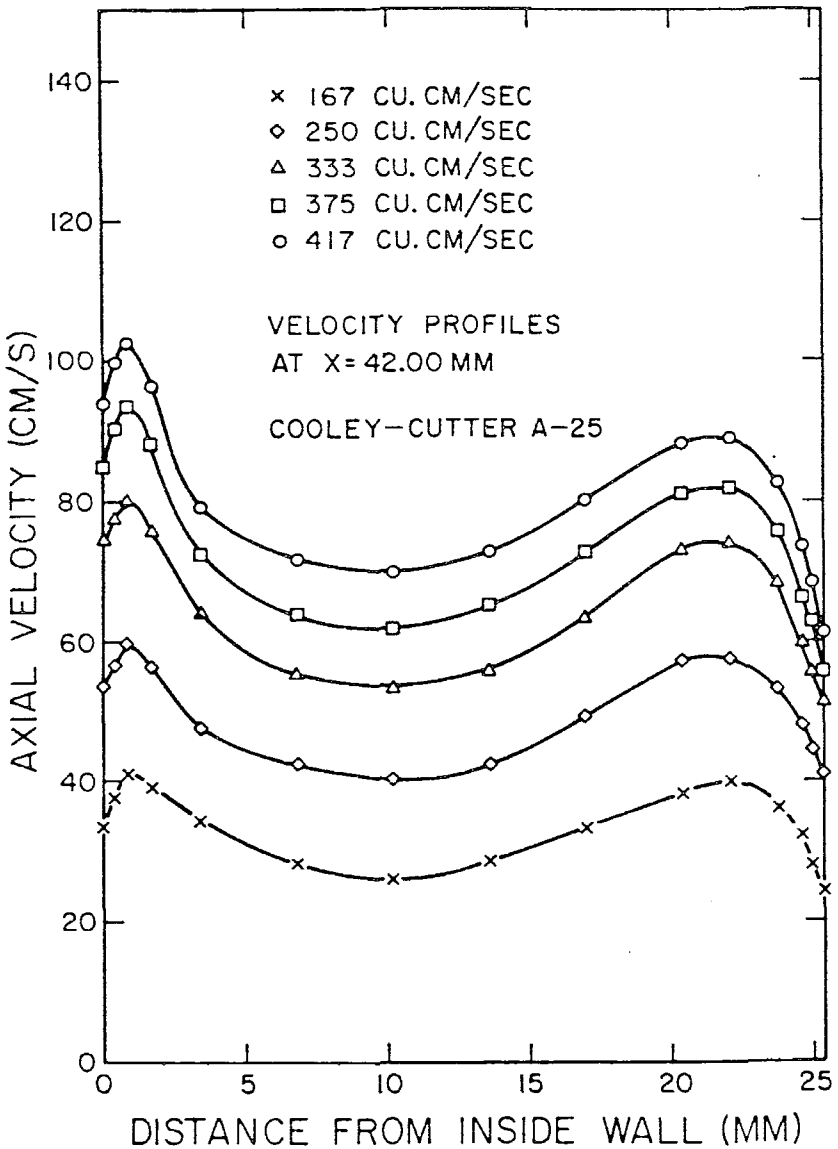

Fig. 135

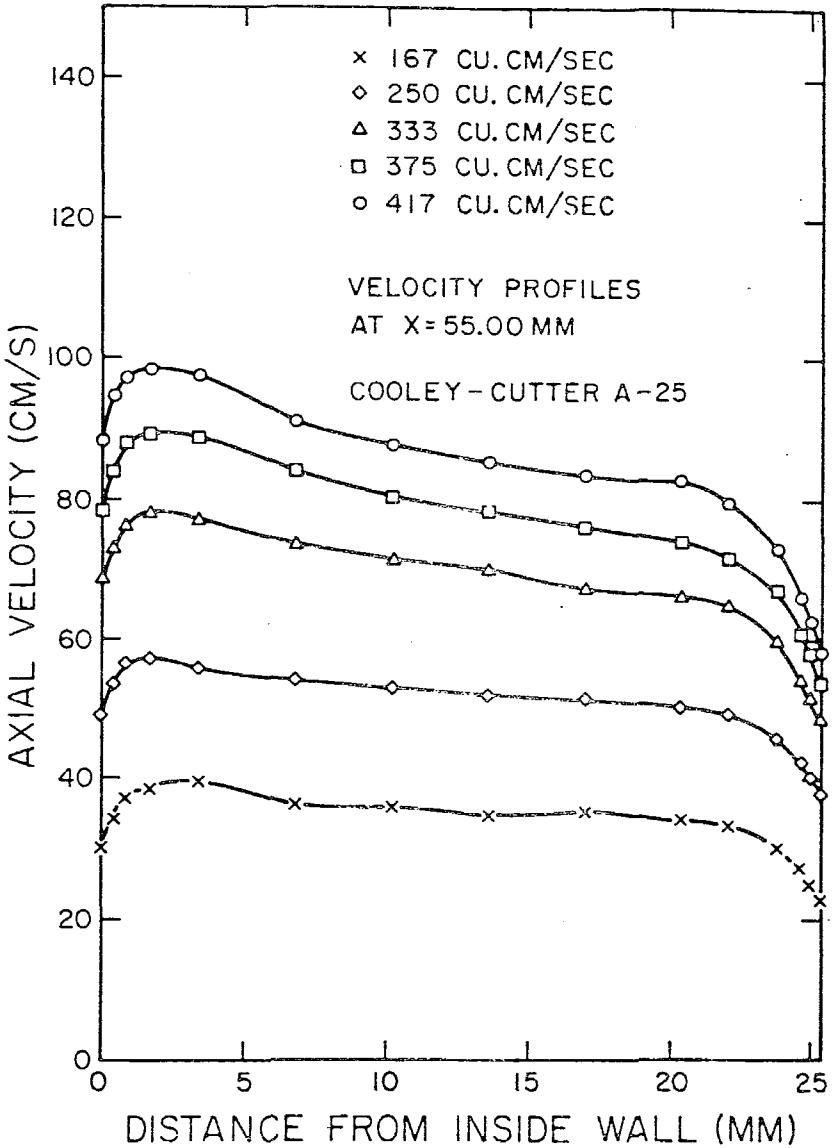

Fig. 136

Velocity profiles downstream from the Cooley-Cutter A25 valve

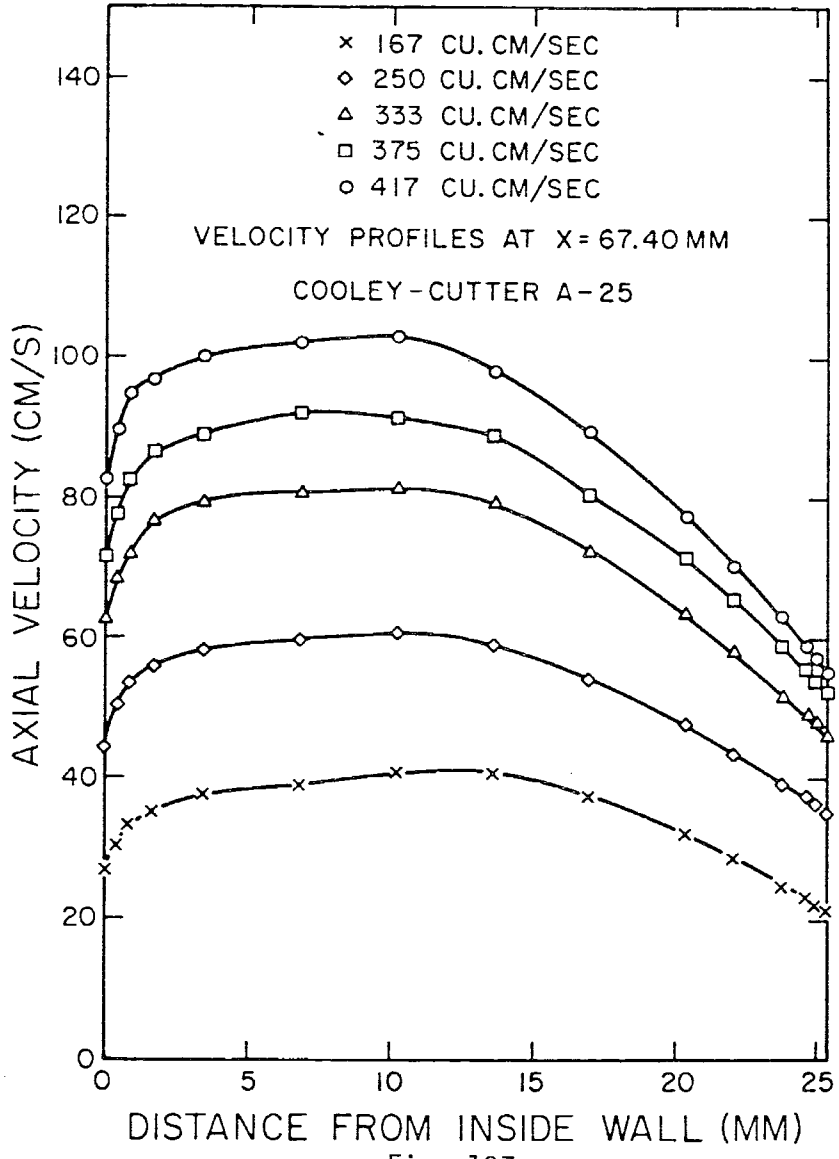

Fig. 137

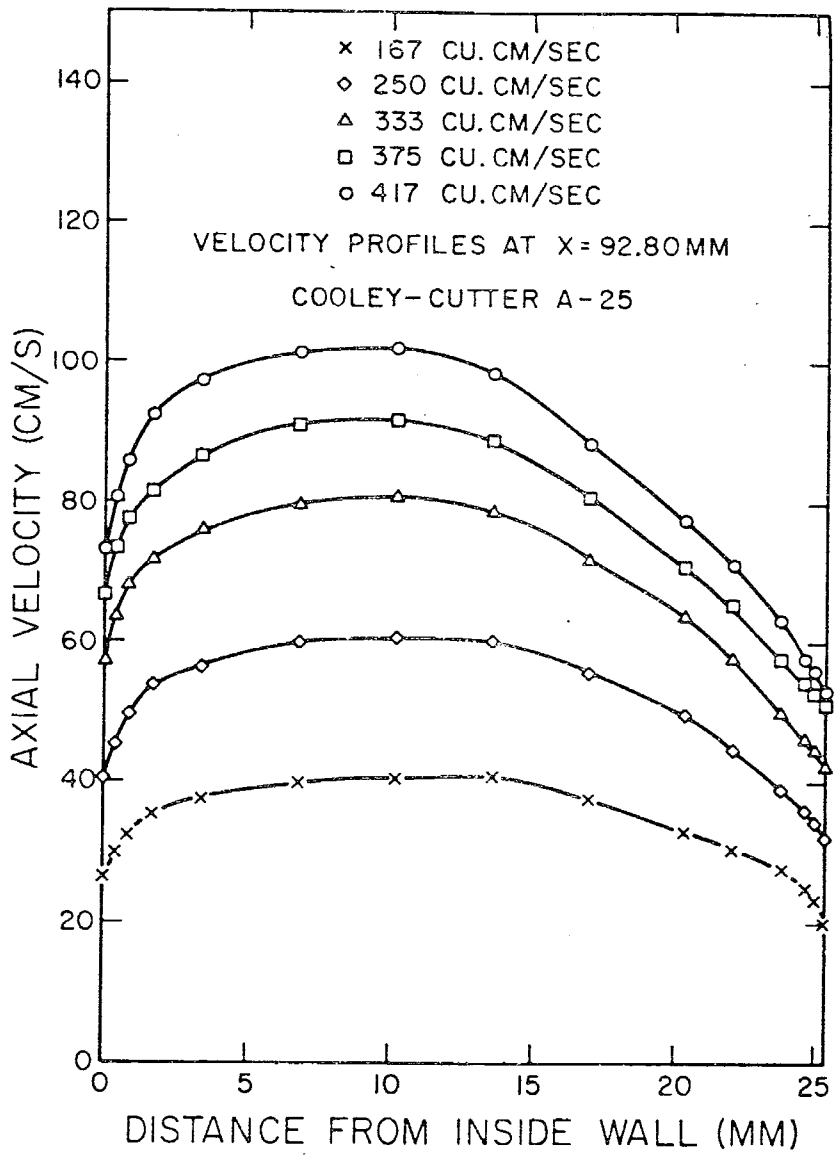

Fig. 138

Velocity profiles downstream from the Cooley-Cutter A25 valve

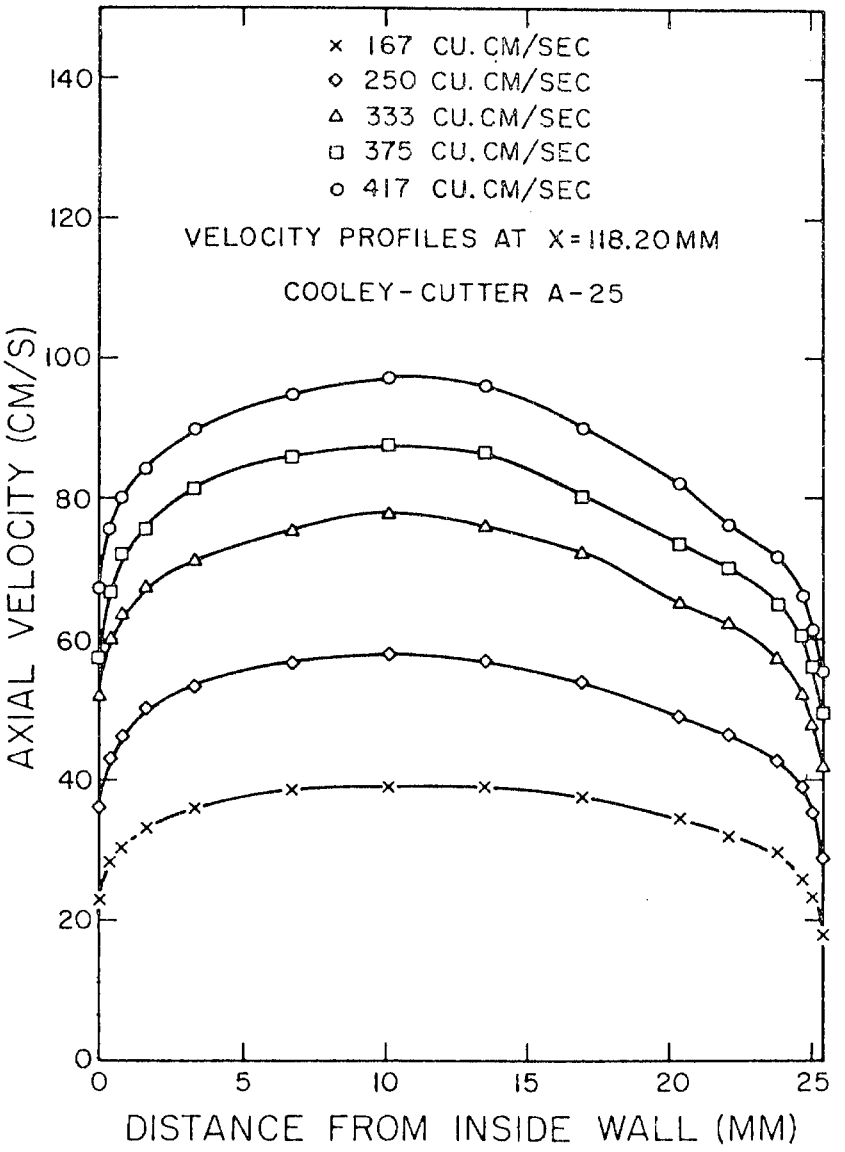

Fig. 139. Velocity profiles downstream from the Cooley-Cutter A25 valve

the steady-flow conditions of this study, the poppet of this valve did not oscillate but it did rotate very slowly. The shear stresses measured on the walls in the sinus area indicate that this valve has larger wall shear stresses compared with the previous three aortic valves in the sinus region (section 'B') of the flow channel. This valve also has negative velocities on the order of -10 to -25 cm/sec near the top of its cage. The location X = 10 mm was about 2 mm downstream from the top of the valve cage (Fig. 133).

Both the Smeloff-Cutter A5 valve and the Cooley-Cutter A25 valve (Figs. 126 and 133) show that in the very near vicinity of the tops of their cages there exist relatively larger (-10 cm/sec to -25 cm/sec) negative velocities which prevent the formation of a zone of stagnation in this area. This phenomenon is probably due to the design of the open cage structure of these two valves. The open cage structure seems to have favorable fluid-mechanical condition compared with the structure of the closed cage valves. Due to the negative velocities (backwash effect) near the top of the struts on the aortic side, deposition of thrombotic or other materials on the struts on the poppet of the prosthesis will probably be prevented to a large extent. A majority of the Smeloff-Cutter ball valves recovered at autopsy at the L.A. County-USC Medical Center exhibited no deposition of thrombotic material on the struts on the aortic side or on the poppet surface. These findings agree with the backwash effect observed in the in vitro steady flow experiments. The qualitative and quantitative measurements of these negative velocities has not been reported before in the literature by other workers.

As the flow develops downstream of the Smeloff-Cutter (see Figs. 126, 127 and 128) and Cooley-Cutter (see Figs. 133, 134 and 135) valves there will be a downstream location at which a stagnation zone exists. The stagnation zone will be confined approximately towards the center of the flow channel. Experimental measurements indicated that the stagnation zone of the Smeloff-Cutter valve existed at about X = 28 mm and was approximately 6 to 9 mm in diameter, while that of the Cooley-Cutter valve existed at about X = 24 mm and was approximately 8 to 11 mm in diameter over a flow rate range of 417 to 167 cm^3/sec. The stagnation zones created by the Smeloff-Cutter and Cooley-Cutter prostheses are probably, however, too far downstream of the superstructure of the valves for any thrombotic material formed in the stagnant zones to deposit on the valves. But a stagnation zone does exist in the downstream vicinity of both the Smeloff-Cutter and Cooley-Cutter valves which could encourage thrombus formation and could lead to thromboembolic complications. A comparison of the velocity profiles of the Smeloff-Cutter and Cooley-Cutter valves at X = 55 mm (Figs. 129 and 136) seems to indicate that the profiles of the Cooley-Cutter valve tend to return to turbulent pipe flow profiles somewhat faster than the profiles of the Smeloff-Cutter valve.

6.2.6 Starr-Edwards 6520-1M

The Starr-Edwards 6520-1M is a flat disc type valve which is at present used only in the mitral position. In the mid-1960's, however, a valve of this design was used in the aortic position. Therefore, as a comparison with the existing aortic prostheses, velocity measurements

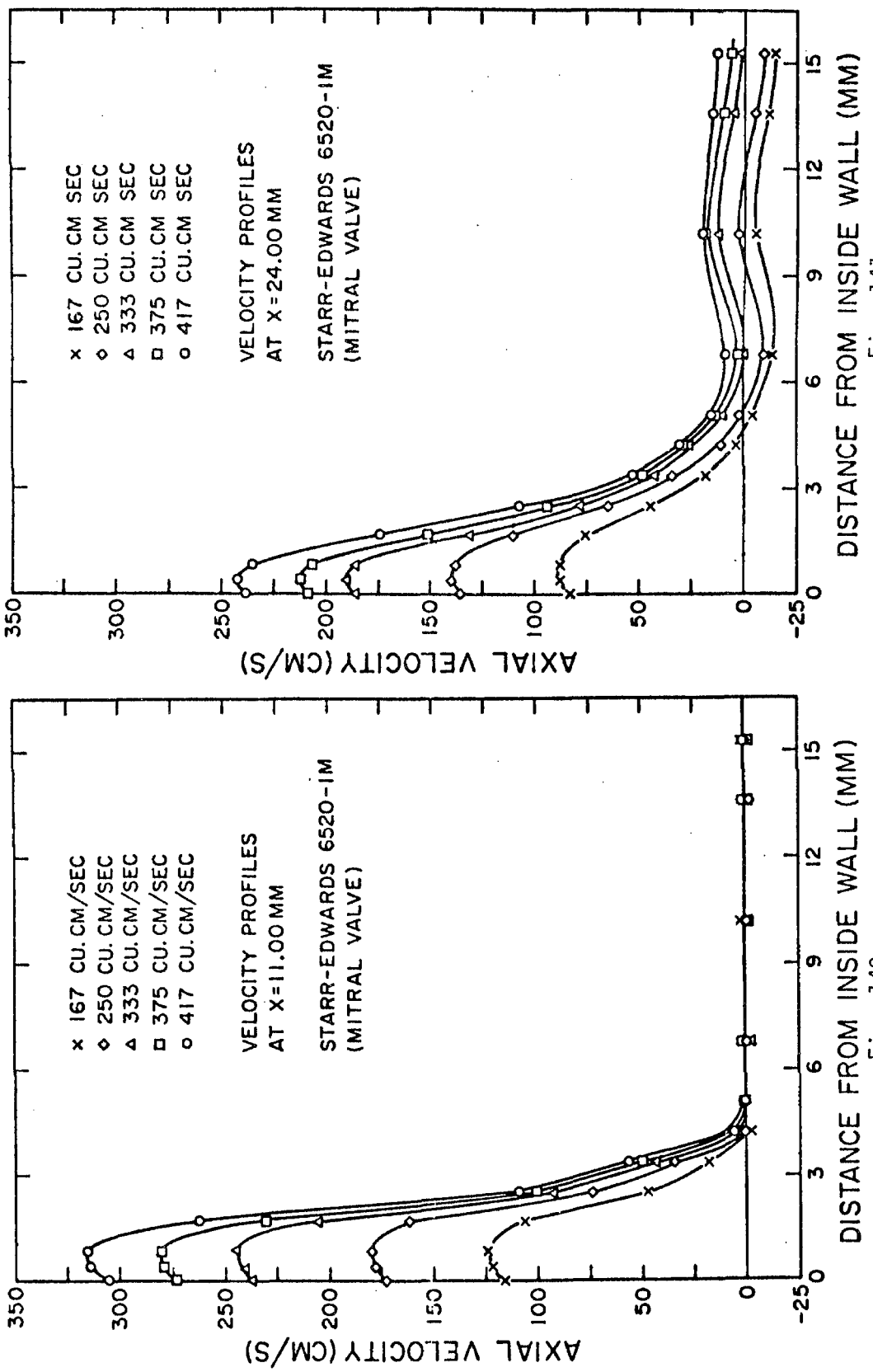

Fig. 140

Fig. 141

Velocity profiles downstream from the Starr-Edwards 6520-1M mitral valve

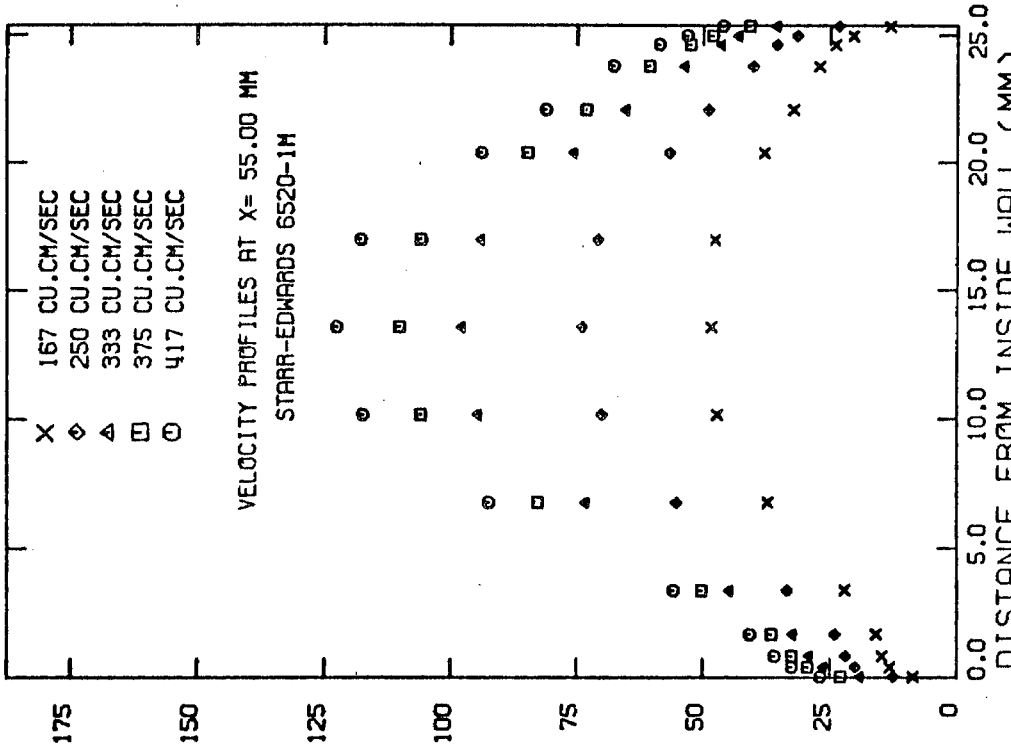

Fig. 143

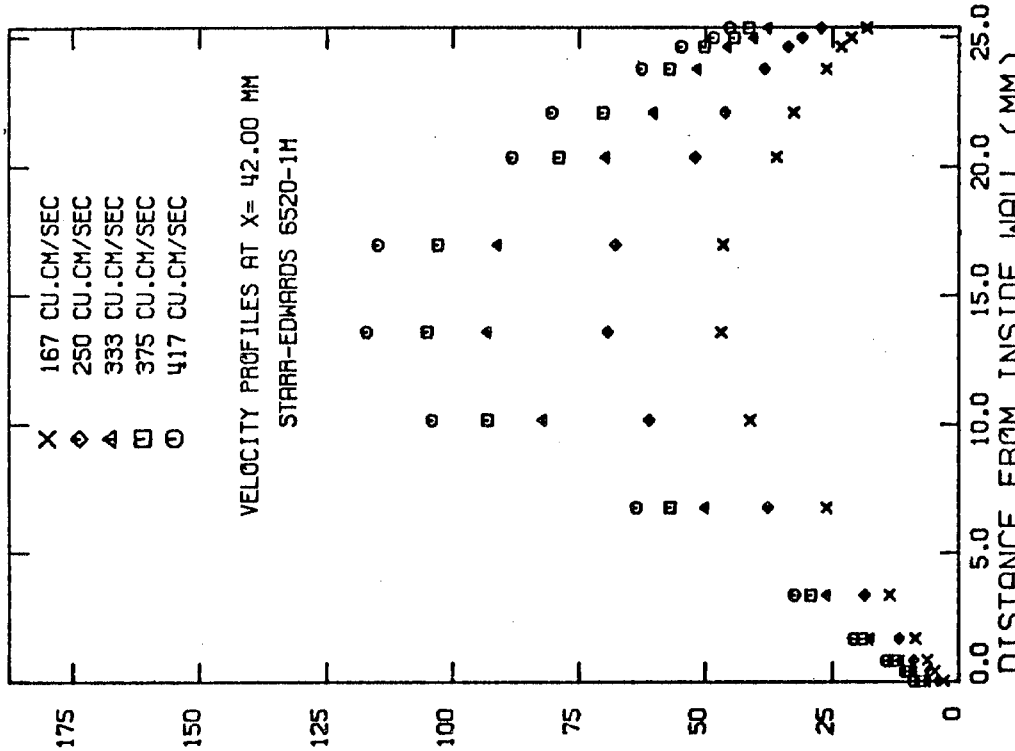

Fig. 142

Velocity profiles downstream from the Starr-Edwards 6520-1M mitral valve

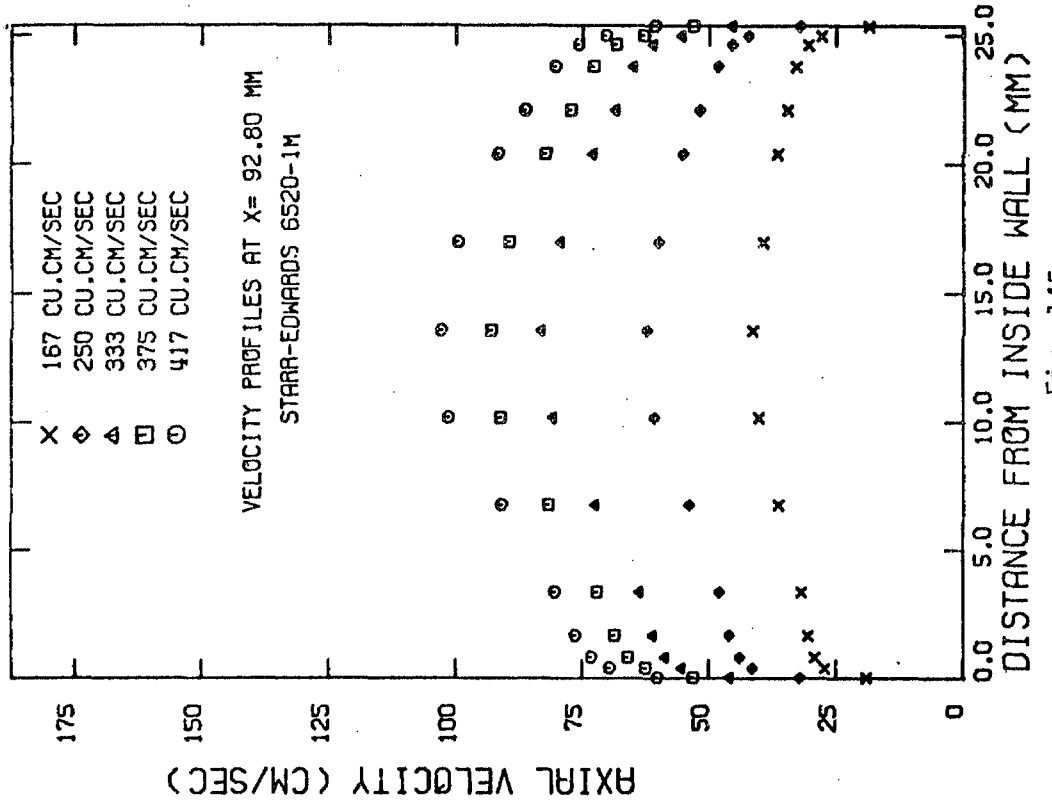

Fig. 145

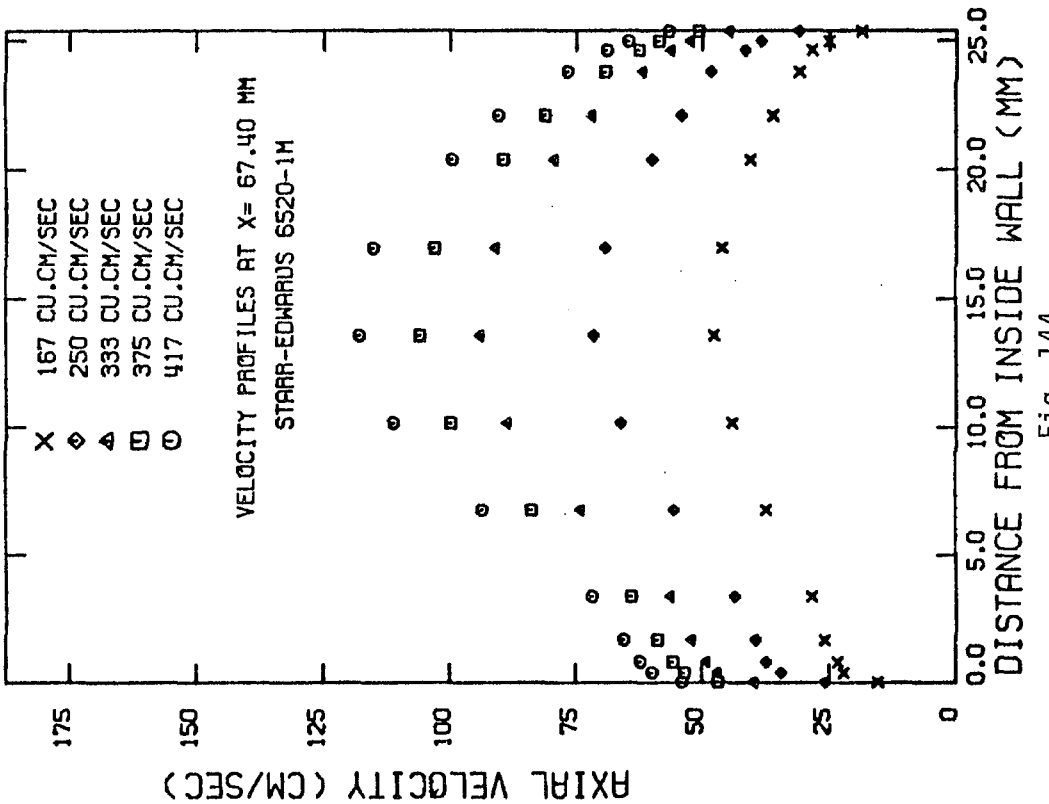

Fig. 144

Velocity profiles downstream from the Starr-Edwards 6520-1M mitral valve

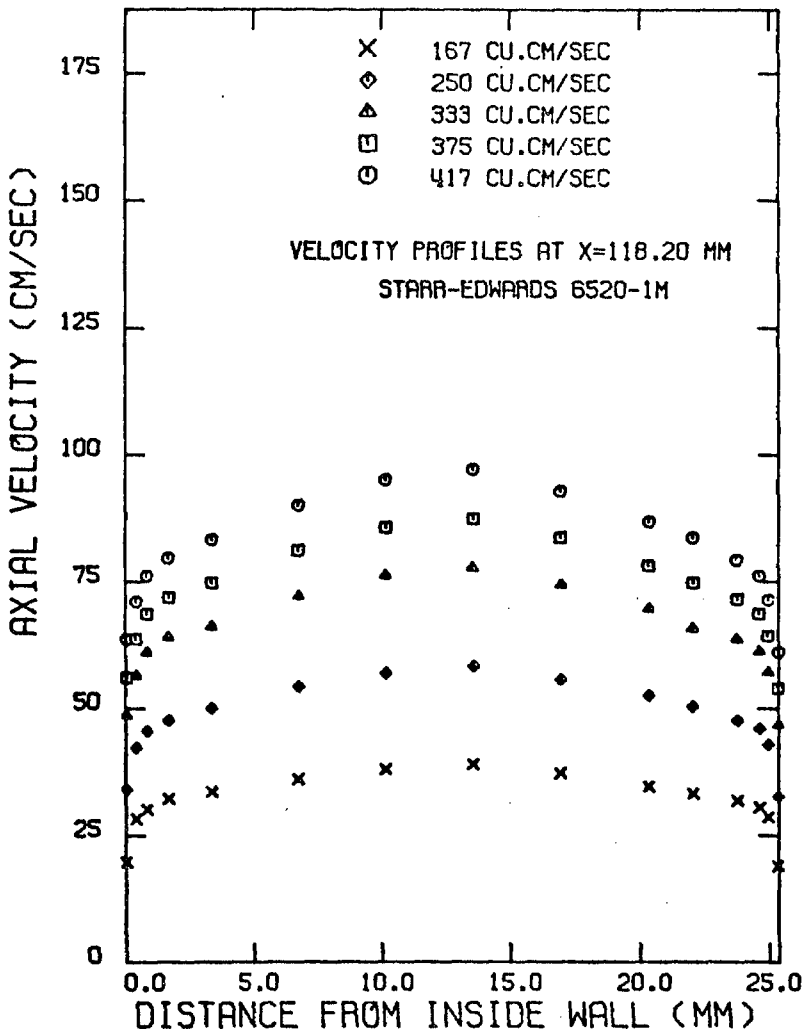

Fig. 146. Velocity profiles downstream from the Starr-Edwards 6520-1M mitral valve

were made with this mitral valve. Figures 140 through 146 show the velocity profiles obtained downstream of the Starr-Edwards 6520-1M mitral valve (26 mm sewing ring diameter). This valve created a large stagnation zone in the very near proximity of its disc (see Fig. 140) similar in size to that created by the Björk-Shiley tilting disc prosthesis. The flow further downstream, however, develops rapidly and by the distance X = 42.0 mm the velocity profiles had lost their velocity defect at the center of the channel. Figure 142, however, indicates that an area of low to stagnant flow has developed along the inside wall of the flow channel. The maximum velocities very close to the inside wall (i.e., within 0.5 mm) were on the order of 10 cm/sec, while at a similar distance from the outside wall velocities on the order of 50 cm/sec were observed. By a downstream distance of at least X = 92.8 mm the profiles have returned to turbulent pipe flow profiles even though the velocities along the walls are much higher than those observed under normal pipe flow conditions. Therefore, the effects of the stagnation zone created by the mitral disc valve disappear faster than the effects created by the tilting disc valve. Of all the prostheses tested, the Starr-Edwards 6520-1M valve created the largest wall shear stresses in the sinus region as shown by Tables 12 and 13.

6.3 Turbulent Intensity Measurements

Turbulent intensity level measurements I_x, as defined by equation (46) in the axial direction were made with all the valves used in this study. It should be noted that a detailed experimental study of the turbulent intensities was not made. Measurements were made to obtain

Table 12. Experimentally Measured Wall Shear Stresses at a Flow Rate of 417 cm^3/sec

Name of Valve	X (mm)	τ_{wi}* dynes/cm^2	τ_{wo}† dynes/cm^2
Lucite Disc	22.0	62	60
	118.2	51	51
Björk-Shiley 27XMBRP	12.0	1400	1379
	24.0	1385	1342
	118.2	463	461
Starr-Edwards 1260-12A	22.0	1510	1501
(ball tied)	32.0	1432	1401
	118.2	594	533
Starr-Edwards 1260-12A	22.0	1666	1751
(ball untied)	32.0	1598	1669
	118.2	584	624
Smeloff-Cutter A5	16.0	1630	1705
	24.5	1577	1625
	118.2	715	615
Cooley-Cutter A25	10.0	2246	2345
	20.0	2077	1982
	118.2	693	570
Starr-Edwards 6520-1M	11.0	3146	3264
	24.0	2457	2539
	118.2	741	712

* τ_{wi} = shear stress on inside wall

† τ_{wo} = shear stress on outside wall

Table 13. Experimentally Measured Wall Shear Stresses at a Flow Rate of 167 cm^3/sec

Name of Valve	X (mm)	τ_{wi}* dynes/cm^2	τ_{wo}† dynes/cm^2
Lucite Disc	22.0	21	18.5
	118.2	16.5	16.5
Björk-Shiley 27XMBRP	12.0	530	502
	24.0	520	499
	118.2	88	83
Starr-Edwards 1260-12A	22.0	676	659
(ball tied)	32.0	650	636
	118.2	173	102
Starr-Edwards 1260-12A	22.0	726	750
(ball untied)	32.0	685	706
	118.2	142	109
Smeloff-Cutter A5	16.0	680	722
	24.5	670	702
	118.2	170	154
Cooley-Cutter A25	10.0	872	911
	20.0	765	801
	118.2	236	182
Starr-Edwards 6520-1M	11.0	1190	1249
	24.0	966	1001
	118.2	231	222

* τ_{wi} = shear stress on inside wall

† τ_{wo} = shear stress on outside wall

estimates of the magnitudes of the turbulent-shear fields. In the close vicinity of all the valves ($X \leq 70$ mm) at the Reynolds numbers studied, these intensities varied from 25 to 50 percent. All the valves created very turbulent flows compared with the flow with no prosthesis in the flow channel. From the turbulence-intensity measurements made, it was not possible to predict which valves created more flow disturbance and which did not, because, depending on the position of the velocity measurement, it was possible to observe maximum values of I_x as high as 50 percent in the very close vicinity ($X \leq 35$ mm) of all the valves. Values of I_x decreased as a function of distance downstream, and at the furthest downstream position ($X = 118$ mm), the values of I_x were about 15 to 20 percent in the bulk fluid.

6.4 Estimation of Wall Shear from Pressure-Drop Measurements

For fully developed, steady flow in a circular tube, a force balance gives the following relationship

$$\tau_w = \frac{\Delta \bar{p}}{L} \cdot \frac{d_o}{4} \tag{45}$$

where

τ_w = wall shear stress

d_o = internal diameter of tube

$\frac{\Delta \bar{p}}{L}$ = mean pressure drop over a length L of the tube

Force balance in the heart valve chamber (i.e., in the very near vicinity of the prosthesis) (see Fig. 147):

$$\Delta p = p_a - p_b \tag{46}$$

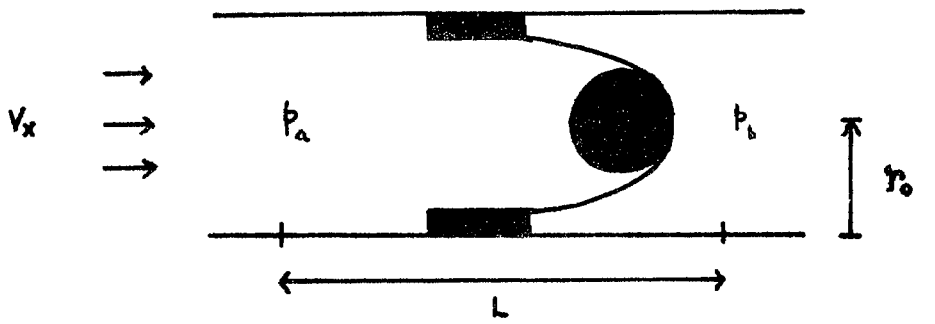

Fig. 147. Schematic of pressure-drop across an aortic valve in the heart valve chamber

where p_a = pressure immediately upstream of valve,

p_b = pressure immediately downstream of valve ($X \simeq 10$ to 20 mm)

Assume that there is no radial variation in pressure (i.e., $\partial p/\partial r = 0$) and that the wall shear stress is constant over the distance L in which Δp is measured. A force balance therefore gives

$$\underset{\text{(Pressure Force)}}{\Delta p \cdot \pi r_o^2} = \underset{\text{(Shear Force)}}{\tau_w \cdot 2\pi r_o L} + \underset{\text{(Drag Force)}}{C_D \cdot \frac{1}{2} \rho V_x^2 \cdot A_p} \qquad (47)$$

where

τ_w = wall shear stress in the very near vicinity of the valve

A_p = projected area of valve poppet

C_D = drag coefficient of the valve

r_o = radius of valve chamber (assumed to be constant)

L = distance over which Δp is measured

V_x = mean velocity immediately upstream of valve

In equation (47) there are two quantities that are very hard to estimate accurately. The first is Δp in the very near vicinity ($X \leq \sim 30$ mm) across the prosthesis. In this study p_b was measured at X = 40 mm. It was not experimentally possible to obtain accurate pressure measurements of p_b immediately downstream or extremely close to the valves (i.e., $X \simeq 10$ to 30 mm) with the instrumentation presently available. The pressure fluctuations in the very close vicinity ($X \leq \sim 30$ mm) of the valves are large and rapid, and the time response of the pressure transducers are not rapid enough to accurately measure the

pressures in such highly turbulent and disturbed flow regions. The reasons for the large and rapid pressure fluctuations are the flow separations and wakes that occur in the very near vicinity of the valve poppets. Also, due to the turbulent and disturbed flow fields, the pressures in the very near vicinity of the valve would vary with radial position (i.e., $dp/dr \neq 0$).

In order to obtain a handle on the pressure drops extremely near the valve poppets, a long bent hypodermic needle was used via pressure tap II (see Fig. 3). With all the valves studied, the pressure drops very close to them were about twice as large or larger than those measured between taps I and II. Jorgensen et al. [25] also observed that very close to the valve the pressure drop was twice as large as that measured further downstream of the valve.

The second quantity in equation (47) that is very hard to estimate accurately is C_D, the valve drag coefficient. Drag coefficients around spheres, circular discs, etc. that are available in the literature are obtained in large channels in which wall effects due to the channel are negligible. In the case of aortic prostheses the size of the prosthesis is comparable to the diameter of the flow channel. Therefore, due to the increased fluid interaction with the channel walls, the drag coefficient will be different compared with an experiment conducted in a channel where the wall effects would have been negligible. Very little experimental or theoretical work exists in the study of drag coefficients around bodies in confined channels.

Richter and Naudascher [98] conducted experiments on a long circular cylinder in a narrow rectangular duct. At an Re of 2×10^4 at a cylinder

diameter to channel breadth ratio (d/b) of 0.5, the mean drag coefficient was ∿1.87. When d/b tends to zero the drag coefficient was ∿1.20. They also observed that as confinement ratio (d/b) increased, the confinement coefficient also increased in value. Shaw in his studies [99] observed for flow past a flat plate in a rectangular channel as the confinement ratio varied from zero to 0.67 the drag coefficient increased from ∿2.0 to ∿4.3. A literature survey did not reveal any studies conducted in circular channels. Also, no work seems to have been performed on spheres.

Due to the inability to measure the pressure drops in the very near vicinity of the aortic prosthesis ($X \leq 30$ mm) and the inability to estimate the drag coefficients C_D, it was not possible to utilize equation (47) to predict average wall shear stresses in the sinus region from pressure drop measurements in that region. The wall shear was therefore estimated from the pressure-drop measurements between taps I and II and taps I and III, by assuming that the pressure drops occurred in a circular channel. The pressure drop in a circular channel is related to the wall shear by equation (45). In estimating the average wall shear in the sinus region it was assumed that Δp_1 varied linearly over the distance between the pressure taps I and II. In estimating the average wall shear in section 'C' it was assumed that Δp_2 varied linearly with distance in this section. Therefore,

$$\tau_{we_1} = \frac{\Delta p_1 \cdot d_1}{L_1 \cdot 4} \tag{48}$$

and

$$\tau_{we_2} = \frac{\Delta p_2 \cdot d_2}{L_2 \cdot 4} \tag{49}$$

Table 14. Wall Shear Stresses Estimated from Pressure Drop Data*

Name of Valve	Flow Rate (cm^3/sec)	τ_{we_1} ($dynes/cm^2$)	τ_{we_2} ($dynes/cm^2$)
Björk-Shiley 27XMBRP	167	249	73
	417	1470	410
Starr-Edwards 1260-12A (ball tied)	167	333	90
	417	1911	518
Starr-Edwards 1260-12A (ball untied)	167	403	132
	417	2406	775
Smeloff-Cutter A5	167	414	133
	417	2385	778
Cooley-Cutter A25	167	579	173
	417	3450	1115
Starr-Edwards 6520-1M	167	883	279
	417	5532	1795
Lucite Disc	167	19	17
	417	58	50

*Based on equations (48) and (49).

where

τ_{we_1} = estimate of the average wall shear in sinus region

τ_{we_2} = estimate of the average wall shear in section 'C'

d_1 = average diameter of sinus region

d_2 = diameter of section 'C'

L_1 = distance between pressure taps I and II

L_2 = distance between pressure taps I and III

The results obtained from these calculations are shown in Table 14.

6.5 Estimation of Turbulent Shear Stresses in the Near Vicinity of the Aortic Prostheses

The turbulent-shear stress could be estimated from the turbulent-intensity level measurements in the axial direction in the following way. First, the turbulence intensity level I_x is defined as

$$I_x = \frac{\sqrt{\overline{v_x'^2}(r)}}{\overline{v}_x(r)} \times 100 \qquad (46)$$

where

$\overline{v}_x(r)$ = time averaged velocity in the axial direction

$\sqrt{\overline{v_x'^2}(r)}$ = root mean square of the fluctuating component in the axial direction

$$|\hat{\tau}_{xx}| = \overline{v_x' v_x'} \cdot \rho \qquad (50)$$

$$|\hat{\tau}_{rx}| = \overline{v_x' v_r'} \cdot \rho \qquad (51)$$

where

$|\hat{\tau}_{xx}|$ = magnitude of turbulent normal stress

$|\hat{\tau}_{rx}|$ = magnitude of turbulent shear stress

ρ = density of the fluid

In the majority of the turbulent flow fields that have been studied [100,101] the turbulent shear stress is generally less than the turbulent normal stress ($\hat{\tau}_{xx}$). A physically realistic estimate for the turbulent shear stress is

$$\frac{|\hat{\tau}_{rx}|}{|\hat{\tau}_{xx}|} \simeq 0.5 \text{ to } 0.75 \tag{52}$$

Figliola [102], however, in his measurements in the very near vicinity of aortic prostheses found that at certain positions of measurement $|\hat{\tau}_{rx}| \simeq |\hat{\tau}_{xx}|$.

From equations (46) and (50)

$$|\hat{\tau}_{xx}| = \rho \cdot \left(\frac{I_x \bar{v}_x}{100}\right)^2 \tag{53}$$

Therefore, from the assumptions

$$|\hat{\tau}_{rx}| = c_1 \rho \cdot \left(\frac{I_x \bar{v}_x}{100}\right)^2 \tag{54}$$

where $c_1 \simeq 0.5$ to 0.75 . Also assume that

$$|\hat{\tau}_{rx|max}| \simeq |\hat{\tau}_{xx}| \tag{55}$$

where $|\hat{\tau}_{rx|max}|$ is the maximum estimated absolute value of the turbulent shear stress. Table 15 shows values of $|\hat{\tau}_{xx}|$ ($= |\hat{\tau}_{rx|max}|$) for different values of $\bar{v}_x(r)$ and I_x.

The laminar component τ_{rx} of the total shear stress is obtained from the equation

$$\tau_{rx} = \mu \frac{d\bar{v}_x}{dr} \tag{56}$$

where $d\bar{v}_x/dr$ is the velocity gradient and μ is the viscosity of the fluid.

Table 15. Estimated Turbulent Shear Stresses*

I_x (%)	$\bar{V}_x(r)$ (cm/sec)	$\hat{\tau}_{xx} \simeq \hat{\tau}_{rx\|max}$ (dynes/cm^2)
50	150	5681
50	120	3636
50	100	2525
50	80	1616
50	60	909
50	40	404
25	150	1420
25	100	631
25	80	404
25	60	227
25	40	101

*Based on equations (53) and (55).

The total shear stress τ_{rx}^{T} is given by

$$\tau_{rx}^{T} = \tau_{rx} + \hat{\tau}_{rx} \tag{57}$$

In flow past all the valve prostheses studied, flow separation occurs and a wake is created immediately downstream of the poppet of the prosthesis. In addition to the wake the flow in the neighborhood of the walls of the channel is very high in the very near vicinity ($X \leq \sim 35$ mm) of the valve. The flow as it emerges from the orifice of the valve is forced to flow around the poppet of the valve (exception to this being the Björk-Shiley prosthesis). The flow that now forms between the poppet surface and the flow channel walls is accelerated, jet-like, and of very high velocity compared with the flow which would exist if there were no valve in the heart valve chamber. It was not possible to make velocity measurements in the region between the poppet surfaces and the flow channel walls because the laser light beams were obstructed by the poppets, and therefore the scattered light could not be picked up by the photomultiplier tube. The estimated maximum velocities in the region between the various poppet surfaces and flow channel walls were on the order of about 200 to 400 cm/sec at a flow rate of 417 cm^3/sec. Therefore the velocities in the neighborhood of the flow channel walls in the very near vicinity of the valve are relatively large. The flow in the region between the poppet surface and the flow channel walls may be assumed to be jet-like, in order to obtain estimates of maximum turbulent shear stresses in that region. In the case of the Björk-Shiley tilting disc valve, the flow near the wall in the very near vicinity of the valve was also jet-like.

By modelling the flow as a wake and a jet, it is possible to obtain estimates of the maximum turbulent shear in the very near vicinity of the valve and compare these estimates with those obtained from the turbulent intensity level measurement. For a jet, the maximum turbulent shear stress is given by the expression [103,104]

$$\hat{\tau}_{rx|max} = C_2 \rho U_o^2 \tag{58}$$

where

C_2 = 0.0165 to 0.025

U_o = center line velocity of the jet

For a wake behind a sphere [104] the maximum turbulent shear stress is given by the equation

$$\hat{\tau}_{rx|max} \simeq 0.272 \rho U_o^2 \tag{59}$$

For a wake behind a disc [104] the maximum turbulent shear is given by the expression

$$\hat{\tau}_{rx|max} \simeq 0.471 \rho U_o^2 \tag{60}$$

where

$U_o \simeq$ free stream velocity.

It should be noted that equations (58), (59) and (60) are obtained after the jets and the wakes have become self-preserving. In addition, the flows were unbounded (i.e., no wall effects). In the very near vicinity of the jets and the wakes due to the non-self-preserving flow, and due to the presence of channel walls, the maximum turbulent shear stresses could be larger than those estimated from equations (58), (59) and (60). There-

fore, the values of maximum turbulent shear that are obtained from these equations are only estimates like those given in Table 15, in order to obtain a handle on the turbulent shears that occur in the bulk fluid in the very near vicinity of the prostheses. Tables 16 and 17 give values of the turbulent shear stresses estimated from equations (58), (59) and (60).

Table 16. Maximum Estimated Turbulent Shear Stresses in a Jet*

U_o cm/sec	$\hat{\tau}_{rx\|max}$ dynes/cm^2
200	1010
250	1578
300	2273
350	3093
400	4040

*Based on equation (58), with $C_2 = 0.025$

Table 17. Maximum Estimated Turbulent Shear Stresses in the Wake behind a Sphere and a Disc

U_o cm/sec	Sphere* $\hat{\tau}_{rx\|max}$ dynes/cm^2	Disc** $\hat{\tau}_{rx\|max}$ dynes/cm^2
50	687	1189
75	1545	2676
100	2747	4757
125	4293	7433
150	6181	10703

*Based on equation (59)

**Based on equation (60)

6.6 Estimation of Shear Stress on the Surface of the Poppet of an Aortic Ball Valve

The drag force on a sphere in an unbounded fluid is given by the expression

$$f_D = \frac{1}{2} \rho U_o^2 f \cdot A_p \tag{61}$$

where

f_D = drag force on sphere

U_o = velocity of fluid upstream of the sphere

ρ = density of fluid

f = drag coefficient

A_p = projected area of sphere = πR^2

R = radius of sphere

For $500 < Re_{sphere} < 10^5$

$$f \simeq 0.44$$

where Re_{sphere} is the Reynolds number based on the sphere diameter. As discussed in Section 6.4, the drag force on the body will increase when the bluff body and the flow channel are of comparable size. There has been no work performed on spheres in circular channels to measure the increase in the drag force due to the effects of the channel walls.

For the ball valves used in the present study, the ratio of sphere diameter to flow channel diameter is approximately 0.60 to 0.75. Assume under these conditions that the drag force on the sphere is about twice as large as the drag force on the sphere in an unbounded flow field.

$$\therefore f \simeq 0.88$$

Also assume the velocity approaching the sphere is equal to the mean velocity across the orifice of the valve. Therefore, at a flow rate of 417 cm^3/sec for the Starr-Edwards 1260-12A ball valve,

$$U_o \simeq 192 \text{ cm/sec}$$

$$R \simeq 9.50 \text{ mm}$$

$$\simeq \text{Drag Force} \simeq 0.5 \cdot 1.01 \cdot (192)^2 \cdot 0.88 \cdot \pi(0.95)^2$$

$$= 46{,}450 \text{ dynes}$$

According to Hoerner [105] at a Re_{sphere} on the order of 10^3, the skin friction drag is approximately 5 to 10 percent of the total drag. Therefore shear force on the sphere

$$\simeq 5 \text{ to } 10 \text{ percent of total drag force}$$

For the Starr-Edwards ball valve,

$$\text{Shear Force} \simeq 2323 \text{ to } 4645 \text{ dynes}$$

Assuming that the shear force on the sphere is evenly distributed over its surface,

$$\text{Avg. shear stress on sphere} = \left(\frac{\text{shear force}}{4\pi R^2}\right)$$

$$= 205 \text{ to } 410 \text{ dynes/cm}^2$$

Therefore the estimated shear stress on the surface of the ball of a ball valve aortic prosthesis at high flow rates will be on the order of 10^2 dynes/cm^2.

6.7 Estimation of the Ratio Eddy Viscosity to Molecular Viscosity in the Near Vicinity of an Aortic Prosthesis

The following calculations were performed as examples in order to obtain order of magnitude estimates of the ratio of eddy viscosity (μ_t) to molecular viscosity (μ) in the immediate downstream vicinity of aortic prostheses.

In the immediate downstream vicinity of the prosthetic valves studied the velocity profiles have the generalized shape shown in Figure 148. Assume that the corresponding shear stress profile has shape as given in Figure 149. In order to obtain the shape given in Figure 149 the following assumptions were made.

(i) The shear decays linearly from the wall shear τ_w to zero over the distance a_1.

(ii) τ_m occurs at or near the location at which the maximum turbulent intensity in the bulk fluid was measured.

(iii) $\tau_m = \hat{\tau}_{rx|max}$

(iv) The shear stress in the bulk fluid also increases and decreases linearly with distance.

The shear stress τ^T_{rx} is composed of a laminar component and a turbulent component as given by equation (57)

$$\tau^T_{rx} = \tau_{rx} + \hat{\tau}_{rx} \tag{57}$$

now

$$\tau_{rx} = \mu \cdot \frac{d\bar{v}_x}{dr} \tag{56}$$

and

$$\hat{\tau}_{rx} = \mu_t \cdot \frac{d\bar{v}_x}{dr} \tag{62}$$

where μ_t is the eddy viscosity and $d\bar{v}_x/dr$ is the velocity gradient.

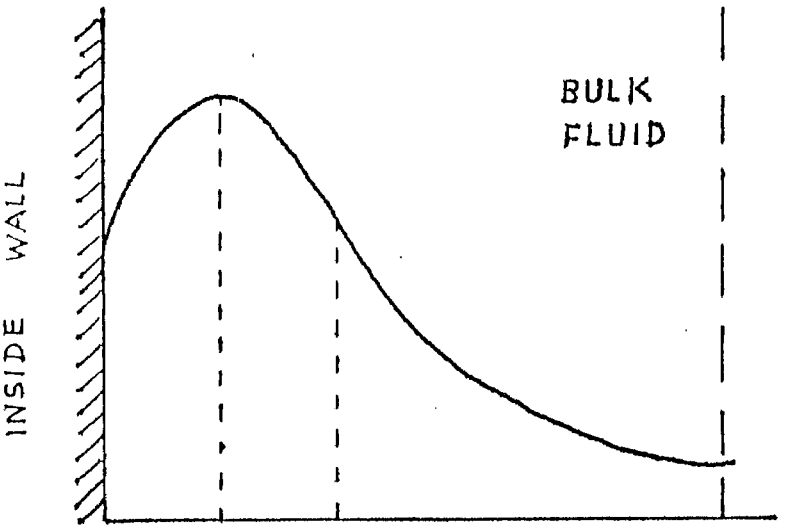

Fig. 148. Schematic of velocity profile immediately downstream from an aortic valve.

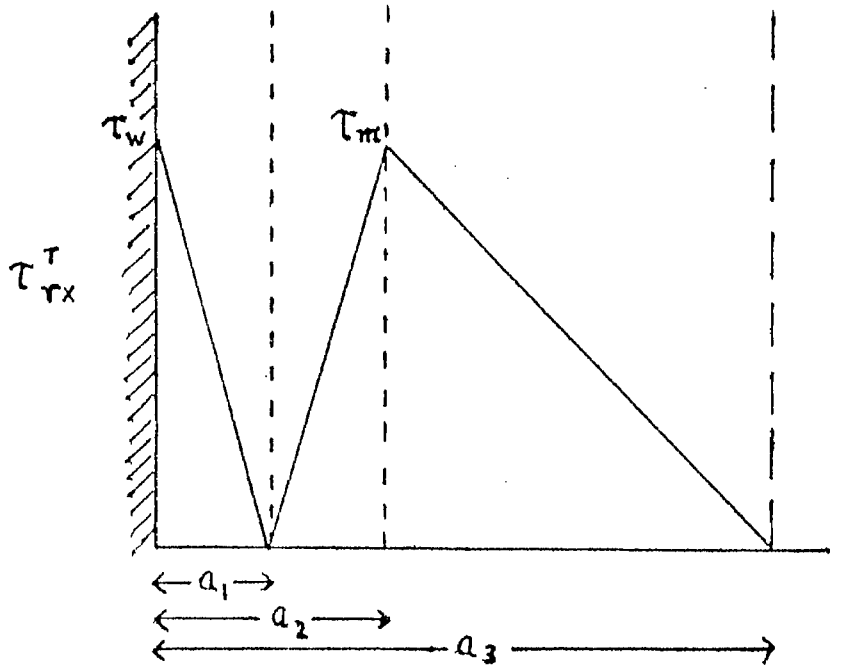

Fig. 149. Schematic of shear stress profile immediately downstream from an aortic valve

$$\tau^{T}_{rx} = (\mu + \mu_t) \frac{d\bar{v}_x}{dr} \tag{63}$$

$$\mu_t = \frac{\tau^{T}_{rx}}{\left(\frac{d\bar{v}_x}{dr}\right)} - \mu \tag{64}$$

$$\frac{\mu t}{\mu} = \frac{\tau^{T}_{rx}}{\tau_{rx}} - 1 \tag{65}$$

Consider the example of the velocity profile at a flow rate of 417 cm^3/sec with the Smeloff-Cutter A5 ball valve at X = 16.0 mm (see Fig. 126). For this example

a_1 = 1.8 mm

a_2 ≃ 4.25 mm (Note: The maximum turbulent intensity was measured at about $a_2 \pm 0.5$ mm)

a_3 ≃ 15.0 mm

τ_w = 1630 dynes/cm^2

$\tau_m = \hat{\tau}_{rx|max} \simeq 2000$ dynes/cm^2

The value of $\hat{\tau}_{rx|max}$ used is only an order of magnitude estimate (see Tables 15, 16 and 17), and is assumed to be of nearly the same value as τ_w.

Using the values given above and applying them to Figure 149, the shear stress profile is obtained. Using the values of τ^{T}_{rx} from the shear stress profile and the values of $d\bar{v}_x/dr$ measured from Figure 126, μ_t/μ is calculated from equation (65), and some of the values are given in Table 18.

Table 18. Ratio of μ_t to μ with Distance from the Inside Wall for the Smeloff-Cutter A5 Valve

a (mm)	μ_t/μ
0.0	0
0.6	168
1.2	272
1.8	*
2.1	55
3.0	66
3.9	95
4.25	96
5.0	115
6.0	310
7.0	428
8.0	473
9.0	606
10.0	644
11.0	877
12.0	836
13.0	758
14.0	475
15.0	*

*Indeterminate value

A similar calculation for the velocity profile obtained with the Björk-Shiley 27XMBRP valve at X = 12.0 mm at a flow rate of 417 cm^3/sec (see Fig. 120) gives values as shown in Table 19. In this calculation the following values were used:

a_1 = 1.25 mm

a_2 ≃ 3.0 mm

a_3 ≃ 6.0 mm

τ_w = 1400 dynes/cm^2

$\tau_m = \hat{\tau}_{rx|max} \simeq$ 1500 dynes/cm^2

In order to compare results obtained in Tables 18 and 19, consider the shear stress profile obtained from the velocity profile downstream of the lucite disc at X = 22.0 mm at a flow rate of 417 cm^3 (see Fig. 103). In this calculation τ_w = 60 dynes/cm^2, and the shear stress ($\hat{\tau}^T_{rx}$) decays linearly from 60 to zero dynes/cm^2 over a distance of about 16 mm. Table 20 gives the results of the calculations.

The results shown in Tables 18 and 19 indicate that in the bulk fluid the ratio of eddy to molecular viscosity could be on the order of 10^2 to 10^3. The results obtained downstream of the valves are quite different from those obtained downstream of the lucite disc, indicating once again the flow is more turbulent and disturbed in the near downstream vicinity of an aortic prosthesis. Even though the calculations of μ_t/μ for the two prosthetic aortic valves were based on a crude mode with many assumptions, the results obtained at least give an order of magnitude estimate for the ratio of μ_t to μ. If the turbulent shear stress ($\hat{\tau}_{rx}$) could be measured accurately, together with the velocity

Table 19. Ratio of μ_t to μ with Distance from the Inside Wall for the Björk-Shiley 27XMBRP Valve

a (mm)	μ_t/μ
0.0	0
0.6	420
1.2	120
1.5	108
2.1	76
3.0	84
3.9	57
4.5	64
4.8	113
5.1	157
5.4	160
5.7	146
6.0	*

Table 20. Ratio of μ_t to μ with Distance from the Inside Wall for the Lucite Disc

a (mm)	μ_t/μ
0.0	0
2.0	24
4.0	28
6.0	34
8.0	44
9.0	55
10.0	51
12.0	35
14.0	20
16.0	*

*Indeterminate value

profile no assumptions would be required to calculate μ_t/μ.

An ideal prosthetic aortic valve should cause minimal flow disturbance and have values of μ_t/μ of the same order as those obtained downstream of the lucite disc (see Table 20).

6.8 General Discussion

The velocity profiles obtained with the four aortic and one mitral prostheses indicate that the flow fields in the near vicinity of the valves are very complex. None of the five valves studied showed symmetric velocity profiles at X = 42 mm. Farther downstream, except for the Björk-Shiley valve which gave profiles which were almost symmetric and the Starr-Edwards 6520-1M valve which gave symmetric profiles at about $X \geq 92.8$ mm, the other three valves gave velocity profiles which were skewed towards one wall. In the sinus area very close to the valve (i.e., immediately downstream, within 2 to 3 mm of the fully open poppet) the wall shear stress measurements indicated velocity profiles that are fairly symmetric, because the shears on both walls were within ±120 dynes/cm^2 of each other. These observations are very interesting because the three symmetrical aortic valves gave asymmetrical profiles and the asymmetric Bjork-Shiley valve gave symmetric profiles. No conclusions can be drawn from these observations because by placing the valves in the aortic heart valve chamber in different orientations it is possible to obtain profiles which are asymmetric and skewed toward one of the walls, and randomly it is possible to obtain symmetric profiles. It should be noted that in these experiments all the valves were placed as symmetrically as possible in the heart valve chamber, which was not

exactly symmetric due to the presence of the three sinuses. Figures 150, 151, 152 and 153 show profiles obtained with the Smeloff-Cutter A5 valve placed asymmetrically in the valve chamber. The velocity profiles are very heavily skewed toward the outside wall, while with the valve placed symmetrically the profiles obtained were skewed toward the inside wall (Figs. 126 to 132). The velocity profiles that were obtained during the experiments were the result of very complex interactions of the fluid with the valves and the solid surfaces. The effects of the complex interactions of the fluid with the valves and the walls of the flow channel are highlighted by the following example. In unbounded flow past a sphere the velocity defect created by the sphere can be observed up to at least 100 diameters downstream of the sphere. In the experiments conducted with the two types of ball valves in this study the velocity defect phenomenon disappeared within about 2 to 3 diameters downstream of the ball. The reason for the disappearance of the velocity defect phenomenon in such short distance is because of the effect of the flow channel walls on the flow field.

In this study the upstream velocity profiles approaching the valves were symmetric. In the human body, however, the velocity profiles approaching the valve are generally asymmetric. In addition, the root of the ascending aorta need not be symmetric due to the three sinuses. The three sinuses need not be of equal size. Therefore, it is only logical to assume that in most instances the velocity profiles downstream from a prosthetic aortic valve in the body will be asymmetric. Weiting [14] in his work assumed the velocity profiles downstream from the prosthetic valves were symmetric. He therefore only measured

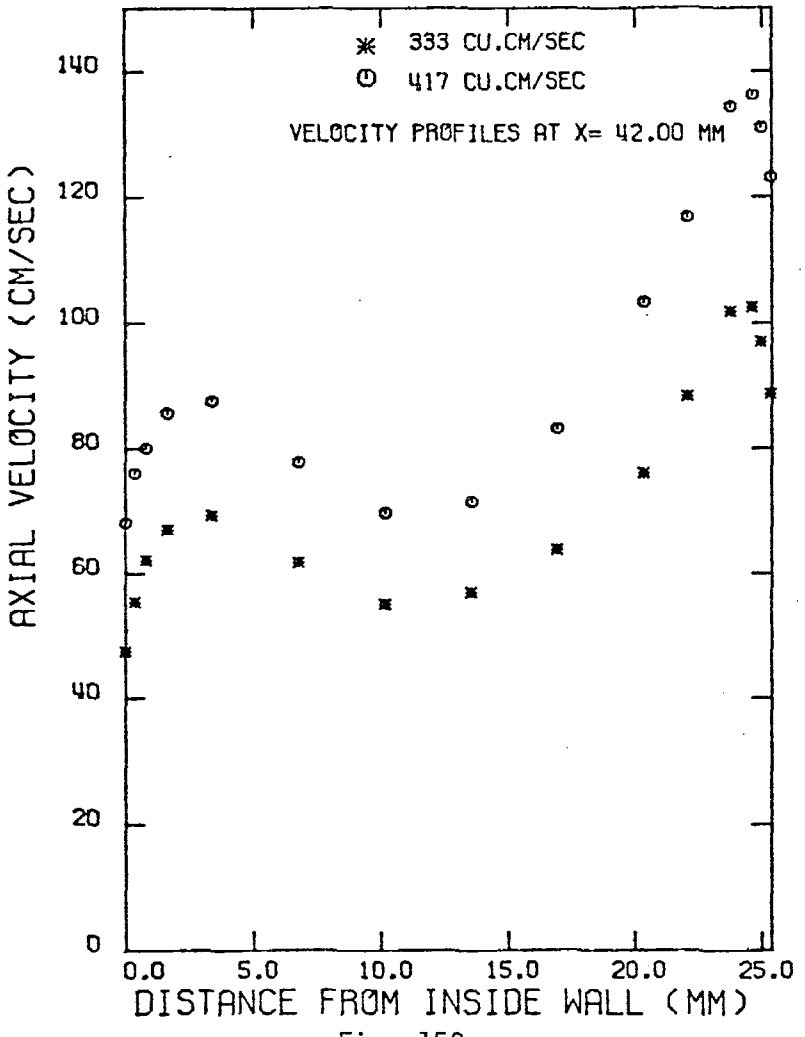

Fig. 150

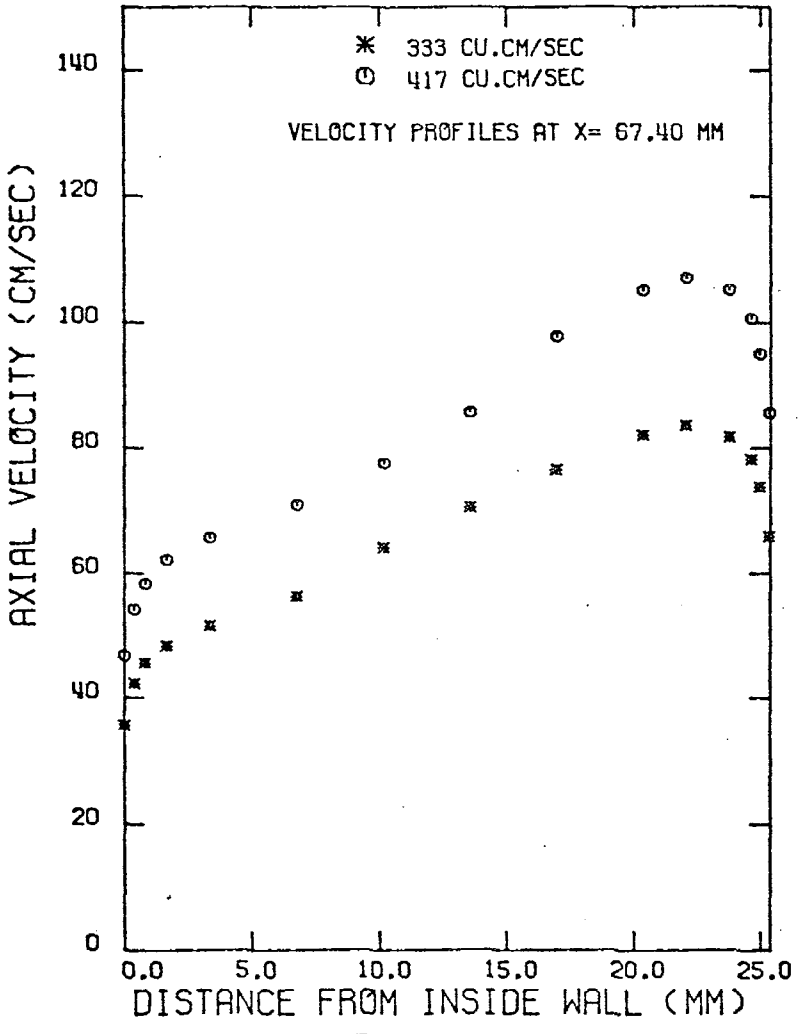

Fig. 151

Velocity profiles downstream from the Smeloff-Cutter A5 valve placed asymmetrically in the valve chamber

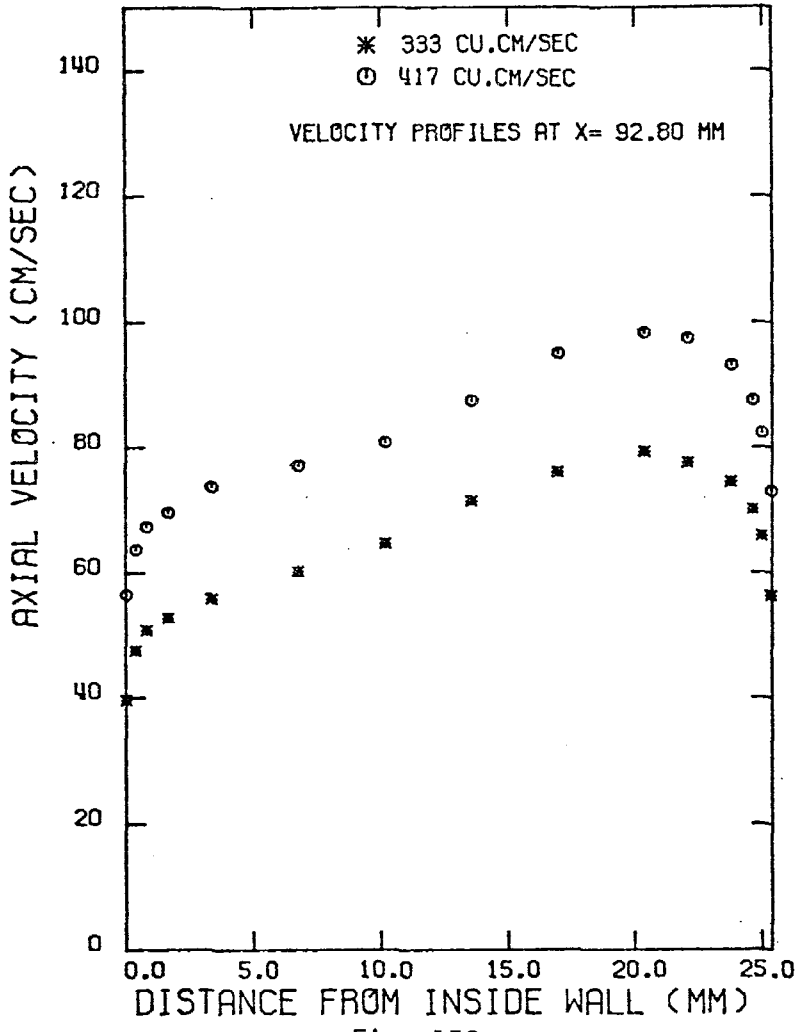

Fig. 152

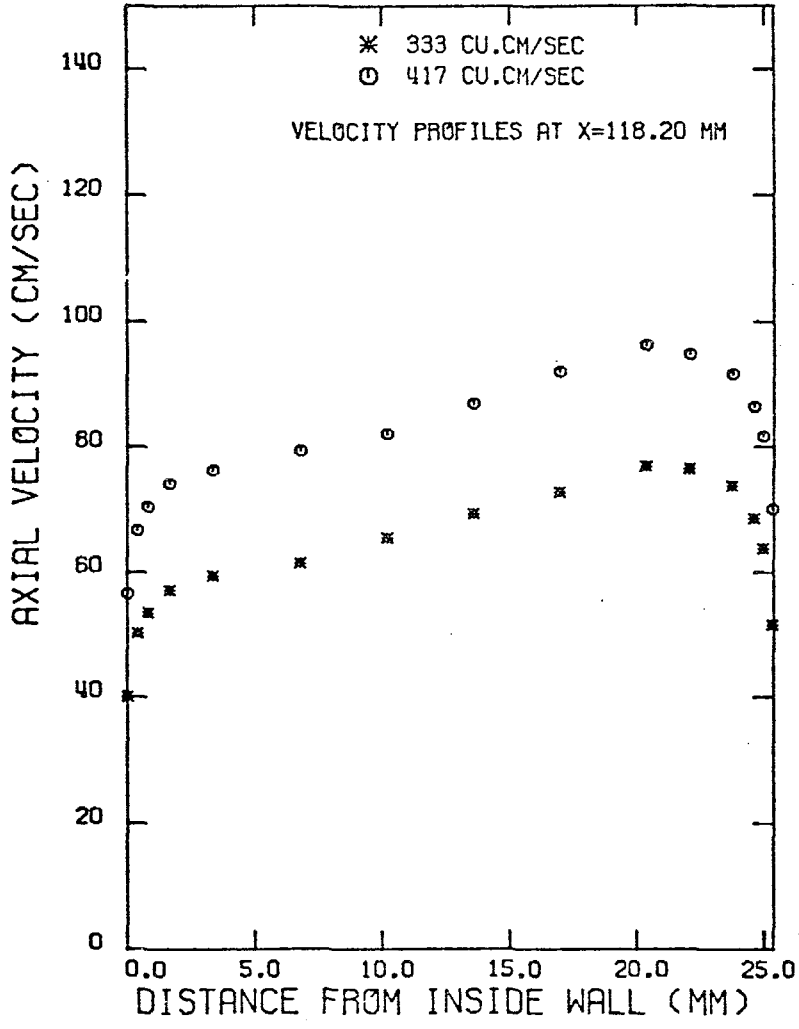

Fig. 153

Velocity profiles downstream from the Smeloff-Cutter A5 valve placed asymmetrically in the valve chamber

velocities from the inside wall to the center of the channel. He then used these values to plot his profiles from wall to wall. The present results show clearly that it is wrong to assume that the velocity profiles downstream from a prosthetic valve are symmetric. The present results also show that none of the velocity profiles for any of the valves studied had reached a steady state at X ≃ 118 mm and that the wall shears at that point are still large compared with flow in a tube with no heart valve placed upstream. Therefore the effects of the valve on the flow field are observed even at a distance as far downstream as X = 118 mm.

The velocity profile measurements made with all the heart valve prostheses studied indicate quite clearly that in the near vicinity of the valve the velocity in a region close to the channel walls is relatively large, while the flow in the center of the channel is low. The phenomenon is to be expected because with the exception of the Björk-Shiley valve the valves studied are all peripheral flow valves. The flow that emerges from the orifices of these valves is forced to flow around their poppets, resulting in higher velocities in a region close to the vessel walls. As stated before, the flow in the region between the poppet surface and the vessel walls is jet-like and of very high velocity. In the case of the Björk-Shiley valve, because it creates an area of stagnation in the immediate downstream vicinity of the fully open disc, the majority of the flow emerging from the valve flows in a region close to the vessel walls leading to high velocities close to the walls. Because the prosthetic valves lead to high velocities in a region close to the flow channel walls, the wall shear stresses

measured in the near vicinity of all the valves studied are very high compared to if there were no heart valve in the aortic valve chamber, as shown by the values given in Tables 12 and 13. All valves studied created wall shears of the order of 10^2 to 10^3 dynes/cm^2 in their near vicinity ($X \leq 120$ mm) for a steady flow range of 167 to 417 cm^3/sec.

Of all the prosthetic aortic valves used in this study, the Björk-Shiley valve created the least amount of wall shear in the sinus region (section 'B') while the Cooley-Cutter valve exhibited the largest wall shear in this region. The mitral disc valve, however, had the largest wall shear in the sinus region of all five valves studied. It was observed, as is shown in Tables 12, 13 and 14, that the wall shear in the sinus region was more or less directly proportional to the pressure drop Δp_1 in that region. As the fluid moved downstream ($X \simeq 118$ mm) all the valves created wall shears of about the same order of magnitude. Even at $X \simeq 118$ mm all the valves created elevated wall shear stresses (see Tables 12 and 13) over the entire range of flow rates studied. If the measured velocity profiles are skewed heavily towards one wall, as in the case of the Cooley-Cutter A25 valve at X = 42 mm (Fig. 135), the measured shear on one wall may differ from the shear on the other wall by a factor of 1.5. In the case of the Smeloff-Cutter A5 valve, which was placed asymmetrically in the heart valve chamber, at X = 42 mm (Fig. 150) the shear on the outside wall was larger than the shear in the inside wall by about a factor of two. If at a given downstream location ($X = X_1$) of measurement the two measured wall shear stresses differed by a factor f, it is then possible that in this area of measurement there may exist a shear stress on some region of the wall which is larger by

about a factor f than the largest measured wall shear in that area. In other words, the wall shears measured in this study may not be the largest that exist under the experimental conditions used. The values obtained, however, represent the order of magnitude of the wall shears created by the different types of prostheses. The comparison of the measured wall shear stresses with those estimated from pressure-drop data, as discussed in Section 6.4 and shown in Table 14, indicates that it is possible to predict the wall shear in the very near vicinity of an aortic prosthesis ($X \leq \sim 30$ mm) in the sinus region to within a factor of 2 or 3 from pressure-drop data. This result is very useful, since at present pressure drop measurements about 40 to 60 mm downstream of the valve are easier to obtain than accurate velocity measurements in the sinus region very close to the flow channel walls. Therefore, from comparative pressure drop measurements it seems possible to predict whether valve type A causes larger wall shear in its very near vicinity compared with valve type B. A comparison of Tables 12, 13 and 14 also indicates that it is possible to predict the average wall shear stresses in section 'C' to within a factor of 2 or 3 from pressure drop measurements between taps I and III.

As stated before in Chapter 2, there is a lack of data on velocity measurements in the vicinity of aortic prostheses. Weiting [14] in his work measured velocities under pulsatile flow using a photographic technique. His technique has many drawbacks. He could not measure velocities immediately distal to the valve. The closest location at which he could measure velocities was 51 mm downstream from the valve. At distances closer than 51 mm the flow field was too turbulent and

and disturbed for him to make measurements with his technique. Also he was limited as to how close he could get to the flow channel wall. In most cases his first point of velocity measurement was 2 mm from the wall. Due to the above mentioned difficulties the largest wall-shear stress he measured was about 8 dynes/cm^2 compared with 3000 dynes/cm^2 here. Recently Falsetti [23] presented a paper in which he and his coworkers measured velocities in the vicinity of prosthetic valves under steady-flow conditions. They used a hot-film-anemometer system to carry out their measurements. The largest flow rate they investigated was 133 cm^3/sec (8 liters/min) which seems to have very little physiological significance. At this flow rate the largest wall shear they measured was 7.6 dynes/cm^2. This result does not seem reasonable because in section 'A' of the present flow system at a flow rate 167 cm^3/sec (10 liters/min) the measured wall shear stresses were about 15 dynes/cm^2. It is believed that Falsetti and coworkers in their experiments did not measure velocities close enough to the wall. All of the present data in this study suggest clearly that in the vicinity of an aortic prosthesis the velocities very close to the walls are relatively high. Figliola [102] measured velocities under steady flow conditions in the near vicinity of the Kay-Shiley, Björk-Shiley and Starr-Edwards ball valve. He used a hot-wire anemometer and air as the test fluid. In order to obtain a Reynolds number of 6000 he had used an average air flow of about 360 cm/sec. It is doubtful that at a Re of 6000 the turbulent transport properties such as shear stress would be the same in air as in blood or a blood analog fluid with a viscosity of 0.035 dyne sec/cm^2 and density

of $\sim$1.015 g/cm^3. To obtain a Re of 6000 with the blood analog fluid an average velocity of about 80 cm/sec would be sufficient. Also, he did not measure velocities close to the walls of his flow channel. The closest distance he got to the wall was 2.75 mm, and in most instances he was even further away from the wall. Therefore he was unable to obtain accurate measurements of the wall shear stresses.

The use of hot-wire or hot-film probes to measure velocities in _in vitro_ cardiovascular studies is undesirable. The probe when inserted into the flow channel causes disturbances in the flow, and this effect leads to artifacts in the measured velocity profiles. Hot-wire and hot-film anemometers have also problems with electrostatic build-up in the fluid. It was because of the above that Figliola [102] used air as the test fluid instead of a glycerine-water solution. The signal-to-noise ratio of the hot-wire anemometer is not as good as that of the laser-Doppler anemometer. For a given component of velocity the hot-wire/film anemometer cannot indicate the direction (i.e., positive or negative) of the flow. Therefore the investigator has to know beforehand the direction of the component velocity he wants to measure. In a region of stagnation where the velocities keep oscillating about zero velocity, the hot-wire/film anemometer would read small positive values. It would not indicate that the velocity was oscillating about zero. During a velocity profile measurement if the velocity component of interest changes direction, as in the case of the Smeloff-Cutter A5 (Fig. 126) and the Cooley-Cutter A25 (Fig. 133) valves, the hot-wire/film anemometer will not indicate this change. Therefore, the velocity profile obtained

will be wrong and very misleading. One of the major assets of the laser-Doppler anemometer is that it indicates the direction of flow of the component of velocity that is being measured. Because of the above cited reasons the results done with a hot-wire/film anemometer in the close vicinity of aortic prostheses may not be reliable.

In addition to the measurements of wall shears, it was possible to make predictions on the turbulent shear stresses in the near vicinity of the prostheses, as described previously. Tables 15, 16 and 17 show estimates of the maximum turbulent shear stresses that can occur under the experimental conditions of this study. The laminar component of the shear stresses in the bulk fluid in the vicinity of an aortic valve could be measured from the velocity profiles in that region, as given by equation (56). Such measurements yielded estimates of the laminar stress on the order of 1 to 25 dynes/cm^2 (very near the Starr-Edwards 6520-1M valve a laminar shear of about 60 dynes/cm^2 was measured). The values in Tables 15, 16, 17, 18 and 19 indicate that in the vicinity of the five prostheses studied, even though the laminar component may be on the order of 1 to 25 dynes/cm^2, the turbulent shear-stress component could be two to three orders of magnitude larger. Therefore, it is incorrect to say that the shear stresses in the bulk fluid in the near vicinity of a valve are only on the order of 1 to 25 dynes/cm^2. It is important that the turbulent shear component be taken into consideration. The LDA system, together with the auxiliary instrumentation we have at present cannot directly measure the turbulent shear stress component at a given location. The equipment can, however, be modified to make such measurements. From

the estimates of the turbulent shear stresses and the measured wall shears, it is quite clear that the five prostheses that were studied created large wall and bulk shear stresses. The magnitude of these shears are such that they can damage the various components of blood and the endothelial lining of the aortic wall. Shear stresses under pulsatile flow would probably be greater than under steady flow conditions. It has been shown [106,107] that boundary layers are thinner near fixed or moving surfaces under accelerating flow conditions and lead to correspondingly higher shear stresses. Similar effects have been observed in unsteady and pulsatile flows in tubes [108,109]. Roschke and Harrison state [51] that the early effects of accelerating impulsive motion or pulsatile flow could result in shear stresses about five times higher than a comparable steady flow.

As discussed in Chapter 5, red blood cell damage or hemolysis thrombus formation and non-endothelialization of the wall of the proximal ascending aorta that are associated with prosthetic aortic heart valves, are mainly due to the excessive shear created in the near vicinity of these valves. Hemolysis, thrombus formation and vessel wall damage observed in aortic heart valve patients and/or in recovered aortic prostheses are interlinked to one another in complex ways under the conditions of high shear. Vessel wall damage can lead to both thrombus formation and red cell damage. Hemolysis also can induce thrombus formation. Thrombus formation could lead to red cell damage and hemolysis.

The wall shear measurements obtained in the near vicinity of all the valves studied which were on the order of 10^2 to 10^3 dynes/cm^2

(see Tables 12 and 13) indicate that such shear stresses could cause damage to the endothelial lining of the proximal ascending aorta. In addition, the velocities very close to the channel walls are relatively high and lead to high wall shears which are large enough to damage and/or lyse RBCs that adhere to the wall of the ascending aorta. The bulk turbulent shear stresses in the near vicinity of the aortic prosthesis which are estimated to be on the order of 10^2 to 10^3 dynes/cm^2 (see Tables 15, 16 and 17) are large enough that they could damage and/or lyse RBCs which adhere onto the superstructure of the valve or get trapped in the fibrin network of thrombi. In addition, these bulk shears could damage platelets in the bulk of the fluid. It is possible that RBCs which enter a zone of bulk turbulent shear on the order of 10^3 dynes/cm^2 may be morphologically damaged. As stated previously, it has been clinically observed that the Starr-Edwards ball valves with cloth covered struts cause more hemolysis compared with the non-cloth-covered Starr-Edwards ball valves. The probable explanation for this phenomenon is that the cloth covering which is rough provides an ideal foreign surface for the adhesion of the red blood cells. Once adhered, the red cells undergo shear stresses on the order of 10^2 dynes/cm^2 (or larger, see Section 6.6) which lead to their destruction and cause hemolysis. As discussed in Chapter 5, RBCs which adhere to the vessel wall or to a foreign surface could be damaged by shear stresses on the order of 10^2 dynes/cm^2.

Koncar-Djudjević and Duduković [110] in a very interesting study examined the effects of local mass transfer to the tube walls when spheres with diameters comparable to the diameter of the tube were

suspended in the center of the tube. They found that in some instances the rate of local mass transfer increased by as much as a factor of two in some locations in the near vicinity (1 to 2 sphere diameters downstream) of the sphere, compared with the rate of mass transfer obtained in the empty tube (i.e., no sphere suspended). They attribute the increase in mass transfer to the complex fluid mechanical interactions between the boundary layer at the tube wall and the wake formed by the body. All the prosthetic valves studied form wakes immediately downstream of their structure. These wakes interact in a very complex manner with the boundary layers on the flow channel walls. Therefore, in the near downstream vicinity of the aortic prostheses, the mass transfer rate toward the vessel walls will be increased, which could lead to problems such as atherosclerosis.

An ideal aortic prosthesis should create minimal flow disturbance and minimal wall and bulk-turbulent shear stresses, like that observed downstream of the lucite disc (see Tables 12, 13 and 20). It should not cause slow separation and areas of stagnation, and should not damage the cellular components of blood and the endothelial lining of the vessel walls.

Chapter 7

CORRELATION OF IN VITRO VELOCITY MEASUREMENTS WITH CLINICAL FINDINGS OF RECOVERED BJÖRK-SHILEY AORTIC PROSTHESES

As stated previously, many fluid mechanical studies have been performed on different designs of aortic prostheses. Very few of these studies, however, have attempted to correlate in vitro results with clinical findings observed in recovered prostheses. In order to improve the designs of existing aortic valve prostheses and to increase their implanted hemodynamic lifetimes (on the order of 25 years), correlation of clinical pathological findings of recovered prostheses with in vitro velocity measurements are very important. For such studies to be successful there must be close collaboration between clinical cardiologists and engineers. It should be noted that the present designs of prostheses have an average implanted lifetime of 5 to 7 years.

In this chapter a detailed study of the in vitro velocity measurements in the near vicinity of the Björk-Shiley aortic prosthesis are correlated with two late pathological failure modes observed in nine recovered valves examined at the LA County-USC Medical Center. The Björk-Shiley tilting disc valve is one of the more commonly used aortic prostheses. It has been in clinical use since January 1969, and has received the standard in vitro fluid dynamic tests. Detailed velocity measurements in the near vicinity of the Björk-Shiley aortic prosthesis have, however, not been obtained previously.

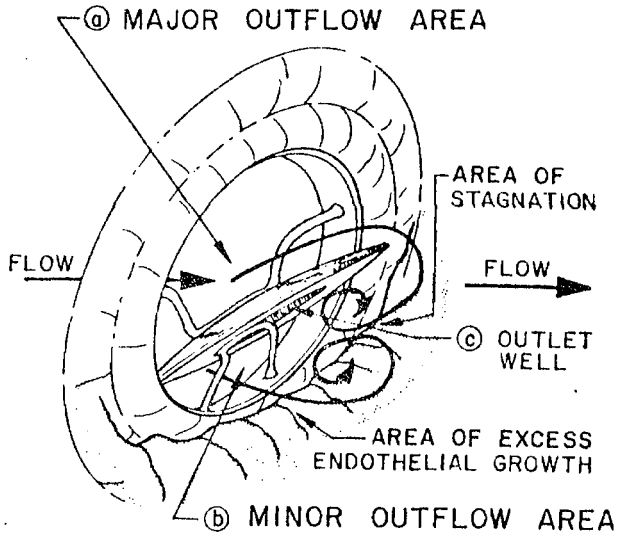

Fig. 154. Schematic of Björk-Shiley valve showing areas of stagnation and excess endothelial growth.

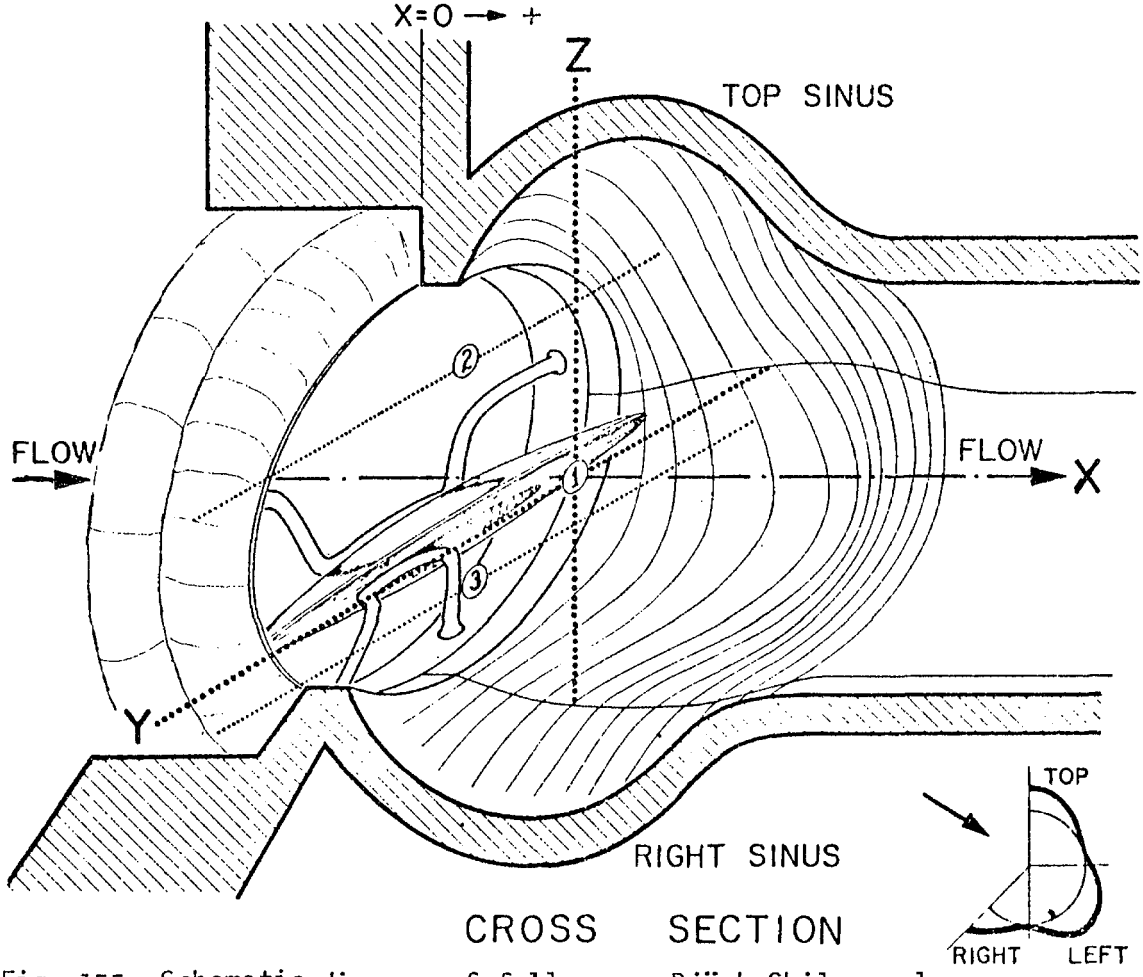

Fig. 155. Schematic diagram of fully open Björk-Shiley valve in the aortic valve chamber.

The nine recovered Björk-Shiley acrtic prostheses which were examined at the LA County-USC Medical Center had been implanted for 6 months or longer. Table 21 lists the duration of valvular implant and other pertinent information. The clinical studies of the nine recovered prostheses indicated varying amounts of thrombus formation in and around the outlet well (see Fig. 154) and/or on the hinge mechanism. The amount of thrombus observed varied from a thin layer to a very thick layer. Such thrombus formation on the outflow face of the disc has been observed by others [37,111,112,113,114,115]. They have, however, been unable to show why the thrombus formation occurred on the outlet face of the disc. In addition, these nine prostheses exhibited excessive endothelial tissue growth along the perimeter of the valve adjacent to the minor outflow area as shown schematically in Figure 154. Such endothelial tissue overgrowth has not been reported before in the literature. Examples of the thrombus formation and excess endothelial growth are shown photographically in Figures 156 and 157.

The in vitro steady flow experiments were performed in the flow channel described previously. Two sets of velocity measurements were performed with a Björk-Shiley 27XMBRP valve. One set was performed with the valve operating normally. The second set was conducted with the minor outflow area partially occluded. The partial occlusion was accomplished with cotton wool and water-proof gray tape. Under both sets of conditions experiments were performed at the steady flow rates of 167 cm^3/sec and 417 cm^3/sec. Velocity profile measurements were made in the axial direction in the X-Y plane at the locations marked

Table 21. Pertinent Information on the Recovered Björk-Shiley Aortic Prostheses

Patient #	Duration of Implant	Prosthetic Valve Examination	Cause of Death
1	6 mos	Paravalvular leak. Thrombus on outlet face of disc. Mild endothelial overgrowth on portion of sewing ring adjacent to minor outflow area	Infectious endocarditis Severe hemolytic anemia
2	6-1/2 mos	Valve occluded by thrombus and endothelial tissue overgrowth*	Infectious endocarditis Cerebral vascular accident
3	7 mos	Endothelial tissue overgrowth*. Thrombus on outlet face of disc	Acute heroin intoxication
4	12 mos	Paravalvular leak. Thrombus on outlet face of disc. Endothelial tissue overgrowth*	Congestive heart failure Ventricular arrhythmia
5	12 mos	Valve occluded by thrombus. Mild endothelial tissue overgrowth*	Survived prosthetic valve replacement at surgery
6	16 mos	Valve occluded by thrombus. Mild endothelial tissue overgrowth*	Severe congestive heart failure
7	8 mos	Thrombus on outlet face of disc. Endothelial tissue overgrowth*	Severe congestive heart failure
8	14 mos	Thrombus on outlet face of disc. Endothelial tissue overgrowth*	Infectious endocarditis Congestive heart failure Cerebral abcesses
9	33 mos	Valve occluded by thrombus. Mild endothelial tissue overgrowth*	Severe congestive heart failure

*Endothelial tissue overgrowth was observed on the portion of sewing ring adjacent to the minor outflow area (see Fig. 154).

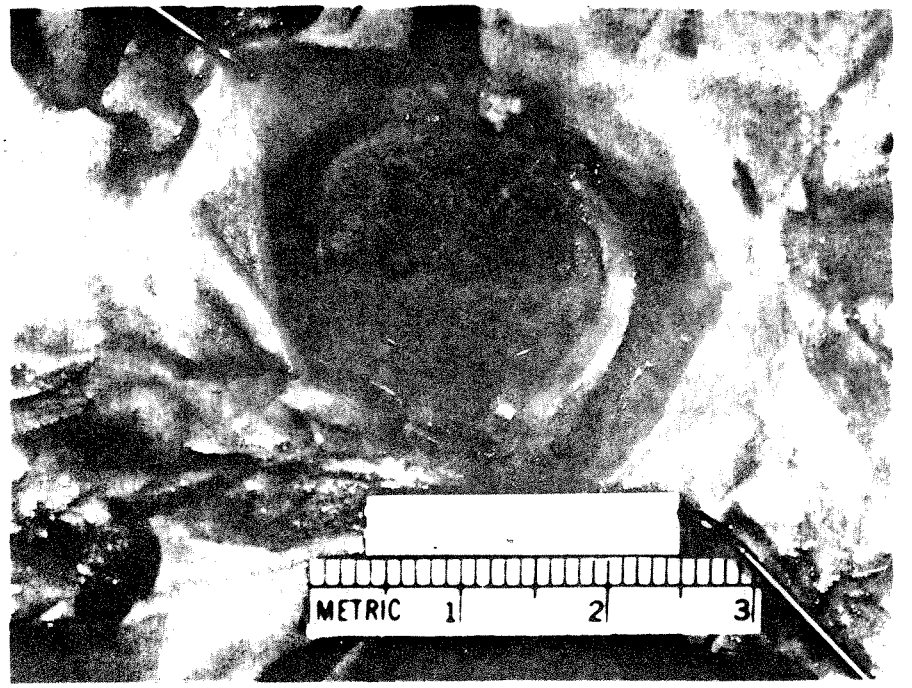

Fig. 156. Photograph of a recovered valve showing thrombus formation and mild endothelial overgrowth

Fig. 157. Photograph of a recovered valve showing excess endothelial tissue growth and thrombus formation

1 , 2 , and 3 as shown schematically in Figure 155. In addition, one set of axial velocity profiles was obtained at position 1 in the X-Z plane. Positions 2 and 3 were ∿3 mm downstream from the front end of the valve sewing ring (i.e., position marked X = 0) and 7.5 mm above and 8 mm below the diameter of the valve orifice in the Y direction, respectively. Position 1 was at the center of the flow channel and 12.2 mm downstream from the position X = 0. It should be noted that when the disc was fully open it extended approximately 11 mm downstream from the position marked X = 0. Position 1 was therefore immediately downstream (∿ 1 mm) of the fully open disc. One set of velocity profiles was also obtained in the X-Y plane at position 4 (not shown in Fig. 155) which was 25 mm downstream from the front end of the valve seat. Velocity profiles in the X-Y plane were obtained from the inside wall to about the center of the channel, while one set of profiles in the X-Z plane were obtained from wall to wall.

Figures 158, 159, 160 and 161 show the velocity profiles measured at locations 1 , 1 , 2 , and 3 respectively (see Fig. 155) with the Björk-Shiley valve operating normally. Figures 152 and 153 show the large stagnation zone created by the valve in the near vicinity of the outflow face of the disc. Velocity measurements at positions 2 and 3 as shown in Figures 154 and 155 indicate quite clearly that the major portion of the flow occurs in flow area ⓐ (major outflow area, shown schematically in Figure 154) and not a sufficient amount in flow area ⓑ (minor outflow area).

The results of the experiments conducted with the minor outflow area of the prosthesis partially occluded are shown in Figures 162, 163, 164 and 165. The profiles in these figures were measured at locations

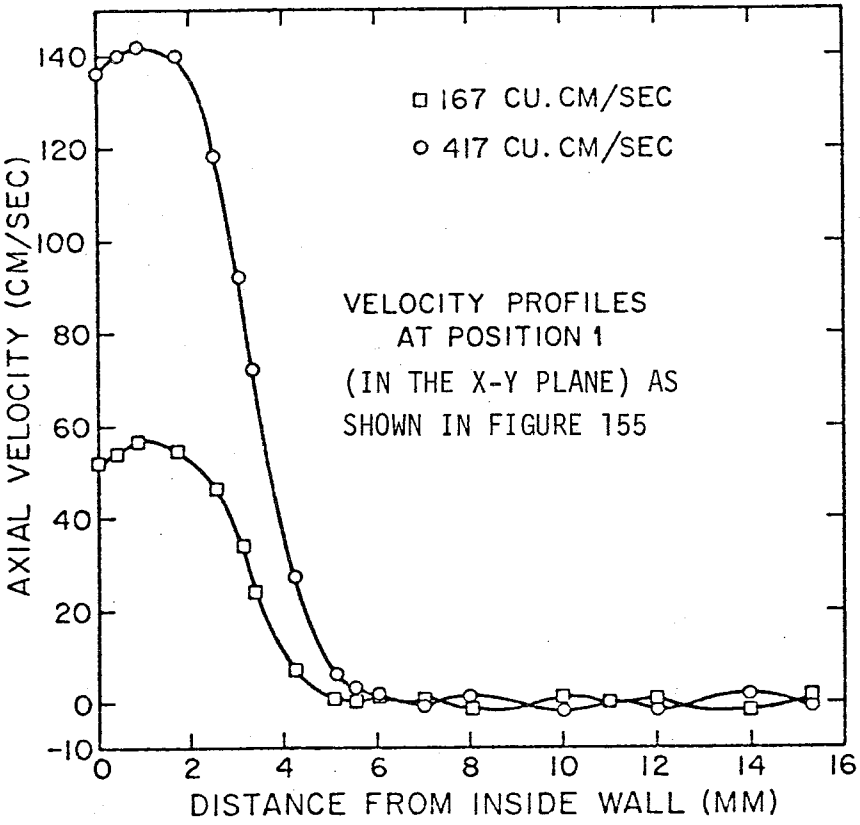

Fig. 158

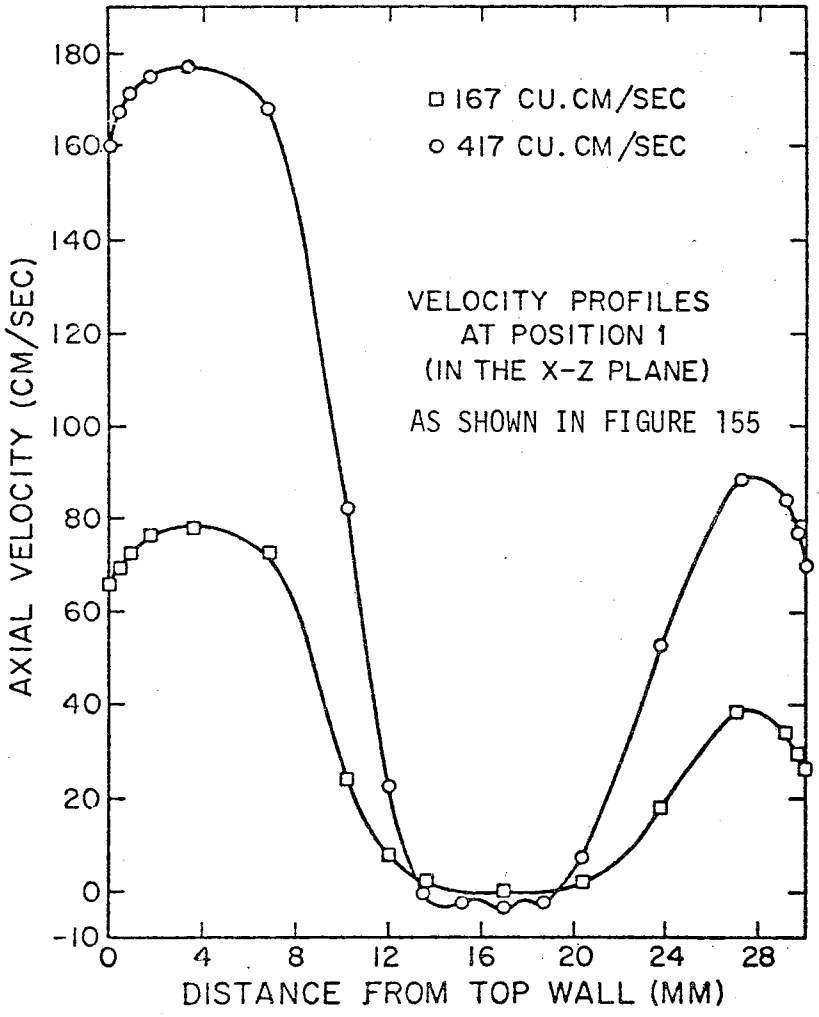

Fig. 159

Velocity profiles in the very near downstream vicinity of the normally functioning Björk-Shiley valve

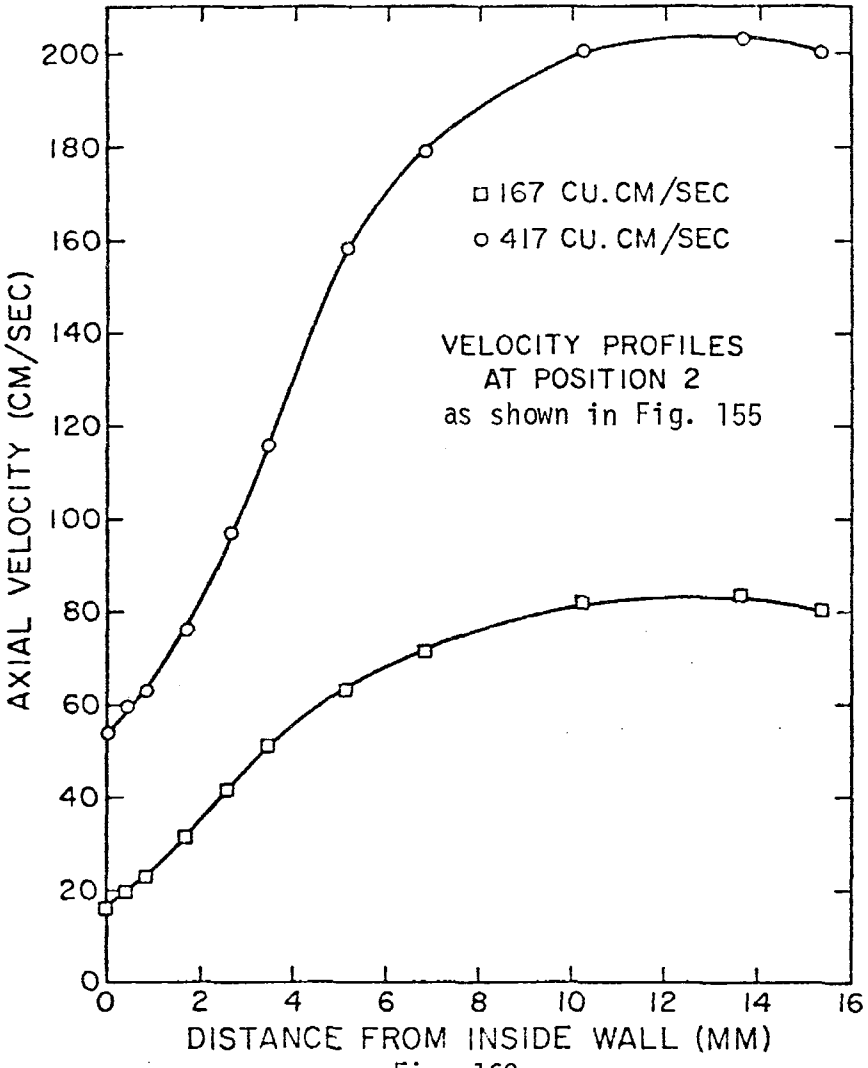

Fig. 160

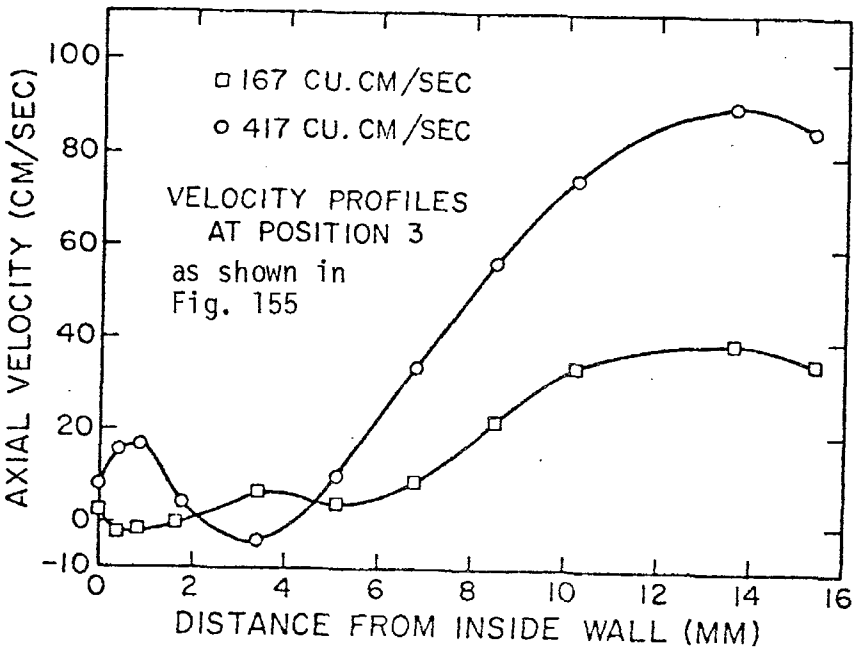

Fig. 161

Velocity profiles in the very near downstream vicinity of the normally functioning Björk-Shiley valve

1 , 4 , 2 , and 3 respectively (see Fig. 155). The velocity profiles in Figures 162 and 163 indicate that by partially occluding the valve, the size of the stagnation area increases and spreads at least as far downstream as X = 25 mm. Figures 164 and 165 show clearly that in addition the flow in the minor outflow area decreased, while the flow in the major outflow area increased compared with the experiments conducted with the non-occluded valve (cf. Figs. 160 and 161).

The stagnation zone observed in the very near vicinity of the outflow face of the disc has not been quantitatively measured, or if measured not reported previously in the literature. Figliola [102] observed the stagnation zone qualitatively in his flow visualization studies under pulsatile flow conditions, at about the same time the present study was being conducted. The observations of the present study are also to be presented elsewhere [116,117]. It is well known that areas of stagnation encourage thrombus formation [9,88,89,90,91]. The in vitro velocity measurements strongly indicate that the stagnation zone in the near vicinity of the outflow face of the disc leads to the thrombus formation in and around the outlet well and/or on the hinge mechanism of the disc. Once the thrombus formation begins, it promotes further growth on the rest of the outflow face of the disc. The degree to which the thrombus formation occurs is probably related to the adequacy of anticoagulant therapy.

With the normally functioning Björk-Shiley valve, the velocity profiles in the near vicinity of the portion of the sewing ring adjacent to the major outflow area (Fig. 154) indicate velocities on the order of 15 to 55 cm/sec very close (0.034 mm) to the inside wall. Such

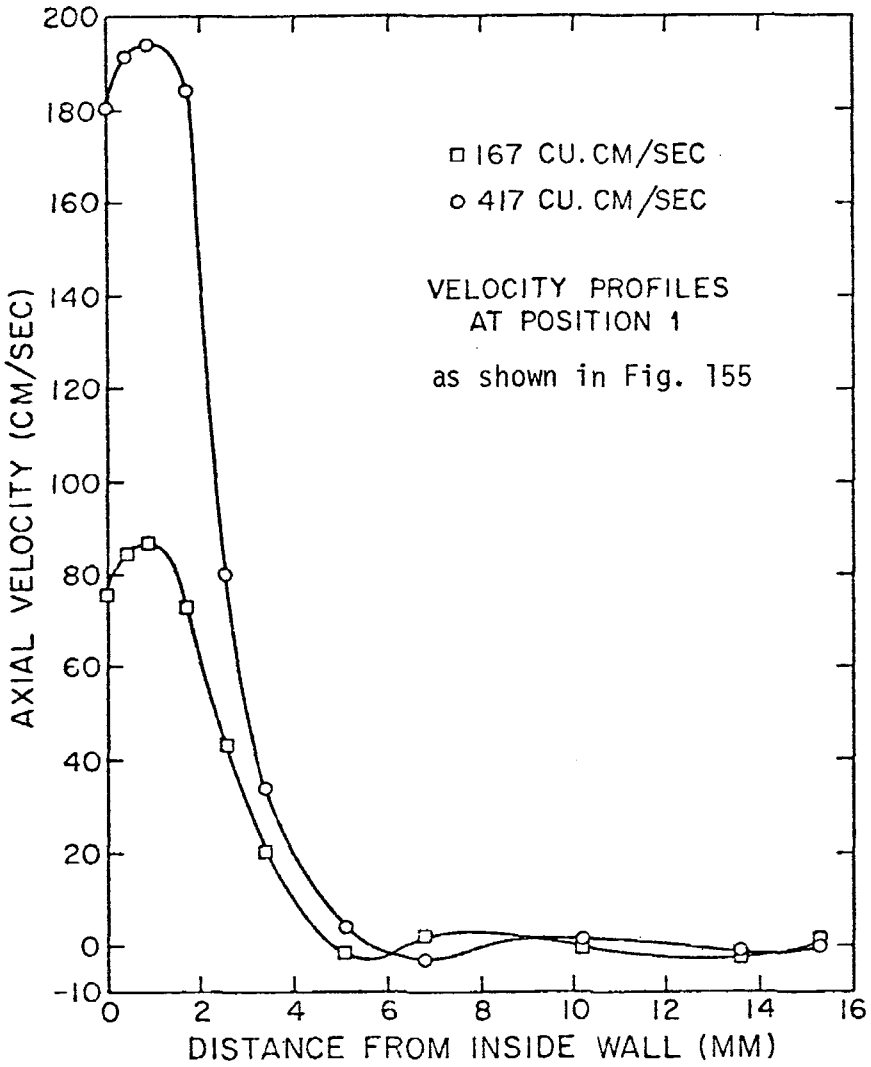

Fig. 162

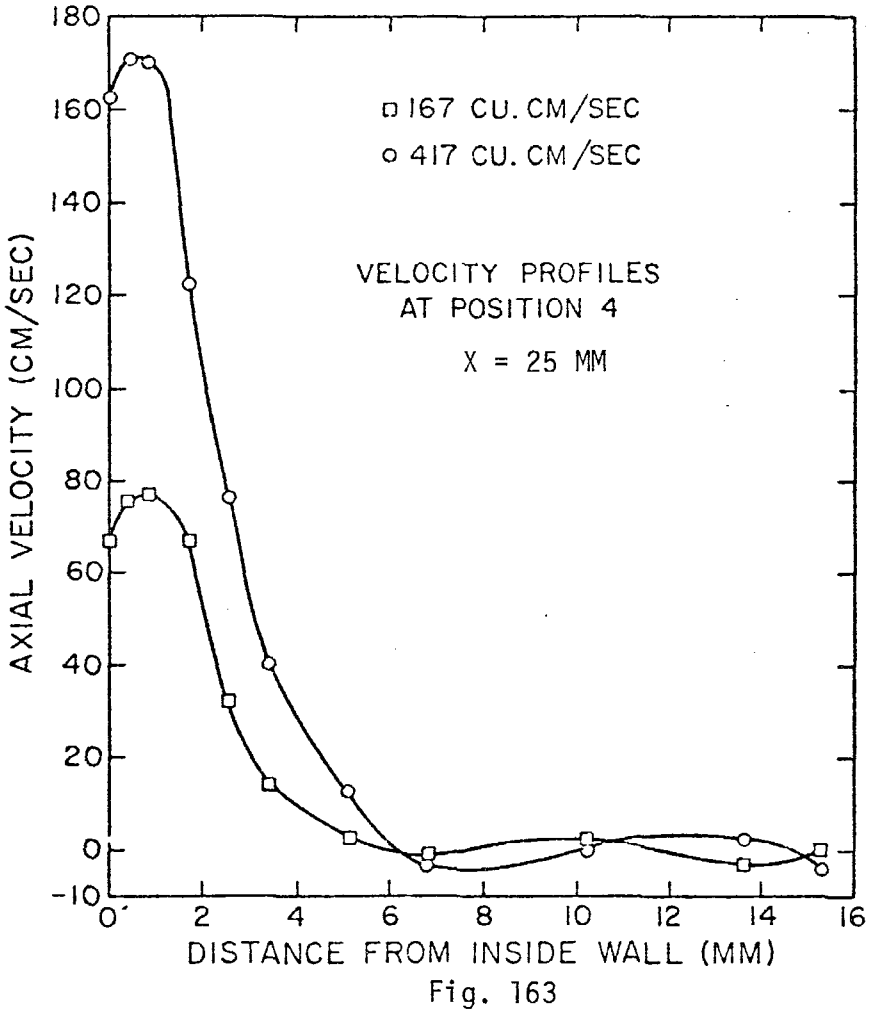

Fig. 163

Velocity profiles in the very near downstream vicinity of the partially occluded Björk-Shiley valve

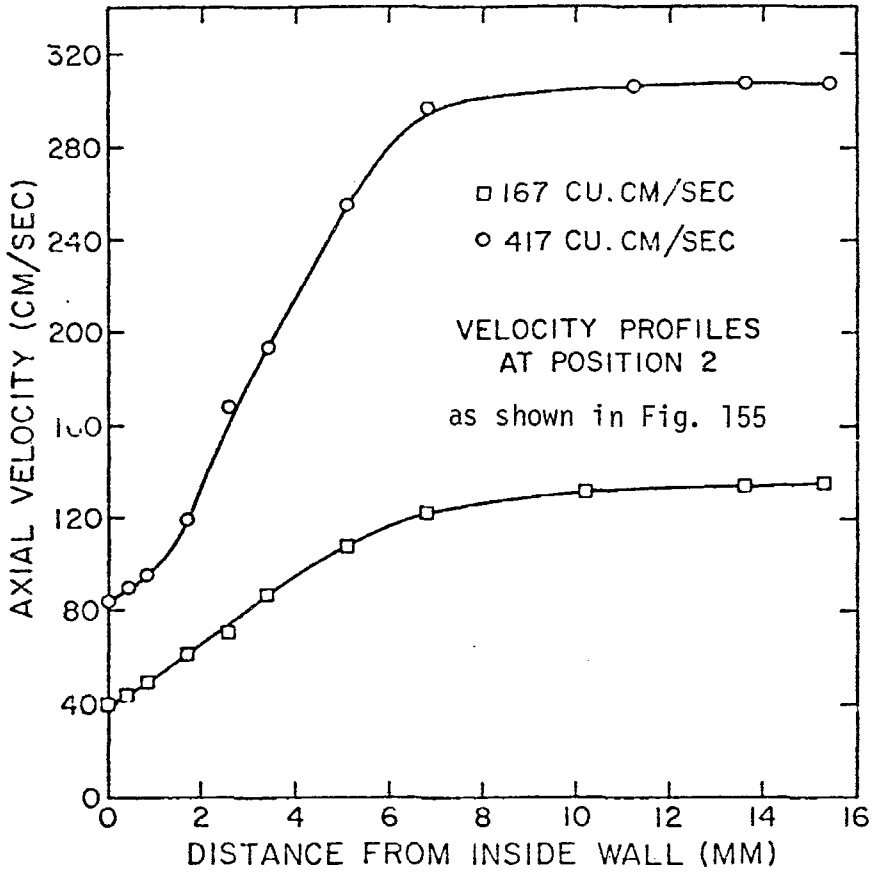

Fig. 164

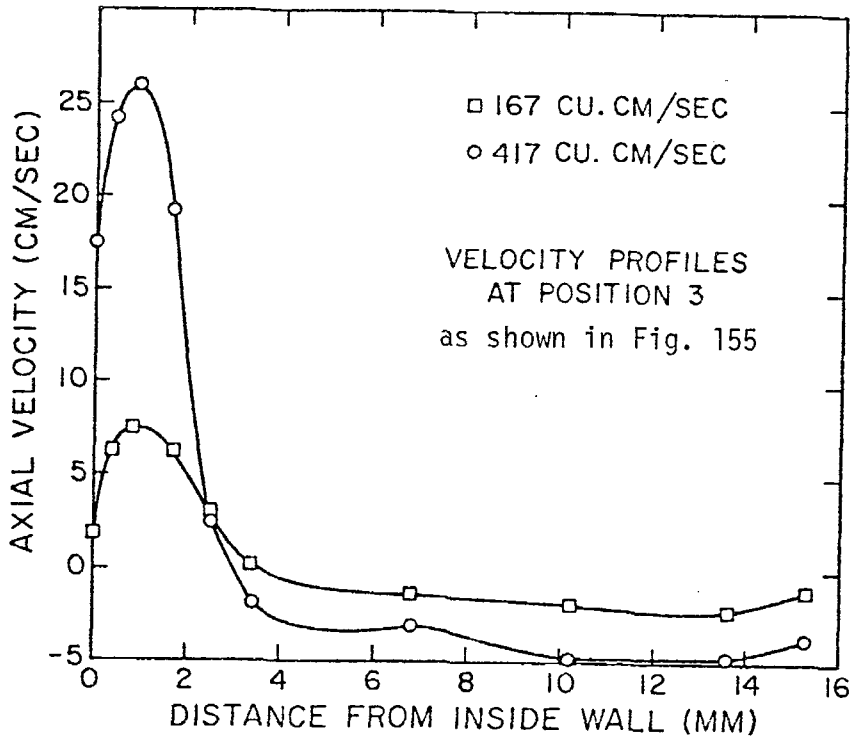

Fig. 165

Velocity profiles in the very near downstream vicinity of the partially occluded Björk-Shiley valve

velocities lead to wall shear stresses of the order of 150 to 550 dynes/cm^2. Similar estimates from the velocity measurements in the minor outflow area (Fig. 155) yield wall shear stresses on the order of 10 to 100 dynes/cm^2. It was also possible to measure velocities within about 0.5 mm from the sewing ring of the prosthesis in both the major and minor outflow areas. Such measurements yielded maximum velocities on the order of 25 to 70 cm/sec and 5 to 15 cm/sec in the major and minor outflow areas respectively. Assuming that such velocities occurred within a distance of about 0.034 mm from the sewing ring (perimeter) of the valve (cf. velocities very close to the inside wall at positions 2 and 3) it is possible to estimate the shear stresses on the sewing ring in both the major and minor outflow areas. Such estimates yield values on the order of 250 to 700 dynes/cm^2 in the major outflow area and 50 to 150 dynes/cm^2 in the minor outflow area. These values are comparable to those observed on the inside wall in the major and minor outflow areas respectively. Fry [94,95] in his studies observed that endothelial cells were damaged and eroded off at shear stresses on the order of 400 to 950 dynes/cm^2. Because the estimated maximum shear stresses on the portion of the sewing ring adjacent to the minor outflow area are well below the critical value of 400 dynes/cm^2, endothelial cells could theoretically grow quite freely and rapidly. In contrast, shear stresses on the portion of the sewing ring adjacent to the major outflow area are in the same range as the critical value and would therefore retard or prevent the formation of endothelial tissue overgrowth on that portion of the sewing

ring. It is clearly the low flow in the minor outflow area that leads to the excessive growth of endothelial tissue in that area. If the prosthesis design could be modified or if it could be implanted in the root of the ascending aorta such that the flow in the minor outflow area was increased, the excessive endothelial growth might be retarded or prevented. Of the above two suggestions the latter one seems quite favorable. In the in vitro experiments the flow approaching the valve was symmetric. In the human body, however, the velocity profiles immediately upstream of the aortic valve are asymmetric. Therefore, it may be advantageous, all else being equal, to implant the Björk-Shiley aortic prosthesis such that the maximum flow approaches the minor outflow area of the valve. It should be noted that the degree to which endothelial tissue build-up occurs at the perimeter of the minor outflow area will probably not be affected by the adequacy of anticoagulant therapy.

The experiments conducted with the minor outflow area of the valve partially occluded are analogous to the clinical cases in which the minor outflow area is partially occluded by thrombus formation, excessive endothelial tissue growth or both. The velocity measurements with the partially occluded valve indicate that not only does the size of the stagnation zone increase in the downstream X direction it also spreads towards the minor outflow area as shown very clearly by Figures 162, 163 and 165. In the velocity profile plot shown in Figure 165 the velocities at distances greater than or equal to 2.5 mm from the inside wall are very small ($\sim \pm 5$ cm/sec). Closer to the

occlusion (X ≃ 1 mm) velocities on the order of ±2 cm/sec were observed. Velocities measured within about 0.5 mm from the sewing ring had maximum values on the order of 2 to 7 cm/sec and 55 to 100 cm/sec in the minor and major outflow areas, respectively. These velocities lead to estimates of shear stresses on the sewing ring on the order of 20 to 70 dynes/cm^2 in the minor outflow area, and 550 to 1000 dynes/cm^2 in the major outflow area. The flow and shear are therefore reduced in the minor outflow area, while they are elevated in the major outflow area, compared with the results obtained with the non-occluded prosthesis. For the partially occluded valve, wall shear stresses on the order of 750 to 1800 dynes/cm^2, 670 to 1620 dynes/cm^2, 400 to 850 dynes/cm^2 and 15 to 175 dynes/cm^2 were measured at positions 1 , 4 , 2 , and 3 respectively.

Therefore, the experiments conducted with the prosthesis partially occluded strongly suggest that once the thrombus formation, excessive endothelial tissue growth, or both processes begin they continue to escalate. The above observation is supported by the clinical findings of the recovered prostheses. The longer the valve is implanted in the patient the greater the chances that one or both of these pathological conditions will probably occur. It should be noted that the nine prostheses recovered were implanted for 6 months or longer. As either or both occluding processes begin to escalate, they begin to impede the movement of the disc of the valve. When a valve is functioning normally, the disc makes an angle of 60° to the Z axis in the fully open position. As the movement of the disc is impeded, the angle the disc makes with the Z axis in the fully open

position decreases. Some of the valves that were recovered only opened to about 30°, while one of the valves had its disc immobilized at an angle of ∿15°. Fernandez et al. [113] have observed seven Björk-Shiley aortic prostheses in which the discs were found to be fixed by thrombus at an angle of about 15°.

When the opening angle of the disc decreases, the pressure drop across the prosthesis increases. The increase in pressure drop leads to additional strain on the left ventricle and could lead to decreased volume of blood flow in the arterial system. Also as the angle of opening of the disc decreases, the velocities and shear stresses in the major outflow area would definitely increase if the volume flow through the valve was about the same as when the valve was functioning normally. If the disc is immobilized in a given position due to one or both of the pathological conditions discussed previously, the valve would become both stenotic and incompetent. It would probably be a matter of days before the patient would die if his condition went undiagnosed. The thrombus formation and excessive endothelial tissue growth, in addition to restricting the opening angle of the disc, also impede the rotation of the disc in the hinge. In a normally functioning valve the disc is free to rotate. When implanted in the cardiovascular system, the disc tends to rotate slowly at random (not a continuous rotation) due to the pulsating nature of the flow in the human body. This phenomenon has also been observed in the pulse duplicator. The random rotation does not eliminate the stagnation zone observed in the very near vicinity of the outflow face of the disc, since the

stagnation zone has been observed qualitatively under pulsatile flow conditions [102]. Because of the rotation, no particular area of the disc undergoes excessive wear due to contact with the hinge mechanism. Assuming a heart rate of 70 min^{-1} the disc would open and shut 3.68×10^7 times per year. If in an implanted Bjork-Shiley prosthesis the disc was unable to rotate, it would probably undergo excessive wear at the location at which the disc contacts the hinge mechanism. The excessive wear of the disc could change its thickness to an extent that it may not be retained in the hinge mechanism, or the disc could undergo material fatigue and fracture. In either case, the whole disc or part of it would be set afloat into the arterial system, and in all probability would lead to the death of the patient.

The thrombus formation and excessive endothelial tissue growth observed in the nine recovered Björk-Shiley prostheses are definitely correlated to the in vitro velocity measurements in the near vicinity of the valve. The two late pathological failure modes, thrombus formation on the outlet face of the disc and excessive endothelial tissue growth along the perimeter of the valve adjacent to the minor outflow area, are attributed to the fluid mechanical design of the Björk-Shiley aortic prosthesis. Correlative studies such as the one described in this chapter are virtually nonexistent in the literature.

Due to the pathological complications associated with the Björk-Shiley prosthesis some design changes are being made on the valve. A tantalum loop has been inserted in the outlet well of the valve. This loop is visible to radiography (X-rays) and therefore by taking

radiographical pictures or movies of the valve it will be possible to calculate the opening angle of the disc. The insertion of the tantalum loop was brought about due to suggestions made to the manufacturer by cardiologists at LA County-USC Medical Center. Also, at present the manufacturer is attempting to make other design changes which will increase the amount of flow in the minor outflow area of the valve.

Chapter 8

SUMMARY AND RECOMMENDATIONS

8.1 Summary

A laser-Doppler anemometer was used for *in vitro* measurements of velocity profiles in the vicinity of aortic prostheses at steady flow rates of 167 cm^3/sec to 417 cm^3/sec. The results showed that all the valves studied created very disturbed flow fields which led to relatively high velocities very close to the flow channel walls and therefore to high wall shear stresses, compared with flow through the channel with no prosthesis placed in the aortic valve chamber. At the higher flow rates the wall shear stresses were on the order of 10^3 dynes/cm^2 in the near vicinity of all the aortic prostheses studied. The wall shear stresses observed in this study are at least two orders of magnitude greater than those reported previously in the literature. The reason that previous workers have been unable to accurately measure wall shears is because their experimental techniques had drawbacks, and they did not measure velocities close enough to the flow channel walls.

Maximum turbulence-intensity levels of about 25 to 50 percent were also measured in the near vicinity of all the prostheses studied, and they decayed to about 15 to 20 percent at 120 mm downstream from the valves. The pressure-drop measurements across the valves gave good order-of-magnitude estimates of the wall-shear stresses. As pressure drops increased across the valves, measured wall-shear

stresses in the sinus region of the flow channel increased. In the near vicinity of the aortic prostheses, estimated bulk turbulent shear stresses were on the order of 10^2 to 10^3 dynes/cm^2. If such wall and bulk shear stresses occurred *in vivo* they could lead to non-endothelialization of the ascending aorta, hemolysis and thrombus formation, which are three of the major complications observed with prosthetic aortic valves. With pulsatile flow, where there is an acceleration phase, the shear stresses would be even larger.

The velocity measurements also revealed the existence of stagnation zones immediately downstream (within 1 to 2 mm) of the fully open poppet of the Starr-Edwards 1260 ball valve (see Figs. 108 and 114), the Starr-Edwards 6520 disc valve (see Fig. 140), and the Björk-Shiley tilting disc valve (see Fig. 120). These areas of stagnation lead to thrombus formation on the superstructure of the valves immediately adjacent to them. The Smeloff-Cutter and Cooley-Cutter aortic valves had relatively high negative velocities immediately downstream of the apex (top) of their cages (see Figs. 126 and 133), which created a backwash effect. Due to the backwash effect the incidence of thrombus formation on the apex of the cages of these two valves is minimal. The quantitative measurements of the stagnation and backwash zones have not been reported previously in the literature.

Velocity measurements in the near vicinity of prosthetic aortic valves are essential in order to improve valve designs for favorable flow characteristics. Such data are virtually nonexistent in the literature, and some were developed in this work.

In the study of the Björk-Shiley tilting disc aortic prosthesis it was possible to correlate successfully the in vitro velocity measurements with two late pathological failure modes observed clinically in nine recovered aortic prostheses at the LA County-USC Medical Center. The two pathological failure modes were thrombus formation on the outflow face of the disc and excessive endothelial tissue growth along the perimeter of the valve adjacent to the minor outflow area. Both failure modes are directly attributable to the fluid mechanics of the valve. The thrombus formation is due to the large stagnation zone created in the immediate downstream vicinity of the fully open disc. The excessive endothelial growth is caused by the low flow, and therefore the low shear stresses ($\leq \sim 150$ dynes/cm^2) on the portion of the sewing ring adjacent to the minor outflow area.

The pressure drops across the ten prosthetic aortic valves studied were observed to be independent of the viscosity of the liquid used for a viscosity range of 0.01 dyne sec/cm^2 to 0.035 dyne sec/cm^2 and flow rates of 83.0 cm^3/sec to 500.0 cm^3/sec. The experiments were conducted under both steady and pulsatile flow conditions. Under steady flow conditions, all valves showed a parabolic relationship between pressure drop and flow rate, as is observed in plain orifices. Pressure drops across prosthetic aortic valves of different designs, however, are not simple functions of their primary orifice sizes, but are complex functions of bluff-body shape and size, and interactions between the fluid and the solid surfaces. For a prosthetic valve of a given design, it is not possible at present to predict pressure drops across a valve of sewing

ring diameter d_1 from experimental data obtained for a valve of the same design of sewing ring diameter d_2.

It was possible for pulsatile flow to predict peak and mean systolic pressure drops from experimental pressure-drop data for steady flow in the same flow channel. The correlation coefficients between the experimental and predicted values were at least 0.98. Therefore, in order to obtain systolic pressure-drop information across aortic prostheses, it may not be necessary to perform extensive experiments under pulsatile flow conditions.

8.2 Recommendations

In this study a laser-Doppler anemometer was used to obtain accurate *in vitro* velocity measurements in the near vicinity of aortic prostheses. In order to obtain further information on the velocity fields in the near vicinity of aortic prostheses, so that better and longer-lasting prostheses may be designed, the author suggests that the work be continued according to the following sequence:

1. Modify the laser-Doppler system so that it may be used in the back-scatter mode. In the backscatter mode velocities which could not be measured in the forward-scatter mode due to the obstruction of the laser beams by the valve poppet can be obtained. For example, the annular flow region between the flow channel wall and poppet surface can be examined in detail.
2. Modify and expand the experimental apparatus in order to measure bulk turbulent shear stresses. In order to measure turbulent shear stresses, the axial and radial velocities at a given location will

have to be measured simultaneously and their fluctuating components cross correlated. A two-color laser-Doppler system will be required to measure the axial and radial velocities simultaneously. An alternative method would be to measure the axial and radial velocities separately, record them on tape, and then process the data on a computer to obtain the turbulent shear stresses. The latter method assumes that the flow field at a given location does not vary with time.

3. Over the past two years the use of Porecine valves has increased. It is predicted that by 1980 Porecine valves will account for about 50 percent of all prosthetic valves used. It is therefore very important that velocity and shear stress profiles be obtained in the near vicinity of Porecine valves.
4. Mock up the aortic valves to be defective, and study the flow fields created by the defective valves, as was done with the Björk-Shiley tilting disc aortic valve in this work. The failure modes used should be those observed in recovered valves at autopsy. Such studies will help in understanding the failure modes from a fluid mechanics standpoint, and could lead to design modifications of the valves.
5. The velocity measurements in this study were conducted under steady flow conditions. In order to test the valves under *in vivo* conditions, *in vitro* velocity measurements must be obtained under pulsatile flow. To obtain velocity measurements under pulsatile flow, an on-line minicomputer would be needed for data acquisition and processing.

In addition, the laser-Doppler anemometer should be used to measure velocity and shear stress profiles in the near vicinity of mitral valve prostheses. For such a study an appropriate valve chamber should be fabricated and appropriate flow rates should be used.

REFERENCES

1. J. H. Knowles, The Struggle to Stay Healthy, Time, August 9 (1976), p. 60-62.

2. C. Casci, R. Fumero and F. Montevecchi in Cardiovascular Flow Dynamics and Measurements, Eds. N.H.C. Hwang and N. A. Normann (University Park Press, Baltimore, Maryland, 1977), Ch. 22, p. 851-875.

3. J.T.M. Wright, The Heart, Its Valves and Their Replacement, Bio-Med. Eng. 7, 26-33 (1972).

4. J.T.M. Wright, Prosthetic Heart Valves: Clinical Requirements, Design and Performance, Bio-Med. Eng. 7, 160-170 (1972).

5. D. Soderlund, The Evaluation of Prosthetic Aortic Valves in Pulsatile Flow, MSc. Thesis, University of Washington (1975).

6. K. A. Merendino (Ed.), Prosthetic Valves for Cardiac Surgery (C. Thomas, Springfield, Ill., 1961).

7. R. Herr, A. Starr, C. W. McCord and J. A. Wood, Special Problems Following Valve Replacement, Ann. Thorac. Surg. 1, 403-410 (1965).

8. D. A. Cooley, R. D. Bloodwell, G. L. Hallman, G. A. Guinn and J. M. Strong, Mitral Valve Replacement with Discoid Prosthesis, Medical Record Ann. 60, 487-502 (1967).

9. J. C. Davila, T. E. Palmer, R. S. Sethi, D. A. DeLaurentis, F. E. Enriquez, N. Rincorm and E. V. Lautsch, The Problem of Thrombosis in Artificial Cardiac Valves, in Heart Substitutes, Mechanical and Transplant, Ed. A. N. Brest (Charles C. Thomas, Springfield, Ill., 1966), p. 25-36.

10. H. P. Chin, E. C. Harrison, D. H. Blankenhorn and J. Macanin, Lipids in Silicone Rubber Valve Prostheses after Human Implantation, Circulation Suppl. I 43-44, 51-56 (1971).

11. W. R. Pierie, W. D. Hancock, S. Koorajiran and A. Starr, Materials and Heart Valve Prostheses, Ann. N.Y. Acad. Sci. 146, 345-359 (1968).

12. W. C. Roberts and W. J. Hammer, Cardiac Pathology after Valve Replacement with a Tilting Disc Prosthesis (Björk-Shiley Type), Am. J. Cardiol. 37, 1024-1033 (1976).

13. W. C. Roberts, Choosing a Substitute Cardiac Valve: Type, Size, Surgeon, Am. J. Cardiol. 38, 633-644 (1976).

14. D. W. Wieting, Ph.D. Thesis, Dynamic Flow Characteristics of Heart Valves, University of Texas, Austin (1969).

15. T. B. Davey, B. Kaufman and E. A. Smeloff, Pulsatile Flow Studies of Prosthetic Heart Valves, J. Thorac. Cardiovasc. Surg. 51, 264-267 (1966).

16. E. A. Smeloff, A. C. Huntley, T. B. Davey, B. Kaufman and F. Gerbode, Comparative Study of Prosthetic Heart Valves, J. Thorac. Cardiovasc. Surg. 52, 841-848 (1966).

17. V. O. Björk and C. Olin, A Hydrodynamic Evaluation of the New Tilting Disc Valve (Björk-Shiley)for Mitral Replacement, Scand. J. Thorac. Cardiovasc. Surg. 4, 37-43 (1970).

18. W. R. Duff, Fluid Dynamics of Prosthetic Cardiac Valves, Ph.D. Thesis, Purdue University (1969).

19. R. L. Kaster, W. C. Lillehei and P.J.K. Starek, The Lillehei-Kaster Pivoting Disc Aortic Prosthesis and a Comparative Study of Its Pulsatile Flow Characteristics with Four Other Prostheses, Trans. Am. Soc. Artif. Intern. Organs 16, 233-243 (1970).

20. W. M. Swanson, Observations on Flow Dynamics of Caged Ball Valves, Proc. 25th ACEMB 14, 113 (1972).

21. E. L. Saklad, A. W. Haln and H. H. Sunn, A Technique for Studying Flow Profiles through Valves, Proc. 20th ACEMB 9, 16.5 (1967).

22. J.T.M. Wright, Private communication (1975).

23. H. L. Falsetti and R. D. Swope, Velocity Profiles in Prosthetic Heart Valves under Steady Flow Conditions, Proc. 29th ACEMB (1976), p. 339.

24. J. H. Forrester, D. W. Wieting, C. W. Hall and M. E. DeBakey, A Comparative Study of the Fluid Flow Resistance of Prosthetic Heart Valves, Cardiovasc. Cent. Bull. (Houston) 7, 83-99 (1969).

25. J. E. Jorgenson, M. G. Harris, W. G. Yates and H. Mohri, Experimental Study of the Steady Flow through a Prosthetic Trileaflet Aortic Heart Valve, Paper #73-WA/Bio-19, ASME Winter Annual Meeting, Detroit, Mich. (1973), pp. 1-13.

26. A. Nauman and C. Kramer, Flow Investigations on Artificial Heart Valves, AGAR Conf. Proc. #65, Paper #4 (1970), pp. 4-1 to 4-8.

27. G. E. Klinzing, R. J. Kuborick and J. E. Marmo, Pressure Distribution Downstream from a Heart Valve for Steady Flow in a Foam Damped Silastic Tube, J. Biomed. Mat. Res. 3, 207-212 (1969).

28. E. J. Roschke, An Engineer's View of Prosthetic Heart Valve Performance, J. Biomat. Med. Dev. Art. Org. 1, 249-288 (1973).

29. S. K. Brockman, H. E. Snyder and H. A. Collins, Jr., Dynamics of Ventricular Pressure, Aortic-Pressure and Flow, and Their Changes after Insertion of the Starr Aortic Valve, Thorac. Cardiovasc. Surg. 50, 253-259 (1965).

30. Edwards Publication on the Starr-Edwards Valves (1974).

31. Shiley Publication on the Björk-Shiley Valve (1976).

32. C. Clark, The Fluid Mechanics of Aortic Stenosis. I. Theory and Steady Flow Experiments, J. Biomech. 9, 521-528 (1976).

33. R. B. Bird, E. W. Stewart and E. N. Lightfoot, Transport Phenomena (Wiley International Ed., Tokyo, Japan, 1960), p. 194.

34. S. Whitaker, Introduction to Fluid Mechanics (Prentice-Hall, Inc., Englewood Cliffs, New Jersey, 1968), p. 444

35. R. F. Steerns, R. R. Johnson, R. M. Jackson and C. A. Larson, Flow Measurements with Orifice Meters (Van Nostrand, New York, 1951), p. 192.

36. S. Whitaker, Introduction to Fluid Mechanics (Prentice-Hall, Inc., Englewood Cliffs, New Jersey, 1968), p. 335.

37. S. Goldstein, Modern Developments in Fluid Mechanics (Oxford University Press, London, 1938), p. 65.

38. A. Fage and F. C. Johnson, On the Flow of Air behind an Inclined Flat Plate of Infinite Span, Proc. Roy. Soc. (London) 116A, 170-197 (1927).

39. J. G. Knudsen and D. Katz, Fluid Dynamics and Heat Transfer (McGraw-Hill, New York, 1958), p. 321

40. H. W. Wallace, D. L. Kenepp and W. S. Blakemore, Quantitation of Red Blood Cell Destruction Associated with Valvular Disease and Prosthetic Valves, J. Thorac. Cardiovasc. Surg. 60, 842-852 (1970).

41. C. Crexell, N. Aerochide, Y. Bonny, G. Lepage and L. Campean, Factors Influencing Hemolysis in Valve Prosthesis, Am. Heart J. 84, 161-170 (1972).

42. B. M. Rodgers and D. C. Sabiston, Hemolytic Anemia Following Prosthetic Valve Replacement, Circulation Suppl. I 39 and 40, I-155 to I-161 (1969).

43. J. R. Walsh and A. Starr, Intravascular Hemolysis in Patients with Valvular Heart Disease, Circulation Suppl. I 39 and 40, I-135 to I-140 (1969).

44. M. T. Brodeur, D. W. Sutherland, R. D. Koler, A. Starr, J. A. Kimsey and H. E. Griswold, Red Blood Cell Survival in Patients with Aortic Valvular Disease and Ball-Valve Prostheses, Circulation 32, 570-581 (1965).

45. P. L. Blackshear Jr., Ch. 19, Mechanical Hemolysis in Flowing Blood in Bio-Mechanics: Its Foundation and Objectives, Eds. Y. C. Fung, N. Perone and M. Anliker (Prentice-Hall Inc., Englewood Cliffs, New Jersey, 1972), pp. 501-528.

46. T. D. Stevenson and H. J. Baker, Hemolytic Anemia Following Insertion of Starr-Edwards Valve Prosthesis, Lancet 2, 982-988 (1964).

47. G. N. Marsh, Intravascular Hemolytic Anemia after Aortic Valve Replacement, Lancet 2, 986-988 (1964).

48. W. C. Roberts, M. C. Fisher and A. Golden, Cardiac Pathology after Valve Replacement by Disc Prosthesis, Am. J. Cardiol. 35, 740-760 (1975).

49. S. D. Slater, I. A. Sallam, W. H. Bain, M. A. Turner and T.D.V. Lawrie, Hemolysis with Bjork-Shiley and Starr-Edwards Prosthetic Heart Valves: A Comparative Study, Thorax 29 624-632 (1974).

50. E. C. Lynch and C. P. Alfrey Jr., Erythrocyte Fragmentation: A Diagnostic Clue in Hemolytic Anemias, Medical Times 97, 125-134 (1969).

51. E. J. Roschke and E. C. Harrison, Fluid Shear Stresses in Prosthetic Heart Valves, J. Biomech. 10, 299-311 (1977).

52. K. A. Mercendino and D. R. Manhas, Man-made Gallstones--A New Entity Following Cardiac Valve Replacement, Ann. Surg. 177, 694-703 (1973).

53. E. F. Bernstein, A. R. Castaneda, P. L. Blackshear Jr. and R. L. Varo, Prolonged Mechanical Circulatory Support: Analysis of Certain Physical and Physiologic Considerations, Surgery 57, 103 (1965).

54. J. D. Hellums and C. H. Brown III Blood Cell Damage by Mechanical Forces, in Cardiovascular Fluid Dynamics and Measurements, Eds. N.Y.C. Hwang and N. A. Normann (University Park Press, Baltimore, Maryland, 1977), pp. 1-42.

55. P. L. Blackshear Jr., F. D. Dorman, J. H. Steinbach, E. J. Maybach, A. Single and R. E. Collingham, Shear, Wall Interaction and Hemolysis, Trans. Am. Soc. Artif. Int. Organs 12, 113 (1966).

56. E. F. Bernstein, P. L. Blackshear Jr. and K. H. Keller, Factors Influencing Erythocyte Destruction in Artificial Organs, Am. J. Surg. 114, 126-138 (1967).

57. C. G. Nevaril, E. C. Lynch, C. P. Alfrey Jr. and J. D. Hellums, Erythrocyte Damage and Destruction Induced by Shearing Stress, Lab. Clin. Med. 71, 784-790 (1968).

58. L. B. Leverett, J. D. Hellums, C. P. Alfrey Jr. and E. C. Lynch, Red Blood Cell Damage by Shear Stress, Biophys. J. 12, 257-273 (1972).

59. S. P. Sutera and M. H. Mehrjardi, Deformation and Fragmentation of Human Red Cells in Turbulent Shear Flow, Biophys. J. 15, 1-10 (1975).

60. E. Richardson, Deformation and Hemolysis of Red Cells in Shear Flow, Proc. Roy. Soc. (London) A338, 129-153.

61. P. L. Blackshear Jr. in Chemistry of Biosurfaces, Vol. 2, Ed. M. Hair (Marcel Dekker, New York, 1971), p. 89.

62. B. N. Najappa, H. Chang, and C. A. Glomski, Trauma of the Erythrocyte Membrane Associated with Low Shear Stress, Biophys. J. 13, 1212-1222.(1973).

63. R. P. Rand, Mechanical Properties of Red Cell Membrane. II. Viscoelastic Breakdown of the Membrane, Biophys. J. 4, 303-316 (1964).

64. P. L. Blackshear Jr., F. D. Dorman and J. H. Steinback, Shear, Wall Interaction and Hemolysis, Trans. Am. Soc. Artif. Int. Organs 11, 112-120 (1965).

65. S. I. Shapiro, M.S. Thesis, University of California, Berkeley (1968).

66. R. M. Hochmuth, N. Mohandas, E. E. Spaeth, J. R. Williamsom, P. L. Blackshear Jr. and D. W. Johnson, Surface Adhesion, Deformation and Detachment at Low Shear of Red Cells and White Cells, Trans. Am. Soc. Artif. Int. Organs 18, 325-332 (1972).

67. J. A. Kochen, Viscoelastic Properties of the Red Cell Membrane, in Hemorheology, Proc. First Int. Conf. University of Iceland, Reykjavik, 1968, p. 421.

68. P. L. Blackshear, Jr. and C. Watters, Observations of Red Blood Cells Hitting Solid Walls, Am. Inst. of Chem. Eng., 65th Natl. Meeting, Cleveland, Ohio, 1969.

69. R. H. Phibbs and A. C. Burton in Hemorheology, Proc. First Intl. Conf. University of Iceland, Reykjavik, 1968, p. 617.

70. K. H. Keller, Effects of Fluid Shear on Mass Transport in Flowing Blood, Federation Proc. 30, 1591-1599 (1971).

71. B. Friedli, N. Aerochide, P. Grondin and L. Campeau, Thrombo-embolic Complications of Heart Valve Prostheses, Am. Heart J. 81, 702-708 (1971).

72. W. C. Roberts and A. G. Morrow, Late Postoperative Pathological Findings after Cardiac Valve Replacement, Suppl. I Circulation 35 and 36, I-48 to I-62 (1967).

73. L. A. Harker and S. J. Slichter, Studies of Platelet and Fibrinogen Kinetics in Patients with Prosthetic Heart Valves, New England J. Med. 283, 1302-1305 (1970).

74. H. S. Wiley, P. P. Steele, H. Davis, G. Pappas and E. Genton, Platelet Survival in Patients with Substitute Heart Valves, New England J. Med. 290, 534-537 (1974).

75. J. R. Walsh, A. Starr and L. W. Ritzman, Intravascular Hemolysis in Patients with Prosthetic Valves and Valvular Heart Disease, Suppl. I Circulation 34 and 35, I-135 to I-140.

76. S. M. Manohitharajah, A. N. Rahman, R. T. Donnelly, P. B. Deverall and D. A. Watson, Platelet Survival in Patients with Homograft and Prosthetic Heart Valves, Thorax 29, 639-642 (1974).

77. C. H. Brown III, L. B. Leverett, C. W. Lewis, C. P. Alfrey and J. D. Hellums, Morpholigical, Biochemical and Functional Changes in Human Platelets Subjected to Shear Stress, J. Lab. and Clinical Med. 86, 462-471 (1975).

78. C. H. Brown III, R. F. Lemuth, J. D. Hellums, L. B. Leverett and C. P. Alfrey, Response to Human Platelets to Shear Stress, Trans. Am. Artif. Int. Organs 21, 35-38 (1975).

79. T. C. Hung, R. M. Hochmuth, J. H. Joist and S. P. Sutera, Shear-Induced Aggregations and Lysis of Platelets, Trans. Am. Soc. Artif. Int. Organs 22, 285-290 (1975).

80. H. Stormorken, Platelets, Thrombosis and Hemolysis, Federation Proc. 30, 1551-1555 (1971).

81. H. Stormorken and P. A. Owren, Physiopathology of Hemostatis, Seminars Haematol. 8, 3-29 (1971).

82. E. W. Salzman, The Events that Lead to Thrombosis, Bull. N.Y. Acad. Med. 48, 225-234 (1972).

83. A. S. Hellem, The Adhesiveness of Human Platelets in Vitro, Scand. J. Clin. Lab. Invest. 12, Suppl. 51, 1-117 (1960).

84. A. Gaarder, J. Johnsen, S. Laland, A. J. Hellem and P. A. Owren, Adenosine Diphosphate in Red Cells as a Factor in the Adhesiveness of Human Blood Platelets, Nature 192, 531-532 (1961).

85. E. Lechler, Die Erythrozytäre Gerinnang-Saktivität, Throm. Diath. Haemorrhag. Suppl. 22, 139-169 (1967).

86. M.J.G. Harrison and J.R.A. Mitchell, The Influence of Red Blood Cells on Platelet Adhesiveness, Lancet, 2, 1163-1164 (1966).

87. Y. Nose, C. S. Kwangett, K. Hino, W. J. Koeff and D. B. Effler, Clot Formation inside the Artificial Heart Device, J. Thorac. Cardiovasc. Surg. 54, 697-706 (1967).

88. H. E. Petschek and R. F. Weiss, Hydrodynamic Problems in Blood Coagulation, AIAA 8th Meeting, Paper #70, 143 (1970), pp. 1-15.

89. J. F. Mustard, H. G. Downie, E. A. Murphy and H. C. Roswell, Extracorporeal Circulation: A Device for the Quantitative Study of Thrombus Formation in Flowing Blood, Circ. Res. 12, 441-448 (1963).

90. B. Kingsley, B. L. Segal and W. Likoff, Principle of Hydrodynamics: Comments on Thrombus Formation, in Engineering in the Practice of Medicine, Eds. B. L. Segal and D. G. Kilpatrick (Williams and Wilkins, Baltimore, Md., 1967).

91. J. F. Mustard, E. A. Murphy, H. C. Rowsell and H. G. Downie, Factors Influencing Thrombus Formation in Vivo, Am. J. Med. 33, 621-647 (1962).

92. P. N. Madras, W. A. Morton and H. E. Petschek, Dynamics of Thrombus Formation, Federation Proc. 30, 1665-1676 (1971).

93. W. C. Roberts and A. G. Morrow, Anatomic Studies of Hearts Containing Caged-Ball Prosthetic Valves, John Hopkins Med. J. 121, 271-295 (1967).

94. D. L. Fry, Acute Vascular Endothelial Changes Associated with Increased Blood Velocity Gradients, Circ. Res. 22, 165-197 (1968).

95. D. L. Fry, Certain Histological and Chemical Responses of the Vascular Interface to Acutely Induced Mechanical Stress in the Aorta of the Dog, Circ. Res. 24, 93-108 (1969).

96. N. Woolf and K. C. Carstairs, Infiltration and Thrombosis in Atherogenesis, Am. J. Path. 51, 373-381 (1967).

97. H. Schlichting, Boundary-Layer Theory (McGraw-Hill, New York, 1968), p. 583.

98. A. Richter and E. Naudascher, Fluctuating Forces on a Rigid Circular Cylinder in Confined Flow, J.F.M. 78, 561-576 (1976).

99. T. L. Shaw, Steady Flow Past Flat Plate in Channel, J. Hy. Div. Proc. Am. Soc. Civil Eng. 6, 2013-2028 (1969).

100. H. Schlichting, Boundary-Layer Theory (McGraw-Hill, New York, 1968),

101. J. O. Hinze, Turbulence (McGraw-Hill, New York, 1976).

102. R. S. Figliola, A Study of the Hemolytic Potential of Prosthetic Heart Valve Flows Based on Local In Vitro Stress Measurements, M.S. Thesis, University Notre Dame, Indiana (1976).

103. R. A. Antonia and R. W. Bilger, The Prediction of the Axisymmetric Turbulent Jet Issuing into a Co-Flowing Stream, Aeronautical Quart. 25, 77-80 (1974).

104. W. Rodi, A Review of Experimental Data of Uniform Density-Free Turbulent Boundary Layers, in Studies in Convection, Ed. G. L. Launder (Academic Press, London, 1976), p. 79-165.

105. S. F. Hoerner, Fluid Dynamic Drag (Hoerner Fluid Dynamics, Midland Park, New Jersey, 1965).

106. L. H. Back, Acceleration and Cooling Effects in Laminar Boundary Layers--Subsonic, Transonic, and Supersonic Speeds, AIAA J. 8, 794-802 (1970).

107. L. H. Back, A Note on Laminar Shear Flow over Impulsively Started Bodies, ASME Trans. Series E, Appl. Mech. 38, 1065-1068 (1971).

108. A. S. Jones, Wall Shear in Pulsatile Flow, Bull. Math. Biophys. 34, 79-86 (1972).

109. H. Daneshyar, Development of Unsteady Laminar Flow of an Incompressible Fluid in a Long Circular Pipe, Int. J. Mech. Sci. 12, 435-445 (1970).

110. S. K. Koncar-Djudjevic' and A. P. Dudukovic', The Effect of Single Stationary Objects Placed in the Fluid Stream on Mass Transfer Rates to the Tube Walls, AIChE J. 23, 125-128 (1977).

111. J. Ben-Zvi, F. J. Hildner, P. A. Chandraratne and P. Samet, Thrombosis on Björk-Shiley Aortic Valve Prosthesis, Am. J. Cardiol. 34, 538-544 (1974).

112. P. A. Chandraratne, J. M. Lopez, F. J. Hildner, P. Samet and J. Ben Zvi, Diagnosis of Björk-Shiley Aortic Valve Dysfunction by Echocardiography, Am. Heart J. 91, 318-324 (1976).

113. J. Fernandez, A. Samuel, S. S. Yang, Sumathisena, A. Gooch, V. Maranhao, G. M. Lemole and H. Goldbert, Late Thrombosis of the Aortic Björk-Shiley Prosthesis, Chest 70, 12-16 (1976).

114. A. Y. Bozer and A. Karamehmetoglu, Thrombosis Encountered with Björk-Shiley Prosthesis, J. Cardiovasc. Surg. 13, 141-143 (1972).

115. D. V. Cokkinos, G. Bakoulas, A. Theodossian and G. D. Skalkeas, Thrombosis of Two High-Flow Prosthetic Valves, J. Thorac. Cardiovasc. Surg. 62, 947-949 (1971).

116. A. P. Yoganathan, W. H. Corcoran, E. C. Harrison and J. R. Carl, Steady-Flow In Vitro Measurements in the Near Vicinity of the Björk-Shiley Aortic Prosthesis, to be presented at the 30th ACEMB meeting, Los Angeles, November 1977.

117. E. C. Harrison, A. P. Yoganathan, W. H. Corcoran and J. R. Carl, The Björk-Shiley Aortic Prosthesis; Flow Characteristics, Thrombus Formation and Tissue Overgrowth, to be presented at the American Heart Association Meeting, Miami Beach, November 1977.

Appendix A-1

The steady flow pressure drop data obtained across pressure taps I and III (Δp_2) and taps I and IV (Δp_3) are presented in tabular form in this appendix. In addition, the peak pulsatile pressure drop data across taps I and III ($\Delta \hat{p}_2$) are presented in graphical form. It should be noted that in Figure A1 through A20 the length of the y-axis is longer than that of the x-axis, even though the figures are log-log plots. The predicted values were obtained from equation (19).

Table A-1. Björk-Shiley 27XMBRP

	Q cm^3/sec	Δp_2 $dynes/cm^2$	Δp_3 $dynes/cm^2$
Test Fluid:	Polyol		
	83	706	600
	167	1833	1426
	250	4039	3013
	333	6985	5199
	375	8898	6572
	417	10877	8011
Test Fluid:	Water		
	85	846	733
	170	2119	1693
	255	4512	3493
	340	7698	5959
	383	9118	7212
	425	11384	8425

Table A-2. Björk-Shiley 25XMBRP

	Q cm^3/sec	Δp_2 $dynes/cm^2$	Δp_3 $dynes/cm^2$
Test Fluid:	Polyol		
	83	766	786
	167	2299	1800
	250	4486	3253
	333	7851	5492
	375	9678	7132
	417	12617	8851
Test Fluid:	Water		
	85	786	767
	170	1953	1573
	255	4952	3933
	340	8431	6065
	383	10351	7638
	425	13203	9504

Table A-3. Smeloff-Cutter A-5

Q cm^3/sec	Δp_2 $dynes/cm^2$	Δp_3 $dynes/cm^2$
Test Fluid: Polyol		
83	840	667
167	3532	3253
250	7511	6838
333	13177	11997
375	16942	15596
417	20808	19182
Test Fluid: Water		
85	1193	1120
170	3699	3253
255	7918	7092
340	13516	12224
383	17516	16263
425	21488	19635

Table A-4. Smeloff-Cutter A-4

Q cm^3/sec	Δp_2 $dynes/cm^2$	Δp_3 $dynes/cm^2$
Test Fluid: Polyol		
83	1066	1013
167	3699	3253
250	7858	7185
333	14076	12557
375	17556	16036
417	21875	19408
Test Fluid: Water		
85	1020	1026
170	3752	3466
255	8431	7585
340	14676	13090
383	18375	16463
425	22834	20035

Table A-5. Cooley-Cutter A-25

Q cm^3/sec	Δp_2 $dynes/cm^2$	Δp_3 $dynes/cm^2$
Test Fluid: Polyol		
83	1246	1146
167	4492	3706
250	9651	8305
333	18969	16516
375	23234	19209
417	29746	26847
Test Fluid: Water		
85	1286	1120
170	4945	4052
255	10564	9331
340	19368	16742
383	24267	20475
425	30886	28206

Table A-6. Cooley-Cutter A-24

Q cm^3/sec	Δp_2 $dynes/cm^2$	Δp_3 dynes/cm
Test Fluid: Polyol		
83	1286	1120
167	5272	4599
250	11497	10091
333	20302	18062
375	25854	23221
417	31799	28380
Test Fluid: Water		
85	1846	1453
170	4992	4599
255	11783	10437
340	20695	18169
383	27033	24234
425	32878	29513

Table A-7. Starr-Edwards 1260-10A (Ball Oscillating at Top of Cage)

Q cm^3/sec	Δp_2 $dynes/cm^2$	Δp_3 dynes/cm
Test Fluid: Polyol		
83	840	667
167	3366	3026
250	7798	7065
333	13683	12450
375	17102	15250
417	21315	19409
Test Fluid: Water		
85	840	786
170	3419	3026
255	7685	6958
340	13629	12344
383	17162	15596
425	21588	19849

Table A-8. Starr-Edwards 2320-10A (Ball Oscillating at Top of Cage)

Q cm^3/sec	Δp_2 $dynes/cm^2$	Δp_3 $dynes/cm^2$
Test Fluid: Polyol		
83	1120	893
167	3646	3253
250	7965	6958
333	14130	12223
375	17836	15596
417	22101	19408
Test Fluid: Water		
85	900	786
170	3646	3253
255	8131	7293
340	14223	12344
383	18342	16383
425	22528	20035

Table A-9. Starr-Edwards 1260-12A (Ball Oscillating at Top of Cage)

	Q cm^3/sec	Δp_2 $dynes/cm^2$	Δp_3 $dynes/cm^2$
Test Fluid: Polyol			
	83	933	800
	167	3386	3106
	250	7531	6892
	333	13277	12290
	375	16762	15396
	417	20681	18742
Test Fluid: Water			
	85	1100	1000
	170	3799	3532
	255	7598	7065
	340	13603	12277
	383	17429	16063
	425	21455	19355

Table A-10. Starr-Edwards 1260-12A (Ball at Middle of Cage)

	Q cm^3/sec	Δp_2 $dynes/cm^2$	Δp_3 $dynes/cm^2$
Test Fluid:	Polyol		
	83	1180	960
	167	4685	4359
	250	10544	9651
	333	18735	17169
	375	23594	21635
	417	29099	26287
Test Fluid:	Water		
	85	1346	1226
	170	5225	4785
	255	11024	10304
	340	19289	17542
	383	24094	21995
	425	29719	26833

Table A-11. Starr-Edwards 1260-12A (Ball at Bottom of Cage)

	Q cm^3/sec	Δp_2 $dynes/cm^2$	Δp_3 $dynes/cm^2$
Test Fluid:	Polyol		
	83	1400	1120
	167	5885	5492
	250	13463	12344
	333	24114	21981
	375	30339	27820
	417	37411	33765
Test Fluid:	Water		
	85	1566	1453
	170	6565	5945
	255	14310	13463
	340	24907	22648
	383	30712	29179
	425	38337	35018

Table A-12. Starr-Edwards 1260-12A (Ball Tied at Top of Cage)

Q cm^3/sec	Δp_2 $dynes/cm^2$	Δp_3 $dynes/cm^2$
Test Fluid: Polyol		
83	1066	893
167	2359	1573
250	5212	3812
333	9251	6612
375	11217	7851
417	14023	9984
Test Rluid: Water		
85	1513	1013
170	2526	1800
255	5045	3479
340	8918	7065
383	11271	8304
425	14136	10984

Table A-13. Starr-Edwards 1260-12A (Ball Removed from Valve)

	Q cm^3/sec	Δp_2 $dynes/cm^2$	Δp_3 $dynes/cm^2$
Test Fluid: Polyol			
	83	667	667
	167	1853	1800
	250	3986	3932
	333	7238	6958
	375	9311	8971
	417	11497	11104
Test Fluid: Water			
	85	613	560
	170	2186	2133
	255	4879	4705
	340	7551	7345
	383	9771	9318
	425	11957	11397

Table A-14. Starr-Edwards 2400-10A (Ball Oscillating at Top of Cage)

	Q cm^3/sec	p_2 $dynes/cm^2$	p_3 $dynes/cm^2$
Test Fluid: Polyol			
	83	1126	1013
	167	3539	3146
	250	8025	6958
	333	14356	12677
	375	18282	16263
	417	22267	19635
Test Fluid: Water			
	85	1106	1013
	170	3759	3452
	255	8138	7038
	340	14616	13211
	383	18795	16809
	425	22754	20181

Table A-15. Starr-Edwards 2400-10A (Ball at Middle of Cage)

Q cm^3/sec	Δp_2 $dynes/cm^2$	Δp_3 $dynes/cm^2$
Test Fluid: Polyol		
83	1180	1013
167	4512	4039
250	10377	9198
333	18055	16035
375	23101	20528
417	28546	25354
Test Fluid: Water		
85	1480	1346
170	4739	4332
255	10457	9611
340	18402	16129
383	23367	21075
425	28806	26274

Table A-16. Starr-Edwards 2400-10A (Ball at Bottom of Cage)

	Q cm^3/sec	Δp_2 $dynes/cm^2$	Δp_3 $dynes/cm^2$
Test Fluid:	Polyol		
	83	1886	1680
	167	6538	5865
	250	14303	13130
	333	25634	23554
	375	32472	29726
	417	40130	36844
Test Fluid:	Water		
	85	1933	1746
	170	6878	6145
	255	14043	13143
	340	26367	23954
	383	33964	30672
	425	42089	38178

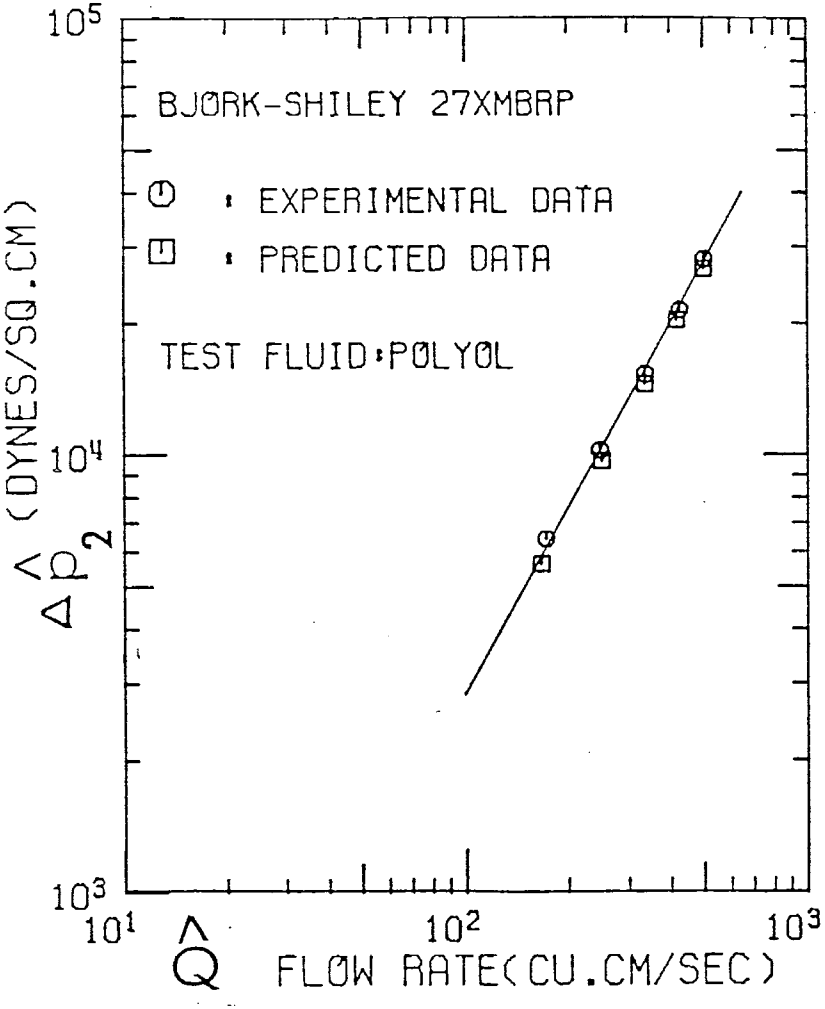

Fig. A1

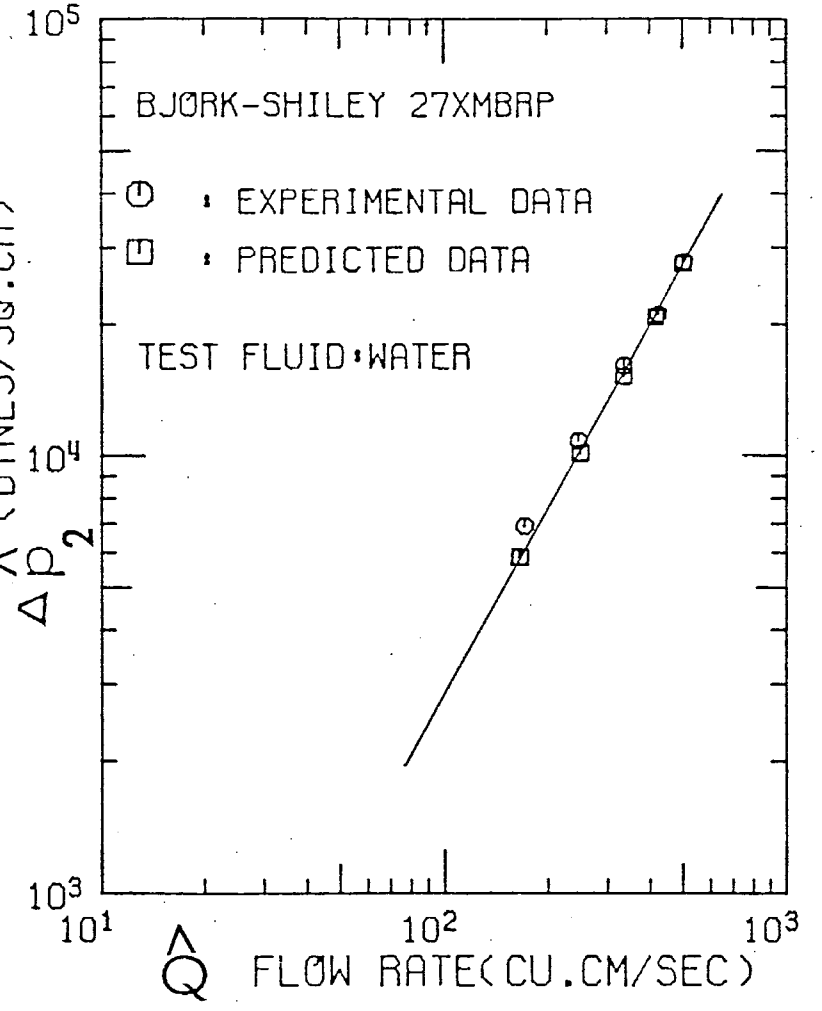

Fig. A2

Peak systolic pressure drop across the Björk-Shiley 27XMBRP valve

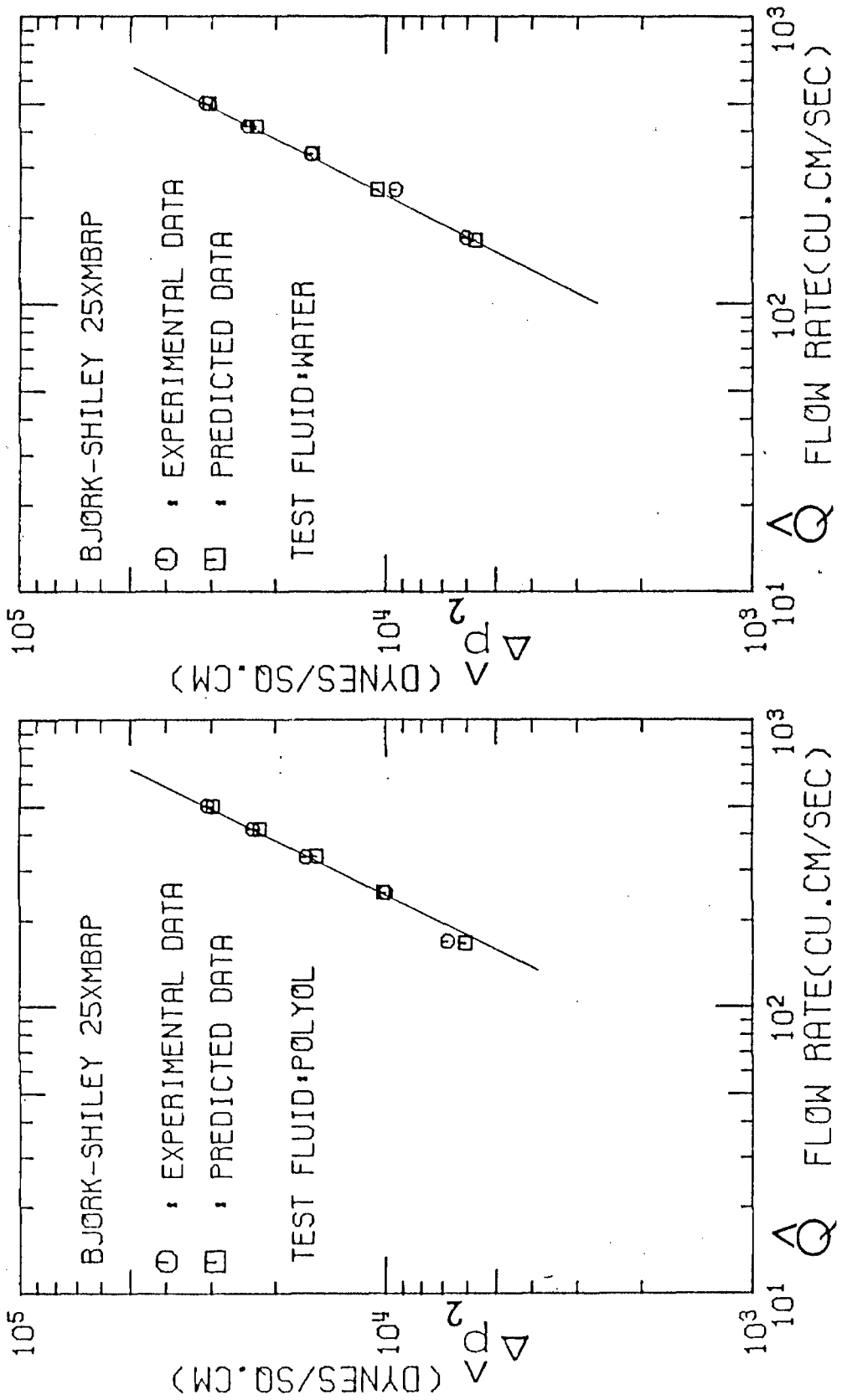

Fig. A3

Peak systolic pressure drop across the Björk-Shiley 25XMBRP valve

Fig. A4

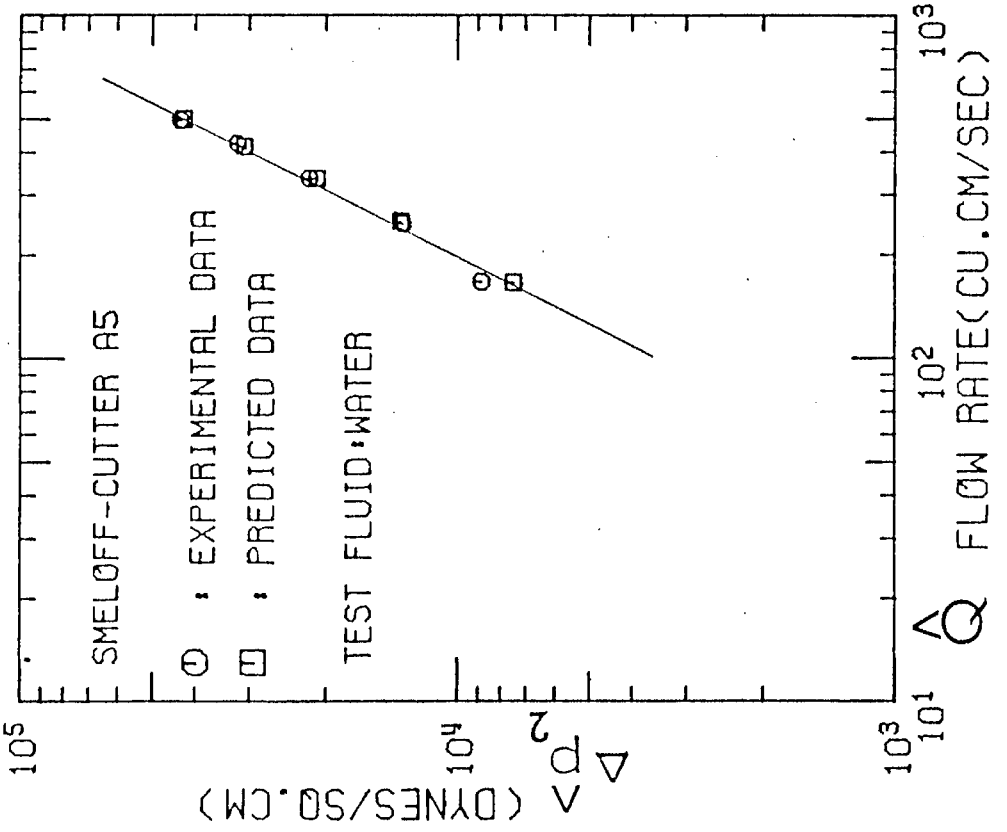

Fig. A6

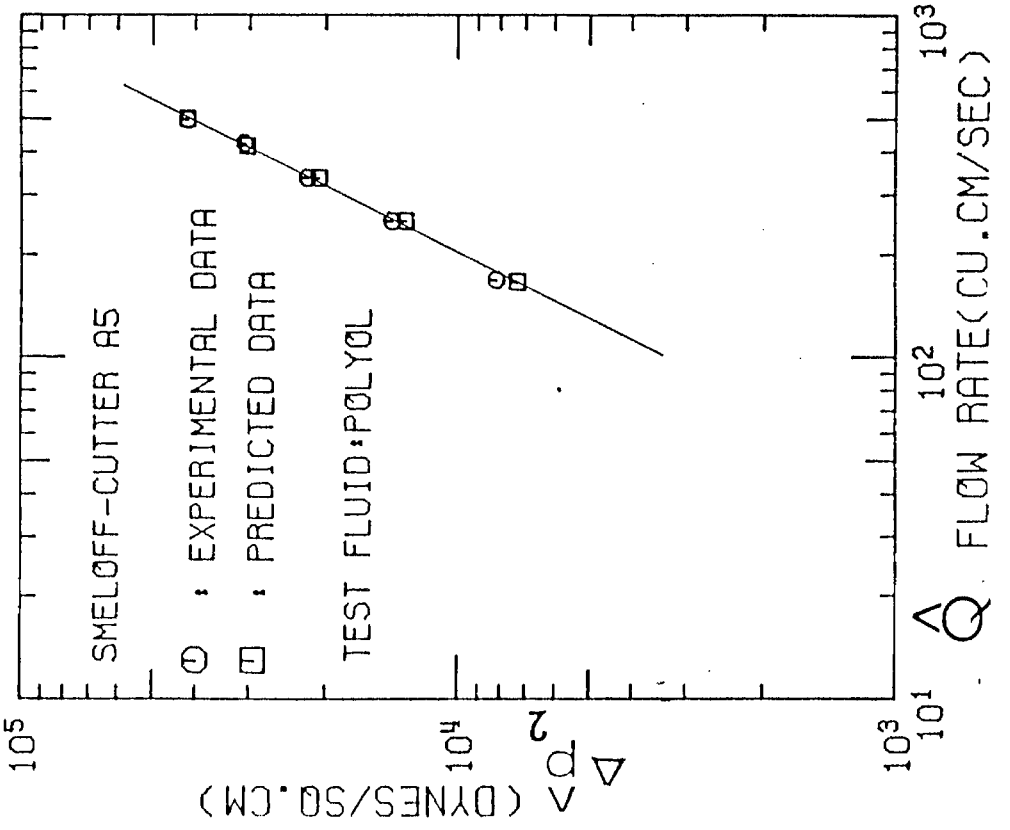

Fig. A5

Peak systolic pressure drop across the Smeloff-Cutter A5 valve

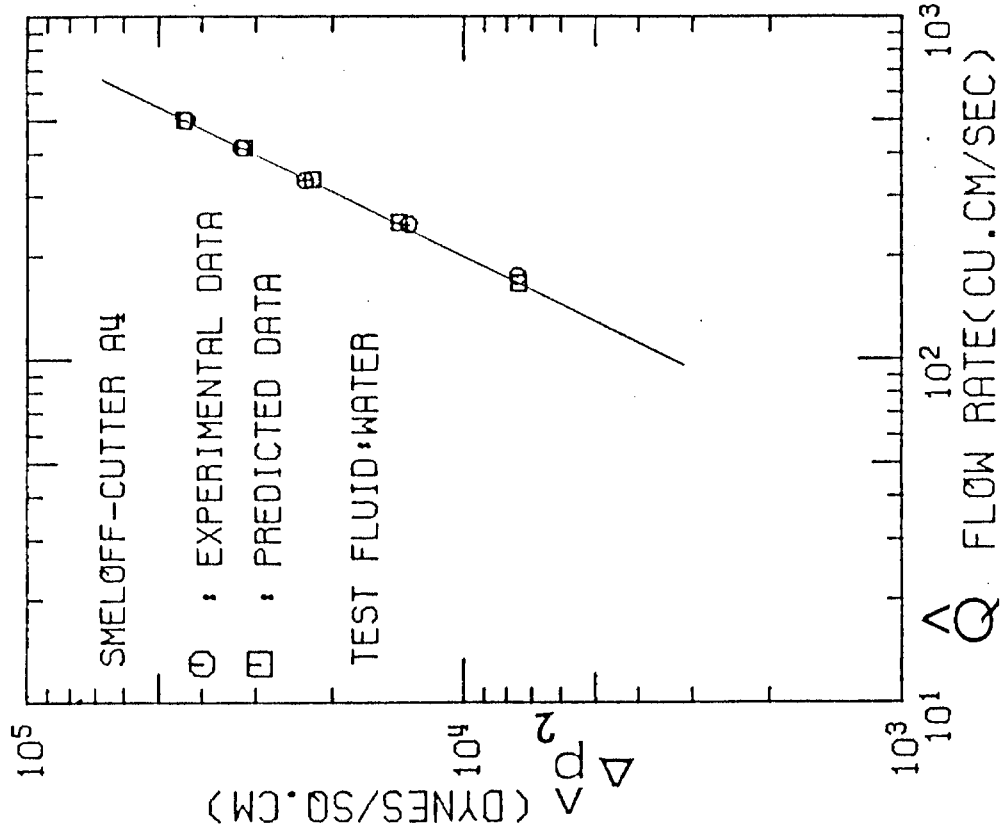

Fig. A8

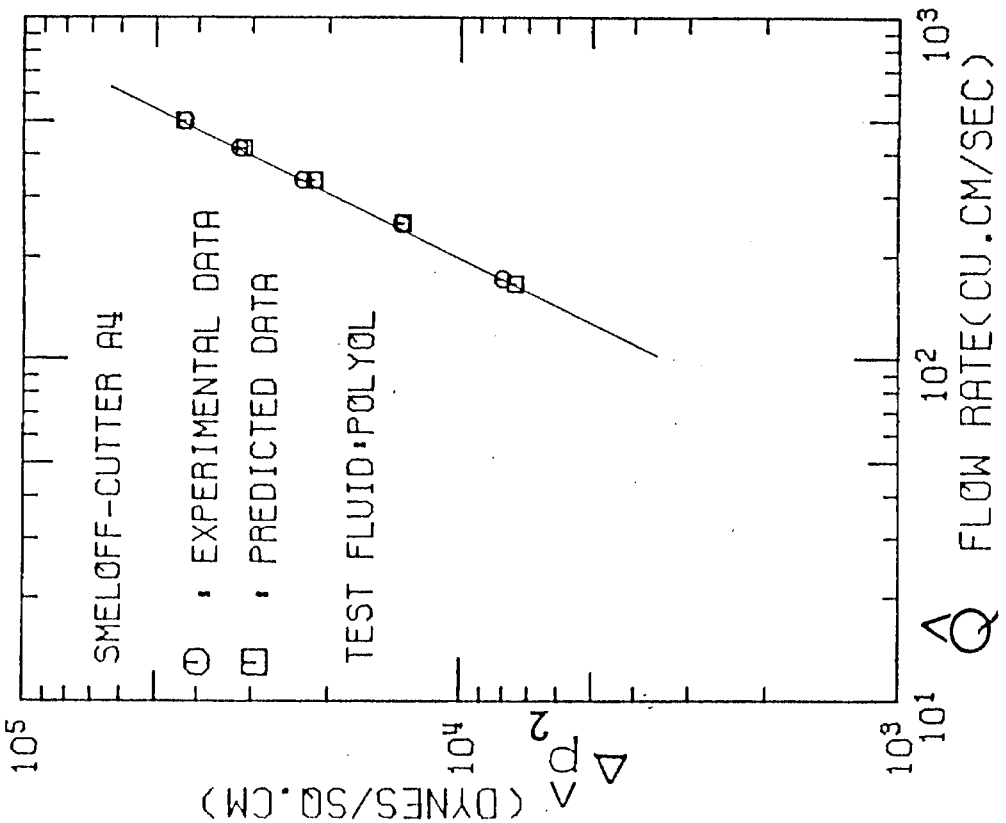

Fig. A7

Peak systolic pressure drop across the Smeloff-Cutter A4 valve

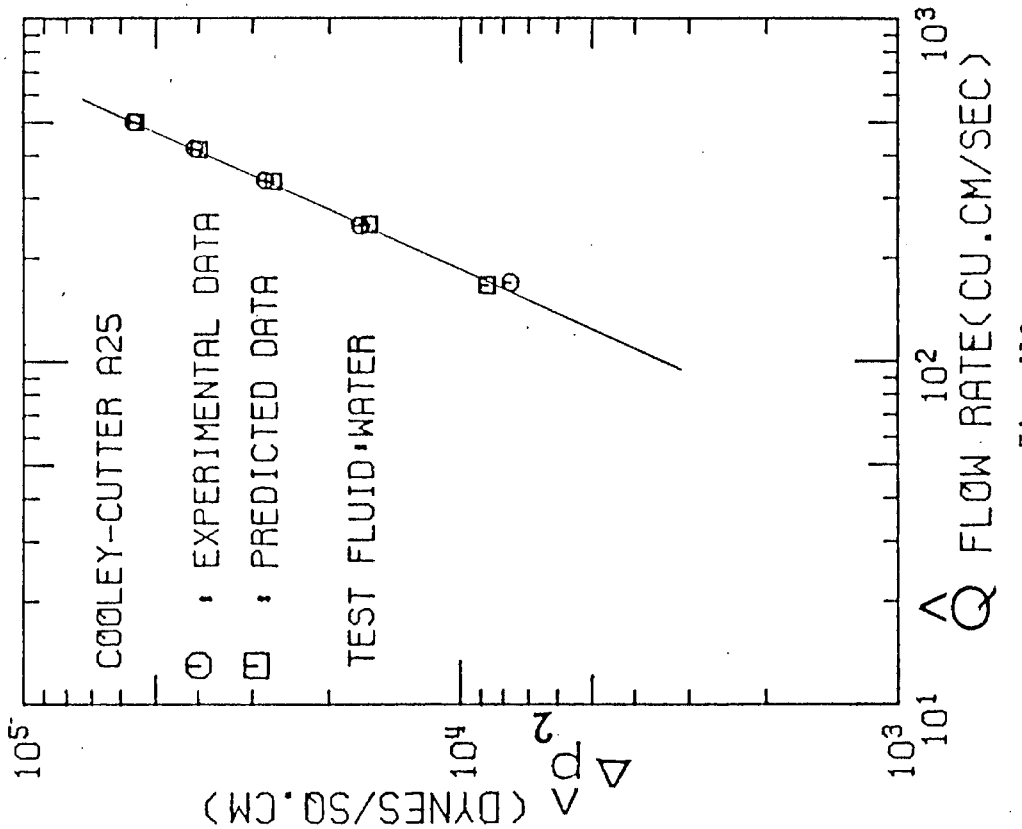

Fig. A10

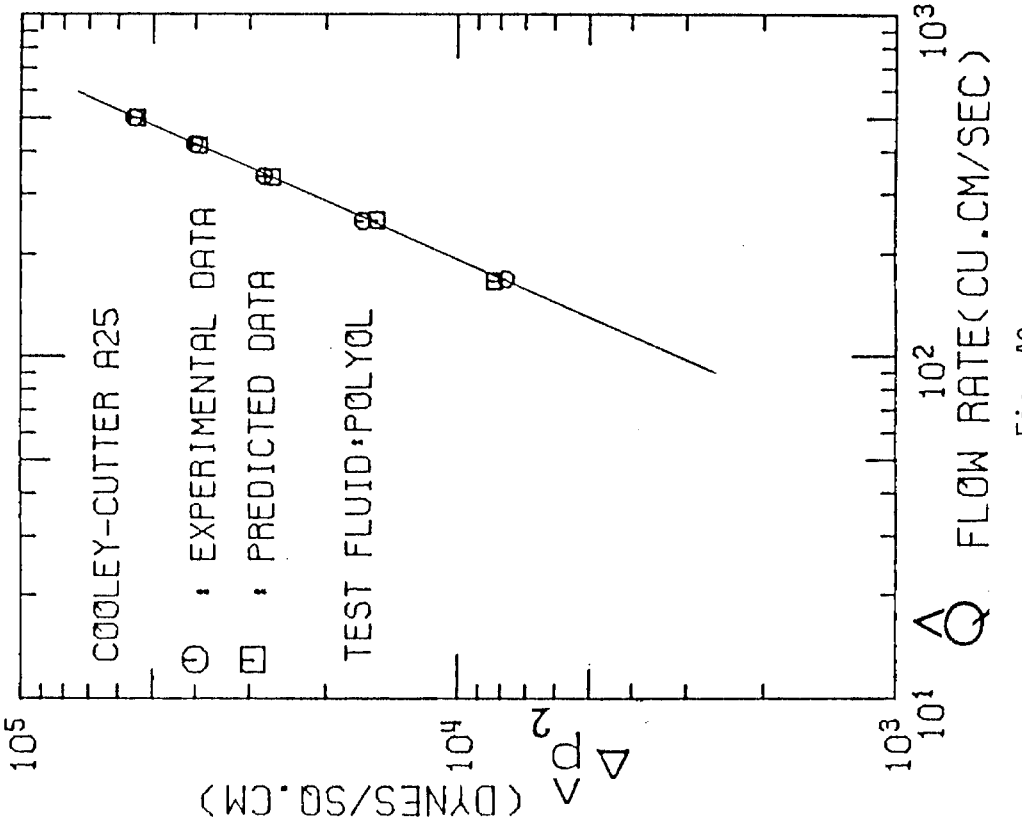

Fig. A9

Peak systolic pressure drop across the Cooley-Cutter A25 valve

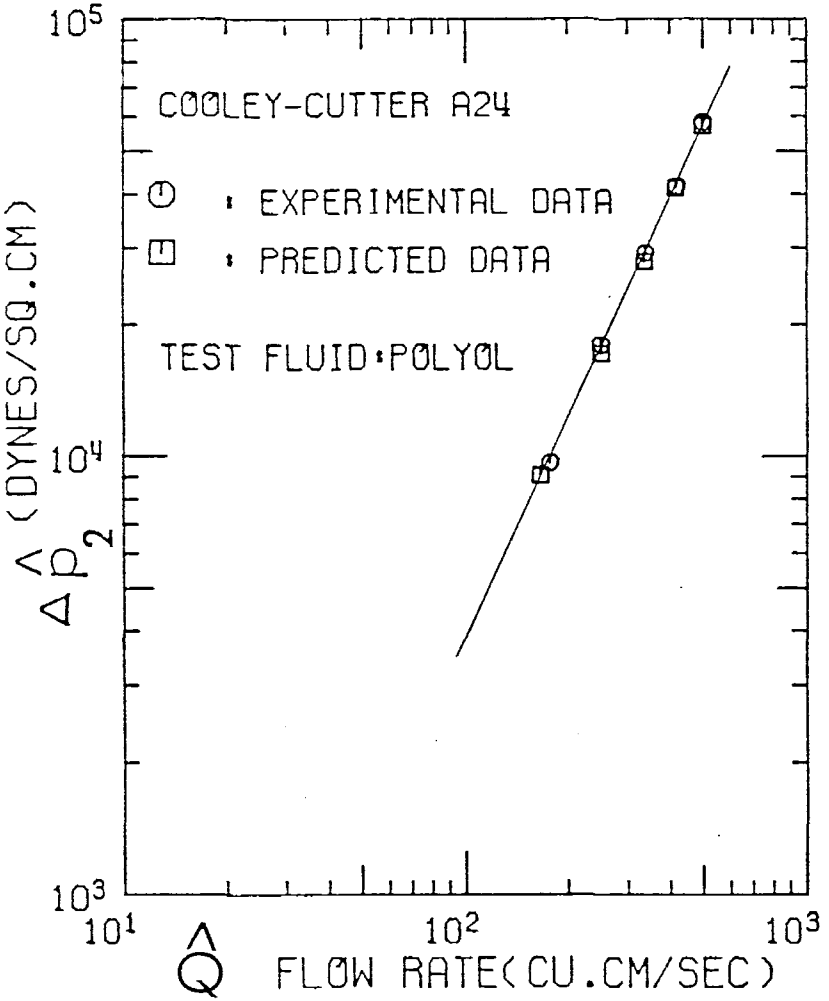

Fig. A11

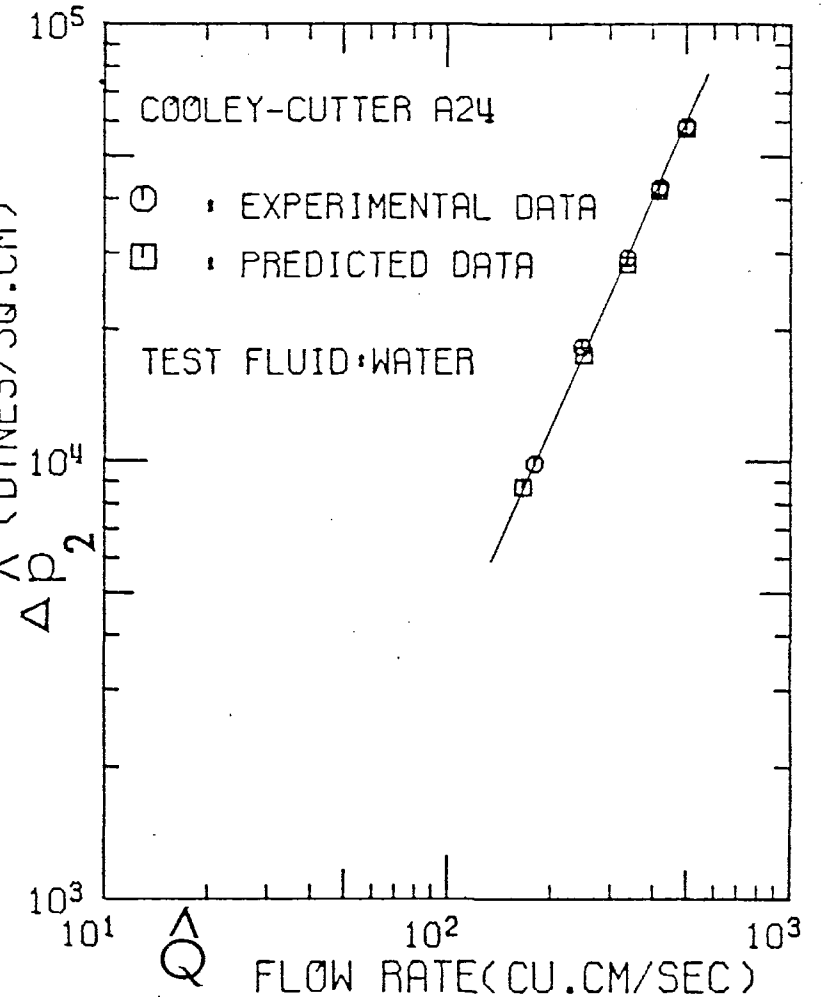

Fig. A12

Peak systolic pressure drop across the Cooley-Cutter A24 valve

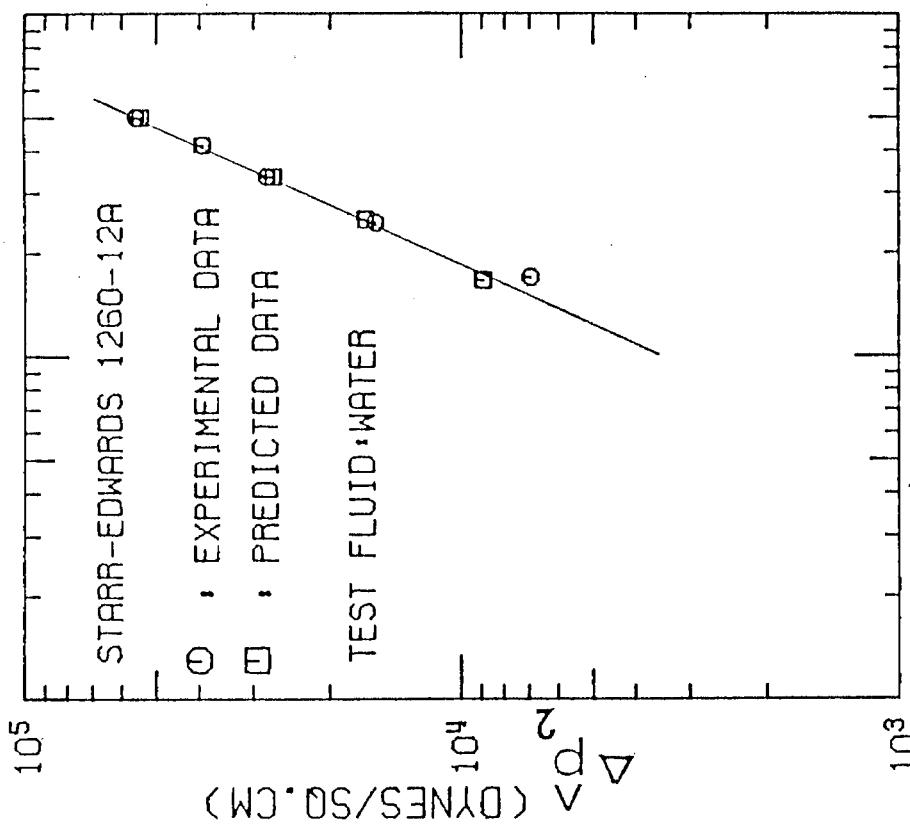

Fig. A14

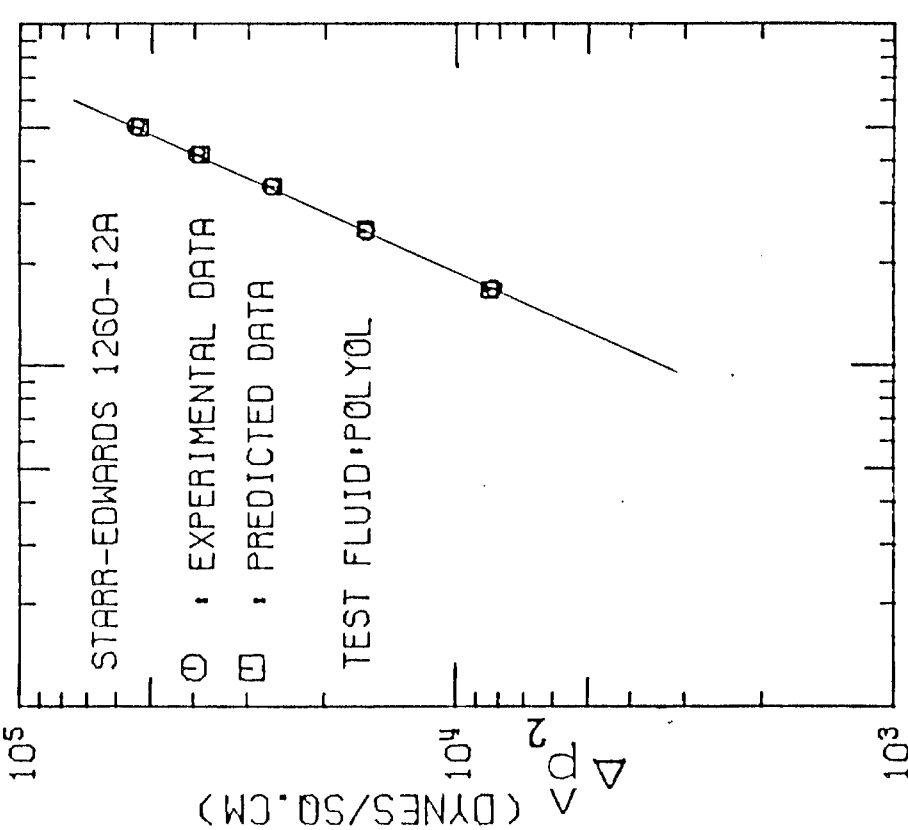

Fig. A13

Peak systolic pressure drop across the Starr-Edwards 1260-12A valve

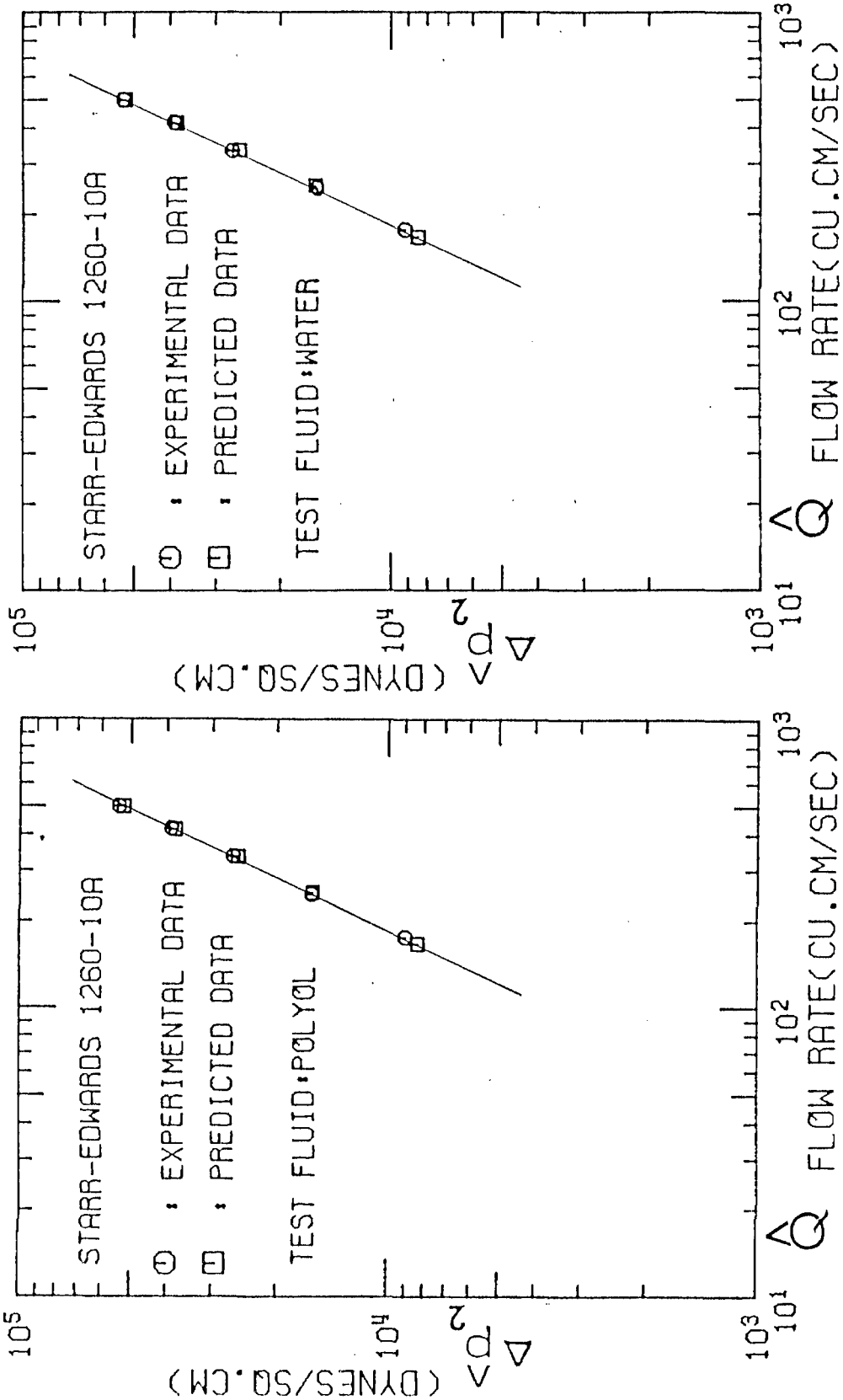

Fig. A15

Fig. A16

Peak systolic pressure drop across the Starr-Edwards 1260-10A valve

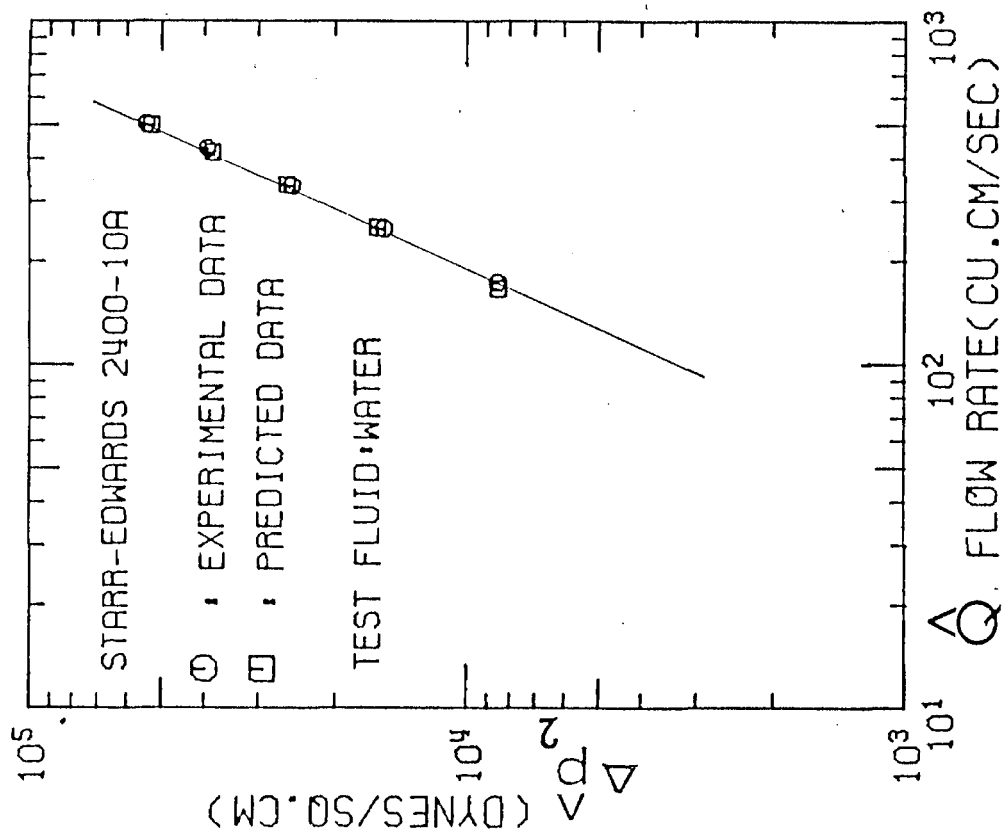

Fig. A18

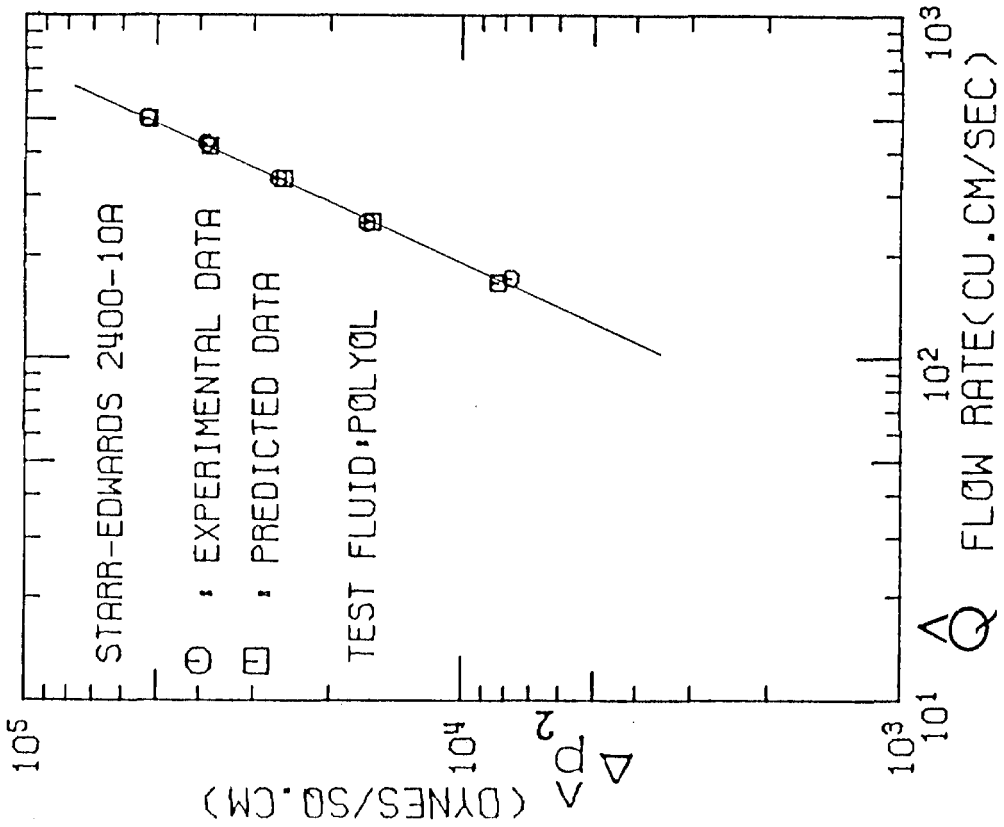

Fig. A17

Peak systolic pressure drop across the Starr-Edwards 2400-10A valve

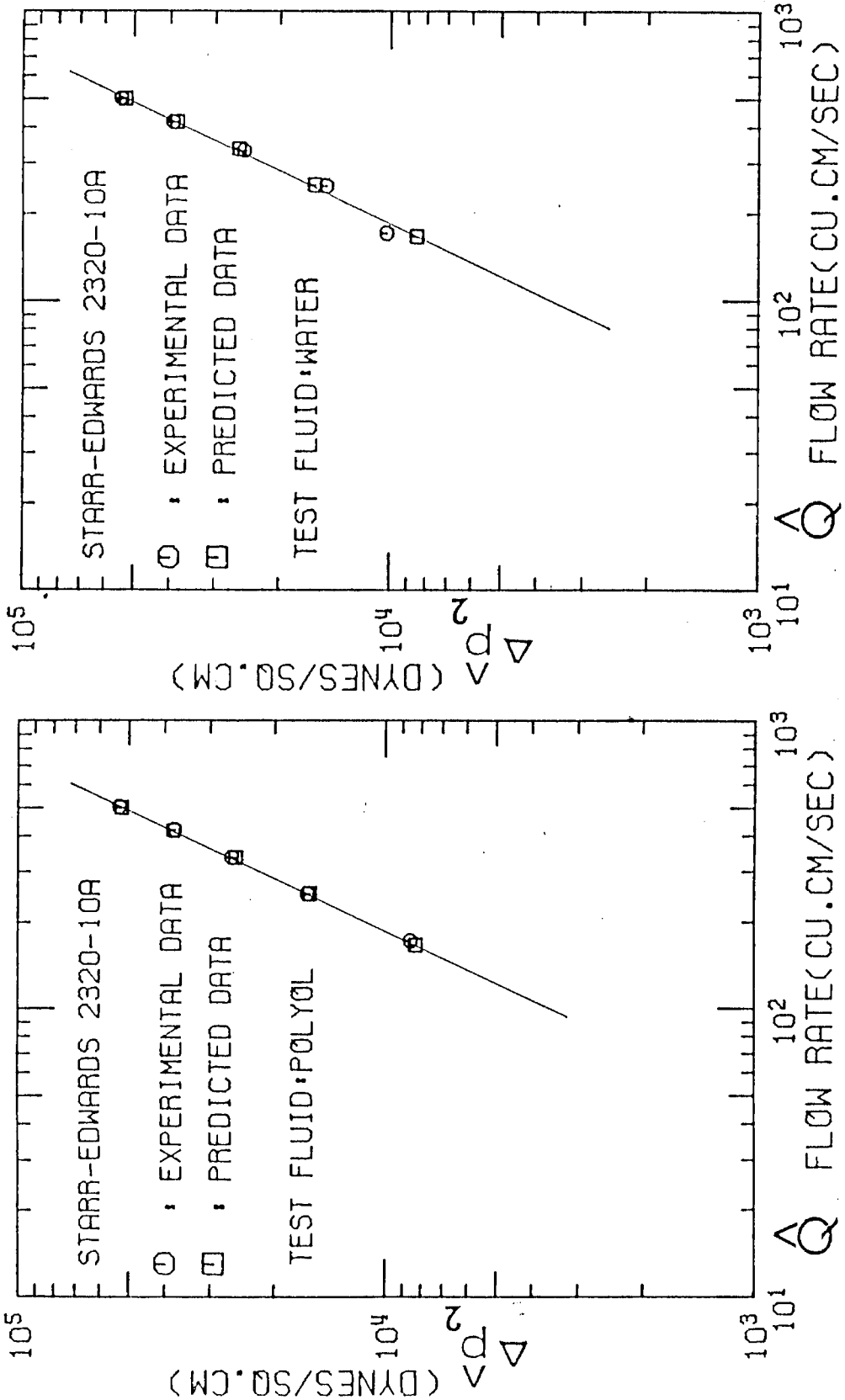

Fig. A19

Fig. A20

Peak systolic pressure drop across the Starr-Edwards 2320-10A valve

PART II: USE OF THE FAST FOURIER TRANSFORM IN THE ANALYSIS OF CARDIOVASCULAR SOUNDS

Chapter 9

INTRODUCTION

Production of heart sounds in the human cardiovascular system has been of interest for many years to cardiologists. Recording of these sounds by means of a microphone is known as phonocardiography. They may be picked up by a microphone placed on the chest of the patient, or by a phonocatheter inserted from the outside into the patient's cardiovascular system. The former technique is non-invasive while the latter is invasive and does cause a certain amount of discomfort to the patient.

The present concept on the production of heart sounds is that the sounds are created by dynamic events related to the blood, walls, and vessels of the cardial structure (i.e., the acceleration and deceleration of blood in the vessels and chambers of the heart)(Rushmer 1970, Luisada 1971). The concept seems to be of value in analyzing cardiovascular action.

The normal human heart produces two main sounds, namely, the first heart sound and the second heart sound. The first heart sound is composed of four main components associated with the hemodynamic events which lead to the ejection of blood from the ventricles into the aortic and pulmonary arteries. The second heart sound which is composed of two main components, is associated with the closing of the semilunar valves in the left and right heart. The normal first heart sound consists of low-frequency signals (< 200 Hz) while the normal second heart sound consists mainly of medium frequency signals (100 to 400 Hz).

Sounds produced by a diseased heart are generally different from those produced by a normally functioning heart. One such common category of sound is produced by murmurs. Murmurs are generally high-frequency sounds and may consist of frequencies as high as 1000 Hz. Heart murmurs are at present attributed to the turbulence created in rapidly flowing blood (Sabbah and Stein 1976). Implanted prosthetic heart valves could also create high frequency sounds because these prostheses lead to very turbulent and disturbed flows in the heart. Some of the prostheses also have high pitched opening and closing clicks.

Phonocardiography is used as a non-invasive method of detecting changes in the heart. As stated by Rushmer (1970) "frequently, murmurs or alterations in the heart sounds are the only definite signs of organic heart disease, appearing long before the stress on the cardiovascular system is sufficient to produce other signs and symptoms". As in many sensitive physiologic-functional tests the distinction between normal and abnormal is difficult to establish in many borderline cases. Nevertheless, phonocardiography is a very useful tool and will be of greater value to cardiologists when a clearer understanding of the nature of the various sounds is obtained. In some cases a distinctive murmur can be definitely associated with an anatomic lesion at the early stages of its development. For example, an aortic stenosis or aortic regurgitation could be identified.

The most common analyses performed with phonocardiograms are:

(1) comparison of amplitudes of different sounds;

(2) comparison of amplitudes of different components of a particular heart sound;

(3) comparison of time intervals between different sounds;

(4) comparison of time intervals between different components of a particular sound;

(5) comparison of the time interval between a known cardiac event and a heart sound;

(6) recognition of a murmur in the amplitude vs time plot of the phonocardiogram.

These analyses provide useful information to the cardiologists. One area for analysis that has not been used extensively is the frequency analysis of heart sounds. Frequency analysis of the various sounds produced in the cardiovascular system should provide information regarding the functional integrity of the heart. Until now, very few studies have been conducted on the frequency content of various heart sounds. The development of the Fast Fourier Transform (FFT) technique by Cooley and Tukey (see Chapter 12) has made frequency analysis of heart sounds and murmurs relatively straightforward and very attractive. In Chapters 10 and 11 the FFT analysis technique has been applied in analyzing the first and second heart sounds in normal man, and was made in order to try out the FFT analysis for studying cardiovascular sounds and to obtain an accurate evaluation of the frequency spectra of the normal sounds. Chapter 14 is an in-depth review of the FFT technique and its application to analysis of biomedical signals. Chapters 10, 11 and 12 are reprints of articles published previously in Medical and Biological Engineering.

Not only may phonocardiography be used to detect and analyze the frequency contents of different types of murmurs, it may be used to monitor the functional integrity of implanted prosthetic heart valves. This area of application is relatively new and may be of great value to cardiologists in detecting a malfunctioning prosthetic valve before fatal damage could occur to the patient. As the first step in such a study, the in vitro sounds produced by six different types of aortic prostheses were analyzed, and the results are shown in Chapter 13.

REFERENCES

A. A. Luisada (1971), Am. J. Cardiol. 28, 127.

R. F. Rushmer (1970), Cardiovascular Dynamics (3rd edition), W. B. Sauders Company, Philadelphia, Pa.

H. N. Sabbah and P. D. Stein (1976), Circ. Res. 38, 513.

Chapter 10

Use of the fast Fourier transform for frequency analysis of the first heart sound in normal man*

Ajit P. Yoganathan Ramesh Gupta Firdaus E. Udwadia†
J. Wayen Miller William H. Corcoran‡

Chemical Engineering Laboratory, California Institute of Technology, Pasadena, California 91125, USA

Radha Sarma John L. Johnson Richard J. Bing

Huntington Memorial Hospital, Pasadena, California 91105, USA

Abstract—*The first heart sound of 29 normal, young males, recorded at the apex of the heart, was analysed for the power content as a function of frequency using the technique of the fast Fourier transform. The frequency spectra were seen to contain peaks in the low-frequency range (10–50 Hz) and the medium-frequency range (50–140 Hz). The average spectrum of the entire study shows a peak at 30 Hz, and an average attenuation of the first heart sound at the apex, of 16 dB/octave. The peaks are probably related to the elastic properties of the heart muscles and the dynamic events causing the first sound. Therefore important diagnostic information might be obtained from frequency studies of heart sounds. Such studies should increase the clinical importance of phonocardiography.*

Introduction

AUSCULTATION is one of the sensitive tests of the functional integrity of the heart. In many cases, murmurs or alterations in the heart sounds are the only definite signs of organic heart disease, appearing long before the stress on the cardiovascular system is sufficient to produce other signs and symptoms (RUSHMER, 1970). Therefore, the recorded phonocardiogram contains very valuable information, which, if analysed quantitatively in a proper manner, could lead to important diagnostic results. Phonocardiography has over the last three decades become a widely used clinical procedure (MCKUSICK, 1958). It is one of the noninvasive techniques available to study and analyse the condition of the human heart. Cardiac auscultation and phonocardiography have significantly improved in recent years because of modern electronic instrumentation and new methods of data collection and analysis. Application of simple, inexpensive, and noninvasive diagnostic methods has long been overdue. Phonocardiography has much to offer towards this goal.

Studies on the various aspects of heart sounds have been carried out by many cardiologists. Of these, LUISADA (1959, 1971) and RUSHMER (1970) have done much of the pioneering work. Recently, ADOLPH *et al* (1970) and VAN VOLLENHOVEN *et al.* (1968) have suggested that significant information can be obtained from frequency analysis of heart sounds. Thus, if diagnostic information has to be extracted from the frequency spectrum of heart sounds, it is essential that accurate studies be done on the various heart sounds both for normal subjects and those with known cardiac diseases.

Until now, very few studies have been made on the frequency spectrum of heart sounds. Moreover, the methods used in these studies have been approximate. For example, frequency spectra have been obtained by sweeping the heart-sound signals with bandpass filters (ADOLPH *et al.*, 1970; SAKAI *et al.*, 1971),

In this study, we have used the fast Fourier transform (f.f.t.) to analyse the first heart sound in 29 normal, healthy, young males. This method of analysis has a high degree of accuracy and was used previously in the analysis of the Korotkoff sounds (GUPTA *et al.*, 1974). The frequency spectra obtained by this method contain peaks, which in turn may be related to the elasticity of the heart muscles and the various dynamic events leading to the production of the first heart sound. These spectra should be of value in the design of filters for heart-sound analysis, as well as in the diagnosis of cardiac disease.

Clinical methods and instrumentation

Healthy, young, 'normal' males from 18 to 38 years of age were used for this study. The absence of heart disease was established on the basis of no known heart ailments and a normal reading for the first six leads of a standard electrocardiogram. All sound recordings were performed in a quiet room, with the subject in a supine position and the microphone placed on the apex area of the precordium.

The equipment used in data collection and analysis is shown in Fig. 1. A contact-type microphone (Hewlett Packard 21050A) was used to obtain the heart-sound signals. A retaining rubber belt ensured that the microphone was maintained at the correct location on the subject's chest. The signal picked up

* *First received 16th December 1974 and in final form 1st January 1975*

† *Department of Civil Engineering, University of Southern California Los Angeles, California 90033*

‡ *To whom all correspondence should be sent*

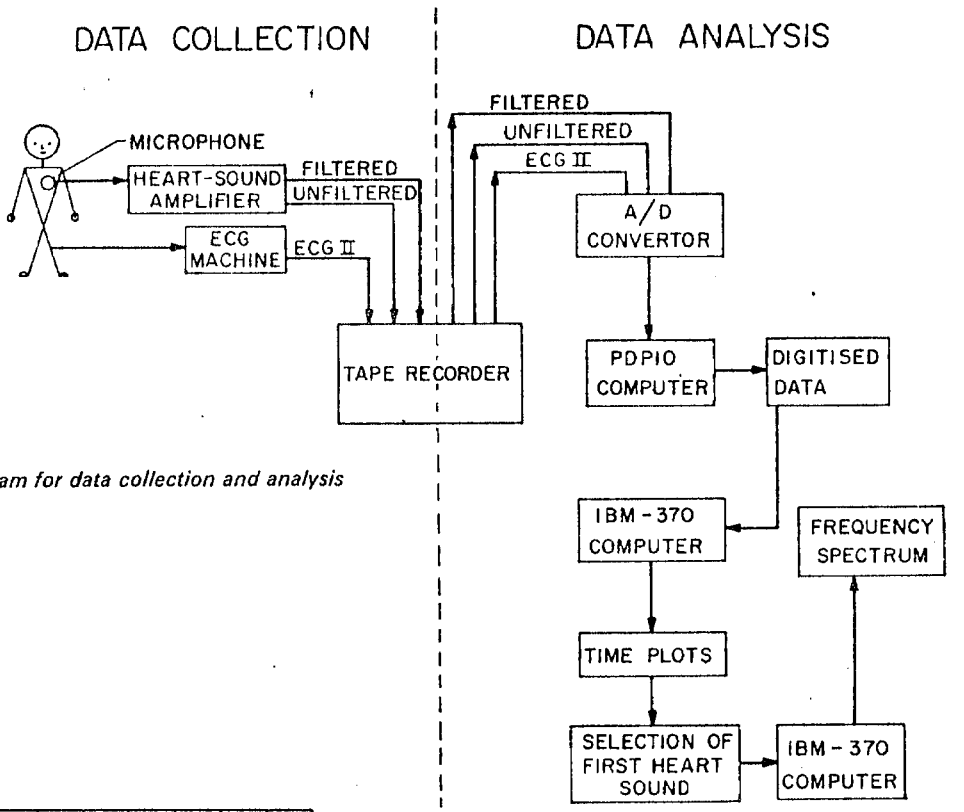

Fig. 1 Flow diagram for data collection and analysis

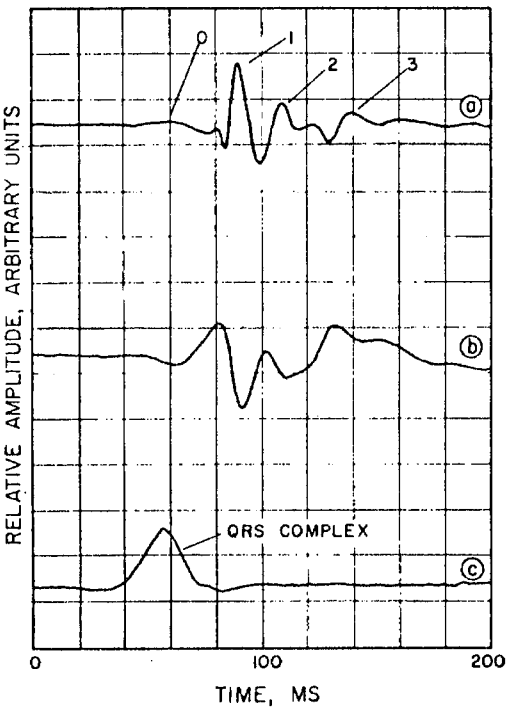

Fig. 2 Typical amplitude/time plot
(a) Filtered first heart sound
(b) Unfiltered first heart sound
(c) e.c.g. lead II

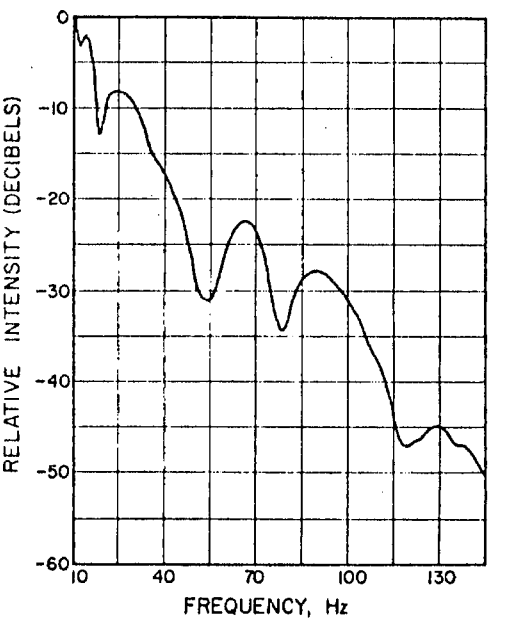

Fig. 3 Frequency spectrum of the first heart sound of subject S 16

by the microphone was amplified by a high-pass amplifier (Hewlett Packard 8813A) and then recorded on an f.m. tape recorder (Hewlett Packard 3960). To ensure that the low-frequency signals would not dominate the high-frequency signals and to improve the signal-to-noise ratio at the higher frequencies, a 12 dB/octave filter with a cutoff frequency of 200 Hz was used on the amplifier. In addition to the filtered heart sound, the unfiltered heart sound and lead II of the e.c.g. were recorded simultaneously on the tape recorder. The lead II of the e.c.g. was used as a time base for the heart sounds. The first sound was identified by its time separation from the QRS complex of the e.c.g. signal.

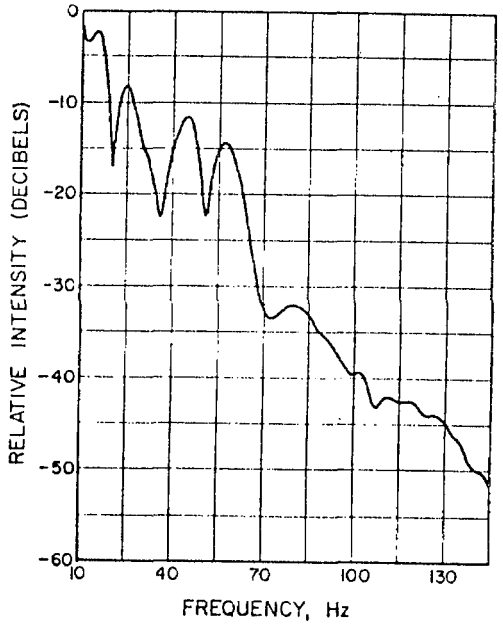

Fig. 4 Frequency spectrum of the first heart sound of subject S 19

Data analysis

The recorded signals were played back from the tape recorder to an analogue-to-digital convertor at the Caltech computing centre, and 30-second epochs of date were digitised for each experiment (digitisation rate of 1000 points per second). The digitised data were stored on a magnetic tape. This tape was then used to generate the time plots on the Calcomp plotter. Fig. 2 shows a portion of a typical plot of the digitised data.

A 250 ms time segment, or window, containing the first heart sound, was selected from each cardiac cycle of the plotted data. A frequency spectrum of each of these 250 ms time segments was obtained using the fast-Fourier-transform algorithm of COOLEY and TUKEY (1965). Finally, a mean-frequency spectrum for each subject was obtained by averaging the spectra of 15 first-heart sounds. This average spectrum was corrected for the 12 db/octave filtering, and the resulting spectrum with a frequency least count of 1 Hz was plotted in graphical form. Typical spectra are shown in Figs. 3 and 4.

The frequency spectra of the 29 subjects were averaged. This average spectrum is shown in Fig. 5. The average frequency spectrum assumes that the 29 spectra have a value of 0 dB at 10 Hz.

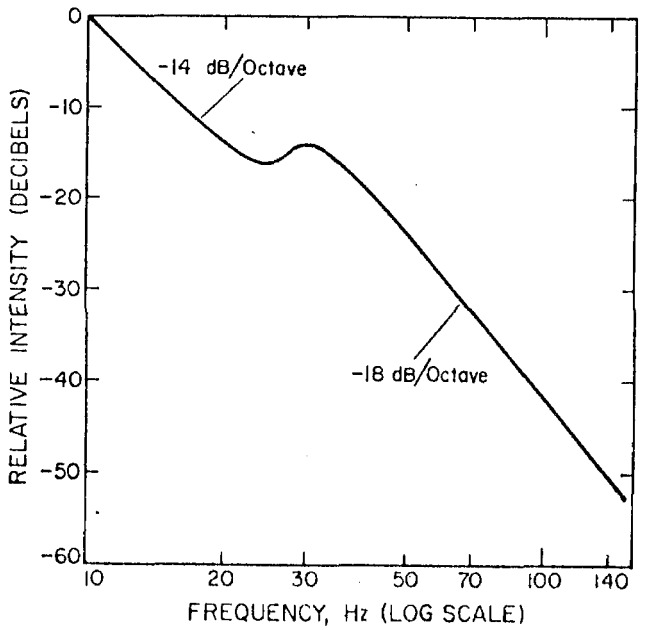

Fig. 5 Average frequency spectrum of 29 subjects

Results

The frequency spectra of the first heart sound of 29 normal healthy males were analysed. It was observed that the first heart sound contains peaks in its frequency spectrum. The observed peaks, which are greater than 2 dB in height, are tabulated in Table 1. For the present study, the analysis was conducted on the heart sounds recorded at the apex. The recordings at the apex are the least attenuated, because the heart is in direct contact with the thorax and should therefore give a good indication of the frequency content of the first heart sound. The reproducibility of the resonant peaks was verified by recording the heart sounds of three of the volunteers twice within a period of four weeks and carrying out the frequency analysis.

Table 1. Frequency peaks in the frequency spectra of the first heart sound of 29 normal males

Subject	Age	Frequency peaks
	years	Hz
S 1	37	30, 46, 70, 97, 124
S 2	24	38, 53, 67, 91
S 3	26	36, 45, 68
S 4	22	27, 40, 67
S 5	28	33, 60
S 6	27	38
S 7	32	21, 44, 76, 97
S 8	23	28, 46
S 9	25	43, 97
S 10	23	33
S 11	23	22, 33, 67
S 12	25	25, 39, 99
S 13	22	22, 33, 48, 130
S 14	24	33, 60, 107
S 15	21	16, 25, 42, 100
S 16	35	25, 66, 89, 128
S 17	26	21, 36, 66, 103
S 18	23	28, 52, 81
S 19	19	25, 45, 58
S 20	27	34, 64, 133
S 21	22	21, 37, 51, 94
S 22	28	29. 76
S 23	25	25, 112
S 24	32	30, 58, 135
S 25	22	16, 28, 41, 115
S 26	21	16, 25, 42, 63, 93
S 27	24	20, 30, 49, 67, 106
S 28	23	33, 50, 87
S 29	24	30, 58, 72, 122

A majority of the subjects had at least three peaks in the frequency spectrum of the first heart sound. The peaks were divided into two frequency ranges. Peaks in the range 10–50 Hz were called low-frequency peaks, and those in the range 50-140 Hz were classified as medium-frequency peaks.

In the low-frequency range, 28 out of 29 subjects were found to have a peak between 25-38 Hz. Moreover, all of these 28 subjects were found to have only a single peak in the frequency interval 25–38 Hz. In the medium-frequency range, 26 of the 29 subjects were found to have peaks. However, unlike the peaks in the low-frequency range, the peaks in the medium-frequency range were not confined to a narrow frequency band but were widely scattered.

These observations are also manifested by the frequency-spectrum curve averaged over the 29 subjects and shown in Fig. 5. The average spectrum exhibits a peak at about 30 Hz. In the medium-frequency range, however, peaking is much less obvious because of the individual variation from subject to subject. The average spectrum has an attenuation of 14 dB/octave between 10 and 25 Hz and 18 dB/octave between 40 and 150 Hz.

There have been very few studies on the frequency analysis of the heart sounds reported in the literature. ADOLPH *et al.* (1970) carried out a frequency analysis of the first heart sound during the isovolumic contraction period, and observed a peak in the power spectrum. This frequency peak was related to the ventricular elasticity. SAKAI *et al.* (1971) have also observed peaks in the power spectrum of the first heart sound. In all of these studies, power spectra were obtained by sweeping the signal with a bandpass filter having a band width of 20 Hz. This procedure gives only an approximate result because the technique has very poor frequency resolution. Also, very narrow bandpass filters must be used if narrow and small peaks are to be detected. The data-analysis technique used in the present study has a higher degree of accuracy and is capable of detecting small peaks in the frequency spectrum of the heart sounds.

Studies by MAAS and WEBER (1952) and HOLLDACK (1952) indicated that in general the attenuation of the first heart sound was about 12 dB/octave. Recently, SAKAI *et al.* (1971) reported that this attenuation is less than 12 dB/octave. In the present study, however, an attenuation of 14 to 18 dB/octave has been observed for the first heart sound at the apex. The difference can, perhaps, be attributed to the different clinical methods and instrumentation used. A knowledge of the true attenuation will help in the design of electronic equipment used to study heart sounds.

An understanding of the peaks observed in the frequency spectra of the first heart sound should give valuable information about the anatomical structure of the heart and may provide important diagnostic information for certain cardiovascular diseases. Generally speaking, these peaks are probably related to the various dynamic events associated with the production of the first heart sound. Thus if each of these peaks can be associated with a different dynamic event or element in the heart, then an important investigative tool will be available to check the functional integrity of the heart.

It is generally accepted that the zeroth and the third components of the first heart sound (Fig. 2) are composed of the low frequencies, and the first and

second components are composed of the medium frequencies. Thus, the peaks in the low-frequency range should correspond to the events associated with the zeroth and the third components. Similarly, peaks in the medium-frequency range should correspond to the first and second components of the first heart sound.

Work is under way to develop a more complete model to explain the observed results. It involves the use of intracardiac phonocatheterisation measurements to associate the peaks with the various dynamic events that give rise to the first heart sound. Also, external and intracardiac phonocardiographic data will be collected from patients with known cardiovascular diseases.

Acknowledgment—We wish to express our appreciation to Hilton Buggs for experimental help. Financial support from the Donald E. Baxter and Ahmanson Foundations is gratefully acknowledged.

References

ADOLPH, R. J., STEPHENS, J. F. and TANAKA, K. (1970) The clinical value of frequency analysis of the first heart sound in myocardial infarction. *Circulation* **41**, 1003.

COOLEY, J. W, and TUKEY, J. W. (1965) An algorithm for the machine calculation of complex Fourier series. *Math. Comput.* **19**, 297.

GUPTA, R., MILLER, J. W., YOGANATHAN, A. P., KIM, B. M., UDWADIA, F. E. and CORCORAN, W. H. (1974) Spectral analysis of arterial sounds: a noninvasive method of studying arterial disease. Submitted to the *J, Med & Biol. Eng.*

HOLLDACK, K. (1952) Ergebrise der inneran Medizin und Kunderheilkunde 3, 407.

LUISADA, A. A. (Ed.) (1959) Symposium on phonocardiography. *Am. J. Cardiol.* **4**, 1.

LUISADA, A. A. (Ed.) (1971) Symposium on cardiovascular sound. *Ibid.* **28**, 127.

MAAS, H. and WEBBER, A. (1952) *Cardiologia* **21**, 773.

MCKUSICK, V. A. (1958) *Cardiovascular sounds in health and disease*. Williams and Wilkins Co., Baltimore.

RUSHMER, R. F. (1970) *Cardiovascular dynamics* 3rd edn. W. B. Saunder Co., Philadelphia.

SAFONOV, Yu D. (1969) The biohydraulic mechanisms producing heart sounds. *Cor Vasa* **10**, 295.

SAKAI, A., FEIGEN, L. P. and LUISADA, A. A. (1971) Frequency distribution of the heart sounds in normal man. *Cardiovas. Res.* **5**, 358.

VAN VOLLENHOVEN, E., VAN ROTTERDAM, A., DURENBOS, T. and SCHLESINGER, F. G. (1968) Frequency analysis of heart murmurs. *Med. & Biol. Eng.* 7, 227.

Usage de la transformation rapide de Fourier pour l'analyse de la fréquence du premier son cardiaque chez l'homme

Sommaire—On an analysé le premier son cardiaque enregistré au sommet cardiaque chez 29 jeunes hommes normaux, pour déterminer sa composition en fonction de la fréquence à l'aide de la technique de transformation rapide de Fourier. On remarqua que la spectre des fréquences contenait des pointes dans la zone des basses fréquences (10–50 Hz) et dans la zone des moyennes fréquences (50–140 Hz). La moyenne du spectre complet de l'étude présente une pointe a 30 Hz et une atténuation moyenne de 16 dB/octave au sommet du premier son cardiaque. Les pointes sont probablement apparentées aux propriétés élastiques de muscle cardiaque et les phénoménes occasionnant le premier son. Des informations diagnostiques importantes peuvent donc être dérivées de l'étude des fréquences des sons cardiaques. De telles études pourraient augmenter l'importance clinique de la phonocardiographie.

Verwendung der schnellen Fourier-Transformierten zur Frequenzanalyse des ersten Herztones beim normalen Menschen

Zusammenfassung—Der erste Herzton von 29 normalen jungen Männern an der Herzspitze wurde auf seinen Energiegehalt als Frequenzfunktion überprüft, wobei das Verfahren der schnellen Fourier-Transformierten verwendet wurde. Es wurde festgestellt, daß die Frequenzspektren Spitzen im niedrigen Frequenzbereich (10–50 Hz) und im mittleren Frequenzbereich (50–140 Hz) enthielten. Das mittlere Spekrtum der gesamten Untersuchung zeigt eine Spitze bei 30 Hz und eine durchschnittliche Dämpfung des ersten Herztons an der Herzspitze von 16 dB/Oktave. Die Spitzen beziehen sich wahrscheinlich auf die elastischen Eigenschaften des Herzmuskels und die dynamischen Vorgänge, die den ersten Ton verursachen. Aus Frequenzuntersuchungen der ersten Herztöne könnte man daher wichtige diagnostische Angaben erhalten. Solche Untersuchungen dürften die klinische Bedeutung der Phonokardiografie erhöhen.

Chapter 11

Use of the fast Fourier transform in the frequency analysis of the second heart sound in normal man*

Ajit P. Yoganathan, Ramesh Gupta
William H. Corcoran

Chemical Engineering Laboratory, California Institute of Technology, Pasadena, California 91125, USA

Firdaus E. Udwadia

Department of Civil Engineering, University of Southern California, Los Angeles, California 90033, USA

Radha Sarma, M.D. Richard J. Bing, M.D.

Huntington Memorial Hospital, Pasadena, California 91105, USA

Abstract—*The second heart sounds of 26 normal, young males, recorded at the aortic and pulmonary areas, were analysed for their frequency content by means of the fast Fourier transform. For both locations of measurement, peaks were observed in the frequency spectra in the low-frequency range (10–80 Hz), the medium-frequency range (80–220 Hz), and the high-frequency range (220–400 Hz). In both the aortic and pulmonary areas, 25 of the 26 subjects had at least two peaks in the 80–400 Hz range, and a majority had one peak in the low-frequency range. A correlation coefficient of 0·75 was obtained between the medium frequency peaks in the aortic and pulmonary areas. The average frequency spectrum obtained for the entire study at each area indicates that the attenuation characteristics are nonlinear in the region of 10–160 Hz. For 160–400 Hz the attenuation in the pulmonary area is about 18 dB per octave and in the aortic area about 23 dB per octave. The observed peaks are probably related to the fluid-dynamic events causing the second heart sound. Thus important diagnostic information can probably be obtained from frequency analysis studies of cardiovascular sounds, and these studies will help in understanding the basic mechanisms which produce the sounds.*

Keywords—*Frequency analysis of heart sounds, Fast Fourier transform*

Introduction

CARDIOVASCULAR disease is a leading cause of death in the United States. It is estimated that nearly half of all the deaths in the United States are caused by disease of the cardiovascular system (Statistical Abstracts of USA 1969). Over the years, modern medicine has developed sophisticated techniques for diagnosing various types of cardiovascular disease. Some of these techniques are invasive such as angiocardiography and catheterisation, and some, such as phonocardiography and electrocardiography, are noninvasive. The need for noninvasive methods has always been present, and phonocardiography could be of great use in achieving this goal.

Even though phonocardiography has been available for 60 years or more, it has been mainly used by physicians in a qualitative manner. It is only over the past 15-20 years that some cardiologists have begun to realise that the ordinary phonocardiogram may contain valuable quantitative information (MCKUSICK, 1955; MCKUSICK, 1959; SAFONOV, 1968; ADOLPH *et al.*, 1970; ARAVANIS *et al.*, 1971; SAKAI *et al.*, 1971). Studies by VAN VOLLENHOVEN *et al.* (1969) have indicated that important diagnostic information may be obtained by the frequency analysis of various heart sounds.

* *First received 23rd June and in final form 12th August 1975*

The frequency analysis of the first heart sound using the fast Fourier transform (f.f.t.) produced some very interesting observations (YOGANATHAN *et al.*, 1975). Therefore a similar study of the second heart sound was undertaken. The use of the f.f.t. to analyse biomedical data is becoming popular (MURRAY *et al.*, 1975; GUPTA *et al.*, 1975). The advantages and proper use of this powerful technique are discussed in a paper by YOGANATHAN *et al.* (1975). Such quantitative analyses of data from normal subjects will help in obtaining a more basic understanding of phonocardiography and the fluid-dynamic mechanisms of production of cardiovascular sounds for application to medical problems. The work reported here was performed to provide that basis. Once such a reference frame is obtained, phonocardiography will become a more powerful diagnostic tool for the clinician.

Clinical methods and instrumentation

This present study was conducted on 26 healthy, young, 'normal' males in the age group of 18 to 38 years. We defined our 'normal' on the basis of no known heart ailments and a normal reading of the first six leads of a standard electrocardiogram. All data were collected in a quiet hospital room with the subject in a supine position and the microphone

placed on the aortic and pulmonary areas of the precordium.

The instruments used for these sound recordings contain up-to-date electronic circuitry. Fig. 1 in the article on the first heart sound by YOGANATHAN *et al.* (1975) shows the equipment used in data collection and analysis. The heart-sound signals were obtained via a contact-type microphone (Hewlett-Packard 21050A). This microphone has a flat frequency response from 0·02 to 2000 Hz. A retaining rubber belt was used to ensure that the

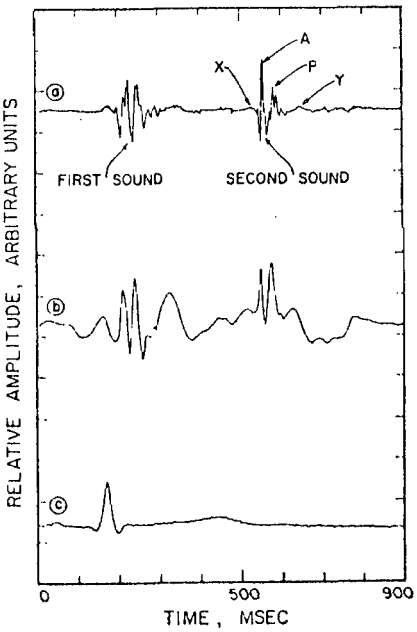

Fig. 1 A typical amplitude time plot
(a) Filtered heart sound
(b) Unfiltered heat sound
(c) Lead II of e.c.g.

microphone was maintained at the correct location on the precordium. The signal from the microphone was fed into a high-pass heart-sound amplifier (Hewlett Packard 8813A) for amplification, and then recorded on an f.m. tape recorder (Hewlett Packard 3960). The heart-sound amplifier consists of two independent amplifying systems. One system amplifies and filters heart sound signals within the frequency range of 25 Hz to 1·5 kHz. The second system simultaneously amplifies low-frequency pulsations within a bandwidth of 0·1 to 100 Hz. The tape recorder is a portable, 4-channel, 3-speed instrument. It is capable of f.m. recording over a bandwidth of d.c. to 5000 Hz. To ensure that the low-frequency signals would not dominate the high-frequency signals and to improve the signal/noise ratio at the higher frequencies, a filter of 12 dB per octave was used on the amplifier. As indicated in Fig. 1, the unfiltered heart sound and lead II of the e.c.g. were recorded simultaneously on the tape recorder in addition to the filtered heart sounds. The lead II of the e.c.g. was used as a time base to identify the different heart sounds.

Data analysis

To analyse the recorded data, the first step was to convert the analogue signal into a digital signal. This was done by playing back on the tape recorder the recorded analogue signal to an analogue/digital converter at the Caltech computing centre. Epochs of data of 30 s duration were digitised for each experiment at a digisation rate of 1000 points per second. The digitised data were then stored on a magnetic tape. This magnetic tape was then used to generate the time plots on the Calcomp plotter, and Fig. 1 shows a portion of typical time-domain plots. By this method of analogue/digital conversion, both the analogue signal and the digital signal were preserved intact.

The next step was the selection of a 250 ms time segment or window, containing the second heart sound, from each cardiac cycle of the plotted data. The method of selection of these time segments is discussed by YOGANATHAN *et al.* (1975). A frequency spectrum of each of these time segments was obtained using the fast Fourier transform algorithm of COOLEY and TUKEY (1965). Then a mean-frequency spectrum for each subject was obtained by averaging the spectra of 15 individual second heart sounds. This averaging procedure helps to eliminate any small variations due to a slight aperiodicity in successive cardiac cycles. Finally, this average spectrum was corrected for the 12 dB per octave filtering, and the resulting spectrum with a frequency least count of 1 Hz was plotted in graphical form. Typical spectra obtained are shown in Figs. 2 and 3.

The frequency spectra of the 26 subjects were averaged. The average spectra for both the aortic and pulmonary locations are shown in Figs. 4 and 5.

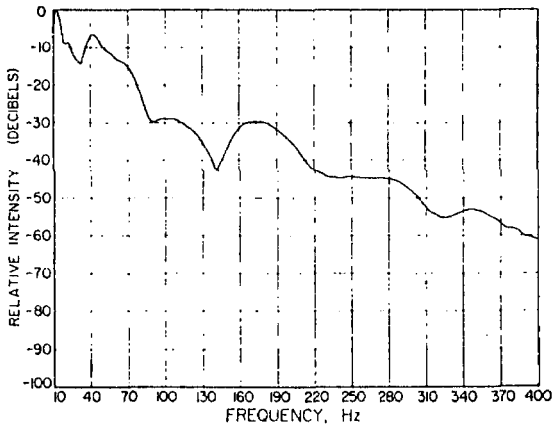

Fig. 2 Frequency spectrum of the second heart sound of subject S 4 at the aortic area

The average frequency spectrum assumes that the 26 spectra have a value of 0 dB at 10 Hz.

Results and discussion

The second heart sound recorded from 26 normal healthy male volunteers was analysed by the fast Fourier transform. The frequency spectra so obtained were found to contain resonant peaks. The observed peaks which are greater than 2 dB in height are tabulated in Tables 1 and 2. Since the second heart sound is heard best in the pulmonary and aortic areas, analysis of the signal from these areas should give a good indication of the frequency content of the second heart sound. The reproducibility of the frequency spectra was confirmed, by recording and analysing the second heart sound from three of the volunteers twice, over a period of a month.

The frequency spectra were obtained over a range of 390 Hz, from 10 Hz to 400 Hz. This range was then divided into three subranges for convenience. The subrange from 10-80 Hz was called low frequency, 80-220 Hz was called medium frequency, and the 220-400 Hz subrange was classified as high frequency. Since no peaks were observed above 400 Hz, the high-frequency range was terminated at this frequency.

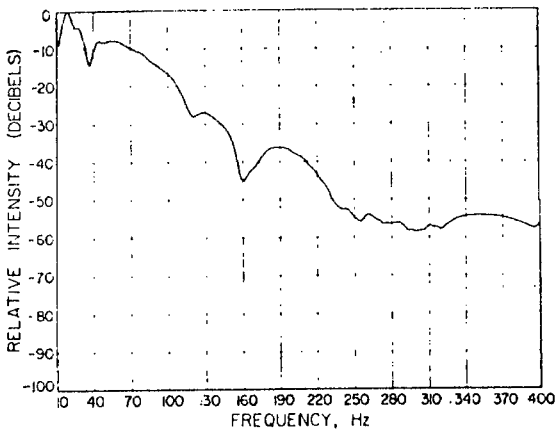

Fig. 3 Frequency spectrum of the second heart sound of subject S 4 at the pulmonary area

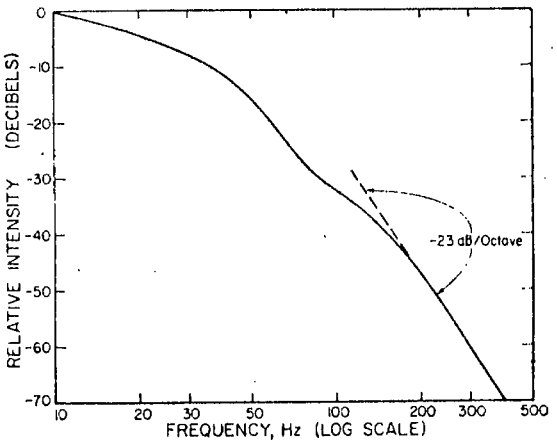

Fig. 4 Average frequency spectrum of 26 subjects at the aortic area

Table 1. Aortic area

Subject	Age	10–80 Hz	80–220 Hz	220–400 Hz
S–1	37	30, 69	115, 187	
S–2	24	31, 57	184, 209	
S–3	26	27, 47	130, 158	295
S–4	22	42	175	347
S–5	28	34	145, 190	
S–6	26	34, 64	108, 163	270
S–7	27	24	136, 187	
S–8	32	25	143	
S–9	25	30	85, 193	
S–10	23	19	93, 159	
S–11	23	24	175, 205	
S–12	25	40	100, 139, 162	
S–13	22	29	103, 175	242, 313
S–14	35	79	122	
S–15	26		158	225, 340
S–16	19	25, 49	123, 182	233
S–17	27	22	100, 183	
S–18	22		115	226
S–19	28	30	175	310
S–20	25	22	115, 220	
S–21	32		112, 181	
S–22	22	25	145	340
S–23	21	28	108	258
S–24	24	28	168	
S–25	23	40	127, 175	
S–26	24	16, 50	130, 178	

The majority of the subjects had at least three peaks in the frequency spectrum of the second heart sound obtained from the aortic area. In this area, 23 of the 26 subjects had peaks in the low-frequency range. Every subject had at least one peak in the medium-frequency range, and the majority (17 out of 26) had two peaks within this range. In the high-frequency range, only ten of the subjects were observed to have resonant peaks in their spectra.

In the pulmonary area, all the subjects had at least three peaks in the frequency spectrum while a majority had four peaks. In this area 25 out of 26 subjects had at least one peak in the low-frequency and medium-frequency ranges. Only half the subjects had two peaks in the medium-frequency range. In the high-frequency range, however, 17 of the 26 subjects were observed to have had resonant peaks in their spectra. Fig. 2 shows a typical frequency spectrum from the aortic area, and Fig. 3 shows the corresponding spectrum from the pulmonary area. A correlation coefficient of 0·75 was obtained between the medium-frequency peaks in the pulmonary area and the aortic area. This correlation coefficient has a 99% confidence limit.

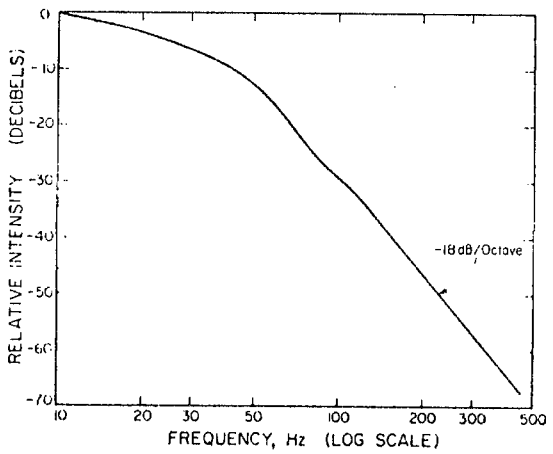

Fig. 5 Average frequency spectrum of 26 subjects at the pulmonary area

It should be noted that the low-frequency and high-frequency peaks in both locations were in most cases smaller in relative intensity (i.e. height) as compared to the medium-frequency peaks. The results tend to show that the second heart sound consists mainly of a medium-frequency (80–220 Hz) signal. There have been very few studies on the frequency analysis of heart sounds. The majority of the studies reported in the literature have been on the first heart sound. Only SAKAI *et al.* (1971) and SAFONOV (1968) have carried out a frequency analysis of the second heart sound in normal man. SAKAI *et al.* report observing gentle 'peaking' between 60 and 220 Hz. The reason for SAKAI *et al.* observing only gentle peaking is probably because they used bandpass filters to obtain their spectra. The disadvantages of using such a technique are discussed by YOGANATHAN *et al.* (1975) in the paper on the

Table 2. Pulmonary area

Subject	Age	10–80 Hz	80–220 Hz	220–400 Hz
S–1	37	25, 42, 70	156	
S–2	24	28, 54	137, 205	
S–3	26	28	152	272
S–4	22	21, 55	190	355
S–5	28	21, 32	168	
S–6	26	31	103, 215	307
S–7	27	49	212	318
S–8	32	25	153	292, 308
S–9	25	40	85, 175	
S–10	23	30	163, 181	
S–11	23	73	156	258
S–12	25	25, 48	130, 198	
S–13	22	46	85	272, 362
S–14	35	25, 70	108, 190	298
S–15	26		85, 148	220
S–16	19	16	116, 212	265
S–17	27	16, 52	203	235
S–18	22	23	157, 202, 216	
S–19	28	25, 46	93, 175, 218	257, 325
S–20	25	36, 70	160, 196	
S–21	32	24		232, 253, 318
S–22	22	30	197	262
S–23	21	28	108	292
S·24	24	27, 46	153	288
S·25	23	40	130, 205	257
S·26	24	22	130, 210	

analysis of the first heart sound. Safonov reports observing peaks in the frequency bands 57–72 Hz, 112–142 Hz and 360–570 Hz. In his study, he analysed the spectral phonocardiograms of 60 young, healthy subjects. In his article, however, he does not discuss the details of his analysis technique.

It is generally accepted that the second heart sound consists of two main components, namely an aortic A and a pulmonary P component (Mori *et al.*, 1964 and Luisada, 1971). It has also been observed by cardiologists (by looking at phonocardiograms) that these components consist of frequencies in the approximate range of 100–500 Hz. Mori *et al.* (1964) also report observing low-frequency vibrations before the aortic component (which they call X) and after the pulmonary component (which they call Y). Components X and Y have also been observed in the study reported here and are shown in Fig. 1. The low-frequency peaks observed in the frequency spectra may be due to the presence of the X and Y components in the time signal. The presence of the aortic and pulmonary components is exhibited by the fact that the majority of peaks obtained are in the range 100–400 Hz. A close look at the results shows that 25 of the 26 subjects have at least *two* peaks in the 80–400 Hz range (i.e., medium-high frequency range) at both the locations. This result suggests that there are at least two mechanically resonant events occurring in the production of the second heart sound.

The present medical theory for the production of the second heart sound is as follows: vibrations of the closed valve, infundibulum, and vessel wall, due to the rebound of the last part of the stroke-mass over the already closed semilunar valves, in both the left and right heart (Luisada, 1971). If the observed peaks in the frequency spectra could be related to various fluid dynamic events occurring in the cardiovascular system, it would then be possible to get a better understanding of the mechanisms which give rise to the second sound.

The average frequency spectrum obtained from the 26 subjects in the aortic and pulmonary areas are shown in Figs. 5 and 6. Because in both locations the peaks in the various ranges are not confined to any narrow frequency bandwidths, the average curves do not exhibit any peaking phenomena which are contrary to the observations with the first heart sound (Yoganathan *et al.*, 1975). The attenuation characteristics of the second heart sound are similar in both locations as can be observed from the average curves presented in Figs. 4 and 5. The amount of attenuation at a particular frequency is on the average 3 to 4 dB less at the pulmonary area than the aortic area. From 10 Hz to about 160 Hz the attenuation in both locations is nonlinear. In the frequency range of 160 Hz ot 400 Hz, however, the attenuation is almost linear. Over this range the pulmonary area shows an attenuation of 18 dB per octave and the aortic area 23 dB per octave. Sakai *et al.* (1971) obtained the attenuation for the pulmonary and aortic components of the second heart sound at the second left intercostal space. They did not, however, report on overall attenuation for the second sound.

Acknowledgment—The authors wish to thank Mr. Wayne Miller for his help in collecting the data. Financial support provided by the Donald E. Baxter and Ahmanson Foundations is gratefully acknowledged.

References

Adolph, R. J., Stephens, J. F. and Tanaka, K. (1970) The clinical value of frequency analysis of the first heart sound in myocardial infarction. *Circulation* **41**, 1003.

Aravonis, C., Feigen, L. and Luisada, A. A. (1971) Durations and intervals of normal heart sounds in man. *Am. Heart J.* **82**, 187.

Gupta, R., Miller, J. W., Yoganathan, A. P., Kim, B. M., Udwadia, F. E. and Corcoran, W. H. (1975) Spectral analysis of arterial sounds: a noninvasive method for studying arterial disease. Accepted by *Med. & Biol. Eng.*

Luisada, A. A. (1971) The second heart sound in normal and abnormal conditions. *Am. J. Cardiol.* **28**, 150.

McKusick, V. A. (1955) Further observations by means of spectral phonocardiography. *Circulation* **11**, 849.

McKusick, V. A. (1959) Spectral phonocardiography. *Am. J. Cardiol.* **4**, 200.

Mori, M., Shah, P. M., MacCanon, D. M. and Luisada, A. A. (1964) Hemodynamic correlates of the various components of the second heart sound. *Cardiologia* **44**, 65.

Murray, A. and Neilson, J. M. M. (1975) Diagnostic percussion sounds: a qualitative analysis. *Med. & Biol. Eng.* **13**, 19.

Safonov, Yu. D. (1968) The biohydraulic mechanism producing heart sounds. *Cor Vasa* **10**, 295.

Sakai, A., Feigen, L. P. and Luisada, A. A. (1971) Frequency distribution of heart sounds in normal man. *Cardiovas. Res.* **5**, 358.

Van Vollenhoven, E., Van Rotterdam, A., Derenbos, T. and Schelsinger, F. G. (1969) Frequency analysis of heart murmurs. *Med. & Biol. Eng.* **7**, 227.

Yoganathan, A. P., Gupta, R., Udwadia, F. E., Miller, J. W., Corcoran, W. H., Sarma, R., Johnson, J. L. and Bing, R. J. (1975) Use of the fast Fourier transform for the frequency analysis of the first heart sound in normal man. Accepted by *Med. & Biol. Eng.*

Yoganathan, A. P., Gupta, R. and Corcoran, W. H. (1975) The fast Fourier transform in the analysis of biomedical data. Accepted by *Med. & Biol. Eng.*

Chapter 12

Fast Fourier transform in the analysis of biomedical data*

Ajit P. Yoganathan Ramesh Gupta William H. Corcoran

Chemical Engineering Laboratory, California Institute of Technology, Pasadena, California 91125, USA

Abstract—*The fast Fourier transform (f.f.t.) is a powerful technique which facilitates analysis of signals in the frequency domain. This paper reviews some of the important features of the fast Fourier transform which are relevant to its increasing application to biomedical data. A distinction is made between the power spectrum of ergodic signals, computed from the autocorrelation function, and the frequency spectrum of nonstationary biomedical signals. The major practical pitfalls that are encountered in applying the f.f.t. technique to biomedical data are discussed, and practical hints for avoiding such pitfalls are suggested.*

Keywords—*Biomedical data, Frequency analysis, Fast Fourier transform*

Introduction

THIS article is written as a review paper on the application of the fast Fourier transform (f.f.t.) in the analysis of biomedical data. Many articles have been written about the fast Fourier transform in the electrical-engineering literature (Special issue on fast Fourier transform, 1969; BERGLAND, 1969; COCHRAN *et al.*, 1967). As expected, however, these articles are oriented towards applications in the electrical-engineering field. Since the f.f.t. algorithm for the computation of Fourier coefficients was reported by COOLEY and TUKEY (1965), this technique has found increasing applications in the biomedical field (RAUTERKUS *et al.*, 1966; GUPTA *et al.*, 1975; YOGANATHAN *et al.*, 1975).

Physically, the Fourier transform $S(f)$ represents the distribution of signal strength with frequency (i.e. a density function). The fast-Fourier-transform algorithm is a method for computing the finite discrete Fourier transform (d.f.t.) of a series of N complex data points in approximately $N \log_2 N$ operations. Prior to the formulation of the f.f.t. algorithm, computing the finite discrete Fourier transform involved approximately N^2 operations. The f.f.t. algorithm has not only reduced the computation time from several minutes to seconds, but has also substantially reduced the round-off errors and the computation costs from dollars to cents. In fact, both computation time and round-off error are reduced by a factor of about $1/N \log_2 N$. If $N = 2048$ (i.e. 2^{11}), then $N \log_2 N = 22\,528$ and $N^2 = 4\,193\,304$. Hence the conventional method would require an effort of more than 180 times that required by the f.f.t.

The discrete Fourier transform is a transform in its own right, like the Fourier integral transform or the Fourier series transform. It is a powerful reversible mapping operation for time series. Its mathematical properties are analogous to those of the Fourier integral transform.

The discrete Fourier transform is defined by

$$S(k) = \frac{1}{N} \sum_{r=0}^{N-1} s(r) \exp(-2\pi irk/N) \quad . \quad . \quad (1)$$

for $r = 0, 1, 2, \ldots, N-1$, and $k = 0, 1, \ldots M-1$. $i = \sqrt{-1}$ where $S(k)$ is the kth coefficient of the d.f.t. and $s(r)$ is the rth sample of the time series, consisting of N samples. The inverse transform is given by

$$s(r) = \sum_{k=0}^{N-1} S(k) \exp(2\pi irk/N) \quad . \quad . \quad . \quad . \quad (2)$$

The Fourier transform for a continuous signal may be written as:

$$S(f) = \int_{-\alpha}^{\alpha} s(t) \exp(-2\pi ift) dt \quad . \quad . \quad . \quad . \quad (3)$$

and the inverse transform as

$$s(t) = \int_{-\alpha}^{\alpha} S(f) \exp(2\pi ift)\, df \quad . \quad . \quad . \quad . \quad (4)$$

for $-\alpha < f < \alpha$, and $-\alpha < t < \alpha$

where $S(f)$ describes the frequency-domain function and $s(t)$ describes the time-domain function.

In reality, however, the signal is usually of finite duration. Therefore, one sets $s(t) = 0$ for $t < 0$, and $t > T$ when the signal is available over the time range $(0, T)$.

*First received 10th February and in final form 7th March 1975

It is more customary to use the power spectrum $P(f)$ instead of the amplitude or voltage spectrum. The power spectrum is given by

$$P(f) \quad \lim_{T\to\infty} \frac{1}{T} |S(f)|^2 \quad . \quad . \quad . \quad . \quad . \quad (5)$$

In order to make $P(f)$ relatively independent of the time duration T of the data, the factor $1/T$ is inserted in the above equation.

Concept of the power spectrum

Using the property of Fourier transforms that

$$S^*(f) = \tilde{F}\,[s(-t)] \quad . \quad . \quad . \quad . \quad . \quad . \quad (6)$$

where the asterisk indicates a complex conjugate, and $\tilde{F}$ indicates Fourier transform of [ ], eqn. 5 may be rewritten as:

$$P(f) = \lim_{T\to\infty} \frac{1}{T} S(f)\,S^*(f) \quad . \quad . \quad . \quad . \quad (7)$$

From the convolution theorem and eqn. 6

$$P(f) = \lim_{T\to\infty} \frac{1}{T} \tilde{F}\left[\int_{-T}^{+T} s(-t')\,s(t-t')\,dt'\right] \quad (8)$$

Now we can define

$$R(\tau) = \lim_{T\to\infty} \frac{1}{T} \int_{-T}^{+T} s(t'')\,s(\tau+t'')\,dt'' \quad . \quad . \quad (9)$$

where $t'' = -t'$.

From eqn. 9, it is seen that $P(f)$ is just the Fourier transform of $R(\tau)$, i.e.

$$P(f) = \int_{-\infty}^{\infty} R(\tau) \exp(-2\pi i f\tau)\,d\tau \quad . \quad . \quad . \quad (10)$$

The function $R(\tau)$ is commonly known as the autocorrelation function of the continuous time signal $s(t)$. Eqn. 10 is widely used in the field of electrical engineering. The equation states that the power spectrum of a random continuous signal is the Fourier transform of its autocorrelation function. This is known as the Wiener–Kinchine theorem (LEE, 1960). Another form of this theorem is:

$$P(f) = \tilde{F}[R(\tau)]$$

$$= \int_{-\infty}^{\infty} \overline{s(t)\,s(t+\tau)} \exp(-2\pi i f t)\,d\tau \quad . \quad (10a)$$

The above power-spectrum approach is profitably applied when the signal consists of a recurring phenomena, plus any random noise. The autocorrelation step (eqn. 9) in the power-spectrum-analysis technique helps to nullify the random components (i.e. noise) in the signal. Therefore, the Fourier transform of the resulting autocorrelation function (eqn. 10) then yields the relative power spectrum of the recurring components of the original time signal. This technique is extremely attractive, especially since it more or less eliminates the contribution of random noise to the original signal.

If we step back, however, and look at the underlying conditions in the derivation of eqn. 10, it becomes apparent that this technique cannot be used in most biomedical applications (e.g. heart sounds, arterial sounds etc.). Such signals cannot be subject to Fourier analysis by this technique because they are nonstationary in nature, transient, and changeable in form. Implicit in eqn. 10*a* is the condition that $\overline{s(t)\,s(t+\tau)}$ depends only on τ, i.e. the source must be ergodic. For nonstationary sources, the power spectrum obtained from eqn. 10 would be a function of both frequency and time. This condition is in total contradiction to the concept of frequency-domain descriptions. Therefore the autocorrelation step to yield the power spectrum can only be applied to ergodic, and hence stationary, signals or sounds.

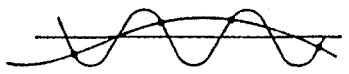

Fig. 1 Aliasing effect: a high-frequency signal impersonating a low-frequency signal

In the case of biomedical data, for example the heart sounds, the Fourier analysis is applied directly, using the COOLEY and TUKEY algorithm (1965), to each individual sound, and then an average frequency spectrum may be obtained for 10 such sounds. This method of analysis is described in detail in the papers by GUPTA *et al.* (1975) and YOGANATHAN *et al.* (1975). The approach yields the frequency distribution of the relative sound intensity for each sound, without assuming that the sounds are stationary or periodic. The frequency spectrum obtained in the analysis of such biomedical data should not be confused with the power spectrum obtained via the Fourier transform of the autocorrelation function.

Computing the frequency spectrum by the direct-Fourier-transformation method does have one drawback. In this analysis technique, it is not possible to distinguish between the signal and background noise. This problem is not major, however, in most experimental situations because it is possible to produce signal levels which are large compared to the baseline noise level (i.e. a high signal-to-noise ratio).

Convolution theorem

The convolution theorem states that the product of two Fourier transforms $S(f)\,R(f)$ is itself the Fourier transform of a third time function, which is

is known as the convolution of $s(t)$ and $r(t)$. It is defined as:

$$s(t) \circledast r(t) = \int_{-\alpha}^{\alpha} s(t')\, r(t-t')\, dt' \quad . \quad . \quad . \quad . \quad (11)$$

Thus the product of two Fourier transforms $S(f)\, R(f)$ may be written as

$$S(f)\, R(f)$$

$$= \int_{-\alpha}^{\alpha} \left[\int_{-\alpha}^{\alpha} s(t')\, r(t-t')\, dt' \right] \exp(-2\pi i f t)\, dt$$

$$= \int\int_{-\alpha}^{\alpha} s(t')\, r(t'') \exp[-2\pi i f(t'+t'')]\, dt''\, dt' \quad (12)$$

where t' and t'' are dummy variables, and $t = t'+t''$. Similarly, we have

$$s(t)\, r(t) = \int_{-\alpha}^{\alpha} \left[\int_{-\alpha}^{\alpha} S(g)\, R(f-g)\, dg \right] \times \exp(2\pi i f t)\, df \quad . \quad (13)$$

The above mathematical expression states that the product of $s(t)\, r(t)$ in the time domain is the inverse Fourier transform of the frequency convolution

$$S(f) \circledast R(f) = \int_{-\alpha}^{\alpha} S(g)\, R(f-g)\, dg \quad . \quad . \quad (14)$$

Pitfalls

In the following Sections we will discuss the major pitfalls that are encountered in analysing biomedical data using the f.f.t. technique. If care is taken in avoiding these pitfalls, the f.f.t. analysis will give a high degree of accuracy.

(*a*) *Time sampling and aliasing:* For purposes of analysis, most continuous signals $s(t)$ will be digitised at a fixed rate and converted to digital signals via an analogue-to-digital convertor. These digital data may then be used for calculations on the computer. The digital signal may be considered as the result of multiplying the original continuous signal by a signal $a(t)$ which consists of a train of delta functions. The quantity $a(t)$ is defined as:

$$a(t) = \sum_{n=-\alpha}^{+\alpha} \delta(t-n\Delta t) \quad . \quad . \quad . \quad . \quad . \quad . \quad (15)$$

where Δt = (digitisation rate)$^{-1}$. This procedure produces an impulse-modulated signal $s_i(t)$, where

$$s_i(t) = s(t)\, a(t) \quad . \quad . \quad . \quad . \quad . \quad . \quad . \quad . \quad (16)$$

Using the convolution theorem

$$S_i(f) = \int_{-\alpha}^{\alpha} S(f-f')\, A(f')\, df' \quad . \quad . \quad . \quad (17)$$

where $A(f)$ is the Fourier transform of $a(t)$. Using the result that the Fourier transform of a train of delta functions

$$a(t) = \sum_{n=-\alpha}^{\alpha} \delta(t-n\Delta t),$$

is

$$A(f) = \frac{1}{\Delta t} \sum_{n=-\alpha}^{\alpha} \delta\left(f - \frac{n}{\Delta t}\right) \quad . \quad . \quad . \quad . \quad (18)$$

and substituting this into eqn. 17 yields

$$S_i(f) = \int_{-\alpha}^{\alpha} S(f-f') \frac{1}{\Delta t} \sum_{n=-\alpha}^{\alpha} \delta\left(f' - \frac{n}{\Delta t}\right) df'$$

$$= \frac{1}{\Delta t} \sum_{n=-\alpha}^{\alpha} S\left(f - \frac{n}{\Delta t}\right) \quad . \quad . \quad . \quad . \quad . \quad (19)$$

Eqn. 19 shows that the impulse-modulated signal $s_i(t)$ has a transform period of $1/\Delta t$, and if $S(f)$ is zero when $f \geqslant 1/2\Delta t$, then $S_i(f)$ is simply a periodic version of $S(f)$. Therefore it is possible to recover $S(f)$ from $A_i(f)$ by multiplying $S_i(f)$ by $R(f)$ where

$$R(f) = \begin{cases} \Delta t, \text{ when } |f| \leqslant \dfrac{1}{2\Delta t} \\ 0, \text{ when } |f| > \dfrac{1}{2\Delta t} \end{cases} \quad . \quad . \quad . \quad (20)$$

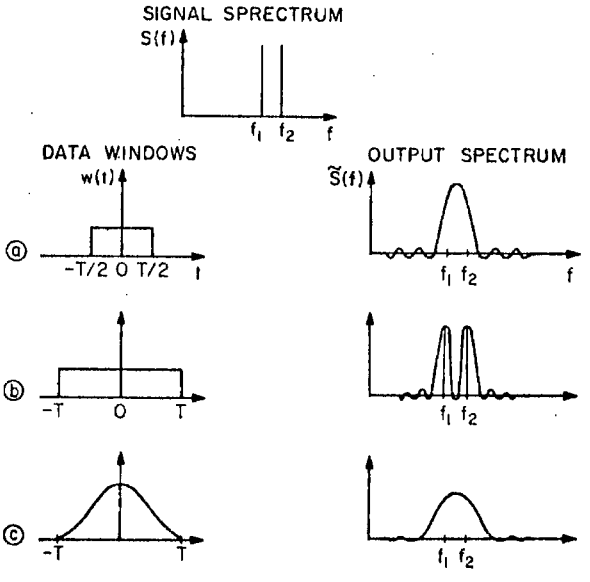

Fig. 2 Effect of data-window duration and shape on the frequency spectrum

The term 'aliasing' refers to the fact that high-frequency components of a time function are capable of impersonating low frequencies if the digitisation rate is too low. This fact is illustrated in Fig. 1. Because the digitisation rate is too low, a high-frequency and a low-frequency sine wave share identical points. To ensure that such an error does not creep in, the Nyquist criterion is used. This criterion demands that the digitisation rate should be at least large enough to be able to sample the highest frequency present in the signal at least twice during each cycle. The Nyquist criterion may be mathematically obtained by referring to eqns. 19 and 20. If the sampling interval is such that $S(f)$ falls to zero before $|f| = 1/2\Delta t$, then it is possible to recover $S(f)$ from $S_i(f)$ [i.e. $s(t)$ from $s_i(t)$]. If $S(f)$ is, however, not zero above $f_{Ny} = 1/2\Delta t$, then frequency components above $1/2\Delta t$ in $S(f)$ appear in $S_i(f)$ in the frequency range $-(1/2\Delta t) \leqslant f \leqslant (1/2\Delta t)$. The frequency f_{Ny} is commonly known as the Nyquist frequency.

Thus the operation of analysing a finite length of recorded data is equivalent to multiplying the actual signal $s(t)$ by the window $w(t)$. Use of eqn. 14 shows that the finite-time interval transformation $\tilde{S}(f)$ is the convolution of the transform of $s(t)$ and $w(t)$, i.e.

$$\tilde{S}(f) = \int_{-\alpha}^{\alpha} S(f')\, W(f-f')\, df' \quad . \quad . \quad . \quad (23)$$

where $W(f)$ is the transform $w(t)$.

The data window given in eqn. 21 is only an illustrative example. One may use any reasonable data window. Such a window will produce a spectral window $W(f)$ which will be centred around $f \equiv 0$ (see Fig. 3), but with sidelobes which will dampen out as f moves away from zero. Further mention will be made about these sidelobes in the section called 'Leakage'. For a small time interval T, $\tilde{S}(f)$ may give a very distorted representation of $S(f)$.

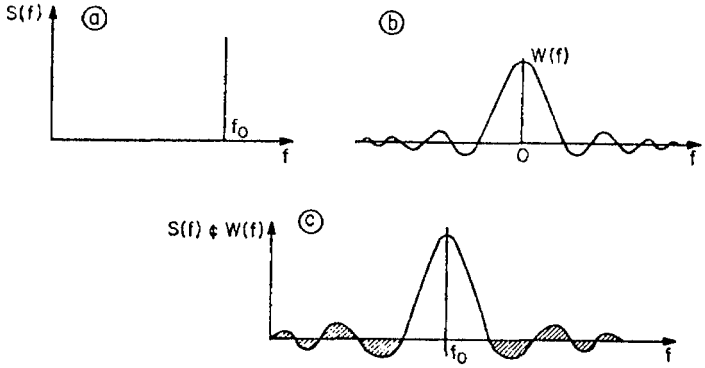

Fig. 3 Leakage of energy into the side lobes due to the analysis of a finite record of data

(*b*) *Finite-length records*: In real life, it is only possible to obtain a signal of finite length. Therefore a certain amount of truncation error arises when $s(t)$ is known only for a finite time interval

$$-T/2 \leqslant t \leqslant T/2.$$

Consider a rectangular data window (Fig. 2*a*) defined by

$$w(t) = \begin{cases} 1 & |t| \leqslant T/2 \\ 0 & |t| > T/2 \end{cases} \quad . \quad . \quad . \quad . \quad . \quad . \quad (21)$$

where $-\alpha < t < \alpha$. Then the signal actually measured in the time interval T is given by

$$\hat{s}(t) = s(t)\, w(t) \quad . \quad . \quad . \quad . \quad . \quad . \quad . \quad . \quad (22)$$

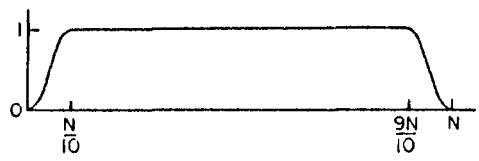

Fig. 4 Cosine data window

That, results because the window $W(f-f')$ will be wide, which leads to values of $S(f')$ that are far removed from $f'-f$ contributing to $\tilde{S}(f)$. As T becomes large, however, the distortion diminishes, and in the limit as $T \to \alpha$, the data window becomes a generalised function $w(t) = 1$, and the transform component at frequency f can be determined. Thus, as $T \to \alpha$, $W(f-f')$ becomes a delta function about $f' = f$, and $\tilde{S}(f) \to S(f)$.

Fig. 2 shows the effect of window shape and duration on the final transform. Only one main peak appears in the output transform of windows *a* and *c* because the two input peaks at frequencies f_1 and f_2 are fused into one peak. This result appears because a data window which was too narrow was used. In windows a and b, the sharp corners also contribute to the spurious peaks which appear in the frequency spectum.

It is possible to divide the finite record length into subsegments and take the Fourier transform over each subsegment. The power spectrum is then estimated by averaging these spectra. This approach is useful when computations have to be performed on a machine with very limited core storage. The

problem of statistical stability of the estimated spectrum has been discussed by WELCH (1967).

(*c*) *Leakage:* The problem of leakage is inherent in the Fourier analysis of any finite record analysis. Consider a rectangular data window and a pure sine wave; if the sine wave is infinite in the time domain, its Fourier transform will result in a single value in the frequency domain (i.e. its fundamental frequency). In Fig. *3a*, this is shown as a single-impulse function of frequency f_0. As we have seen earlier, multiplication of this impulse by the data window in the time domain is equivalent to convolution in the frequency domain. The resulting function is shown in Fig. 3*c*.

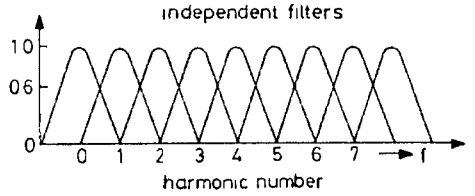

Fig. 5 Picket-fence effect

This function is not localised about a single frequency, but contains a series of spurious peaks known as side lobes as also seen in Figs. 2*a* and *b*. When such a phenomenon occurs, the object is to localise the contribution of a given frequency by reducing the amount of leakage through these spurious peaks. One way to achieve that goal is to apply a window to the time series which has lower side lobes in the frequency domain than a rectangular window. One such data window is the cosine window shown in Fig. 4 (BINGHAM *et al.*, 1967; BERGLAND, 1969). Other windows that can be used are the Hanning window (BLACKMAN and TUKEY, 1958), the Dolph–Chebyshev window (HELMS, 1968), and the Parzan window (WELCH, 1967). As a word of caution, whatever the type of window used, it must be applied to only actual physical data and not to any of the zeros which are added to increase the duration of the time signal.

(*d*) *Picket-fence effect:* Ideally, each Fourier coefficient in the output of the f.f.t. algorithm should represent a rectangular-shaped bandpass filter. In practice, however, because of the leakage effect as discussed in (*c*), each of these filters is deformed to a function of the form $\sin \pi f T/\pi f$, centred at the frequency of the corresponding filter. The main lobes of these filters have been plotted in Fig. 5 to show the nature of the output of the f.f.t. algorithm. As shown, these main lobes act as N independent filters. This means, for example, that an input of the form e^{iwt} with frequency $w = 2\pi/T\,n$, where n is an integer, would result in a response of unit amplitude at the nth harmonic and a response of zero at all other harmonics. Thus the picket-fence effect does not take place when the signal being analysed is one of these discrete frequencies. It will manifest itself when the signal frequency is not one of the above discrete frequencies. For example, a signal between the fourth and fifth harmonics will be seen by both the fourth and fifth harmonic filters but at a value lower than unity. In the worst case, when the signal frequency is exactly midway between two harmonics, the amplitude of the signal will be reduced by a factor of 0·637 in both the harmonic filters. This reduction produces a ripple in the resulting spectrum which is equivalent to viewing the real spectrum through a picket fence.

In practice, the picket-fence effect is not as severe as the above discussion may seem to imply. In the majority of cases, the signal being analysed is not a pure sinusoid but will have a broad frequency content.

It is possible to reduce the picket-fence effect by use of an interpolation function or by modification of the computation algorithm. The latter approach consists of computing the Fourier coefficients at frequencies between the original harmonics. Since the frequency spacing between harmonics is related to the reciprocal of the record length T, the above approach is carried out by increasing the length of the actual physical data by adding a set of samples which are identically zero. Also the use of a data window, other than the rectangular window discussed in (*b*), normally reduces the picket-fence effect by widening the main spectral lobes.

(*e*) *Frequency resolution.* The f.f.t. analysis is used as a tool to study the frequency content of a given time signal. In such an analysis, it may be required to resolve two frequency peaks, which are close to each other, in a continuous signal of finite time duration. The problem of resolving these peaks is analogous to the Rayleigh problem in optics. The Rayleigh criterion states that two sinusoids of frequencies f_1 and f_2 are just resolved if $T = 1/2(f_2 - f_1)$ and are well resolved if $T = 1/(f_2 - f_1)$. T is the record length of the actual physical data.

In practice, the biomedical signals are not pure sinewaves. Thus, to distinguish two peaks at frequencies g_1 and f_2, one may use the criterion

$$T > \frac{1}{f_2 - f_1} \quad \ldots\ldots\ldots\ldots \quad (24)$$

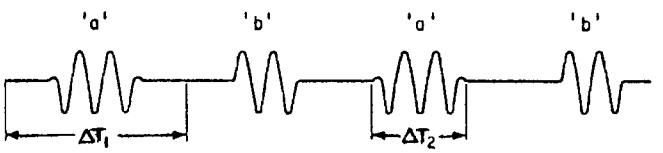

Fig. 6 (a) Proper selection of data window of sound 'a' (ΔT_1)

(b) Incorrect selection of data window of sound 'a' (ΔT_2)

If the lowest expected in the signal is f_{min}, then to observe it in the frequency spectrum, the value of T is computed from eqn. 24, and is

$$T > \frac{1}{f_{min}} \quad . \quad . \quad . \quad . \quad . \quad . \quad . \quad . \quad . \quad . \quad (25)$$

The ability to pick out peaks (resolution) depends not only on the duration of the data window but also on the shape of the window. This fact is illustrated in Fig. 2. In Figs. 2*a* and *b*, both windows have the same shape but different durations, while windows in Figs. 2*b* and *c* have the same duration but different shapes.

(*f*) *Selection of data for analysis:* Blind selection of data in the time domain usually leads to incorrect Fourier spectra. In most instances, the time signals obtained in biomedical data are nonstationary and transient in nature. The proper selection of data is of utmost importance.

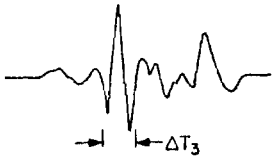

Fig. 7 Time signal of typical first heart sound

Referring to Fig. 6, for example, if the analysis of sounds 'a' are required, the data-window length must be chosen so that it covers the entire signal. Selection of a data window too close to the beginning and the end of the time signal can lead to artefacts in the f.f.t. analysis and produce spurious peaks in the spectrum. Also, the base line on either side of the signal being analysed should be relatively free of background noise.

In the analysis of transient biomedical signals, such as the first heart sound, one may want to use the f.f.t. algorithm for each component of the sound. This procedure may not be possible if the time duration of the component is shorter than the cycle time of the frequencies involved. In Fig. 7, for example the f.f.t. analysis cannot be used to analyse the first component contained in ΔT_3. In such situations, extreme care should be exercised in the analysis and interpretation of f.f.t. results.

Acknowledgment—Funds for support of the work described here were provided by the Donald E. Baxter Foundation. That support is gratefully acknowledged.

References

BERGLAND, G. D. (1969) A guided tour of the fast Fourier transform. *IEEE Spectrum* **6**, 41.

BINGHAM, C., TUKEY, J. W. and GODFREY, M. D. (1967) Modern techniques of power spectrum estimation. *IEEE Trans.* **AU-15**, 56.

BLACKMAN, R. and TUKEY, J. W. (1958) *The measurement of power spectra*. Dover, New York.

COCHRAN, W. T., COOLEY, J. W., FAVIN, D. L., HELMS, H. D., KAENEL, R. A., LANG, W. W., MALING, G. C. Jun., NELSON, D. E., RADER, C. M. and WELCH P. D. (1967) What is the fast Fourier transform? *Proc. IEEE* **55**, 1664.

COOLEY, J. W. and TUKEY, J. W. (1965) An algorithm for machine calculation of complex Fourier series. *Math, Comput.* **19**, 297.

GUPTA, R., MILLER, J. W., YOGANATHAN, A. P., KIM, B. M., UDWADIA, F. E. and CORCORAN, W. H. (1975) Spectral analysis of arterial sounds: a noninvasive method of studying arterial disease. Accepted for publication in the *Journal of Medical and Biological Engineering*

HELMS, H. D. (1968) Nonrecursive digital filters: design method for achieving specifications of frequency response. *IEEE Trans.* **AU-16**, 336.

LEE, Y. W. (1960) *Statistical theory of communications*. Wiley, New York.

RAUTERKUS, T., FELTZ, J. F. and FICKES, J. W. (1966) Frequency analysis of Korotkoff blood pressure sounds using Fourier transform. US Air Force School of Aerospace Medicine, Brooks AFB, Texas. Tech. Report 66-8.

WELCH, P. D. (1967) The use of the fast Fourier transform for the estimation of power spectra: a method based on time averaging over short, modified periodograms. *IEEE Trans.* **AU-15**, 70.

YOGANATHAN, A. P., GUPTA, R., UDEWADIA, F. E., MILLER, J. W., CORCORAN, W. H., SARMA, R., JOHNSON, J. L. and BING, R. J. (1975) Use of the fast Fourier transform for the frequency analysis of the first heart sound in normal man. Accepted for publication in the *Journal of Medical and Biological Engineering*.

Special issue on the fast Fourier transform (1969) *IEEE Trans.* **AU-17**.

La transformation rapide de Fourier dans l'analyse des données biologiques

Sommaire—La transformation rapide de Fourier est une technique puissante qui facilite l'analyse des signaux dans le domaine des fréquences. Le présent article passe en revue quelques uns des traits importants de la transformation rapide de Fourier se rapportant à son application de plus en plus importante en données biomédicales. On fait la distinction entre le spectre de puissance des signaux ergodiques calculés à partir de la fonction d'autocorrélation, et le spectre de fréquence des signaux biomédicaux non stationnaires. Les pièges pratiques principaux rencontrés dans l'application de la technique de transformation rapide de Fourier sont débattus et des conseils pratiques pour éviter de tels pièges sont suggérés.

Chapter 13

IN VITRO SOUND ANALYSIS OF PROSTHETIC AORTIC VALVES

Six different aortic prostheses were used in the study. The experiments were conducted in the pulse duplicator system, and the valves were mounted in the flow channel used in the pressure drop and velocity measurement studies. The sounds were measured by a Millar phonocatheter (PC-480) which was placed in the flow channel via pressure tap II. Therefore sounds in the near vicinity of the prostheses were readily obtained. Experiments were conducted with normally functioning prostheses at a heart rate of 70 beats per minute, an average cardiac output of about 5 liters/min, and a pressure range of 120/80 mm Hg. The test fluid used in the pulse-duplicator was a polyol solution with a viscosity of 3.5 cp.

It was possible to obtain excellent records of the in vitro closing sounds of the prostheses. The closing sound of an aortic prosthesis is one of the main components of the second heart sound. The in vitro opening sounds of the prostheses obtained from the measurements in the pulse duplicator system, however, did not correspond too well with the opening sounds observed in patients with implanted aortic prostheses. The opening sound of an aortic prosthesis is associated with the first heart sound. The first heart sound as stated previously is associated with the pumping of blood from the ventricles into the pulmonary and aortic arteris. More experiments will have to be performed, and some modifications may have to be made in the experimental technique, in

order to obtain more reasonable opening sounds in the pulse-duplicator.

The in vitro sounds obtained from the phonocatheter were passed through a heart-sound amplifier and filtered at 12 db/octave with a cut-off frequency of 100 Hz. The sounds were then recorded, together with the aortic pressure as a time base on a HP-3960 tape recorder. The data were then digitized at a rate of 2000 points per second on the computer, and the time plots were generated. The closing sounds of the valves were then selected as described in Chapters 10, 11 and 12, and 10 to 15 of these sounds were analyzed by the FFT technique. By analyzing 10 to 15 closing sounds, any variability introduced by the pulse-duplicator would be averaged out. An example of the frequency spectrum obtained for the closing sound of an aortic prosthesis is shown in Figure 1. The spectrum in Figure 1 shows that in the frequency range of about 10 to 200 Hz there exist some sharp resonant peaks, and beyond that range there are some smooth, wide peaks. This phenomenon was observed in the frequency spectra of all the valves studied. Resonant peaks larger than 2 db in height that are observed in the frequency spectra of the closing sounds of the different valves are listed in Table 1. No resonant peaks were observed above 750 Hz. The reproducibility of the results were verified by performing sound recordings on each valve about two weeks after the first set of experiments and obtaining sound spectra which were within ±10 Hz of the original sound spectra.

The results of the frequency analysis indicate that with the exception of the Björk-Shiley valve, the other five valves have sharp resonant peaks which are quite similar. The six prostheses, however, have characteristic smooth, wide resonant peaks which distinguish each one of them.

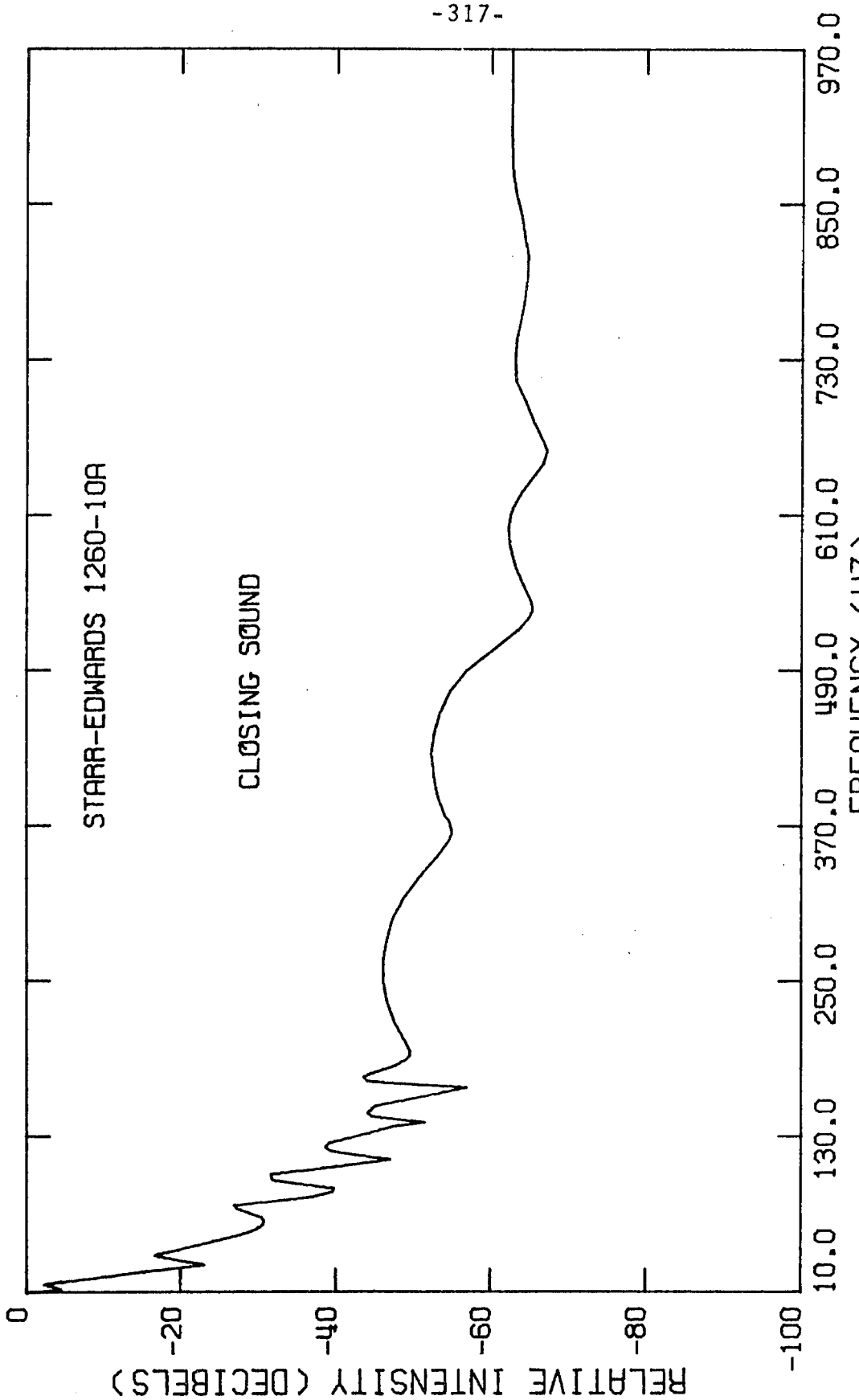

Fig. 1. Frequency spectrum of the closing sound of the Starr-Edwards 1260-10A valve

Table 1. Resonant Frequencies in the Frequency Spectra of the Closing Sound of the Aortic Prostheses

Name of Valve	Resonant Frequency Peaks	
	Sharp Peaks	Smooth Wide Peaks
Starr-Edwards 1260-10A	39,77,101,122,148,176	266,426,599
Smeloff-Cutter A5	29,79,102,125,157,186	314,522,720
Starr-Edwards 2400-10A	39,65,106,132,157,184	283,474,586
Cooley-Cutter A25	32,74,103,122,154,177	263,356,512
Starr-Edwards 2320-10A	39,77,100,132,159	218,372,586
Björk-Shiley 27XMBRP	31,55,98,133,165,198,232,270,321	394,665

In order to use the frequency analysis technique as a method to monitor the functional integrity of a prosthetic aortic valve, it is necessary to use the frequency spectrum of the closing sound of each normally functioning prosthesis as its own base-line, and then see how it changes when pathologically realistic modifications are made to the prosthesis. As discussed in Chapter 7, the Björk-Shiley aortic prosthesis has been observed to have problems associated with it that impede the opening of the disc. Some of the Björk-Shiley valves that have been recovered only opened to an angle of about 15°. Therefore a sound experiment was performed with a normally functioning Björk-Shiley valve (opening angle 60°). The valve was then constrained in a pathologically realistic way to open only to an angle of about 15°, and sound measurements were made. Both experiments were conducted under physiologically reasonable conditions. It was observed that the intensities of the closing sounds for both experiments were only slightly different and could not be differentiated by the human ear. It was possible to listen to the sounds of the prosthesis via the audiophone output on the heart-sound amplifier, which was set at a constant gain for both experiments. The frequency spectra of the closing sounds, however, were very different as shown in Figures 2 and 3. The frequency spectrum of the normally functioning Björk-Shiley valve (Figure 2) had nine sharp resonant peaks in the frequency range of 25 to 325 Hz, and two smooth, wide peaks at 394 and 665 Hz respectively. The frequency spectrum of the closing sound of the malfunctioning valve (Figure 3), however, had no sharp resonant peaks and had three smooth, wide peaks at 58, 234 and

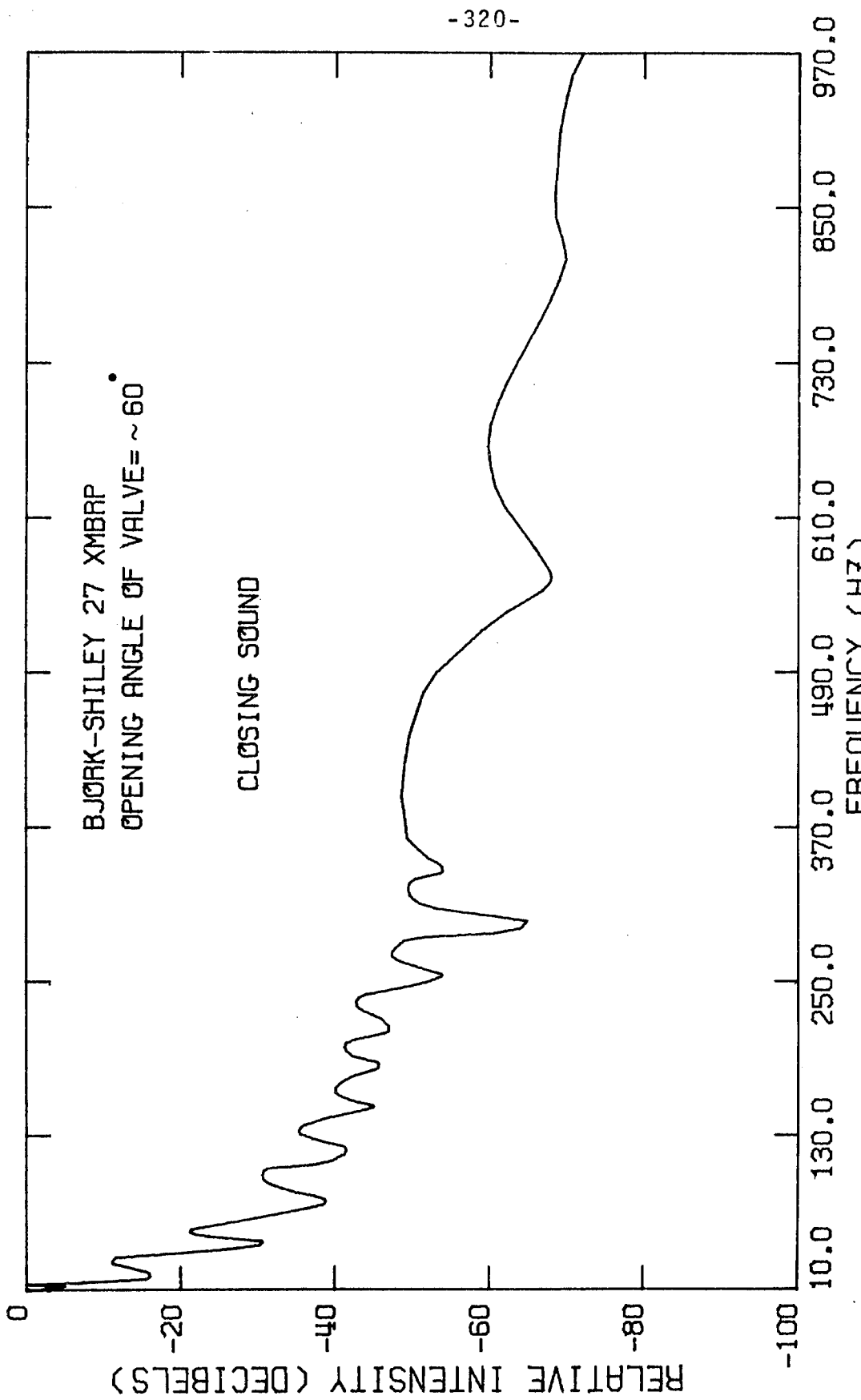

Fig. 2. Frequency spectrum of the closing sound of the normally functioning Björk-Shiley valve

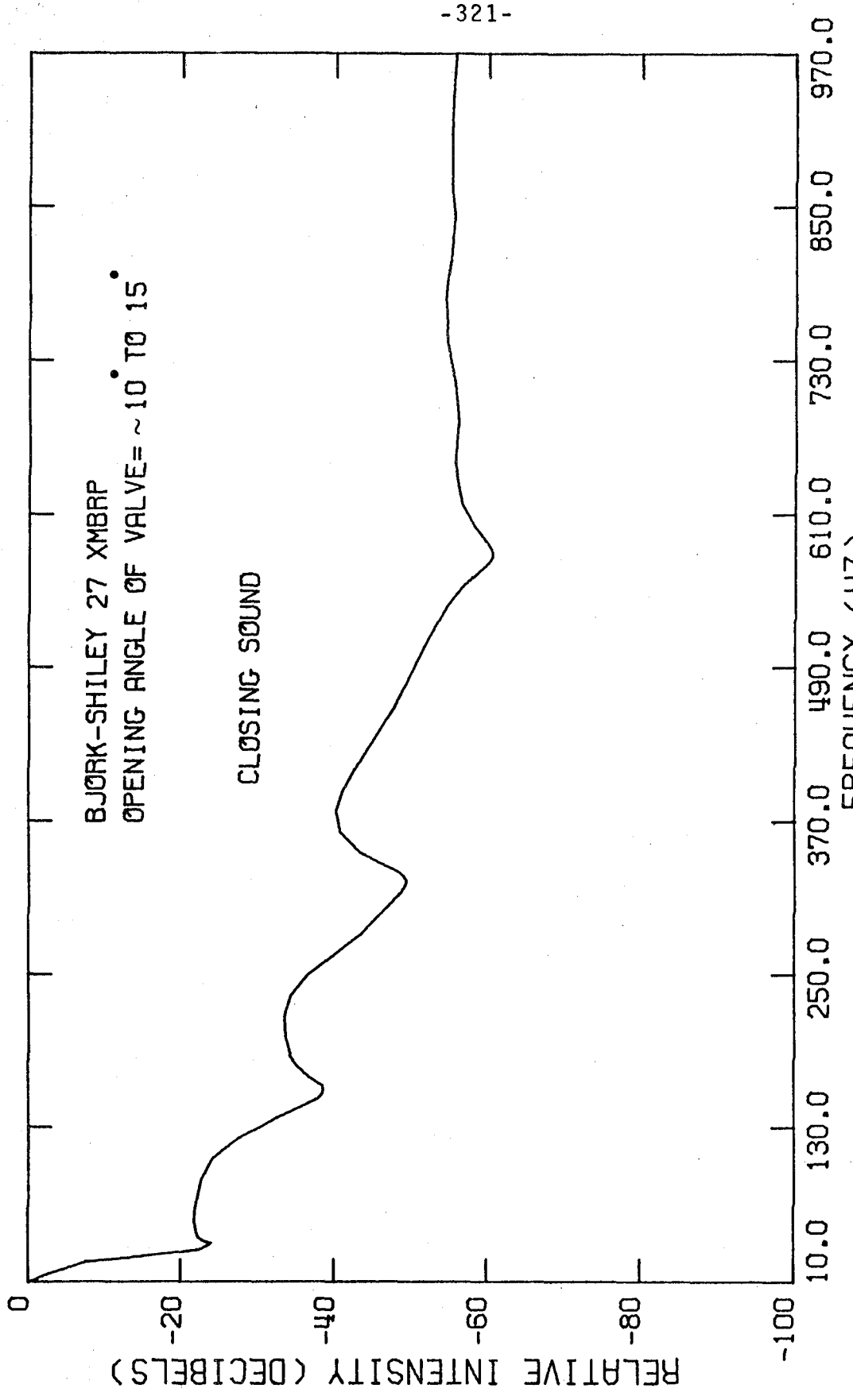

Fig. 3. Frequency spectrum of the closing sound of the malfunctioning Björk-Shiley valve

378 Hz respectively. These results indicate quite clearly that the frequency contents of the closing sounds of the normally operating and malfunctioning Björk-Shiley valve are different and distinguishable. Such a comparative in vitro frequency analysis has not been reported before in the literature.

At present physicians listen to the intensity of the closing click of the Björk-Shiley aortic valve to judge if the valve is opening completely. The in vitro experiments conducted in the pulse duplicator suggest strongly that the change in sound intensity of a normally functioning valve and a valve that opens to about 15° cannot be detected by the human ear. If a physician were to use the intensity of the closing click of the Björk-Shiley aortic valve as a method for detecting the malfunctioning of the valve he could endanger the life of his patient. A comparison of the frequency spectra of the closing sounds of the valve operating under the two different conditions, however, shows that the resonant frequency characteristics are very different, indicating that the valve is not functioning normally.

Chapter 14

SUMMARY AND RECOMMENDATIONS

The frequency analysis of the first and second heart sounds in normal man indicates that there is variability in the frequency spectra from person to person. The resonant peaks of each sound, however, lie within a certain frequency range. Therefore, if a frequency spectrum contains resonant peaks outside these ranges it may be inferred that the sound-producing mechanism is changing and attributable to some pathological condition. It is recommended that studies of patients with particular types of heart disease such as aortic stenosis, aortic regurgitation, and mitral regurgitation be conducted using the FFT analysis to establish the resonant frequency patterns for each disease. For meaningful studies a large group (25 to 50) of patients should be used. Frequency analysis appears to have some major value in diagnosis in some cardiovascular problems.

An initial *in vitro* study of the frequency spectra of the closing sounds of six aortic prostheses indicates that each valve has distinguishable resonant frequency characteristics. The initial comparative study on the Björk-Shiley aortic valve indicates that the frequency spectrum of the closing sound of the normally functioning valve contains nine sharp resonant peaks and two smooth, wide peaks at 394 and 665 Hz, while the frequency spectrum of the malfunctioning valve contains only smooth, wide peaks at 58, 234 and 378 Hz. The frequency analysis of the closing sounds of the Björk-Shiley aortic prosthesis suggests that the FFT analysis could be a useful *in vitro* tool

in diagnosing malfunctioning valve prostheses.

The author therefore recommends a detailed *in vitro* study of the frequency characteristics of the sounds produced by prosthetic valves in the following order:

(1) Obtain base-line frequency spectra of the opening and closing sounds of different designs of prostheses;

(2) Put prostheses into some known failure modes, and obtain sound spectra. The failure modes used should be pathologically realistic and be those observed in recovered valves of a given design;

(3) Characterize the frequency spectra of the different failure modes of a given design of prosthesis.

The suggested experiment should be performed in a pulse duplicator as well as in test animals, such as dogs, if possible. The sound measurements on the dogs should be done non-invasively.

The initial results obtained with the Björk-Shiley valve suggest that if the frequency spectra of the heart sounds of the heart-valve patient are monitored non-invasively on a periodic basis, malfunctioning of the valve should be detectable by observing changes in the spectra. The frequency spectra obtained initially should be used as base-line spectra, assuming that the valve was implanted correctly. At present frequency analysis is not easily possible at the patient's bedside. Microprocessors could be designed, however, to give the cardiologist a frequency-spectrum plot in a couple of minutes.